

Effect of GFRP-Concrete Bond Characteristics on the Flexural and Serviceability Behaviour of GFRP-RC Beams

Omar Gouda Mohamed

A Thesis
In the Department of
Building, Civil, and Environmental Engineering

Presented in Partial Fulfillment of the Requirements for the
Degree of Doctor of Philosophy (Civil Engineering) at
Concordia University
Montréal, Québec,
Canada

July 2022

© Omar Gouda Mohamed, 2022

CONCORDIA UNIVERSITY

School of Graduate Studies

This is to certify that the thesis prepared

By: Omar Gouda Mohamed

Entitled: Effect of GFRP-Concrete Bond Characteristics on the Flexural and Serviceability
Behaviour of GFRP-RC Beams

and submitted in partial fulfillment of the requirements for the degree of

Doctor of Philosophy (Civil Engineering)

complies with the regulations of the University and meets the accepted standards with respect to originality and quality.

Signed by the final examining committee:

_____	Chair
Dr. Andrea Schiffauerova	
_____	External examiner
Dr. Khaled Sennah	
_____	External to program
Dr. Mehdi Hojjati	
_____	Examiner
Dr. Ashutosh Bagchi	
_____	Examiner
Dr. Emre Erkmen	
_____	Thesis supervisor
Dr. Khaled Galal	

Approved by _____
Dr. Mazdak Nik-Bakht, Graduate Program Director

Dr. Mourad Debbabi, Dean
Gina Cody School of Engineering and Computer Science

Date of Defence: 2022-08-30

ABSTRACT

Effect of GFRP-Concrete Bond Characteristics on the Flexural and Serviceability

Behaviour of GFRP-RC Beams

Omar Gouda Mohamed, Ph.D.

Concordia University, 2022

The GFRP bars are characterized by their lower elastic modulus and higher tensile strength compared to steel; hence, the design of the GFRP reinforced concrete (RC) flexural members is controlled by the serviceability limit states, including deflection and crack width. Several research studies have experimentally investigated the flexural and serviceability behaviour of GFRP-RC flexural members. This research contributes to understanding the flexural and serviceability performance of concrete beams reinforced with GFRP bars through analytical, experimental, and numerical work. The main objective is to provide advanced knowledge about the effect of using GFRP bars as an internal reinforcement on the flexural and serviceability response of concrete beams. In addition, this research assesses the current design equations in the North American standards and guidelines; and provides design recommendations to improve the design of GFRP-RC beams.

The study started with a theoretical investigation that included a review of the different factors affecting the bond behaviour of the GFRP-RC beams. The study assessed the different parameters affecting the development length equation in the CSA S806 (2012) standard. This study was performed by analyzing 431 beam-bond tests compiled from the literature. Based on a linear regression analysis, two development length equations were proposed to represent a modified form of the current CSA S806 (2012) equation. The proposed equations were compared to other equations in different design standards and guidelines to determine the efficacy of the proposed equations.

The study then experimentally investigated the different parameters influencing the GFRP bar-concrete bond interaction by testing 24 GFRP-RC beams. Previous studies showed that the GFRP bars' bond performance in concrete affects the crack width of the RC beams. The crack width control in the different standards and guidelines accounts for the bond interaction between

the GFRP bar and the surrounding concrete through the bond-dependent coefficient, k_b . The k_b values of the GFRP bars were obtained from the CSA S806 (2012) crack width equation by performing a well-defined test in the CSA S806 (2012) standard. The studied parameters were the clear concrete cover to GFRP bars, concrete compressive strength, bar diameter, number of GFRP reinforcement layers, confinement effect due to closely spaced stirrups, bar surface profile, and spacing between the reinforcing rebars. The study assessed the current deflection equations in the CSA S806 (2012) standard and ACI 440.1R (2015) guideline. Moreover, the flexural design equations in the different design provisions, including the prediction of the ultimate capacity, cracking moments, and moments at different serviceability limit states, were evaluated. The experimental study evaluated the available approaches in the literature used to quantify the deformability of the GFRP-RC beams to determine the optimal method of the deformability calculation and to check the proposed limits by the CSA S6 (2014) standard. The experimental results showed that the spacing between GFRP bars (at the same reinforcement ratio) and the confinement effect due to closely spaced stirrups influence the cracking and deflection behaviour. Moreover, it was found that the proposed effective moment of inertia equation provided more conservative results than the ACI 440.1R (2015) equation.

Finally, a numerical investigation was conducted using ATENA software. The study validated the numerical model to check the effectiveness of the conducted models in simulating the real beam behaviour. After that, a parametric study was performed to investigate the sensitivity of the nominal moment capacity and deflection values at different service loading levels of the GFRP-RC beams to the different material and cross-sectional parameters. The numerical results showed that the moment capacity and deflection values at the service stage are highly sensitive to the change in the concrete compressive strengths and GFRP bars' elastic modulus. The design of GFRP-RC can be improved through a prudent choice of the different design parameters.

Dedications

To my beloved parents, Hanan and Gouda,

To my beloved and dear wife Nahla,

To my lovely son, Hady

To my dear brother and sister, Ahmed and Sally

Acknowledgments

*In the Name of Allah, the Most Compassionate, Most Merciful.
All gratitude and praises are to Allah the Most Gracious, with the blessings of
Whom the good deeds are fulfilled*

I would like to express my deepest thanks to my supervisor, professor Khaled Galal, for all his effort in helping and guiding me during my Ph.D. journey. Dr. Khaled Galal continuously provides motivation and energy to reach our objectives in an innovative and supportive way. This research would have never been possible without his continuous guidance, encouragement, and positive discussions. It was an honour being one of his graduate students. Also, I would like to thank my committee members, Dr. Khaled Sennah, Dr. Mehdi Hojjati, Dr. Ashutosh Bagchi, and Dr. Emre Erkmen, for their thorough review of the thesis and their valuable and constructive comments and remarks.

I would like to thank the postdoc fellow Dr. Alireza Asadian and former postdoc fellow Dr. Ahmed Hassanein for their appreciated help, fruitful discussions, and precious advice during the Ph.D. I would also like to thank my colleagues Islam Elsayed Nagy, Mostafa Rabea, Omar Elmeligy, AbdulElah Al-Ahdal, Omid Habibi, and Hamed Shaabani for their support and appreciated help during the experimental phase. I would also like to thank Nader Aly, Belal Abd ElRahman, and Mohamed Yousry for their guidance and help in my first days at Concordia University and during the Ph.D.

Besides, I would like to thank the technical staff of the Structures Laboratory at Concordia University, Alexis Gosselin, Alexander McGilton, and the Engineer in Residence Ricky Gioia, for their support, brainstorming, and innovative ideas during the experimental work. I also want to thank the graduate and undergraduate students for their help during the experimental work.

I am very thankful to my lovely parents, Hanan and Gouda, who always provide me with the support and the real cause behind any success. No words sufficiently express my appreciation for their efforts, motivation, and advice. I am sincerely grateful and thankful to my beloved life companion, my wife, Nahla. No words can express my gratefulness to her for her endless support, motivation, advice, discussions, and patience. I am also thankful to my little hero Hady who provided me with love.

I also acknowledge the funding support from the Natural Sciences and Engineering Research Council of Canada (NSERC) and MST Rebar Inc. (formerly B&B. Manufacturing Inc.).

Co-Authorship

This thesis has been prepared in accordance with the regulations of a sandwich (manuscript-based) thesis format. This research presents experimental, analytical, and numerical work carried out solely by Omar Gouda. Advice and guidance were provided for the whole thesis by the academic supervisor Dr. Khaled Galal and Postdoctoral Fellows Dr. Alireza Asadian and Dr. Ahmed Hassanein. This thesis consists of the following chapters:

Chapter 3

Gouda, O., Hassanein, A., and Galal, K. (2021). Proposed Equations for the Development Length of GFRP Bars in Flexural Reinforced Concrete Members. *ASCE Journal of Composites for Construction*. Accepted July 2022.

Chapter 4

Gouda, O., Asadian, A., and Galal, K. (2022). Investigation of different parameters affecting the crack width and k_b coefficient of GFRP-RC beams. Submitted to *Engineering Structures Journal*. August 2022.

Chapter 5

Gouda, O., Asadian, A., and Galal, K. (2022). Flexural and serviceability behaviour of normal strength concrete beams reinforced with ribbed GFRP bars. *ASCE Journal of Composites for Construction*; 10.1061/(ASCE)CC.1943-5614.0001253.

Chapter 6

Gouda, O., Hassanein, A., and Galal, K. (2021). Experimental and numerical study on the deflection performance of GFRP reinforced concrete beams. To be submitted to *Engineering Structures Journal*.

Chapter 7

Gouda, O., Asadian, A., and Galal, K. (2021). Numerical investigation and sensitivity analysis of flexural concrete beams reinforced with GFRP bars. To be submitted to *Engineering Structures Journal*.

Table of Contents

TABLE OF CONTENTS	VIII
LIST OF FIGURES.....	XIII
LIST OF TABLES.....	XVIII
LIST OF ACRONYMS	XX
NOMENCLATURE	XX
1. CHAPTER 1.....	1
INTRODUCTION	1
1.1 BACKGROUND.....	1
1.2 MOTIVATION AND RESEARCH SIGNIFICANCE.....	3
1.3 OBJECTIVES AND SCOPE OF WORK.....	5
1.4 THESIS LAYOUT.....	7
2. CHAPTER 2.....	10
LITERATURE REVIEW	10
2.1 INTRODUCTION	10
2.2 CRACKING CONTROL IN DESIGN CODES	10
2.3 DEFLECTION CONTROL IN DESIGN CODES	11
2.4 SERVICEABILITY PERFORMANCE OF GFRP REINFORCED CONCRETE BEAMS.....	12
2.4.1 Parameters affecting the serviceability behaviour.....	13
2.5 BOND PERFORMANCE AND DEVELOPMENT LENGTH OF GFRP REINFORCEMENT.....	21
2.5.1 Splitting failure theoretical approaches.....	21
2.6 NONLINEAR FINITE ELEMENT MODELLING OF GFRP FLEXURAL MEMBERS	23
2.7 SUMMARY AND GAPS IN LITERATURE.....	24
3. CHAPTER 3.....	26
PROPOSED EQUATIONS FOR THE DEVELOPMENT LENGTH OF GFRP BARS IN FLEXURAL REINFORCED CONCRETE MEMBERS	26
3.1 ABSTRACT	26
3.2 INTRODUCTION	27
3.3 BACKGROUND ON GFRP DEVELOPMENT LENGTH EQUATIONS IN DIFFERENT PROVISIONS	27
3.4 DATABASE CLASSIFICATION	30
3.4.1 Splice specimens.....	32
3.4.2 Beam end, hinged beam, and modified test specimens.....	34
3.5 THEORETICAL APPROACH	34
3.5.1 Bar location modification factor (k_1)	38
3.5.2 Influence of the bar diameter (k_3)	39
3.5.3 Influence of the bar surface profile (k_5).....	42

3.5.4	Influence of the concrete cover	42
3.5.5	Influence of concrete compressive strength	44
3.5.6	Influence of transverse reinforcement on bond strength	46
3.6	REGRESSION ANALYSIS	48
3.7	PROPOSED DEVELOPMENT LENGTH EQUATIONS	49
3.7.1	Analysis of critical pullout and rupture failures	51
3.7.2	Comparison of development length equations	52
3.7.3	Failure mode prediction	55
3.7.4	Comparison of bond strength equations.....	57
3.8	PARAMETRIC STUDY	59
3.9	CONCLUSIONS.....	62
4.	CHAPTER 4.....	64
	INVESTIGATION OF DIFFERENT PARAMETERS AFFECTING THE CRACK WIDTH AND K_B COEFFICIENT OF GFRP-RC BEAMS.....	64
4.1	ABSTRACT	64
4.2	INTRODUCTION	65
4.3	RESEARCH SIGNIFICANCE.....	66
4.4	EXPERIMENTAL PROGRAM	66
4.4.1	Material properties	66
4.4.1.1	Concrete	66
4.4.1.2	GFRP and steel reinforcement.....	67
4.4.2	Design of the tested beams.....	68
4.4.3	Test setup and instrumentation	71
4.5	EXPERIMENTAL RESULTS AND DISCUSSIONS	72
4.5.1	Cracking observations.....	72
4.5.2	Crack widths of GFRP-RC beams	72
4.5.3	Comparison between bottom and side crack widths	75
4.5.4	The bond-dependent coefficient, k_b , of GFRP-RC beams.....	77
4.5.5	Effect of the test protocol and critical crack on the k_b values	84
4.6	RECALIBRATION OF K_B VALUES	86
4.7	CONCLUSIONS.....	88
5.	CHAPTER 5.....	91
	FLEXURAL AND SERVICEABILITY BEHAVIOUR OF CONCRETE BEAMS REINFORCED WITH RIBBED GFRP BARS	91
5.1	ABSTRACT	91
5.2	INTRODUCTION	92
5.3	EXPERIMENTAL PROGRAM	94

5.3.1	Materials	94
5.3.2	Design of test specimens.....	96
5.3.3	Test procedure, setup and instrumentation.....	98
5.4	DISCUSSION OF RESULTS.....	101
5.4.1	Cracking moments and moments at different serviceability limits	101
5.4.2	Failure modes and flexural resistance	106
5.4.3	Strains in reinforcement and concrete.....	109
5.4.4	Curvature	112
5.4.5	Evaluation of Deformability	113
3.4.5.1	Energy-based approach	113
3.4.5.2	Deformation-based approach.....	114
3.4.5.3	Discussion of deformability results	115
3.4.5.4	Comparison with steel RC beams.....	118
5.4.6	Deflection behaviour.....	118
5.4.6.1	Evaluation of theoretical deflection equations.....	119
5.4.6.2	Assessment of the ACI 440.1R (2015) deflection equations	122
5.5	SUMMARY AND CONCLUSIONS	128
6.	CHAPTER 6.....	131
	EXPERIMENTAL AND NUMERICAL STUDY ON THE DEFLECTION PERFORMANCE OF GFRP REINFORCED CONCRETE BEAMS.....	131
6.1	ABSTRACT	131
6.2	INTRODUCTION	132
6.3	EXPERIMENTAL PROGRAM	133
6.3.1	Test specimens.....	133
6.3.2	Material properties.....	134
6.3.2.1	Reinforcing Bars	134
6.3.2.2	Concrete	135
6.3.3	Test Procedure, setup, and instrumentation	136
6.4	TEST RESULTS AND DISCUSSION.....	138
6.4.1	General observations.....	138
6.4.2	Effect of concrete strength level	139
6.4.3	Effect of concrete cover.....	140
6.4.4	Effect of number of tensile reinforcement layers.....	141
6.5	NUMERICAL INVESTIGATION.....	141
6.5.1	FE modelling	141
6.5.2	Geometric models.....	142
6.5.3	Material Models.....	143
6.5.4	Mesh configuration.....	145

6.5.5	Loading and boundary conditions.....	146
6.5.6	Failure criteria and solution strategy.....	147
6.5.7	Model validation results.....	147
6.6	NUMERICAL PARAMETRIC STUDY	149
6.6.1	Results and discussion	149
6.6.1.1	Cracking behaviour and failure mode	149
6.6.1.2	Evaluation of moments and deflections	150
6.6.1.3	Evaluation of the deflection equations in CSA S806 (2012) and ACI 440.1R (2015)	152
6.7	CONCLUSIONS.....	154
7.	CHAPTER 7.....	156
	NUMERICAL INVESTIGATION OF FLEXURAL CONCRETE BEAMS REINFORCED WITH GFRP BARS	156
7.1	ABSTRACT.....	156
7.2	INTRODUCTION.....	157
7.2.1	Verification beams	158
7.3	FINITE ELEMENT MODELLING	160
7.3.1	Geometric models	161
7.3.1.1	Concrete beam and steel plate solid elements.....	161
7.3.1.2	Reinforcement truss elements.....	161
7.3.2	Material Models.....	162
7.3.2.1	Concrete material model.....	162
7.3.2.2	GFRP and steel reinforcement material models	164
7.3.2.3	Loading and supporting plate material model	165
7.3.3	Mesh configuration	165
7.3.4	Contact condition between the GFRP and steel reinforcement with concrete	166
7.3.5	Loading and boundary conditions.....	166
7.3.6	Failure criteria and solution strategy.....	167
7.4	VALIDATION RESULTS	168
7.5	PARAMETRIC INVESTIGATION.....	170
7.6	DISCUSSION OF RESULTS	172
7.6.1	Effect of clear concrete bottom cover	172
7.6.2	Effect of reinforcement ratio and bar spacing.....	173
7.6.3	Effect of steel and GFRP stirrup spacings	174
7.6.4	Effect of steel and GFRP stirrup bar diameters.....	176
7.6.5	Effect of beam size and number of reinforcement layers.....	177
7.6.6	Sensitivity of the beams' performance to material properties.....	179
7.6.6.1	Effect of changing the concrete compressive strength.....	179
7.6.6.2	Effect of changing the GFRP bars' elastic modulus	180

7.7 EVALUATION OF THE DEFLECTION EQUATIONS IN CSA S806 (2012) AND ACI 440.1R (2015).....	181
7.8 COMPARISON BETWEEN NUMERICAL AND THEORETICAL MOMENT CAPACITIES	184
7.9 CONCLUSIONS	187
8. CHAPTER 8.....	190
8.1 SUMMARY.....	190
8.2 CONCLUSIONS.....	190
8.2.1 Findings of the analytical investigation:	190
8.2.2 Findings of the experimental study:.....	192
8.2.3 Findings of the Numerical simulation:	194
8.3 MAIN CONTRIBUTIONS	196
8.4 RECOMMENDATIONS FOR FUTURE WORK	196
REFERENCES	198
APPENDIX A.....	210
A.1 GENERAL.....	210
A.2 CONSTRUCTION AND TESTING OF THE CONCRETE BEAMS	210
APPENDIX B.....	222

List of Figures

Figure 1.1 Different surface profiles of GFRP bars: (i) El-Nemr et al. (2018); (ii) current study; and (iii) (Solyom and Balázs 2020).....	4
Figure 2.1 Idealized moment-curvature relation of FRP reinforced section [Razaqpur et al. (2000)].....	14
Figure 2.2 Primary and secondary cracks in concrete [Goto (1971)]	14
Figure 2.3 Elevation and cross-sectional details of a typical beam for the approved test by CSA S806 (2012).....	16
Figure 2.4 Load-deflection relations for NSC and HSC beams in El-Nemr et al. (2013).....	17
Figure 2.5 Load-crack width relations for GFRP-RC beams in El-Nemr et al. (2018)	18
Figure 2.6 The adapted method proposed by Benzecry et al. (2021).....	20
Figure 2.7 Different modes of failure for GFRP bars in concrete: (a) pullout failure; (b) splitting failure; (c) bar rupture failure; and (d) shear and concrete crushing failure.....	22
Figure 2.8 Tensile force acting on a steel bar embedded in a reinforced concrete member	23
Figure 3.1 Different modes of failure for GFRP bars in concrete: (a) pullout failure; (b) splitting failure; (c) bar rupture failure; and (d) shear and concrete crushing failure.....	31
Figure 3.2 Tensile force acting on a steel bar embedded in a reinforced concrete member	35
Figure 3.3 Relationship between maximum stress at failure and normalized embedment length for different splice specimens.....	37
Figure 3.4 Comparison between the bond strength and normalized embedment length for the experimental results and CSA S806 (2012) equation	38
Figure 3.5 Relationship between factor k_3 and the embedment length for: (a) and (b) Splice tests, and (c) Beam end tests	41
Figure 3.6 Relationship between factor k_5 and the normalized embedment length.....	42
Figure 3.7 Relationship between normalized experimental bond strength and the normalized concrete cover to the bar center for: (a) Beam end tests, and (b) Splice tests	44
Figure 3.8 Relationship between the normalized experimental bond strength and the square root of compressive strength for specimens failed due to: (a) Splitting of concrete; and (b) Pullout of the GFRP bar	46
Figure 3.9 Effect of transverse reinforcement on the bond strength based on the bar surface profile for splice splitting beams.....	48
Figure 3.10 Relationship between the normalized experimental bond strength versus the reciprocal of the normalized embedment length.....	49
Figure 3.11 Comparison between the normalized experimental bond strength and normalized embedment	

length for beams failed by: (a) pullout; and (b) rupture of GFRP bar	52
Figure 3.12 Relationships between the experimental embedment lengths and predicted embedment lengths	55
Figure 3.13 The effectiveness of different equations in the guidelines and standards in predicting the experimental embedment length of beams failed by splitting: (a) Beam end specimens; and (b) Splice specimens	57
Figure 3.14 Proportionating the experimental and theoretical bond strength equations	58
Figure 3.15 Comparison between different development length equations	61
Figure 4.1 The surface profile of steel, ribbed, and sand-coated Grade III GFRP bars	68
Figure 4.2 Elevation, cross-sectional details, and test setup of the beams (Note: all dimensions are in mm)	69
Figure 4.3 Instrumentation of the tested beams	71
Figure 4.4 Extrapolated crack width to tension face versus GFRP extrapolated strain relations	75
Figure 4.5 Comparison between side and bottom crack widths for high-strength beams	76
Figure 4.6 Relationship between the factor β and the bottom measured crack width	77
Figure 4.7 Relation between the k_b coefficient and the extrapolated strains for all the specimens	80
Figure 4.8 Relation between the k_b coefficient and the clear concrete cover to the GFRP bar surface.	80
Figure 4.9 Relation between the k_b coefficient and bar spacing.	81
Figure 4.10 Relation between the k_b coefficient and concrete compressive strength.	82
Figure 4.11 Relation between the k_b coefficient and spacing between stirrups.	83
Figure 4.12 The k_b comparison between the ribbed and sand-coated GFRP bars	84
Figure 5.1 Surface deformation of Grade III ribbed GFRP bars and 10M steel bars	96
Figure 5.2 Elevation and cross-sectional details of the beams (Note: all dimensions are in mm)	98
Figure 5.3 The test setup and instrumentations (Note: all dimensions are in mm)	100
Figure 5.4 Relationship between moments at different serviceability limits and reinforcement ratio at the concrete cover of (a) 30 mm and (b) 50 mm	106
Figure 5.5 Relation between experimental and theoretical moments at different serviceability limits and concrete cover for beams reinforced with (a) 2#5 and (b) 3#6	106
Figure 5.6 Typical compression failure of different beams	107
Figure 5.7 Relation between the ratio of the theoretical values of c/d and (a) maximum theoretical stress in the GFRP reinforcement and (b) theoretical moment resistance	109
Figure 5.8 Concrete and GFRP reinforcement strains of the tested beams: (a-c) measured concrete and GFRP strains; and (d) comparison between the experimental and theoretical GFRP strains for beams 2#5-c50, 2#6-c50, and 2#8-c50	110

Figure 5.9 Moment-curvature relationships of the tested beams	112
Figure 5.10 Energy-based approach for ductility computation.....	113
Figure 5.11 Ductility indices using the energy-based approach	114
Figure 5.12 Ductility indices using the deformation-based approach.....	115
Figure 5.13 Deflection versus applied moment for all GFRP-RC beams (note: the graphs shown are considering the moment due to the self-weight).....	119
Figure 5.14 Distribution of $\delta_{exp.}/\delta_{pred.}$ values of ACI 440.1R-15 (ACI 2015) equation versus: (a) I_g/I_{cr} where $\delta_{pred.}$ is calculated using M_{cr} ; (b) M_a/M_{cr} where $\delta_{pred.}$ is calculated using M_{cr} ; (c) I_g/I_{cr} where $\delta_{pred.}$ is calculated using $0.8M_{cr}$; and (d) M_a/M_{cr} where $\delta_{pred.}$ is calculated using $0.8M_{cr}$	123
Figure 5.15 Distribution of $\delta_{exp.}/\delta_{pred.}$ values calculated assuming $\beta_c = (M_{cr}/M_a)^2$ versus: (a) I_g/I_{cr} where $\delta_{pred.}$ is calculated using M_{cr} ; (b) M_a/M_{cr} where $\delta_{pred.}$ is calculated using M_{cr} ; (c) I_g/I_{cr} where $\delta_{pred.}$ is calculated using $0.8M_{cr}$; and (d) M_a/M_{cr} where $\delta_{pred.}$ is calculated using $0.8M_{cr}$	125
Figure 5.16 Distribution of $\delta_{exp.}/\delta_{pred.}$ values calculated assuming $\beta_c = (M_{cr}/M_a)^3$ versus: (a) I_g/I_{cr} where $\delta_{pred.}$ is calculated using M_{cr} ; (b) M_a/M_{cr} where $\delta_{pred.}$ is calculated using M_{cr} ; (c) I_g/I_{cr} where $\delta_{pred.}$ is calculated using $0.8M_{cr}$; and (d) M_a/M_{cr} where $\delta_{pred.}$ is calculated using $0.8M_{cr}$	126
Figure 5.17 Relationship between the experimental and theoretical I_e for: (a) Eq. 5.14(b), (b) Eq. 5.15 with $m = 2$, and (c) Eq. 5.15 with $m = 3$	127
Figure 6.1 Test setup, specimens' cross section details and reinforcement configuration.....	134
Figure 6.2 GFRP reinforcement surface configuration.....	134
Figure 6.3 Typical test setup for the tested beams	137
Figure 6.4 Typical beam instrumentation	137
Figure 6.5 The typical crack pattern of the tested specimens at $0.33M_n$ crack width	139
Figure 6.6 Moment-deflection for the tested beams specimens.....	140
Figure 6.7 Geometric models of (a) brick element, (b) tetrahedral elements, and (c) truss element (Červenka and Červenka 2013).....	143
Figure 6.8 Concrete material uniaxial stress-strain relation (Červenka and Červenka 2013).....	144
Figure 6.9 Geometric model and mesh configuration of beam N-5#5-c50.....	146
Figure 6.10 Mesh sensitivity of beam N-3#6-c50.....	146
Figure 6.11 Comparison between the experimental and numerical deflections.....	148
Figure 6.12 Cracks propagation of beam 3#6-c50 at different concrete strengths at $0.33M_n$	150

Figure 6.13 Sensitivity of the modelled beams to the concrete compressive strength.....	152
Figure 6.14 Relationships between the concrete strength (f'_c) and the deflection values at $0.33M_n$	153
Figure 7.1 Elevation and cross-sectional details of (a) El-Nemr et al. (2018) and (b) Ballet (2018) and Gouda et al. (2022).	160
Figure 7.2 Geometric models of (a) brick elements; (b) tetrahedral elements; and (c) truss elements (Červenka and Červenka 2013).....	162
Figure 7.3 Uniaxial stress–strain diagram (Červenka and Červenka 2013).....	163
Figure 7.4 Generated mesh for (a) eight elements and (b) 12 elements.....	166
Figure 7.5 Mesh sensitivity of beam 6#15G1 (El-Nemr et al. 2018).....	166
Figure 7.6 Loading and boundary conditions of a typical beam.....	167
Figure 7.7 Comparison between the experimental and numerical results.....	169
Figure 7.8 Details of (a) cross-sectional parametric investigation; and (b) sensitivity analysis of the material properties	172
Figure 7.9 Relationships between the clear concrete bottom cover and (a) moment capacities, and (b) deflection values at different service loading levels	173
Figure 7.10 Relation between the deflection values at different service loading levels and (a) reinforcement ratio; and (b) spacing between tensile GFRP reinforcement	174
Figure 7.11 Comparison between steel and GFRP stirrups using different spacings between stirrups: (a) nominal moment capacities (M_n); and (b) deflections at various service stage limits	175
Figure 7.12 Comparison between steel and GFRP stirrups using different spacings between stirrups: (a) moment capacities; and (b) deflections at the service stage	177
Figure 7.13 Effect on the number of tensile reinforcement layers of (a) moment capacities; and (b) deflection values at different loading levels	178
Figure 7.14 Sensitivity of the (a) moment capacities and (b) deflection values at $0.33M_n$ to the concrete compressive strength and GFRP bars' modulus of elasticity.....	181
Figure 7.15 Comparison between numerical and theoretical deflection values at different loading level	186
Figure 7.16 Comparison between the numerical and theoretical moment capacities	187
Figure A.1 Typical GFRP cages for two concrete beams	210
Figure A.2 GFRP cages for 16 concrete beams	210
Figure A.3 Placing the cages inside the formwork	211
Figure A.4 Preparing the formwork for the concrete pouring by fixing the top steel hooks	211
Figure A.5 Preparing and levelling the formwork for the concrete pouring.....	212
Figure A.6 Pouring of the concrete beams using the concrete bucket	212

Figure A.7 Vibration of poured concrete using the electric vibrator	213
Figure A.8 Careful finishing of the top concrete surface using trowels.....	213
Figure A.9 Concrete top surface after finished and levelling	214
Figure A.10 Pouring, compacting, and levelling of the cylinders and prisms	214
Figure A.11 Covering the concrete surface with a plastic cover for curing.....	215
Figure A.12 Curing of the concrete cylinders and prisms.....	215
Figure A.13 Stacking of the concrete beams after disassembling of the formwork.....	216
Figure A.14 Testing GFRP bar in tension and rupture failure mode	216
Figure A.15 Testing concrete cylinders in compression	217
Figure A.16 Testing the concrete prisms in tension using the four-point bending rupture test	217
Figure A.17 Splitting tensile test for the concrete cylinders	218
Figure A.18 Measuring the initial crack width using a hand-held microscope.....	218
Figure A.19 Attaching the LVDT to the concrete beam at the crack location.....	219
Figure A.20 Six attached LVDTs at the concrete beam side and bottom faces	219
Figure A.21 Typical concrete compression crushing.....	220
Figure A.22 Buckling of the top steel compression bar due to lack of confinement	220
Figure A.23 Failure of beam confined with transverse reinforcement spacing of 100 mm (a) concrete crushing followed by GFRP rupture; (b) concrete crushing failure; and (c) GFRP bar rupture.....	221
Figure A.24 Failure of beam reinforced with 3#6-c50 ribbed GFRP bars (a) normal-strength concrete beam; and (b) high-strength concrete beam.....	221

List of Tables

Table 2.1 Minimum thickness of beams and one-way slabs as per ACI 440.1R (2015)	12
Table 2.2 Deflection limits according to CSA S806 (2012)	12
Table 3.1 Test data for the beam-test specimens.....	31
Table 3.2 Classification of the Database	32
Table 3.3 Transverse reinforcement details	33
Table 3.4 Comparison of the ratio of the experimental to theoretical embedment lengths between splitting failure specimens	53
Table 3.5 Evaluation of design development length equations for the entire test specimens at the ultimate stress.....	57
Table 3.6 Ratio between the theoretical and experimental bond strengths	58
Table 4.1 Properties of GFRP bars.....	67
Table 4.2 Test matrix and details of the tested beams.....	70
Table 4.3 Test results	79
Table 4.4 k_b values for the tested beams using the theoretical strains.....	86
Table 4.5 Crack widths and k_b values of the database.....	88
Table 5.1 Concrete mix design.....	94
Table 5.2 Details of the tested beams.....	95
Table 5.3 Properties of ribbed GFRP bars	95
Table 5.4 Results of the tested beams	103
Table 5.5 Moments of the beams at different serviceability limits	105
Table 5.6. Curvature and strains of the tested beams.....	111
Table 5.7 Ductility indices calculated using the energy and deformation-based approaches	117
Table 5.8 Experimental and theoretical deflection of the tested beams	121
Table 6.1 Test matrix of the tested beams.....	133
Table 6.2 Mechanical properties of GFRP reinforcing bars.....	135
Table 6.3 Concrete mix design.....	136
Table 6.4 Beams' moment, deflection, and failure mode.....	138
Table 6.5 Material properties of concrete, GFRP, and steel reinforcement	145
Table 6.6 Experimental and numerical results of the validated beams	149
Table 7.1 Material properties and details of beams for El-Nemr et al. (2018), Ballet (2019), and Gouda et al. (2022).....	159

Table 7.2 Material properties of the concrete material, GFRP, and steel reinforcement	163
Table 7.3 Experimental and numerical results of the validated beams	169

List of Acronyms

GFRP	Glass Fibre-Reinforced Polymer
FEM	Finite Element Modelling
HSC	High Strength Concrete
LVDT	Linear Variable Displacement Transducer
NFEM	Nonlinear Finite Element Modelling
NSC	Normal Strength Concrete
RC	Reinforced Concrete

Nomenclature

A_b	Cross-sectional area of the bar (mm^2)
A_f	Total area of the GFRP bars (mm^2)
A_{tr}	Area of transverse reinforcement (mm^2)
a	Shear span measured from the center of the support to the point load (mm)
b	Width of the rectangular cross-section (mm)
c	Distance from the extreme compression fibres to the neutral axis (mm)
c_c	Concrete cover to the center of the bar (mm)
C_c	Curvature factor in the deformation-based approach
C_d	Deflection factor in the deformation-based approach
C_s	Ductility strength factor
d	Distance from the extreme compression fibres to the center of the tensile reinforcement (mm)
d_b	Diameter of reinforcing bars (mm)
d_c	Bottom concrete cover thickness measured to the center of reinforcement (mm)
d_{cs}	Concrete cover thickness measured to the center of reinforcement (mm)
$d_{c,side}$	Side concrete cover thickness (mm)
d_s	Side concrete cover thickness (mm)
d^*	Maximum of the side cover (d_s) and $s/2$ for the bottom crack calculation (mm)
E_c	Concrete modulus of elasticity (MPa)
E_e	Elastic absorbed energy
E_{FRP}	Elastic modulus of FRP bars (MPa)
E_f	Elastic modulus of GFRP bars (MPa)
E_s	Elastic modulus of steel bars (MPa)
E_t	Total absorbed energy
F	Applied load from the actuator (N)
f'_c	Concrete compressive strength (MPa)
f_{cr}	Concrete cracking strength (MPa)
f_f	Design stress in GFRP reinforcement in tension (MPa)
f_{fr}	Developed stress in the GFRP bars (MPa)
f_{frpu}	Ultimate stress of the bar (MPa)
f_{fu}	Design tensile strength of FRP reinforcement (MPa)
f_y	Specified yield strength of steel reinforcing bars (MPa)

f_r	Concrete tensile strength (MPa)
$\sqrt{f'_c}$	Square root of the specified compressive strength of concrete
I_{cr}	Transformed moment of inertia of the equivalent cracked concrete section
I_e	Effective moment of inertia of the cross-section (mm ⁴)
I_g	Gross moment of inertia of the cross-section (mm ⁴)
J	Deformability performance factor
j	Lever arm from the center of the compression block to center of tension reinforcement (mm)
k	Ratio between the neutral axis and reinforcement depths
k_b	Bond-dependent coefficient
K_{tr}	Transverse reinforcement index
k_1	Bar location factor
k_2	Concrete density factor
k_3	Bar size factor
k_4	Bar fibre factor
k_5	Bar surface profile factor
L	Support-to-support span of the member (mm)
L_g	Distance from the support to the cracking moment point in a simply supported beam (mm)
l_d	Development length (mm)
l_e	Embedded length of the reinforcing bar (mm)
$l_{e-exp.}$	Experimental embedded length of the reinforcing bar and the same as l_e (mm)
$l_{e-theo.}$	Theoretical embedded length that corresponds to the maximum experimental stress (mm)
M_a	Applied moment on the member (kN·m)
M_c	Moment at a concrete compressive strain of 0.001 (kN·m)
M_{cr}	Cracking moment (kN·m)
M_s	Moments at different serviceability limit states (kN·m)
M_{ult}	Ultimate moment capacity of the section (kN·m)
n	Number of bars developed or spliced along the potential splitting failure plane
n_f	Ratio between the GFRP and concrete elastic moduli
P	Acting load on the member (kN)
P_1	Cracking load (kN)
P_2	Load at the beginning of concrete compression crushing in the over-reinforced sections (kN)
s	Center to center spacing between the tensile bars (mm)
s_s	Spacing of transverse reinforcing bars (mm)
S_1	Initial slope of the loading curve before cracking
S_2	Secant slope of the moment-deflection curve after cracking
S_3	Unloading slope of the elastic region from the failure point
T	Failure load monitored in beams at bond failure (N)
w	Maximum measured crack width (mm)
y_b	Distance from the extreme tensile concrete fibres to the neutral axis (mm)
α	Coefficient accounts for the bar location
α_1	Ratio of the average of the equivalent stress block to the concrete compressive strength

β	Ratio of the distance from the neutral axis to the extreme tension fibre to the distance from the neutral axis to the center of the tensile reinforcement
β_1	Factor converting the actual stress diagram along the cross-section to an equivalent rectangular stress block
β_c	Tension stiffening factor
ε_c	Concrete compressive strain at any acting moment
ε_f	GFRP tensile strain at any acting moment
$\varepsilon_{f.ex}$	Strain extrapolated to the outer surface of the beam
ε_{cu}	Ultimate concrete compressive strain
ρ_f	Reinforcement ratio
ρ_{fb}	Balanced reinforcement ratio
φ_m	Curvature of the beam
φ_u	Curvature at the ultimate moment
$\varphi_{\varepsilon=0.001}$	Curvature at a concrete compressive strain of 0.001
μ_d	Deformation-based ductility index
μ_e	Energy-based ductility index
ψ_c	Curvature at a concrete compressive strain of 0.001
ψ_{ult}	Curvature at the ultimate moment
Δ_u	Maximum deflection at the ultimate moment
$\Delta_{\varepsilon=0.001}$	Deflection at a concrete compressive strain of 0.001
u	Average bond stress (MPa)
τ	Average bond stress (MPa)
δ_{max}	Maximum mid-span deflection at the applied load (mm)
η	Ratio of the difference between the gross and cracked moment of inertia to the gross moment of inertia
γ	Factor accounting for the variation in stiffness along the member length
ψ_s	Steel crack spacing factor
κ	Factor accounting for the crack spacing and bond-dependent coefficient

Chapter 1

Introduction

1.1 Background

Glass fibre-reinforced polymer (GFRP) reinforcement is characterized by a high tensile strength-to-weight ratio, non-magnetic properties, superior corrosion resistance compared to steel, and appropriate fatigue resistance. The corrosion resistance is considered one of the significant features of the GFRP reinforcing bars, particularly in aggressive environments subjected to severe corrosion. The damage to the internal steel reinforcement due to corrosion causes concrete deterioration. Moreover, the GFRP bars-concrete bond behaviour differs from the steel reinforcement bond behaviour with concrete due to the lower elastic modulus of the GFRP bars compared to steel. In addition to the anisotropic nature of the GFRP material, unlike steel, where the physical and mechanical properties in the longitudinal and transverse directions are different (Cosenza et al. 1997). The fibres' characteristics control the mechanical properties in the longitudinal direction, whereas the resin properties dominate the mechanical properties in the transverse direction. The resin strength is lower than the concrete strength, resulting in different bond interactions between the concrete and the GFRP bar and causing GFRP surface damage in most cases rather than concrete cracking.

The bond stress transfer between the GFRP bar and concrete is controlled by: the chemical adhesion, friction due to the GFRP bar roughness, mechanical interlock of the bar against concrete, and shrinkage in the hardened concrete that causes a hydrostatic pressure against the GFRP reinforcement (Cosenza et al. 1997). When a tensile force is applied to a bar, chemical adhesion is the first resisting mechanism that vanishes rapidly. The bond resistance between the bar and surrounding concrete becomes either by friction or mechanical interlock depending on the bar surface profile (for example, sand-coated, ribbed, grooved, and helically wrapped with and without sand-coating). The concrete-GFRP bar bond performance is influenced by several parameters, including the concrete cover, bar diameter, reinforcement ratio, concrete compressive strength, and bar surface profile. Two tests have been recommended to quantify the bond behaviour of GFRP bars embedded in concrete by monitoring the bond stresses versus slip relations; these tests are direct pull-out tests and beam-bond tests. The beam-bond tests have a bending loading scheme

that imitates the actual bond behaviour of the GFRP bars inside the concrete member; hence, they have more reliable results than the direct pull-out tests.

In general, the serviceability limits of the crack width and deflection often control the design of the GFRP-RC flexural members due to the lower elastic modulus of the GFRP reinforcing bars when compared to the steel ones. The crack width control can be achieved by two approaches adopted in different standards and guidelines: a direct approach in CSA S806 (2012), where the crack width is directly calculated based on given parameters; and an indirect procedure considered by ACI 440.1R (2015), where the maximum bar spacing between the longitudinal rebars is limited by limiting the crack width. The experimental tests conducted by Chit and Kirsteint (1958); and Broms (1965) showed that the concrete cover, bar spacing, the developed strains in reinforcing bars, and the bond performance between the reinforcing bars and concrete are considered the primary factors that directly influence the crack width and spacing. Frosch (1999) developed a crack width formulation based on a physical model; the main affecting parameters are the concrete cover, strain in reinforcement, and bar spacing. The bond properties are defined in Frosch's (1999) crack width equation through the bond-dependent coefficient, k_b , which varies according to the bar material (steel, or glass, carbon, and aramid fibre-reinforced polymers), and the bar surface profile (smooth, sand coated, ribbed, grooved, and helically wrapped with and without sand-coating). As the bond performance of the bar with the surrounding concrete increases, the k_b value decreases in an opposite manner. The abovementioned parameters are considered the basis of the crack width equation. However, El-Nemr et al. (2016) showed an effect of the concrete compressive strength on the crack width and k_b coefficient that requires further investigation. In addition, Shield et al. (2019) study highlighted the lack of data that provided the k_b values of the ribbed and grooved GFRP bars.

Therefore, more research studies are required to stand on the main parameters that influence the overall cracking and deflection behaviour of the GFRP-RC flexural members and diminish the inconsistencies between the different research findings. This investigation aims to provide an enhanced understanding of the effect of different parameters, including the clear concrete cover to GFRP rebars, concrete compressive strength, reinforcement ratio, bar diameter, number of GFRP reinforcement layers, confinement effect due to closely spaced stirrups, bar surface profile, and spacing between the tensile rebars through experimental and analytical analyses on the flexural

and serviceability performance of ribbed and sand-coated GFRP-RC beams, comprising the moment capacities, cracking moments, curvature, deformability, and the cracking and deflection behaviour.

1.2 Motivation and research significance

As mentioned previously, one of the shortcomings of steel reinforcement is its susceptibility to corrosion, which reduces the service life of the concrete structures subjected to harsh environments such as bridges, marine structures, and tunnels. The use of glass fibre-reinforced polymer (GFRP) bars provides high durability and longer service life than steel rebars.

GFRP bars are available in different surface profiles and manufactured with different mechanical properties (Solyom and Balázs 2020), as shown in Figure 1.1. Several studies showed the importance of the GFRP bar surface profile in affecting the bond behaviour and cracking progression of the GFRP-RC members (Kassem et al. 2011, McCallum 2013, and El-Nemr et al. 2016). Nonetheless, El-Nemr et al. (2018) reported that the bar surface profile did not exhibit a noticeable effect on the flexural strength and deflection behaviour of the flexural members. Furthermore, El-Nemr et al. (2018) deduced that GFRP bars with a modulus of elasticity greater than 60 GPa were efficient in optimizing the design of the GFRP-RC members. Due to the linear elastic behaviour of the GFRP material up to failure, the ductility of the GFRP-RC members is very low. The inelastic behaviour of the RC member arises from the plastic deformation of the concrete material (ACI 440.1R 2015).

Few studies investigated the effect of using non-sand-coated GFRP bars on the flexural and serviceability performance of RC members (Kassem et al. 2011 and Abdelkarim et al. 2019). Kassem et al. (2011) tested four GFRP-RC beams and found that the sand-coated bars provided better cracking behaviour with more cracks and narrower crack widths than the deformed bars. Abdelkarim et al. (2019) investigated the effect of the reinforcement ratio, bar diameter, and change in concrete strength on the flexural behaviour of eight concrete beams reinforced with ribbed GFRP bars. The normal-strength concrete (NSC) beams had higher curvatures, and narrower crack widths than the high-strength concrete (HSC) beams.

However, the effect of other parameters, including the change in bar spacing, confinement from

transverse reinforcement, and concrete cover on the flexural strength, ductility, curvatures, moment capacity, crack widths, k_b factor, and deflection behaviour of the concrete beams reinforced with ribbed GFRP bars, need to be investigated.

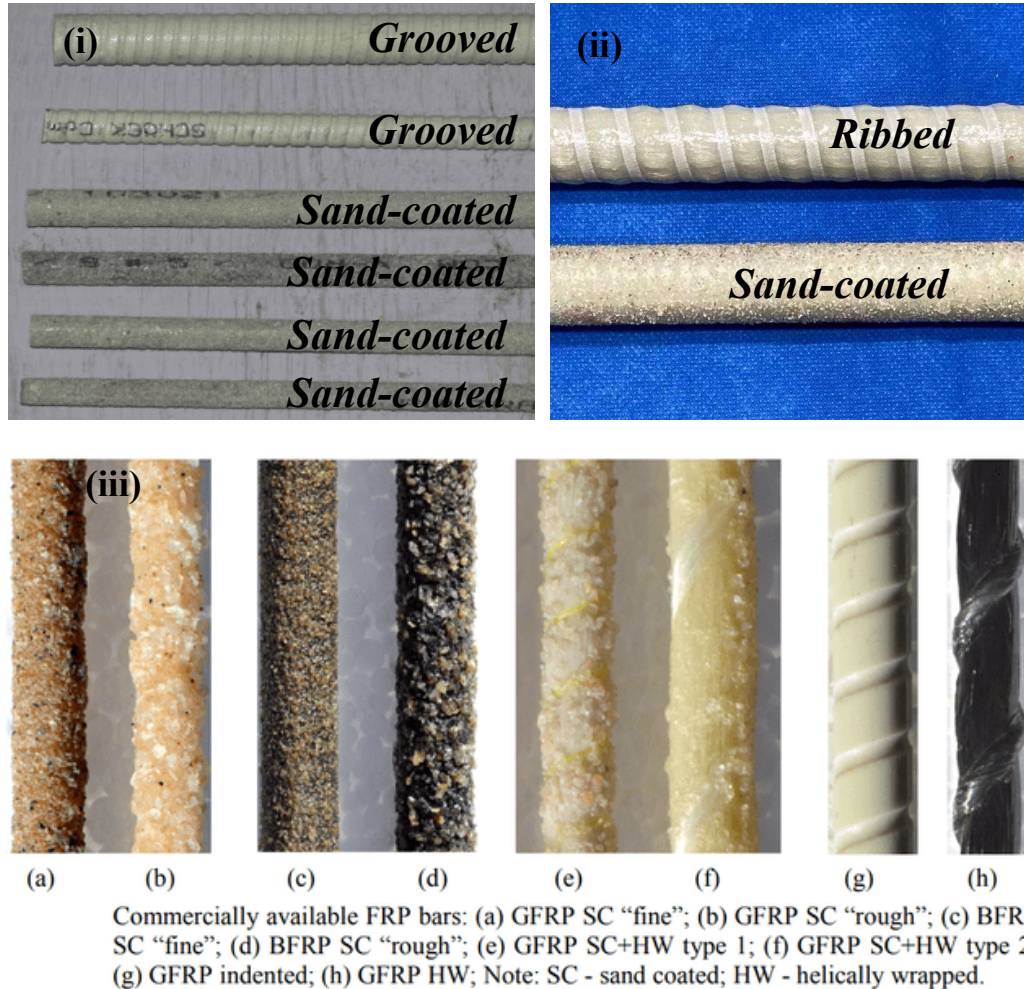


Figure 1.1 Different surface profiles of GFRP bars: (i) El-Nemr et al. (2018); (ii) current study; and (iii) (Solyom and Balázs 2020)

Accordingly, this research aims to: (a) analytically investigate the effect of different cross-sectional and material parameters on the GFRP-concrete bond behaviour and development length of GFRP bars in concrete; (b) experimentally study the influence of several parameters, including the clear concrete cover to GFRP reinforcement (30, 38, and 50 mm), bar spacing, bar diameter #4 (13 mm), #5 (15 mm), #6 (20 mm), and #8 (25 mm), reinforcement ratio, confinement from transverse reinforcement in the middle bending zone (spacing between stirrups of 317 mm, 200

mm, and 100 mm), concrete compressive strength (35 MPa and 65 MPa), bar surface profile (ribbed and sand-coated), and the number of tensile reinforcement layers (one and two layers) on the flexural strength, serviceability performance, and deformability of 24 RC beams; and (c) numerically discuss the effect of different material and cross-sectional parameters on the nominal moment capacity and deflection performance at the service stage of concrete beams reinforced with GFRP bars by extending the parameters of the experimental study. This research will enrich the available experimental dataset with more data for GFRP-RC beams and provide a better understanding of the behaviour of ribbed GFRP bars.

1.3 Objectives and scope of work

The main objective is to provide advanced knowledge about the effect of GFRP-Concrete bond characteristics on the flexural and serviceability behaviour of GFRP reinforced concrete beams; this will be achieved by quantifying the effect of different parameters on the: (1) flexural strength of the beams; (2) cracking moments; (3) strains in concrete and GFRP reinforcement; (4) curvature; (5) deformability; (6) deflection behaviour at the service stages; and (7) cracking performance at the service stage. Furthermore, this study contributes to the body of knowledge in the area of GFRP reinforced concrete beams by:

- 1- Enriching the literature with the k_b values for the ribbed and sand-coated bars;
- 2- Assessing the existing design equations for the ultimate capacity, development length, deflection, and crack width in the different design standards and guidelines; and
- 3- Quantifying the sensitivity of the flexural and serviceability behaviour of the GFRP-RC beams to the different material and cross-sectional parameters by performing a numerical simulation.

In order to achieve the objectives of this thesis, the following is the scope of work:

- Reviewing the different tests used to quantify the bond behaviour of the GFRP-RC members. In addition to assessing the current development length equation in CSA S806 (2012) by analyzing 431 beam test specimens compiled from the literature and comparing the proposed equations with the other development length equations in the different design standards and guidelines.

- Constructing and testing 16 normal-strength concrete (NSC) beams reinforced with ribbed GFRP bars tested monotonically to failure. The test parameters included in these beams are the clear concrete cover to the GFRP reinforcement bottom surface; the center-to-center spacing between the GFRP bars; reinforcement ratio; bar diameter; confinement due to closely spaced transverse stirrups; and the number of tensile GFRP reinforcement layers.
- Constructing and testing eight high-strength concrete (HSC) beams; five of these beams are reinforced with ribbed GFRP bars, and three beams are reinforced with sand-coated, tested monotonically to failure. The test parameters included in these beams are the clear concrete cover to the GFRP reinforcement; the concrete compressive strength effect for the five HSC beams reinforced with ribbed GFRP bars by comparing these beams to their corresponding NSC beams; the number of tensile reinforcement layers; and the bar surface profile effect.
- Conducting a numerical simulation using ATENA software by performing validation for GFRP-RC beams from this study and other studies, then investigating the sensitivity of the GFRP-RC beams' nominal moment capacities and deflection performance to different material and cross-sectional parameters. The results are provided in terms of the ultimate capacities of the beams, cracking progression, and deflection behaviour at the service stage. The deflection equations in CSA S806 (2012) standard and ACI 440.1R (2015) guideline are evaluated.

1.4 Thesis layout

This thesis comprises eight chapters analyzing and discussing the results of the experimental tests and analytical and numerical research work. The contents of the chapters and the appendices are as follows:

- **Chapter 1** presents the introduction, motivation, research significance, research objectives and scope of work, and a brief description of the thesis layout.
- **Chapter 2** provides the literature review of the available research work on the flexural and serviceability behaviour of concrete beams reinforced with GFRP bars. The chapter reviews the GFRP bars-concrete bond interaction and the mechanism of bond stress transfer between the two components. It also reviews the available numerical research work conducted on GFRP-RC flexural beams.
- **Chapter 3** provides a comprehensive analytical study discussing the current development length equations in the different provisions. The study assesses the design parameters in the CSA S806 (2012) development length equation. The study includes 431 beam bond tests compiled from different research studies in the literature and classified according to the type of the test and the failure mode. Furthermore, a regression analysis was conducted on the compiled data points, and two modified forms of the CSA S806 (2012) development length equation are proposed. New limits for the parameters in the CSA S806 (2012) development length equation are proposed, and the proposed equations are compared to the other development length equations in the different standards and guidelines.
- **Chapter 4** presents an experimental study investigating the cracking behaviour of 16 GFRP-RC beams, including 12 normal-strength concrete beams reinforced with ribbed bars, two high-strength concrete beams reinforced with ribbed bars, and two high-strength concrete beams reinforced with sand-coated bars. The included parameters are the clear concrete cover to GFRP reinforcement (30, 38, and 50 mm), bar spacing, bar diameter #4 (13 mm), #5 (15 mm), #6 (20 mm), and #8 (25 mm), reinforcement ratio, confinement effect from closely spaced transverse reinforcement, concrete strength (35 MPa and 65 MPa), and bar surface profile. The study focused on the strain-crack widths relations, the computation of the k_b values for the tested beams at different crack width levels and using different

approaches, recalibration of the k_b values of the different GRP rebars based on a database compiled from the literature.

- **Chapter 5** investigates through an experimental study the effect of concrete cover (30 mm, 38 mm, and 50 mm), bar diameter #4 (13 mm), #5 (15 mm), #6 (20 mm), and #8 (25 mm), spacing between GFRP bars, and confinement due to closely spaced transverse reinforcement on the flexural performance of 11 concrete beams reinforced with ribbed GFRP bars, including the ultimate capacity, cracking moments, failure modes, and curvature. In addition to the influence of these parameters on the deflection behaviour of the tested beams at the service stages and at failure; and on the deformability of the GFRP-RC beams. The deflection equations in CSA S806 (2012) standard and ACI 440.1R (2015) guideline are assessed, and a modified form of the effective moment of inertia equation in the ACI 440.1R (2015) guideline is proposed based on the experimental results.
- **Chapter 6** introduces the results of 11 normal- and high-strength concrete beams reinforced with ribbed GFRP bars. The main testing parameters are the clear concrete cover to GFRP reinforcement (30 mm, 38 mm, and 50 mm), concrete compressive strength (35 MPa and 65 MPa), and the number of tensile GFRP reinforcement layers (one and two layers). The chapter includes the influence of these parameters on the moment capacities, moment-deflection relationships, and deflection behaviour at the service stages. Moreover, in this chapter, a numerical simulation was conducted, starting by validating six GFRP-RC beams from the study. Then, a sensitivity analysis was performed on the validated beams to discuss the effect of changing the concrete strength every 10 MPa increment from 25 MPa to 95 MPa on the beams' ultimate capacity, failure mode, cracking progression, and deflection behaviour at the service stage. The study includes an evaluation of the deflection equations in the CSA S806 (2012) standard and ACI 440.1R (2015) guideline.
- **Chapter 7** numerically investigates the sensitivity of GFRP-RC beams' flexural and serviceability behaviour to different (a) cross-sectional parameters, including the clear concrete bottom cover to GFRP reinforcement (30 mm, 38 mm, 50 mm, and 60 mm); bar spacing; bottom bar diameter #4 (13 mm), #5 (15 mm), #6 (20 mm), and #8 (25 mm); center-to-center spacing between steel stirrups; center-to-center spacing between GFRP stirrups; bar diameter of steel stirrups (10M, 15M, and 20M); bar diameter of GFRP stirrups (#3, #5,

and #6); beam size effect; and the number of tensile reinforcement layers (one, two, three, and four layers), and (b) material parameters, including the concrete compressive strength and GFRP bars' modulus of elasticity. The results are presented in terms of the ultimate capacities of the beams and deflection values at different service loading levels. The deflection equations in CSA S806 (2012) standard and ACI 440.1R (2015) guideline are evaluated to investigate the capability of these design equations in predicting the deflection values for the different parameters at different loading levels.

- **Chapter 8** provides a summary of the conducted research work, the main conclusions drawn from this study, and the recommendations for future work.
- **Appendix A** provides additional figures on the experimental research work presented in chapters 4, 5, and 6 of the thesis. These additional figures cover some construction procedures and failure modes of the tested specimens.
- **Appendix B** provides the specimen details utilized in chapter 3.

It is important to highlight that some overlap in the content might exist. This could be found in the introduction and background of each chapter, the experimental test setup, design and details of test specimens, testing instrumentations, and the loading protocol. This is due to the nature of this paper-based thesis format.

Chapter 2

Literature Review

2.1 Introduction

The design of the GFRP-RC flexural members is controlled by the serviceability limit states (SLS) rather than the ultimate limit states (ULS) in contrast to the steel-reinforced members. The high tensile strengths of the GFRP bars provide high capacities; however, due to the low modulus of elasticity of the GFRP bars, the deflection and crack widths are larger than the steel reinforcement at the service stage. Hence, the structural integrity of the GFRP-RC members should be maintained under service loads by preserving the serviceability performance of these members. The service stage is defined through different limits deduced from several research studies and adopted by the standards and guidelines [ACI 440.1R (2015), ISIS Manual No.3 (2012), CSA S806 (2012), and CSA-S6 (2014)]. The first approach to define the service stage is limiting the strains in the FRP reinforcement by taking a portion from the ultimate strain based on the FRP type (carbon, glass, and aramid). The proposed strain limit for the GFRP reinforcement was 2000 micro-strain ($\mu\epsilon$). The second limit considers design stress limits that represent a reduction in the reinforcing bar ultimate stress under sustained loads to account for various environmental deterioration. The design stress limits are ranging between 0.25 to $0.65f_{fu}$ according to the bar type (carbon, glass, and aramid). The last approach for defining the stress limit was taking a fraction of 30% from the ultimate moments; this approach was defined by Bischoff et al. (2009). The mentioned limits aim at controlling the deflection and crack width for the concrete flexural members reinforced with FRP bars at the service stage. On the other side, the stresses in concrete are limited to prevent longitudinal cracks and micro-cracks initiation. The standards and guidelines did not explicitly limit the concrete compression stresses. Jaeger et al. (1997) concluded from the flexural design capacity and the experimental tests that the onset of the inelastic deformations of concrete begins at a limit of 1000 ($\mu\epsilon$), which corresponds to stress of $0.45f'_c$ is deemed an appropriate limit for the concrete stresses under service conditions.

2.2 Cracking control in design codes

The importance of cracking control in the RC members is to protect the reinforcing bars from corrosion and maintain the durability of structures. The corrosion problem was resolved in the GFRP-RC members due to the non-corrosive nature of the GFRP bars. However, the major

concern is the larger crack widths due to the high deformability of the GFRP reinforcement. Hence, the crack width limits for GFRP-RC members are higher than steel in the guidelines and standards. Most design codes and standards propose 0.3 mm as a crack width limit for the steel-reinforced members; this limit was increased to 0.4 mm in a non-aggressive environment that is not subjected to any corrosion attack. The ACI 318 (2014) code adopted an indirect approach for crack width control by computing the spacing between the bars on the tension side. The CSA A23.3 (2014) recommended two limits, 0.3 mm and 0.4 mm, for exterior and interior exposures.

On the other side, the ACI 440.1R (2015), CSA-S6 (2014) and ISIS Manual No.3 (2012) relaxed the crack width limits of the FRP-RC members to 0.5 mm and 0.7 mm based on the exposure conditions. The ISIS Manual No.3 (2012) suggested limiting the maximum strain in FRP bars to 2000 micro-strains ($\mu\epsilon$) to control the crack width. The 2000 $\mu\epsilon$ limit was obtained by proportioning the steel bars' crack width limit to the FRP bars' limit (i.e., 0.5/0.3 or 0.7/0.4), then multiplying the result by the allowable strain in the steel (1200 $\mu\epsilon$). The CSA S806 (2012) defined a quantity z (where z is a quantity that limits the flexural FRP reinforcement distribution to provide a convenient crack control) that shall not exceed 38000 N/mm for exterior exposure and 45000 N/mm for interior exposure. The CSA S806 (2012) proposed 0.7 mm as a maximum crack width limit for the FRP-RC members.

2.3 Deflection control in design codes

Standards and guidelines recommended different deflection limitations that should not be surpassed to maintain the aesthetic appearance and functionality of the GFRP-RC members. ACI 440.1R (2015) proposed different equations to predict the thickness of the flexural components that would keep the deflection of the members under the recommended limits, as shown in Table 2.1. Others suggested the calculation of the minimum thicknesses for slabs and beams using an empirical equation as a preliminary design assumption that needs to be checked afterwards. These recommended thicknesses can control the deflection and allow the deflection to be under the proposed limits by the standards and guidelines. The CSA S806 (2012) recommended deflection limits based on the relative sensitivity of the supporting elements to the non-structural members, as shown in Table 2.2 (similar to the limits proposed by the CSA A23.3 (2014) standards for steel-RC members). Likewise, ACI 440.1R (2015) adopted the same deflection limits assigned by ACI 318 (2014).

Table 2.1 Minimum thickness of beams and one-way slabs as per ACI 440.1R (2015)

Member	Minimum thickness h			
	Simply supported	One end continuous	Both end continuous	Cantilever
Solid one-way slabs	$l/13$	$l/17$	$l/22$	$l/5.5$
Beams	$l/10$	$l/12$	$l/16$	$l/4$

Table 2.2 Deflection limits according to CSA S806 (2012)

Not supporting sensitive non-structural elements		Supporting sensitive non-structural elements
Roof	Floor	
$\Delta_{il} < \frac{l_n}{180}$	$\Delta_{il} < \frac{l_n}{360}$	$\Delta_{total} < \frac{l_n}{480}$
$\Delta_{total} < \frac{l_n}{240}$	$\Delta_{total} < \frac{l_n}{240}$	

where l is the length of the member; Δ_{il} is the immediate deflection due to specified live load; Δ_{total} is the total deflection due to sustained and immediate loads; and l_n is the clear span of the member.

2.4 Serviceability performance of GFRP reinforced concrete beams

Several researchers have extensively investigated the serviceability behaviour of GFRP-RC members, including the deflection and cracking behaviour (Masmoudi et al. 1999; Theriault and Benmokrane 1998; Vijay and GangaRao 2001; El-Salakawy and Benmokrane 2004; Bischoff et al. 2009; Kassem et al. 2011; El-Nemr et al. 2013; Mccallum 2013; El-Nemr et al. 2016; 2018; Abdelkarim et al. 2019; and Benzecry et al. 2021). The development in the FRP industry introduced GFRP bars with several surface profiles and mechanical properties (Solyom and Balázs 2020). This resulted in different bond performance and serviceability behaviour of these bars with concrete. The available types of GFRP bars in the industry are sand-coated, indented, helically wrapped, ribbed, and grooved bars. These GFRP bars differ in their mechanical properties and surface profile. The FRP design standards and guidelines utilize the crack width and deflection equations of the steel-RC members in quantifying the serviceability behaviour of GFRP-RC elements by incorporating additional factors that would account for the change in the mechanical and bond properties between the GFRP and steel bars. Some research studies in the literature (El-Nemr et al. 2013; Mccallum 2013; El-Nemr et al. 2016; 2018; and Benzecry et al. 2021) focused

on the serviceability behaviour of flexural beams reinforced with sand-coated and helically wrapped GFRP bars. However, there is a great need to investigate the deflection and cracking behaviour of beams reinforced with ribbed and grooved GFRP bars to provide an enhanced understanding of the serviceability performance of different GFRP bars with concrete.

2.4.1 Parameters affecting the serviceability behaviour

Gangarao and Faza (1990) and Theriault and Benmokrane (1998) investigated theoretically and experimentally the serviceability performance of GFRP-RC members. Other studies, including Alsayed (1998), Grace et al. (1998), and Toutanji and Saafi (2000), studied the serviceability of simply supported beams reinforced with different types of GFRP bars. Furthermore, Aiello and Ombres (2000), Yost and Gross (2002), and AbdAllah (2002) formulated different design equations for estimating the deflection of GFRP-RC beams. The previous studies defined the deformability of the members by linear analysis relations using the transformed moment of inertia of the cross-section through the moment-curvature relationship. Razaqpur et al. (2000) introduced a moment-curvature diagram in two linear parts, as shown in Figure 2.1: the first part exemplifies the concrete before cracks, and the second represents the cracked concrete. The definition of the moments-curvature relation provided by Razaqpur et al. (2000) comprised three stages: cracking, just after cracking, and at the ultimate stage. Barris et al. (2009) deduced that increasing the GFRP bars reinforcement ratio remarkably influenced the beams' stiffness and deflection after the first crack.

For the cracking mechanism, when the concrete attains its tensile strength, the first crack is formed. At this level, the reinforcing bars are highly strained, resulting in an exaggerated concrete lengthening. The bond interaction between the reinforcement and concrete transfers the tensile force between the primary cracks from the reinforcing bars to the surrounding concrete; this theory was introduced by Goto (1971). As a result of this bond mechanism, secondary cracks appear between the primary cracks, as shown in Figure 2.2. At a distance (s) between two primary cracks, there is compatibility in deformation between the bars and concrete. The third crack appears when more tensile stresses arise from the bond between the concrete and reinforcement, resulting in attaining the concrete tensile strength between the two primary cracks. Finally, a stabilized cracking stage was attained wherein the number of cracks and spacing between cracks became constant.

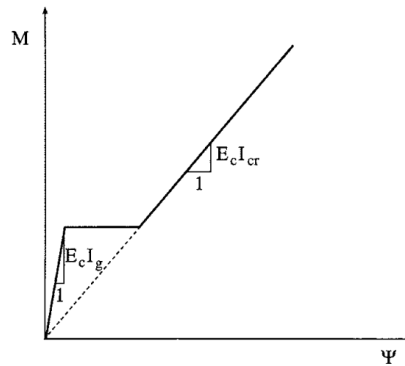


Figure 2.1 Idealized moment-curvature relation of FRP reinforced section [Razaqpur et al. (2000)]

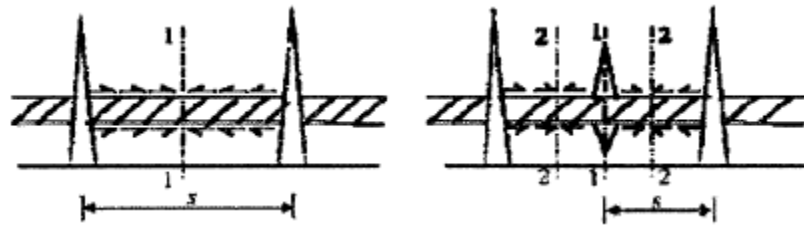


Figure 2.2 Primary and secondary cracks in concrete [Goto (1971)]

Masmoudi et al. (1996) observed a low effect of the GFRP reinforcement ratio on the crack spacing. The crack spacing was mainly affected by the type of the GFRP bar. Moreover, there was a decrease in the residual crack width by increasing the reinforcement ratio, whereas the concrete strength has nearly no influence on the residual crack width. Masmoudi et al. (1996) deduced that the high bond performance of the GFRP bar with concrete results in smaller crack spacing and width. The major findings proved that the GFRP reinforcement bond behaviour was better than steel bars under the same loading conditions.

Theriault and Benmokrane's (1998) findings conformed with Masmoudi et al. (1996) conclusions, where the reinforcement ratio did not influence the crack spacing. In addition, Theriault and Benmokrane (1998) found that the crack spacing was unaffected by the concrete strength; however, at the same applied moment, there was an increase in the crack width as the concrete strength increased. Furthermore, Theriault and Benmokrane (1998) deduced that increasing the stress level for beams with a low reinforcement ratio resulted in wider cracks than beams with a higher reinforcement ratio. There was a slight increase in the beam stiffness (> 10%) and a tenuous decrease in deflection by increasing the concrete strength. The ultimate moment capacity increased significantly by using higher concrete strength and reinforcement ratio;

however, this increased strength was limited by reducing the concrete compressive strain. Ospina and Bakis (2007) concluded that the bond interaction between the FRP bars and concrete influences the formation of flexural cracks. The crack width is wider when the stresses induced at the crack initiation are high. The increase in the reinforcement ratio minimized the crack's growth.

The bond effect was introduced in the crack width equations in the ACI 440.1R (2015) guidelines and CSA S806 (2012) standards through the bond-dependent coefficient (k_b). The k_b factor appeared first in ACI 440.1R (2003) by modifying Gergely and Lutz's (1968) crack width formulation to account for FRP bars bond behaviour. Several k_b values for different GFRP bars were estimated from the ACI 440.1R (2003) crack width equation. The estimated k_b values ranged between 0.71 and 1.83.

Frosch (1999) developed a new crack width equation based on a physical model. ACI 440.1R (2006) guidelines later adopted the equation. The k_b resulting from Frosch's equation ranged between 0.6 to 1.72 with an average of 1.1 ± 0.31 and greater than the k_b value from Gergely and Lutz's (1968) equation by 19%, as reported by El-Nemr et al. (2016). The k_b values are calculated from the crack width Eq. (2.1) and based on an approved test in CSA S806 (2012), as shown in Figure 2.3, by measuring the maximum experimental crack widths at the service stage. It is worth mentioning that the investigations of the k_b values are based only on the surface profile of the FRP bar, which excludes the effect from the other parameters like the concrete cover, bar diameter, bar spacing, compressive strength of concrete, and transverse reinforcement intensification in the bending zone.

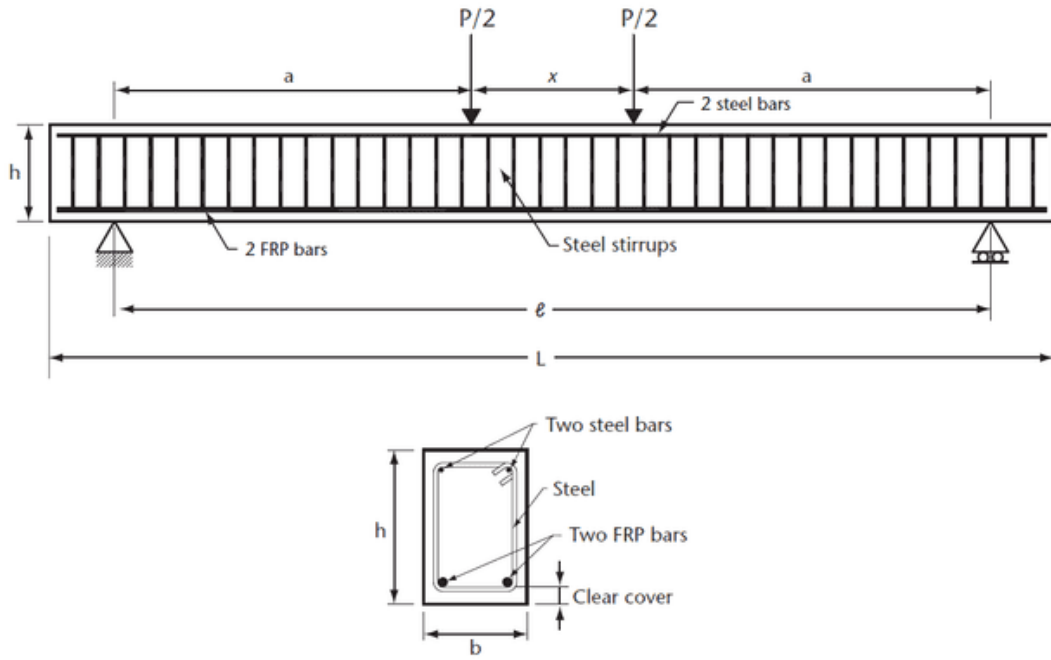


Figure 2.3 Elevation and cross-sectional details of a typical beam for the approved test by CSA S806 (2012)

$$w = 2 \frac{f_f}{E} \beta k_b \sqrt{d_c^2 + (s/2)^2} \quad (2.1)$$

where w is the maximum crack width and shall not exceed 0.7 mm; f_f is the stress in GFRP reinforcement in MPa; E_f is the elastic modulus of the GFRP in MPa; β is the ratio between the distance from the neutral axis to the extreme tension fibre and the distance from the neutral axis to the level of the tensile reinforcement; k_b is the bond-dependent coefficient; d_c is the concrete cover measured from the extreme tension fibre to the center of the tension bar in mm; s is the spacing between GFRP bars in mm. In case of a lack of experimental data, ACI 440.1R (2015) recommends a conservative k_b value of 1.4 for predicting the crack width of any flexural member reinforced with FRP bars, excluding the smooth bars and grids. CSA S806 (2012) recommended a k_b value of 1.2 for the FRP deformed or sand-coated bars, which is much lower than the proposed value by ACI 440.1R (2015). Finally, ISIS Manual No.3 (2012) proposed k_b of 1.2 in case of a shortage of experimental tests.

The k_b factor was investigated by several researchers for different GFRP bars surface profiles. Kassem et al. (2011) concluded that the crack width decreases in an inverse relation as the reinforcement ratios increase. In addition, the sand-coated bars showed superior bond performance

compared to the ribbed bars by increasing the number of cracks and reducing the average crack spacing. The k_b values varied from 0.86 to 1.32 based on the experimental crack width values. Regarding deflection behaviour, the GFRP bars exhibited larger deflection values than the carbon FRP bars at the service stage. Nevertheless, the two FRP types pronounced high deflection and deformability at failure.

El-Nemr et al. (2013) studied the flexural and serviceability behaviour of normal- (NSC) and high-strength concrete (HSC) beams reinforced with GFRP bars. The main findings showed that the NSC beams showed slightly lower strains in the GFRP bars at the same load level than the HSC beams. In addition, HSC enhanced the ultimate load capacity compared with the NSC at the same axial stiffness of the reinforcement ($E_f A_f$), as shown in Figure 2.4. The bar diameter and bar surface deformation showed a negligible effect on the deflection of the beams. One highlighted conclusion was that the crack width decreased by increasing the concrete strength and decreasing the bar diameter while maintaining the same axial stiffness. Finally, the authors proposed a k_b value of 1.2 for the helically grooved bars and 1.0 for the sand-coated bars.

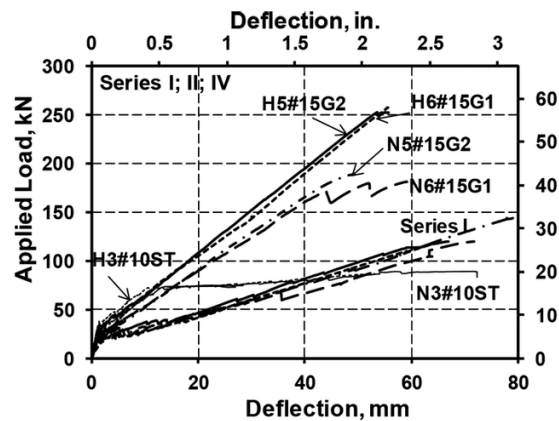


Figure 2.4 Load-deflection relations for NSC and HSC beams in El-Nemr et al. (2013)

El-Nemr et al. (2016) observed that the k_b factor is affected by the fibre type, bar diameter, and bar surface profile. The type of concrete NSC and HSC affected the k_b factor without a clear trend. In addition, the bond performance of the sand-coated GFRP bars was better than the grooved bars. The study showed clearly that the change in the k_b values affects the design of GFRP reinforced members, and more studies are needed to discuss all the expected parameters that would affect the k_b values for different surface profiles of GFRP bars.

Barris et al. (2017) showed that increasing the reinforcement ratio of the GFRP bars and the

concrete cover thickness decreased the crack spacing. Notably, the elastic modulus of the GFRP bars, reinforcement ratio, different bond properties of the indented and helically wrapped bars, and the effective depth of the beam affect the average crack width. Ju et al. (2017) studied the effect of changing the bar spacing of ribbed GFRP bars on the serviceability behaviour of eight RC beams. The study showed that the k_b value of 1.0 yields more released bar spacing than the k_b value of 1.4.

El-Nemr et al. (2018) investigated GFRP-reinforced concrete beams. The conclusions drawn from this study confirmed that the axial-reinforcement stiffness ($E_f A_f$) controls the flexural behaviour of the GFRP-RC members. When the $E_f A_f$ increased, the load-carrying capacity increased, and the deflection and crack widths decreased. In addition, the bar surface deformation affects the strains and crack widths at the same loading level for the same axial-reinforcement stiffness. It was concluded that the larger the bar diameter for the same type of bars, the narrower the crack width with higher cracking performance, without any noticeable effect on the deflection behaviour of the beams, as shown in Figure 2.5.

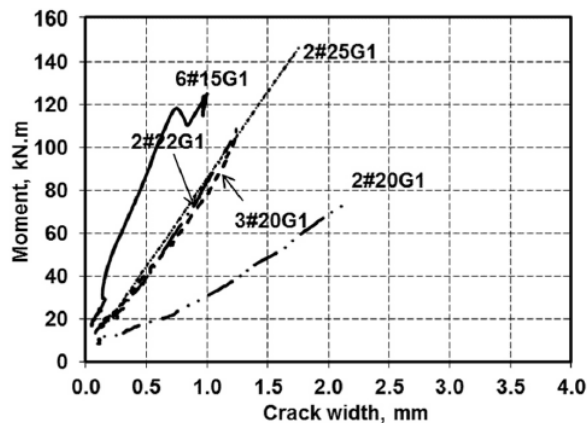


Figure 2.5 Load-crack width relations for GFRP-RC beams in El-Nemr et al. (2018)

Shield et al. (2019) recalibrated the k_b values of different GFRP bars surface profiles using a robust database available in the literature. The database was filtered for consistency by applying specific criteria. Over 200 crack width tests, 39 crack widths data were included in evaluating the k_b values using Eq. (2.1). After the data filtration, the study recommended a k_b value of 1.2 for the sand-coated bars. Due to the lack of data for the ribbed and grooved bars, the proposed k_b value was 1.4, as recommended by ACI 440.1R (2015).

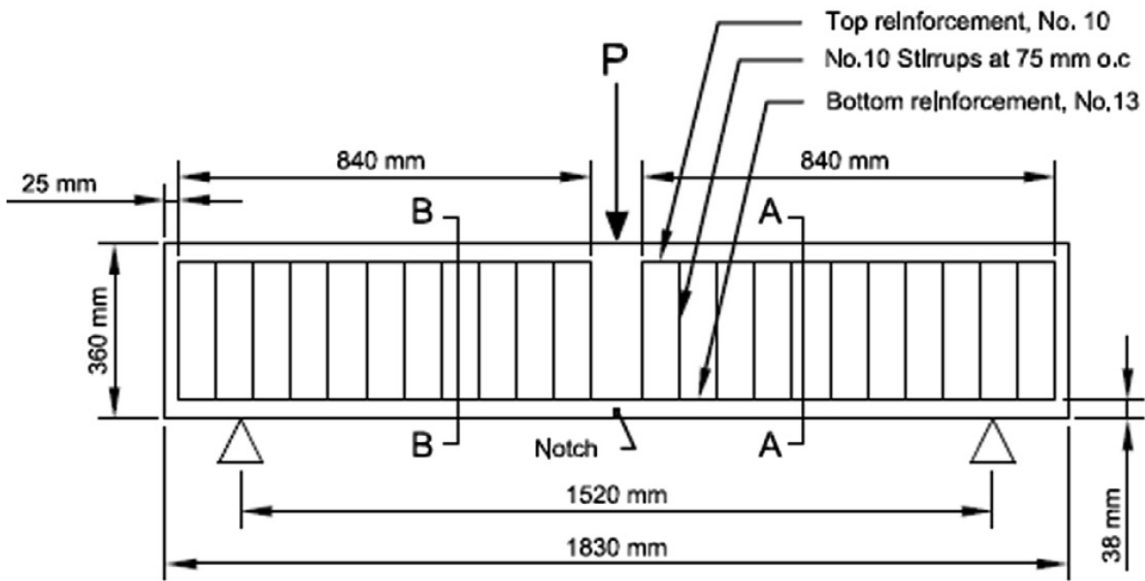
Abdelkarim et al. (2019) investigated the flexural behaviour of normal- and high-strength

concrete beams reinforced with deformed GFRP bars. The conclusions showed an increase in the secant stiffness of the moment–deflection relationship and a decrease in crack width by increasing the GFRP bars reinforcement ratio and the concrete strength. In addition, the NSC beams exhibited higher curvatures and lower moment capacity than the HSC beams. The study highlighted that using smaller bar diameters increased the service moment values more than the bigger diameters. In addition, the proposed curvature ductility method for deformability prediction showed a clear trend for the tested beams. The NSC beams had lower ductility indices than the HSC beams.

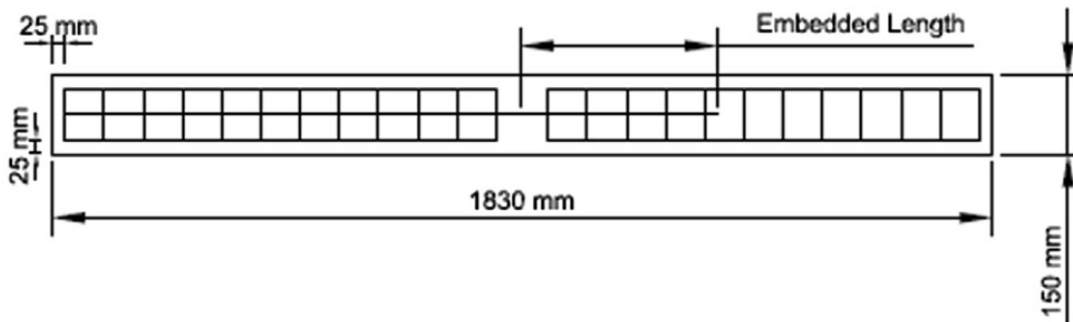
Mousa et al. (2020) studied the flexural and serviceability performance of confined square members reinforced with GFRP sand-coated bars. The results showed that the flexural strength of the GFRP members was approximate twice the steel-reinforced members for the same reinforcement ratio. The capacity of the members increased as well by increasing the reinforcement ratio.

Benzecry et al. (2021) tested 23 concrete beams with different dimensions reinforced with sand-coated with helical wrap and grooved bars to determine the k_b factor per CSA S806 (2012) approved test and using an adopted test, as shown in Figure 2.6. The beams in the adapted approach were pre-notched, and the reinforcement bars were spliced and designed according to ACI 440.1R (2015). The pre-notched adapted specimens showed more consistent k_b values than the unnotched beams. Moreover, obtaining the k_b values at a crack width of 0.7 mm provided consistent results. Finally, the k_b factor of the grooved bars was slightly higher than the k_b of sand-coated with helical wrap bars.

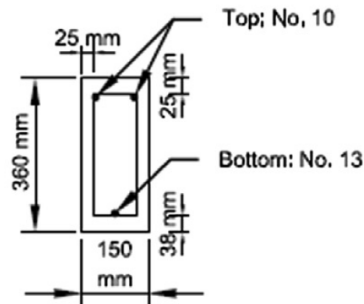
Side View



Plan View



Section A-A



Section B-B

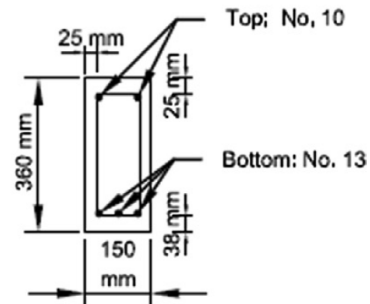


Figure 2.6 The adapted method proposed by Benzecry et al. (2021)

2.5 Bond performance and development length of GFRP reinforcement

The bond behaviour of GFRP bars with concrete has a different mechanism from steel reinforcement due to the anisotropic nature of the GFRP bars since the mechanical and physical properties in the longitudinal and transverse directions are different (Cosenza et al. 1997; and Mosley et al. 2008). The fibre properties control the longitudinal direction behaviour, while the resin controls the transverse direction performance. Different parameters control the bond behaviour between the GFRP bar and concrete, including the bar diameter, concrete cover, concrete compressive strength, embedment length, and bar surface configuration (Cosenza et al. 1997). In order to quantify the bond strength, there are two commonly performed tests. These tests are a) direct pull-out test, which does not simulate the actual bond behaviour in a reinforced concrete member, and b) beam-bond tests, which mimic the real GFRP bar bond behaviour inside the concrete member through the bending loading scheme (Sólyom et al. 2016). Many investigations showed the need to re-evaluate the existing development length equation in the CSA-S806 (2012) (Choi et al. 2012; Yan et al. 2016; and Zemour et al. 2018). Hence, determining the optimum design equation that would fulfill the bond design requirements of the GFRP reinforcement.

2.5.1 Splitting failure theoretical approaches

There are four possible failure modes for a GFRP bar embedded in concrete, as illustrated in Figure 2.7. The first failure mode is the bar rupture before attaining full bond strength. The second failure mode is the local concrete crushing or shear failure in concrete due to the GFRP bar pull-out. The third mode of failure is the pull-out, which depends on several factors, including the surface deformation of the bar, the confinement effect from concrete or transverse reinforcement, and the embedment length. The pull-out failure occurs by increasing the confinement due to concrete or transverse reinforcement and decreasing the embedment length, as Baena et al. (2009) demonstrated. The fourth failure mode is the splitting failure; this failure mode's mechanism is the most critical failure mode that affects the development length design. The force transfer between a conventional steel bar and the surrounding concrete is primarily achieved by the bearing of ribs on the concrete. The bearing of the ribs results in a compressive force acting on the concrete inclined by an angle α to the longitudinal axis of the bar, as shown in Figure 2.8. The inclined force comprises two components: the radial component representing the splitting force and the

tangential component representing the bond force. Splitting failure occurs when the induced tensile stresses from the splitting component exceed the concrete tensile strength. If there is sufficient confinement from the concrete cover or transverse reinforcement, pull-out failure occurs accompanied by shearing off the concrete by the rib's tips (Tepfers 1973).

Tepfers (1973) assumed that the angle α is constant and has a value of 45° since the properties of concrete are equal in tension and compression before the initiation of the first cracks in concrete. However, after the formation of the first cracks, Tepfers (1973) noted that the value of angle α is likely to change depending on the geometrical configuration of the ribs of the steel bar. Faoro (1994) and Fukuyama et al. (1994) highlighted the significance of the low modulus of elasticity and high deformability of the GFRP bars in increasing the potential of splitting failure occurrence in the concrete beams. Achillides (1998) concluded that the embedment length and elastic modulus of GFRP reinforcing bars have an important role in influencing the bond splitting strength by controlling the deformability of the bars inside the concrete and the crack geometry, resulting in a noticeable difference in the slippage between the loaded and the free ends of the bar.

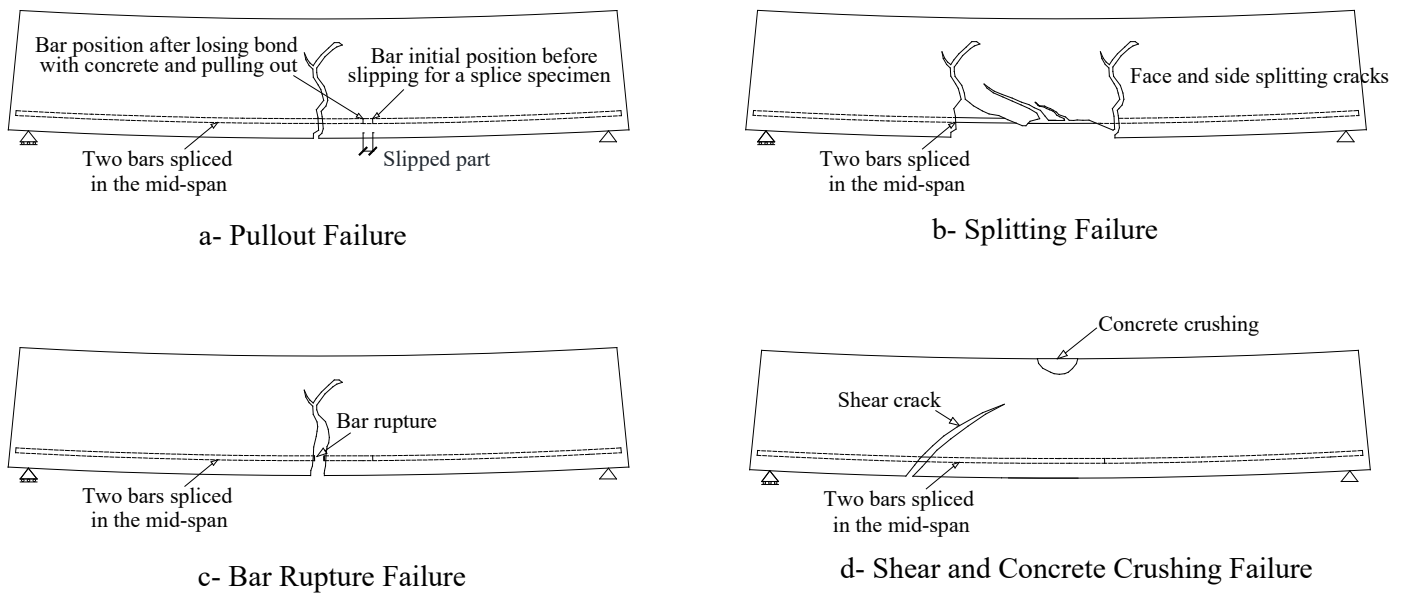


Figure 2.7 Different modes of failure for GFRP bars in concrete: (a) pullout failure; (b) splitting failure; (c) bar rupture failure; and (d) shear and concrete crushing failure

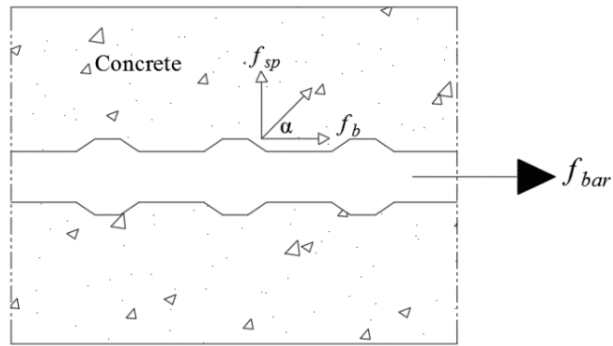


Figure 2.8 Tensile force acting on a steel bar embedded in a reinforced concrete member

2.6 Nonlinear finite element modelling of GFRP flexural members

Nowadays, nonlinear finite element modelling (NFEM) has become an economical and rapid tool for anticipating the behaviour of the different structural members. The modelling of GFRP reinforced concrete members has been conducted in several research studies with different structural components, including the shear walls and columns. The analysis of these members aims at investigating the seismic performance of these members either at a component level or structure level by modelling the whole structure. Some researchers studied the flexural strengthening of slabs and beams reinforced with FRP bars through the external prestressing of tendons, laminates, plates, and sheets. Few studies investigated the flexural and serviceability behaviour of members reinforced with internally embedded GFRP reinforcement.

Adam et al. (2015) investigated experimentally and numerically the flexural capacity and deflection behaviour of concrete beams reinforced with ribbed GFRP reinforcement. The numerical study was performed using ANSYS software. The investigation did not include any parametric study; however, the study mainly verified the experimental work and presented the effectiveness of nonlinear modelling in predicting the behaviour of beams.

Bencardino et al. (2016) modelled concrete beams reinforced with steel, AFRP, GFRP and hybrid steel-FRP reinforcement using ABAQUS software. This study focused on modelling 17 beams compiled from literature with some analytical predictions of load-deflection relations and ultimate capacity. The study proved that the (NFEM) is a reliable numerical tool in figuring out the behaviour of RC beams reinforced with FRP bars and different hybrid configurations.

Kazemi et al. (2020) used ABAQUS software to validate the results of ten simply-supported normal-strength concrete beams having a concrete compressive strength of 30 MPa. The beams

were reinforced with CFRP (carbon fibre-reinforced polymers) and GFRP bars, grouted in sleeves in the middle bending zone for some specimens and along the entire bar length for other specimens. The authors performed a parametric study by increasing the concrete strength of the ten beams to 60 MPa to be high-strength concrete beams.

Saleh et al. (2019) investigated the effect of concrete compressive strength, reinforcement ratio of longitudinal bars, shear span-to-depth ratio, and elastic modulus of the GFRP reinforcement on the deflection performance, moment capacity, and failure modes of RC beams numerically. The developed numerical models were performed using LS-DYNA software, and the conclusions showed that the numerical modelling provides reliable results. In addition, the models could anticipate the deflection behaviour, ultimate moment capacity, and energy absorption capacity.

2.7 Summary and gaps in the literature

The literature review showed some research gaps that should be covered and investigated to optimize the design of GFRP-RC elements. The experimental work conducted on GFRP-RC beams studied the serviceability and flexural performance of these beams. Most of the reinforcing bars utilized in these tests were sand coated and helically wrapped. The previous studies showed a gap in knowledge for the flexural and serviceability performance of the ribbed GFRP bars reinforcing flexural members. The available tests performed on beams reinforced with GFRP ribbed bars provided the literature data set with results regarding crack width, deflection, and moment capacity. However, more experimental data are required for a better understanding of the bond-dependent coefficient (k_b), including the study of different parameters that would affect the crack width and the deflection behaviour, “e.g., bar diameter, bar spacing, concrete cover, reinforcement ratio, number of tensile reinforcement layers, bar surface profile, and effect of confinement due to the closely spaced transverse reinforcement”.

There are discrepancies in the conclusions of the available research studies regarding the effect of the concrete compressive strength on the crack width. Some researchers found that the concrete strength influenced the bond behaviour, strength, and mode of failure of the GFRP-RC members. Other researchers showed that the concrete compressive strength had an effect with no trend on the crack width. Hence, there are uncertainties about the influence of concrete strength on the crack width. Consequently, this discrepancy necessitates a crucial investigation that would explore the effect of the concrete compressive strength on the crack width.

Furthermore, limited studies investigated the confinement effect of the closely spaced stirrups in the flexural zone on the serviceability and flexural behaviour of the ribbed bars. The ribbed bars are analogous to the steel bars in the bar surface profile, even though the steel ribs' height is higher than in the GFRP bars. Researchers expected that the confinement effect from transverse reinforcement would increase the bond resistance of the ribbed GFRP bars, increase the ultimate capacity, decrease the crack width, increase the deformability, and improve the deflection behaviour of the concrete beams.

The literature showed that the CSA S806 (2012) development length equation provides inaccurate results in predicting the required design development length. In addition, a limited number of studies utilized finite element modelling in performing parametric studies on the different parameters that might affect the design of GFRP-RC members. The numerical tool opens the door to perform a sensitivity analysis on the effect of different parameters, either material or configurational, on the flexural and serviceability behaviour of GFRP-RC beams that can not be tested experimentally, including the effect of changing the material properties like the concrete strength and GFRP bars modulus of elasticity. In addition to some configurational parameters, including the concrete cover, confinement effect due to closely spaced steel and GFRP stirrups, top compression bar and top concrete cover, and the number of reinforcement layers (acting as skin reinforcement).

Based on the conclusions of the previous studies, the design provisions of the GFRP-RC members, including the deflection and crack width equations, different serviceability design limits, and the development length design equation, require an assessment to obtain the optimal design equations and limits that would fulfill the safety and cost control.

Chapter 3

Proposed equations for the development length of GFRP bars in flexural reinforced concrete members

3.1 Abstract

The bond at the interface between concrete and the surface of a glass fibre-reinforced polymer (GFRP) bar is the most critical parameter that ensures that the strains between the GFRP bar and the surrounding concrete are compatible. To prevent bond failure, an adequate development length should be provided. The equations for the development length specified in current design codes were developed using experimental data that are now outdated. This study evaluates the current equation for the development length in the CSA S806 (2012) and ACI 4401R (ACI 2015) provisions; the approach is based on a regression analysis of an experimental database of results from 431 recent tests of beam bonding reported in the literature. The main objective herein is to optimize the development length equation through a comprehensive assessment of the influencing parameters. The parameters studied in this investigation are the concrete compressive strength, concrete cover, confinement effect, bar diameter, bar location, bar surface profile, and bar tensile stress. The study proposes equations and design recommendations that provide an optimized estimation of the development length. The proposed equations were compared to the current equations of CSA S806 (2012) and ACI 440.1R (2015).

3.2 Introduction

Glass fibre-reinforced polymer (GFRP) reinforcement has been used for its high tensile strength to weight ratio, superior corrosion resistance, nonmagnetic properties, and appropriate fatigue performance (Ehsani et al. 1996, Mosley et al. 2008, Issa et al. 2011, and ACI 440.1R (2015)). The mechanical properties of GFRP bars are characterized by high strength and low modulus of elasticity compared to steel. The mechanism of the bond between a GFRP bar and concrete differs from that between steel reinforcement and concrete due to the unidirectional nature of the GFRP bars because the mechanical and physical properties are dissimilar in the longitudinal and transverse directions (Cosenza et al. 1997 and Mosley et al. 2008). The fibre properties control the behaviour of a bar in the longitudinal direction, while the resin controls its transverse behaviour. The mechanical properties of the resin are unlike those of concrete, which results in bonding interactions that differ from those between steel reinforcements and concrete, resulting in bar surface damage rather than concrete cracking. Therefore, bond behaviour affects stresses and strains in the longitudinal and transverse directions.

The parameters that control the bond behaviour between GFRP bars and concrete are the bar diameter, concrete cover, concrete compressive strength, embedment length, and bar surface configuration (Cosenza et al. 1997). To quantify the bond strength, two tests are commonly performed: a) the direct pullout test, which does not simulate the actual bonding behaviour in a reinforced concrete member, and b) the beam-bond test, which mimics the actual GFRP bar behaviour inside a concrete member through a bending and loading scheme (Sólyom et al. 2016). Many recent investigations illustrated the need to re-evaluate the current equations for development length (e.g., Choi et al. 2012, Yan et al. 2016, Zemour et al. 2018, and Saleh et al. 2019).

3.3 Background on GFRP development length equations in different provisions

The bond strength, the average interfacial shear stress along the contact surface between the reinforcing bar and concrete, corresponds to the maximum force transferred from the bar to the surrounding concrete. The development length is defined as the length of embedded reinforcement required to develop the design stress of reinforcement. The Canadian Standard CSA S6 (2014) proposed Eq. (3.1) for estimating the development length of straight FRP bars for splitting failure specimens.

$$l_d = 0.45 \frac{k_1 k_4}{d_{cs} + K_{tr} \frac{E_{FRP}}{E_s}} \frac{f_{frp}}{f_{cr}} A_b \quad (3.1)$$

where f_{frp} is the design stress of the FRP bar at the ultimate limit state in MPa; f_{cr} is the concrete cracking strength in MPa, which shall be $0.4\sqrt{f'_c}$ for normal-density concrete where f'_c is the concrete compressive strength, $0.34\sqrt{f'_c}$ for semi-low density concrete, and $0.3\sqrt{f'_c}$ for low-density concrete; $\sqrt{f'_c}$ shall not exceed 8; and E_{frp} and E_s are the elastic moduli of GFRP and steel bars in MPa, respectively. k_1 is the bar location factor given as 1.3 for horizontal reinforcement placed where more than 300 mm of fresh concrete is cast below the development length or splice and 1.0 for other cases; A_b is the bar diameter area in mm²; and k_4 is the bar surface factor calculated as the ratio of the bond strength of the bar to that of a deformed steel bar with the same cross-sectional area. The factor k_4 shall not exceed 1.0 and shall be taken as 0.8 in the absence of experimental data; d_{cs} is defined as the smaller of the two values of the concrete cover measured from the extreme tension fibres to the center of the developed tensile reinforcement, and two-thirds of the center-to-center spacing of the developed bars, in mm; and K_{tr} is the transverse reinforcement index and calculated using Eq. (3.2):

$$K_{tr} = 0.45 \frac{A_{tr} f_y}{10.5 s n} \quad (3.2)$$

where A_{tr} is the area of transverse reinforcement within l_d that crosses the potential bond-splitting crack in mm²; f_y is the specified yield strength of steel reinforcing bars in MPa; s is the spacing of the transverse reinforcing bars in mm; and n is the number of bars developed or spliced along the potential splitting failure plane. The term $(d_{cs} + K_{tr} \frac{E_{FRP}}{E_s})$ shall not be greater than $2.5d_b$.

In ACI 440.1R (2015), Eq. (3.3) was proposed for the average bond stress (u) calculation based on a study by Wambeke and Shield (2006):

$$\frac{u}{\sqrt{f'_c}} = 4 + 0.3 \frac{c}{d_b} + 100 \frac{d_b}{l_e} \quad (3.3)$$

where c is the lesser of the concrete cover to the center of the bar (d_c or $d_{c,side}$) or one-half of the center-to-center spacing of the developed bars in mm; and l_e is the embedded length of the reinforcing bar in mm. According to ACI 440.1R (2015), Eq. (3.4) is currently used to estimate the development length to prevent splitting failure,

$$l_{d,spitting} = \frac{\alpha \frac{f_{fr}}{0.083 \sqrt{f'_c}} - 340}{13.6 + \frac{c}{d_b}} d_b \quad (3.4)$$

where α is a coefficient that accounts for the bar location, taken as 1.0 for the bottom bars and 1.5 for bars with more than 300 mm of the concrete cast below; and f_{fr} is the maximum stress developed in the GFRP bars in MPa, which should be the minimum ultimate stress of the bars, f_{fu} or the design stress, f_f , given by Eq. (7.2.2d) in ACI 440.1R (2015).

The development length equations in CSA S806 (2002) and the current CSA S806 (2012) standards were derived from the CSA A23.3 (1994) development length equation for steel bars with a slight modification, e.g., removing the transverse reinforcement coefficient (K_{tr}) and incorporating the k_5 factor that accounts for the surface profile of the GFRP bar. The CSA A23.3 (1994) development length equation was modified from the general development length equation of deformed bars and wires proposed by ACI Committee 408 (1979, reaffirmed 1990), which was based on the regression analysis performed by Orangun et al. (1977),

$$l_d = 1.15 \frac{k_1 k_2 k_3 k_4 k_5}{d_{cs}} \frac{f_f}{\sqrt{f'_c}} A_b \quad (3.5)$$

where f_f is the design stress in GFRP tension reinforcement at the ultimate limit state in MPa; A_b is the cross-sectional area of the bar in mm²; and k_1 is the same factor found in the development length Eq. (3.1); k_2 is the concrete density factor taken as 1.3 for low-density concrete, 1.2 for semi-low-density concrete, and 1.0 for normal-density concrete; k_3 is the bar size factor taken as 0.8 if A_b is less than or equal to 300 mm² and 1.0 if A_b is greater than 300 mm²; k_4 is the bar fibre factor proposed as 1.0 for carbon fibre-reinforced polymer (CFRP) and GFRP, and 1.25 for aramid fibre-reinforced polymer (AFRP); k_5 is the bar surface profile factor and shall not be taken as less than 0.5 and can be taken as 1.0 for roughened or sand-coated, 1.05 for spiral patterned, 1.0 for braided, 1.05 for ribbed, and 1.80 for indented surfaces. Moreover, CSA S806 (2002) states that $\sqrt{f'_c}$ shall not exceed 8; this was later modified in CSA S806 (2012) such that it shall not exceed 5. In the two standards, d_{cs} is defined as the smaller value of the concrete cover (in mm) measured from the extreme tension fibres to the center of the tensile developed bars and two-thirds of the spacing between the center-to-center of the developed bars. The d_{cs} shall not be greater than $2.5d_b$, where d_b is the bar diameter. The resulting average bond stress equation (τ) presented in Eq. (3.7)

is obtained by substituting Eq. (3.5) in Eq. (3.6), where T is the maximum force (in N) achieved when the FRP bar reaches its design tensile stress at the ultimate limit state:

$$\tau = \frac{T}{\pi d_b l_d} \quad (3.6)$$

$$\tau = \frac{1}{1.15 \pi k_1 k_2 k_3 k_4 k_5} \frac{d_{cs} \sqrt{f'_c}}{d_b} \quad (3.7)$$

The current study evaluates the existing development length equation in CSA S806 (2012). A comprehensive database of 431 beam tests was collected and classified according to the failure modes. The development length equation assessment was based on regression analysis of the gathered database to investigate the influence of different parameters, including the concrete strength, the diameter, surface profile, and location of the bar, and the confinement effects of concrete and transverse reinforcement.

3.4 Database classification

There are four possible failure modes for a GFRP bar embedded in concrete, as displayed in Figure 3.1. The first failure mode is bar rupture before attaining full bond strength. The second is local concrete crushing or shear failure in concrete due to GFRP bar pullout. The third is pullout failure, which depends on several factors, including the surface profile of the bar, the confinement effect from concrete or transverse reinforcement, and the embedment length. Increasing the confinement and decreasing the embedment length will result in bar pullout failure (Baena et al. 2009). The fourth failure mode is splitting failure, which is deemed the most critical mode of failure for the bar length because splitting occurs by aggressive cracking in the concrete without attaining full bond capacity between the bar and surrounding concrete (Baena et al. 2009).

In this study, the results of 431 bond tests on beams reinforced with GFRP bars were collected from the literature, as presented in Table 3.1. The experimental data were analyzed, and the current development length equation in CSA S806 (2012) was assessed. The specimens comprised 132 splice tests, 175 beam end tests, 135 hinged beam tests, and seven modified beam tests. The splice tests were analyzed separately, whereas the other tests were investigated to develop a useful equation that could be used to predict the design development length. Table 3.2 presents the general classification of the experimental tests according to the failure modes.

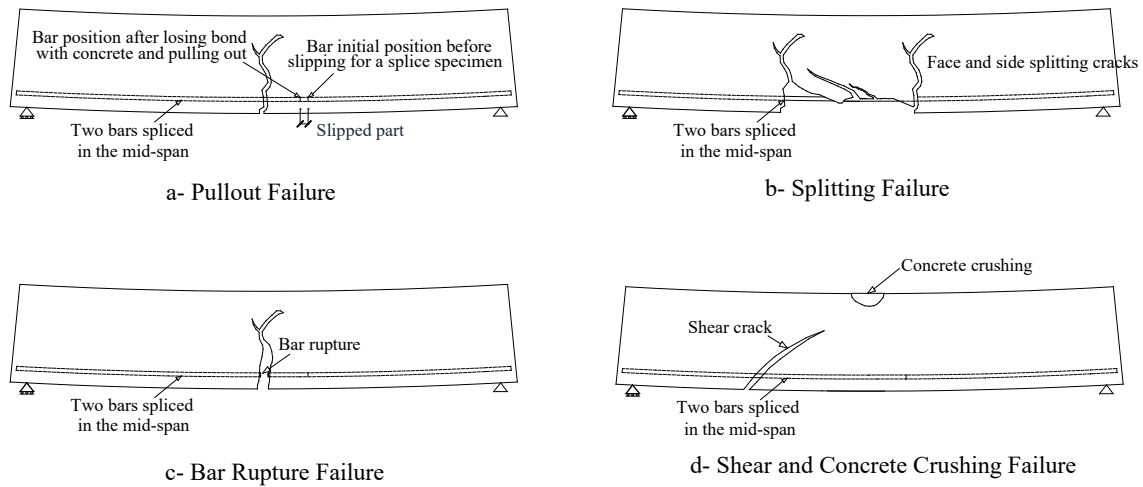


Figure 3.1 Different modes of failure for GFRP bars in concrete: (a) pullout failure; (b) splitting failure; (c) bar rupture failure; and (d) shear and concrete crushing failure

Table 3.1 Test data for the beam-test specimens

Reference	Test Type	Number of beams
	Beam end tests	48
Shield et al. (1997)	Beam end tests	10
Shield et al. (1999)	Beam end tests	65
Defreese and Wollmann (2002)	Beam end tests	40
Kytonia et al. (2017)	Beam end tests	12
Benmokrane et al. (1996)	Hinged beam tests	4
Tighiouart et al. (1998)	Hinged beam tests	14
Okelo (2007)	Hinged beam tests	12
Xue et al. (2014)	Hinged beam tests	10
Hossain (2018)	Hinged beam tests	12
Saleh et al. (2019)	Hinged beam tests	24
Basaran and Kalkan (2020)	Hinged beam tests	37
Makhmalbaf and Razaqpur (2021)	Hinged and notched beam tests	4
Pecce et al. (2001)	Modified beam tests	7
Achillides (1998)	Splice tests	6
Tighiouart et al. (1999)	Splice tests	16
Aly (2005)	Splice tests	11
Aly et al. (2006)	Splice tests	6
Mosely et al. (2008)	Splice tests	6
Harajli and Abouniaj (2010)	Splice tests	12
Choi et al. (2012)	Splice tests	24
Esfahani et al. (2013)	Splice tests	13
Pay et al. (2014)	Splice tests	28
Zemour et al. (2018)	Splice tests	6
Asadian et al. (2019)	Splice tests	2
Asadian et al. (2019)	Splice tests	2
	Total	431

Table 3.2 Classification of the Database

	Splitting Failure	Pullout Failure	Tensile Failure	Other Failure Mode
SPLICE TESTS				
Total number of beams	118	8	4	2
Compressive strength (MPa)	23-72 MPa	39 and 52 MPa	41-45 MPa	31 MPa
Concrete cover to bar center	1.5-4.5 d_b	2.6 and 4.3 d_b	2.5-2.6 d_b	2.4 d_b
Unconfined bottom bars	42	0	0	0
Confined bottom bars	49	8	4	2
Unconfined top bars	27	0	0	0
Confined top bars	0	0	0	0
BEAM END, HINGED BEAM, AND MODIFIED TEST SPECIMENS				
Total number of beams	63	170	60	6
Compressive strength (MPa)	22.8-44.5	17.3-77.9	30.0-55.0	31.3-65.4
Concrete cover to bar center	1.5-3.5 d_b	1.3-9.8 d_b	1.5-9.8 d_b	2.0-3.1 d_b
Unconfined bottom bars	61	105	41	1
Confined bottom bars	0	41	9	5
Unconfined top bars	2	24	10	0
Confined top bars	0	0	0	0

Note: The other failure modes are shear failure, compression failure, and combined shear and compression failure.

3.4.1 Splice specimens

The database includes 132 splice specimens, where 118 beams failed due to splitting, eight failed by GFRP bar pullout, four failed by reinforcement rupture, and two failed by local compression in the splice zone. The splitting results were based on tests performed by Achillides (1998), Tighiouart et al. (1999), Aly et al. (2005), Aly et al. (2006), Mosely et al. (2008), Harajli and Abouniaj (2010), Choi et al. (2012), Esfahani et al. (2013), Pay et al. (2014), Zemour et al. (2018), Asadian et al. (2019a), and Asadian et al. (2019b). Among the 118 beams that failed by splitting, 69 were unconfined, and 49 were confined. The unconfined beams included 27 top bar specimens and 42 bottom bar beams. The 49 confined beams were all bottom bar beams. Table 3.3 shows the confined specimens and the transverse reinforcement details in the splice zone.

From the data for splitting failure, values of the embedment length (l_e) ranged from $10d_b$ to $20d_b$ for 28 beams, from greater than $20d_b$ to $40d_b$ for 59 beams, from greater than $40d_b$ to $60d_b$ for 23 beams, and from $70d_b$ to $100d_b$ for eight beams. The concrete compressive strength (f'_c) of 115 splitting beams ranged from 23 to 52 MPa, and only three beams had an f'_c of 72 MPa. Among the beams that failed by splitting, 14 had a concrete cover to the center of the bar ranging from $1.5d_b$ - $2d_b$, 79 had a concrete cover in the range of $2.5d_b$ - $3d_b$, 24 had a concrete cover greater than $3d_b$, and only one beam had a concrete cover greater than $4.5d_b$. The size of the GFRP bars

in the splitting tests ranged from #3 to #8, with nominal diameters from 8.5 to 25.4 mm. The surface profiles of the GFRP bars were sand-coated, helically wrapped, helically wrapped with sand-coating, and ribbed. For the eight beams that failed by the GFRP bar pulling out, the results were reported by Harajli and Abouniaj (2010) and Esfahani et al. (2013).

Table 3.3 Transverse reinforcement details

	$d_{b-stirrups}$	Stirrups spacing along the splice	Stirrup's type	$E_{stirrups}$ (MPa)
Achillides (1998)	8 mm	75 mm	GFRP	45300
Tighiouart et al. (1999)	11.3 mm	80 mm	Steel	200000
Aly (2005)	8 mm	150 mm	Steel	200000
Aly et al. (2006)	8 mm	150 mm	Steel	200000
Harajli and Abouniaj (2010)	8 mm	60 mm	Steel	200000
		80 mm		
Esfahani et al. (2013)	6 mm	120 mm	Steel	200000
		80 mm		
Okelo (2007)	10 mm	102 mm	Steel	200000
Kytonia et al. (2017)	6 mm	100 mm	Steel	200000
Basaran and Kalkan (2020)	8 mm	58 mm	Steel	200000
Makhmalbaf and Razaqpur (2021)	10 mm	60 mm	Steel	216000

All the specimens were bottom confined bars with embedment lengths of $15d_b$, $18d_b$, or $20d_b$. Six beams were reinforced with threaded wrapped GFRP bars having an f'_c of 52 MPa and a concrete cover to the center of the bar of $1.8d_b$ or $2.6d_b$ with a corresponding nominal diameter of 12 mm. Only two beams had an f'_c of 39 MPa with a concrete cover of $4.3d_b$ and were reinforced with a 10 mm sand-coated bar. Finally, four beams that failed by bar rupture were reported by Aly (2005) and Aly et al. (2006), and two specimens that failed by local compression were reported by Tighiouart et al. (1999). The splitting results from the splice tests were considered in estimating the development length equation. Notably, 15 splice specimens in the database were identified as outliers and excluded from the subsequent analysis.

Two specimens in Zemour et al. (2018) were self-consolidating concrete. The tensile strength of self-consolidating concrete is higher than that of ordinary concrete, as mentioned by Zemour et al. (2018). Accordingly, for these two specimens, the concrete cylinder tensile strength of the self-consolidating concrete was used in the bond strength equations in lieu of $0.6\sqrt{f'_c}$, which is the assumed concrete tensile strength in the bond strength equations.

3.4.2 Beam end, hinged beam, and modified test specimens

The database included 175 beam end tests, 117 hinged beam tests, and seven modified beam tests. Among these specimens, the failure modes were splitting for 63 beams, GFRP bar pullout for 170, GFRP bar rupture for 60, shear and local compression failure for five, and shear failure for one. The splitting results were reported by Ehsani et al. (1996), Shield et al. (1997), Shield et al. (1999), and Xue et al. (2014). All 63 splitting specimens were unconfined, including 61 bottom bar specimens and two top bar beams. From the reported data, the embedment lengths (l_e) ranged from $3.6d_b$ to $20d_b$ for 49 beams and from greater than $20d_b$ to $33.3d_b$ for 14 beams. The concrete compressive strength (f'_c) of the splitting specimens ranged from 22.8 to 44.5 MPa. In addition, the concrete cover to the center of the bar was $1.5d_b$ for four specimens, $2.5d_b$ for 37 beams, $3.1d_b$ for five beams, and $3.5d_b$ for 17 beams. The GFRP bars were sand-coated or helically wrapped with sand coating. The GFRP bars varied in size from #3 to #8 with nominal diameters from 9.5 to 28.6 mm. Nine splitting specimens were considered outliers and not included in the subsequent analysis.

The 170 pullout specimens were based on tests conducted by Ehsani et al. (1996), Benmokrane et al. (1996), Tighiouart et al. (1998), Defreese and Wollmann (2002), Pecce et al. (2001), Okelo (2007), Xue et al. (2014), Kytonia et al. (2017), Hossain (2018), Salah et al. (2019), and Basaran and Kalkan (2020). The specimens include 105 unconfined bottom beams, 24 unconfined top beams, and 41 confined bottom beams. The embedment lengths ranged from $2.5d_b$ to $23.1d_b$, and the values of f'_c ranged from 17.3 to 77.9 MPa for all the specimens. The concrete cover to the center of the bars was in the range from $1.3d_b$ to $2d_b$ for 21 specimens, from $2d_b$ to $2.7d_b$ for 63 tests, greater than $3d_b$ to $4.5d_b$ for 75 specimens, $5.3d_b$ for eight and $9.8d_b$ for three beams. The GFRP bars varied in size between bars #3 to #9, with nominal diameters from 6.0 to 28.6 mm. The surface profiles of the GFRP bars were sand-coated, helically wrapped, helically wrapped with sand coating, and ribbed.

3.5 Theoretical approach

The transfer of force between a conventional steel deformed bar and the surrounding concrete is primarily achieved by ribs bearing on the concrete, resulting in a stress field, as shown in Figure 3.2. The inclined force comprises two components: the radial component representing the splitting force and the tangential component representing the bond force. Splitting failure occurs when

induced tensile stresses from the splitting component exceed the concrete tensile strength. If there is sufficient confinement from the concrete cover or transverse reinforcement, then pullout failure occurs, accompanied by shearing off the concrete by the edge of the rib (Tepfers 1973).

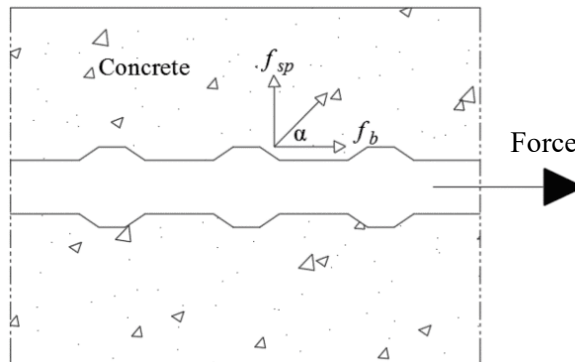


Figure 3.2 Tensile force acting on a steel bar embedded in a reinforced concrete member

Several researchers, including Aly et al. (2006), Choi et al. (2012), Xue et al. (2014), Pay et al. (2014), Hossain (2018), Zemour et al. (2018), and Saleh et al. (2019), concluded that the average experimental bond stress at failure (where the bar reaches its maximum tensile stress) decreases as the embedment length increases. Notably, Eq. (3.7) provides the average bond stress at splitting failure of the beams (when the bar reaches its maximum tensile stress) without considering the change that would occur in the bond strength due to the change in embedment length, unlike Eq. (3.3) from ACI 440.1R (2015). For instance, in the study of Choi et al. (2012), there were six bottom-splice test specimens. The specimens had the same compressive strength (30 MPa), bar diameter (12.7 mm), concrete cover (31.8 mm), and surface profile (helically wrapped with sand coating). The principal investigated parameter was the embedment length, which was $10d_b$, $20d_b$, $30d_b$, $40d_b$, $55d_b$, and $70d_b$. The average experimental bond strengths for the six specimens were 5.1, 4.0, 3.1, 2.6, 2.6, and 2.1 MPa. The experimental bond strength was calculated using the monitored failure loads from Eq. (3.6). The failure loads (T) were calculated for the beam test specimens using Eq. (3.8):

$$T = \frac{\frac{F}{2}a}{j} \quad (3.8)$$

where F is the applied load from the actuator in N; a is the shear span in mm; and j is the lever arm in mm. The theoretical prediction by CSA S806 (2012) Eq. (3.7) was 4.1 MPa for the six specimens (where the bar reaches its maximum tensile stress for each specimen before failure). The results of ACI 440.1R (2015) Eq. (3.3) were 6.7, 4.4, 3.7, 3.3, 3.0, and 2.8 MPa. The

development length estimated by CSA S806 (2012) Eq. (3.5) was directly proportional to the maximum stress at failure with a zero-stress intercept (when maximum stress was plotted vs. embedment length). According to ACI 440.1R (2015), Eq. (3.4) assumes the same linear relationship between the development length and the maximum stress in the GFRP reinforcement at failure; however, the stress intercept value at zero embedment length was $340 \sqrt{f'_c}/\alpha$. Figure 3.3 shows several relationships between the developed stress at failure in the GFRP bars and the normalized embedment length by the bar diameter. Each specimen had the same parameters (concrete compressive strength, concrete cover, bar diameter, and bar surface profile) except for different values of the embedment length, which was the primary variable. It is evident from Figure 3.3 that by increasing the embedment length, the maximum achieved stress at failure also increased. If the relation is assumed to be linear, there will be a notable initial intercept stress value (Y-axis) at zero embedment length. However, the relationship between the maximum stress and the embedment length is not linear; the relation is more likely to follow a power law or parabolic path, as shown in Figure 3.3. For simplicity, and due to the difficulty in solving power law and parabolic equations, a linear relation was assumed with an initial stress intercept, provided that the applicability of this linear equation would be for embedment lengths of the bar normalized by the bar diameter (l_e/d_b) greater than 10.

Assuming a linear relation with a zero intercept between the maximum stress and embedment length results in postulating that the average bond strength at which the bar tensile stress reached its maximum value is constant with increasing embedment length, as presented in Figure 3.4. However, introducing the nonzero intercept stress value would consider such a change when estimating the bond strength values by maintaining the linear relation between the stress and embedment length. The initial stress intercept is derived indirectly through the relation between the normalized experimental bond strength (on the vertical axis) vs. the normalized embedment length (on the horizontal axis) from Eq. (3.7). Notably, the influence of several parameters on the bond strength should be investigated primarily before determining the relationship between the normalized maximum stresses and the normalized embedment length. These parameters represent the effects of the top bar, bar diameter, bar surface profile, confinement due to surrounding concrete, concrete compressive strength, and confinement due to transverse reinforcement.

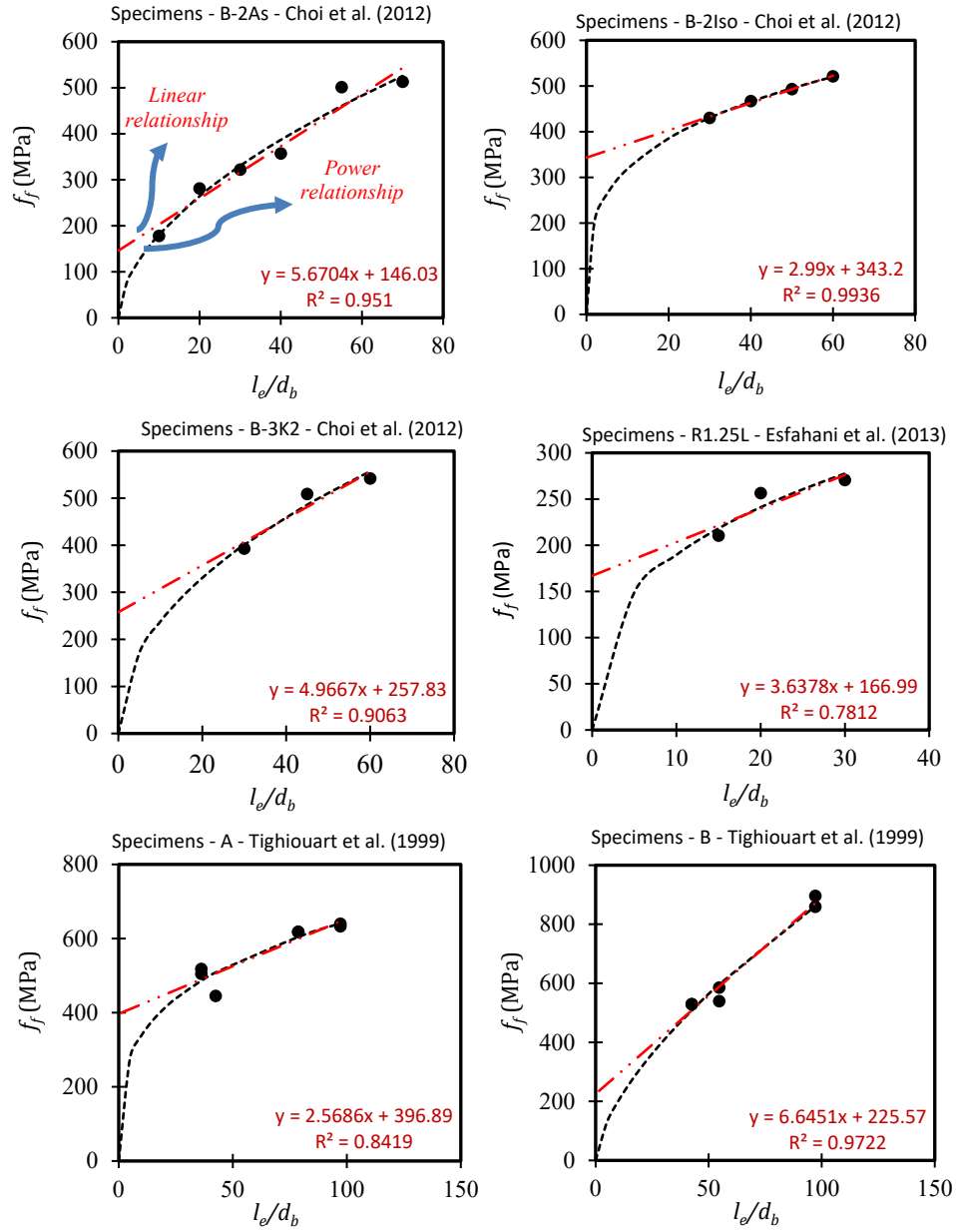


Figure 3.3 Relationship between maximum stress at failure and normalized embedment length for different splice specimens

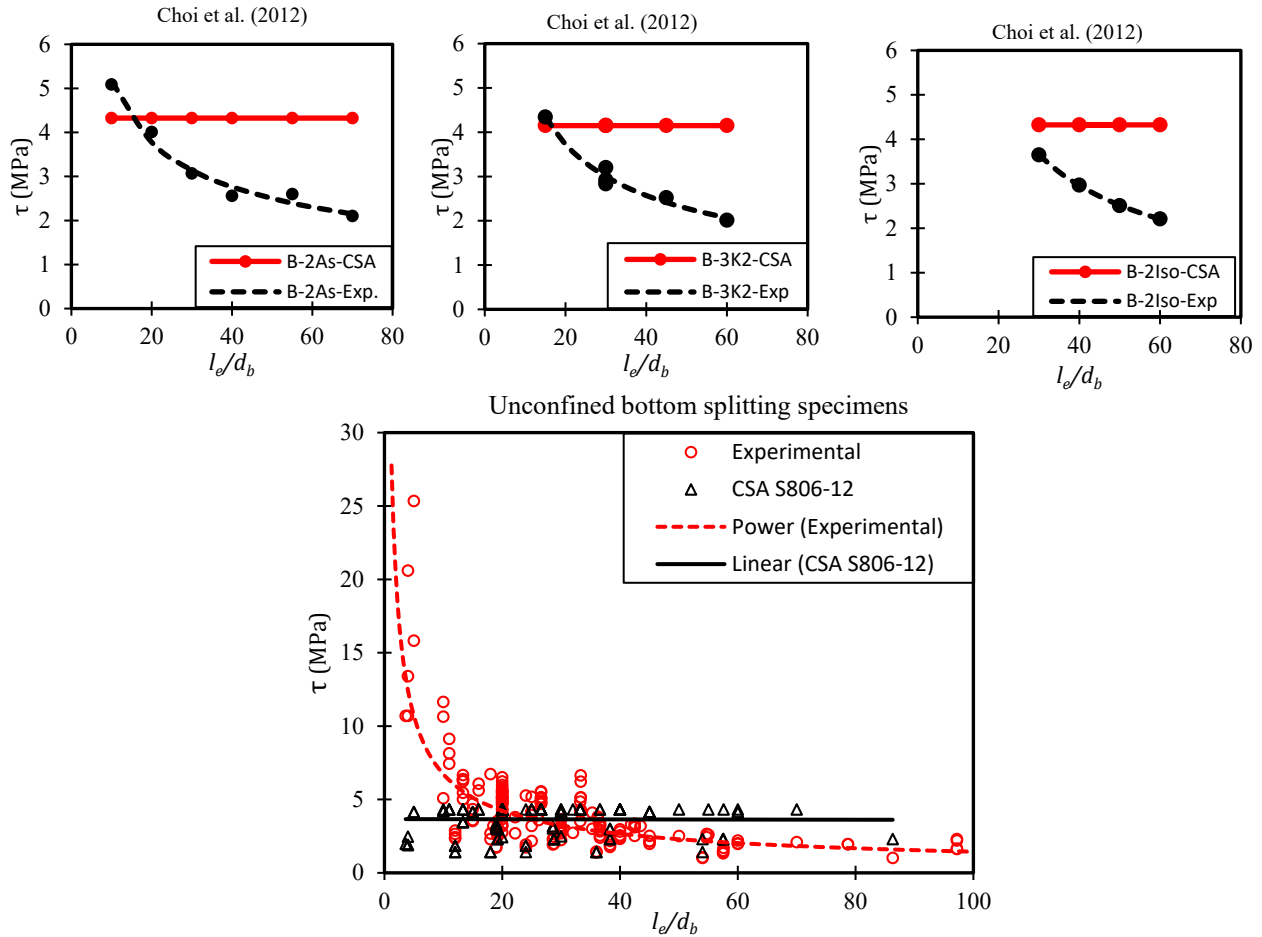


Figure 3.4 Comparison between the bond strength and normalized embedment length for the experimental results and CSA S806 (2012) equation

3.5.1 Bar location modification factor (k_1)

Top bars are commonly defined by the placement of horizontal reinforcement in the member where more than 300 mm of concrete is cast below the bar at the location of the splice or development length. For splitting specimens, 27 unconfined top bar splice specimens were considered only in the analysis based on the tests performed by Mosley et al. (2008) and Pay et al. (2014). According to the available top bar data, the analysis was performed for sand-coated and sand-coated helically wrapped bars with bar diameters 16, 15.9, and 25.4 mm. The embedment lengths ranged from $12d_b$ to $57.5d_b$, and only one specimen had an embedment length of $86.3d_b$; which was excluded from the analysis. The 16 and 15.9 mm bar diameters were treated together and assumed to be 15.9 mm. In addition, the surface profile was postulated to be the same as the profile due to the sand-coating effect for the spirally wrapped bars.

The splice lengths were divided into three groups for analysis. The first group included splice lengths from $12d_b$ to $20d_b$, the second group included those from $20d_b$ to $40d_b$ and the third group consisted of those from $40d_b$ to $57.5d_b$. The third group included five specimens that had no corresponding top bar specimens. Hence, these specimens were excluded as well from the study. Finally, of the 27 beams, 21 specimens were considered in estimating the top bar modification factor. The modification factor was obtained by normalizing the experimental bond strength with the other parameters using Eq. (3.7) and then calculating the ratio of the mean normalized experimental bond strengths of the bottom bars to that of the top bars. The average normalized experimental bond strengths for the top bars for the first group with a bar diameter of 25.4 mm, the second group with a 15.9 mm bar diameter, and the third group with a bar diameter of 15.9 mm were 0.91, 0.66, and 0.48, respectively, the corresponding average normalized experimental bond strengths for the bottom bars were 0.97, 0.84, and 0.50, respectively; and hence, the ratios of the bond strengths of the bottom bars to the top bars were 1.06, 1.28, and 1.05, respectively.

CSA S806 (2012) specified a bar location modification factor of 1.3, whereas ACI 440.1R (2015) recommended a value of 1.5. Hence, ACI 440.1R (2015) overestimated the top bar factor compared to CSA S806 (2012) and the values calculated herein. Based on the analysis of the data conducted in this study, the top bar specimens yielded a minor reduction in strength except for the splice lengths between $12d_b$ and $20d_b$ for a bar diameter of 15.9 mm. Accordingly, the current study recommends using the maximum of the three values as a conservative value of the top bar factor. The value for the bar location modification factor is recommended to remain 1.3, the same as that specified by CSA S806 (2012).

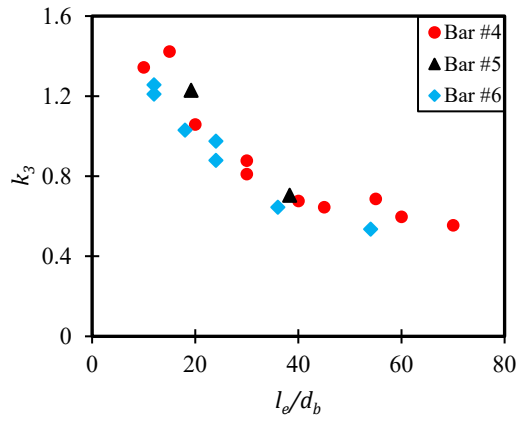
3.5.2 Influence of the bar diameter (k_3)

The GFRP bars are generally characterized by a nonuniform normal stress distribution on the cross-section, which is recognized as the shear lag effect (Tepfers 1973, and Achillides 1998). In addition, when the bar diameter increases, water is trapped beneath the bar due to bleeding, resulting in voids (Tighiouart et al. 1998, and Hao et al. 2009). This occurs more commonly in bars with larger diameters than smaller ones, resulting in lower bond strength. CSA S806 (2012) utilizes a bar size correction factor (k_3) to account for the bar size effect. The values of the k_3 factor for GFRP bars adopted in CSA S806 (2012) are the same as those recommended for steel in CSA A23.3 (2019), which raises many uncertainties about the validity of these values for GFRPs.

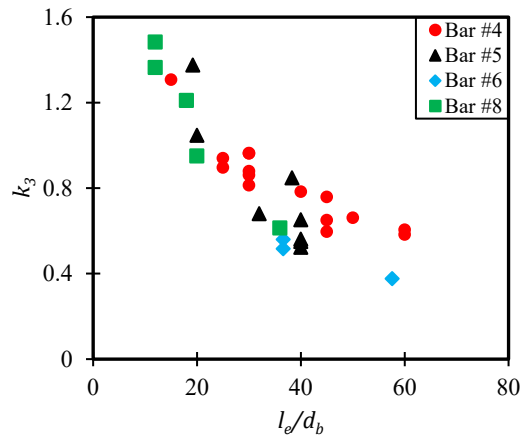
To obtain the values of the k_3 factor, the unconfined splitting failure data were classified according to test type, i.e., splice or beam end tests. In addition, each surface profile type was analyzed separately to account for the bar diameter alone. The square root of the compressive strength was assumed unlimited in the k_3 factor estimation. The normalized experimental bond strength was calculated from Eq. (3.7) to account for the effect of the bar diameter (k_3 factor) only.

For the splice tests, Figures 3.5(a) and (b) show that increasing the embedment length for bars #4, #5, #6, and #8 decreases the factor k_3 by, which is attributed to the increase in the induced stresses in the GFRP bars at failure. For the beam end specimens, the values of factor k_3 fall between 1.01 and 1.30 for size #5 and between 0.77 and 1.42 for size #6, as shown in Figure 3.5 (c). Accordingly, the average data points for each bar diameter were computed and adopted as the bar diameter modification factor. The average values for the k_3 factor for the splice tests were 0.87, 0.97, and 0.94 for the helically wrapped bars with sand-coating #4, #5, and #6, respectively. However, for sand-coated bars #4, #5, #6, and #8, the average values for the k_3 factor were 0.82, 0.80, 0.49, and 1.13, respectively. The specimens reinforced with #6 sand-coated bars were considered outliers and discarded from the analysis.

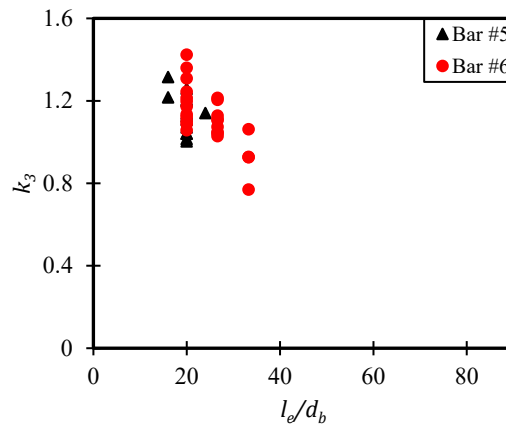
For the beam end tests, the average k_3 factors for bars #5 and #6 were 1.14 and 1.12, respectively. The results showed that the k_3 values for bars #4, #5, and #6 were comparable, while there was a considerable increase in the k_3 factor for bar #8 compared to bars #4, #5, and #6. Thus, the proposed conservative value for the k_3 factor was 0.90 for bars #4, #5, and #6 was 0.90 and 1.10 for bar #8 based on the experimental results.



(a) Helically wrapped with sand coating bars



(b) Sand-coated bars



(c) Sand-coated bars

Figure 3.5 Relationship between factor k_3 and the embedment length for: (a) and (b) Splice tests, and (c) Beam end tests

3.5.3 Influence of the bar surface profile (k_5)

The graph in Figure 3.6 presents the relation between the k_5 factor (accounting for the bar surface profile) and the normalized embedment length for bar #4. Bars #4 and #5 were chosen because those bars comprise many specimens with different embedment lengths for the sand-coated and helically wrapped (and some sand-coated) bars. In addition, only the unconfined splice tests are considered in this analysis. The factor k_5 was calculated by normalizing the bond strength using Eq. (3.7). The average of the factor k_5 was computed at the same embedment length for the same bar surface profile, and hence, the relation is plotted between k_5 and the corresponding embedment length. Figure 3.6 shows that for the sand-coated surface, the factor k_5 is slightly higher at some embedment lengths and lower at other lengths without a noticeable trend. The ACI 440.1R (2015) average bond stress equation did not account for the effect of the bar surface profile. CSA S806 (2012) mentioned that the bonding performance of sand-coated bars was superior to that of helically wrapped and ribbed bars. Accordingly, based on the experimental results, the proposed values of the factor k_5 for the sand-coated and helically wrapped bars were the same as those adopted by CSA S806 (2012), i.e., 1.0 and 1.05, respectively. For the ribbed bars, there was a significant lack of experimental data. All the available data were for 15 confined bottom bar beams and one unconfined beam. Hence, the authors suggest using the 1.05 value, as endorsed by CSA S806 (2012), until further investigations are performed on ribbed bars.

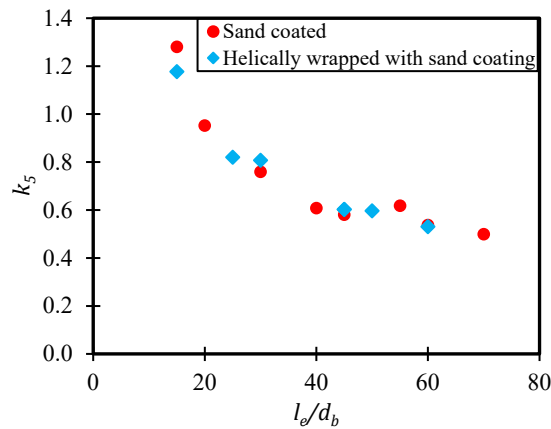


Figure 3.6 Relationship between factor k_5 and the normalized embedment length

3.5.4 Influence of the concrete cover

The concrete cover is deemed one of the critical parameters affecting the bond strength for lapped and anchored reinforcing bars. In general, as the concrete cover thickness increases, the bond stress increases due to the concrete cover confinement pressure (bearing effect) on the bar

surface, which results in a weaker splitting component and delays the development of splitting cracks, which eventually converts the failure mode from splitting to pullout (Tepfers 1973). Ehsani et al. (1996) indicated that the beams failed by splitting when the ratio of the concrete cover to the bar diameter (c/d_b) was 1.0, whereas pullout or bar rupture failures occurred when c/d_b was greater than or equal to 2.0. Alves et al. (2010) investigated three concrete cover thicknesses ($1.5d_b$, $2.0d_b$, and $2.5d_b$) with different bar diameters (15.9 and 18.9 mm). The research findings showed that failure modes changed to pullout failure by increasing the concrete cover. To ensure pullout failure, the concrete cover should be $2.0d_b$ for 15.9 mm and $2.5d_b$ for 18.9 mm bar diameters.

ACI 440.1R (2015) recommends a maximum value of the concrete cover (c) of $3.5d_b$, where c is measured to the bar center, and CSA S806 (2012) proposes a maximum limit of cover (d_{cs}) of $2.5d_b$. Below these limits, splitting failure will occur. All the splice-splitting specimens in the database had a concrete cover to the bar center ranging from $1.5d_b$ to $4.5d_b$, whereas the specimens in splitting beam end tests had concrete covers that ranged from $1.5d_b$ to $3.5d_b$. The unconfined bottom specimens for the splice and beam end tests were considered in the analysis. In addition, the data for the top bar specimens were divided by the top bar factor (k_1) to allow all the data points to be evaluated on an equivalent basis.

Figure 3.7 shows the relationship between the experimental bond strength normalized by the square root of the compressive strength on the vertical axis using Eq. (3.7) and the normalized concrete cover to the bar center on the horizontal axis. The data points were estimated separately for each bar diameter to identify the maximum cover at which splitting failure would occur. Figure 3.7 shows that the concrete cover significantly influenced the bond strength until a specific limit, and then the splitting failure changed to pullout failure. For bar #4, the maximum cover that the splice specimen failed by longitudinal splitting cracks of the cover was $2.5d_b$. For bar #5, the maximum concrete cover for the beam end tests was $3.1d_b$, while for the splice specimens, it was $2.9d_b$. For bar #6 in the beam end tests, Figure 3.7(a) showed that the maximum cover was $2.5d_b$ for most of the specimens, and only five specimens failed with a cover of $3.5d_b$. Finally, for bar #8 in the splice tests, Figure 3.7(b) showed that the maximum concrete cover for splitting failure to occur was $2d_b$. As the bar diameter increased, the maximum limit of the concrete cover to the bar center decreased, which was attributed to the effect of increasing the bar diameter on reducing the maximum attained bond strength.

These observations confirmed that setting one limit for all bar diameters resulted in underestimating the bond strength values in bars #4, #5, and #6. In addition, the bond predictions for larger bar diameters, such as #8, were overestimated. However, limited studies have investigated the effect of concrete covers greater than $2d_b$ for bar diameter #8. Setting $2d_b$ as a concrete cover limit for bar diameter #8 might overestimate the development length. Accordingly, this study proposes the maximum concrete cover to the bar center to be $2.5d_b$ for bars #4, #5, #6, and #8, as proposed by CSA S806 (2012). Further investigations shall be performed to discuss the effect of concrete covers greater than $2d_b$ for bar diameter #8.

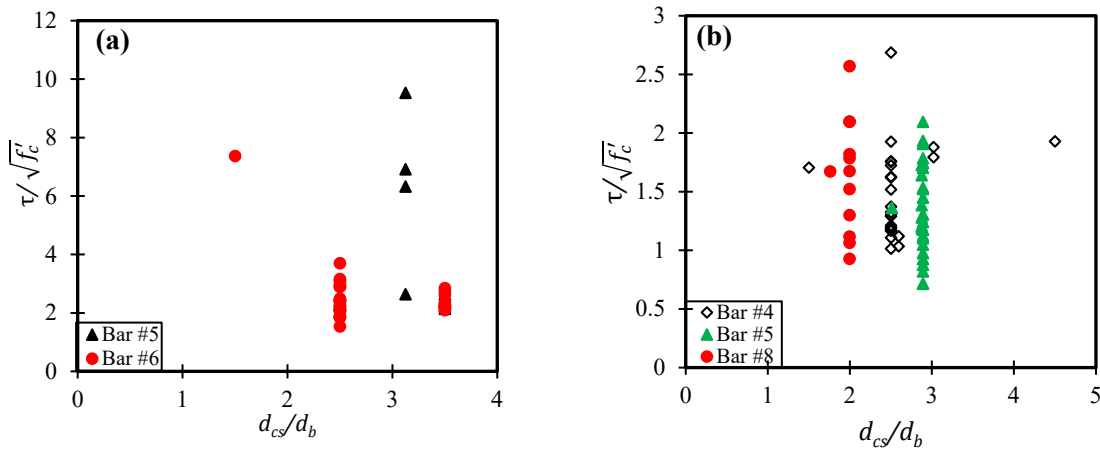


Figure 3.7 Relationship between normalized experimental bond strength and the normalized concrete cover to the bar center for: (a) Beam end tests, and (b) Splice tests

3.5.5 Influence of concrete compressive strength

The concrete compressive strength is one of the significant parameters affecting the bond strength and failure mode of GFRP reinforced members. Tepfer (1973) and Achillides (1998) concluded that when the concrete strength exceeds 30 MPa, failure occurs at the GFRP bar surface. Thus, failure depends on the bar properties, not the compressive strength, whereas, at lower concrete strength (approximately 15 MPa), failure occurs in the concrete matrix.

For high concrete strength, failure might change from concrete splitting to loss of bearing resistance. This change can be initiated by the interfacial failure plane penetrating the GFRP, unlike steel bars where the failure plane goes through the concrete. The failure in GFRP bars can occur by bar splitting through interfacial shear failure inside the bar, failure at the interface between the bar and concrete (including failure of lugs or other surface indentations that are made of pure

epoxy or similar matrix) or through loss of adhesion in the case of sand-coated bars. All these modes of failure can be considered bar pullout failure.

Other studies stated that concrete strength has a substantial influence on bond strength (Aly et al. 2006, Xue et al. 2014, Yan et al. 2016, and Kotynia et al. 2017), while others claimed that compressive strength has no effect (Pecce et al. 2001, Esfahani et al. 2013, and Karlson 2017). Okelo (2007) and Baena et al. (2009) observed that at higher concrete strengths (55 MPa), splitting failure occurs when using larger bar diameters, small concrete covers, and long embedment lengths. CSA S806 (2012) sets a limit of $\sqrt{f'_c} = 5$; this limit is highly conservative since concrete splitting occurs at a lower concrete strength. ACI 440.1R (2015) did not consider any limits on $\sqrt{f'_c}$.

Figures 3.8(a) and (b) show the relationships between the normalized experimental bond strength ($\tau_{exp.}/\tau_{theo.}$, which is defined as the experimental bond strength divided by the theoretical bond strength equation of CSA S806 (2012)) of the splice and beam end splitting specimens and beam end pullout specimens vs. the square root of the concrete compressive strength. The relation in Figure 3.8(a) shows an increase in the bond resistance of the GFRP bar spliced bars with increasing concrete compressive strength up to 8, which is manifested clearly by the trend line of the splice data points. However, the trend line for the beam end tests shows a decrease in the bond strength by increasing the compressive strength, even though splitting failure occurred at higher compressive strengths. Most beam-end points lie between 6.3 and 6.8, with few test results at lower and higher strengths. This raises uncertainties about whether the compressive strength affects the beam end test results, showing a need for more data points for lower- and higher-strength concrete. However, Figure 3.8(b) clearly shows that the bond strengths of the pullout beam end specimens increase with increasing compressive strength up to $\sqrt{f'_c}$ of 8.8. Figure 3.8(a) and (b) illustrate that pullout failures occur at higher compressive strength than splitting failures for the beam end specimens. This was due to the high tensile strength of concrete that provides the beam with more resistance against splitting. In the case of high-strength concrete, the GFRP bar pullout failure mode will depend primarily on the embedment length and bar surface profile, whether an interfacial shear failure occurs inside the bar or failure occurs at the interface between the concrete and the GFRP bar surface, as mentioned earlier. The occurrence of pullout failures in high-strength concrete supports increasing the limit of $\sqrt{f'_c}$ to more than 5 (the value recommended by CSA

2012). Accordingly, the current study recommends a maximum limit for $\sqrt{f'_c}$ of 8, which is higher than that of CSA S806 (2012) and analogous to that of CSA S806 (2002).

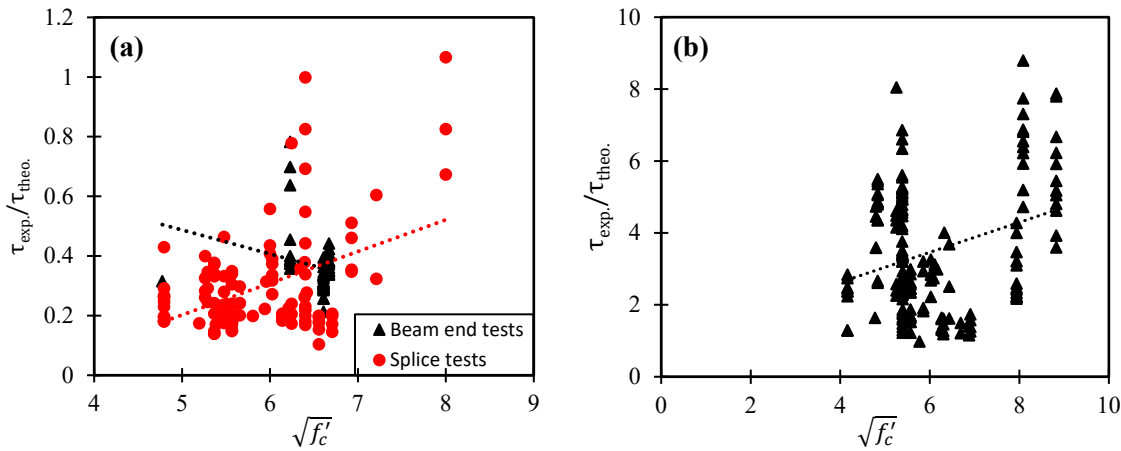


Figure 3.8 Relationship between the normalized experimental bond strength and the square root of compressive strength for specimens failed due to: (a) Splitting of concrete; and (b) Pullout of the GFRP bar

3.5.6 Influence of transverse reinforcement on bond strength

Aly (2005) found that transverse reinforcement significantly affects the bond performance of sand-coated GFRP bars by increasing the bond strength up to 60% compared to unconfined beams. In contrast, Wambeke and Shield (2006) found that confinement did not affect the bond strength of beams reinforced with sand-coated GFRP bars. Harjili and Abouniaj (2010) observed that the presence of transverse reinforcement enhanced the bond strength of threaded, wrapped and ribbed GFRP bars, similar to the effect of steel bars. Esfahani et al. (2013) highlighted that confinement improved the bond strength of spliced ribbed GFRP bars; however, there were no studies on the effect of confinement on the bond strength of spliced sand-coated GFRP bars. Thus, this section conducts a comprehensive investigation to identify the effect of transverse confining reinforcement on the bond strength of GFRP bars.

All the confined specimens correspond to splice data except two beam end specimens reported by Ehsani et al. (1996). The splice specimens and the transverse reinforcement details are presented in Table 3.3. All the stirrups utilized to confine the specimens in the database were fabricated from steel except those used by Achillides (1998), which were GFRP with an elastic modulus of 45300 MPa. Accordingly, for simplicity, the K_{tr} equation was modified to account for the GFRP material

by replacing the term f_y with f_{frpu} . Due to the shortage of data from investigations of the effect of GFRP stirrups on the development length, more experimental studies are required to investigate the effect of using GFRP stirrups instead of steel stirrups to simulate real practical applications. From the new studies, a recalibration of the K_{tr} equation is required to account for the effect of using GFRP stirrups. Figure 3.9 illustrates the relationship between the experimental bond strength normalized by the other parameters ($\tau_{exp.}/\tau_{theo.}$) using Eq. (3.7) and the normalized embedment length. For the helically wrapped specimens, those with transverse reinforcement achieved higher bond strength than the corresponding unconfined specimens at the same embedment length. There was some variation in the results for the sand-coated splice specimens, however. Some confined specimens showed higher bond strength values than the unconfined specimens, specifically as observed at l_e between $35d_b$ and $45d_b$. For the shorter embedment lengths, the confined beams did not enhance the bond strength; regarding the specimens reinforced with ribbed bars, transverse reinforcement confining the splice zone considerably enhanced the bond strength for all the confined specimens compared to the unconfined specimens. The confined beams reinforced with ribbed bars exhibited identical behaviour to the confined steel reinforced beams, which confirms Harjili and Abouniaj (2010) reports.

The transverse reinforcement confinement showed high efficiency in enhancing the bond strength of the spliced beam specimens reinforced with threaded wrapped and ribbed bars. Subsequently, the transverse reinforcement confinement effect was integrated into the bond strength equation, as shown in Eq. (3.9):

$$\tau = \frac{1}{1.15 \pi} \frac{(d_{cs} + K_{tr} \frac{E_{FRP}}{E_s}) \sqrt{f'_c}}{k_1 k_2 k_3 k_4 k_5 d_b} \quad (3.9)$$

Notably, the bond strength computed using Eq. (3.9) corresponds to the maximum stress achieved in GFRP bars at beam failure. The mean of the ratio of the theoretical bond strength for the confined beams reinforced with ribbed bars using Eq. (3.9) to the corresponding experimental bond strength was 0.91, while the mean of the ratio between the theoretical and experimental bond strengths using Eq. (3.7) was 0.84. This shows that the confinement term in the theoretical Eq. (3.9) enhanced the bond strength by approximately 9% compared to Eq. (3.7). For the helically wrapped reinforced beams, the means were 1.54 and 1.49. Although the helically wrapped bars showed an enhancement in the bond strength when calculated using Eq. (3.9), the theoretical values were scattered and not close to the experimental values. This is attributed to the long

embedment lengths utilized in the helically wrapped specimens, which were up to $97d_b$, unlike the ribbed bar specimens where the embedment lengths were up to only $30d_b$. The confinement effect from transverse reinforcement enhanced the bond strength; in a conservative approach, the term K_{tr} can be neglected.

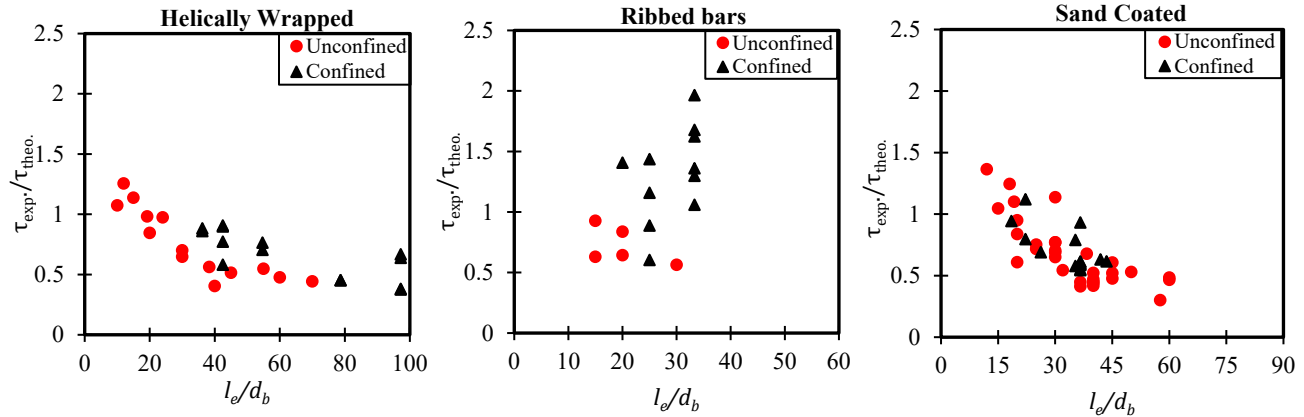


Figure 3.9 Effect of transverse reinforcement on the bond strength based on the bar surface profile for splice splitting beams

3.6 Regression analysis

A regression analysis was conducted using the 118 viable splitting splice specimens and the 63 splitting beam end tests, considering all the studied parameters and excluding all the outliers, as discussed. Figure 3.10 shows the relationship between the normalized experimental bond strength at splitting failure for the splice and beam end specimens ($\tau_{exp}/\tau_{theo.}$) on the vertical axis and the corresponding reciprocal of the normalized experimental embedment length from Eq.(3.7) on the horizontal axis. For simplicity, the ratio between d_b/l_e was used instead of l_e/d_b because the reciprocal ratio (d_b/l_e) provides a linear trend relation, unlike the ratio l_e/d_b that yields a power law relationship. The purpose of this comparison is to show whether the relationship between the normalized experimental bond strength and d_b/l_e will result in a nonzero intercept for the normalized experimental bond strength value. The resulting predictive relationships for the normalized experimental bond strength and the reciprocal of the normalized embedment length are introduced by Eq. (3.10) and Eq. (3.11) for the splice and beam end specimens, respectively:

$$Y = 12.7x + 0.39 \quad (3.10)$$

$$Y = 7.3x + 0.68 \quad (3.11)$$

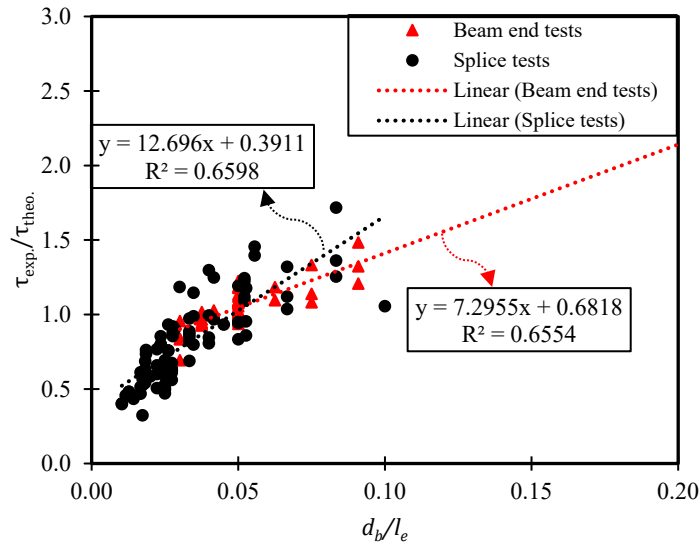


Figure 3.10 Relationship between the normalized experimental bond strength versus the reciprocal of the normalized embedment length

The two trend lines intersect at the reciprocal of the normalized embedment length of 0.05, which shows that at this point, the two equations yield the same maximum bond stress at failure for this embedment length. Moreover, the slopes of the average lines in Figure 3.10 show that any value of d_b/l_e less than 0.05 (which corresponds to l_e/d_b greater than 20) will result in lower normalized experimental bond strength values for the splice specimens than the beam end specimens. For d_b/l_e greater than 0.05, the splice specimens tend to acquire higher bond strength compared to the beam end specimens at the same ratio of d_b/l_e . These results demonstrate that the splice specimens require longer development lengths than the beam end specimens for l_e/d_b greater than 20. This resulted in a lower intercept value on the normalized experimental bond strength axis for the splice beams of 0.39, whereas for the beam end specimens, the intercept was 0.68.

3.7 Proposed development length equations

This study proposes two development length equations based on different approaches to the reassessment of the different parameters influencing the bond strength of GFRP reinforced concrete beams. The proposed equations were validated by ensuring that the mean ratio between the experimental and theoretical embedment lengths (using the experimental failure stresses in the GFRP reinforcement) is less than one and that the standard deviation represents the scatter of points around the mean is the minimum. The derivation of the first equation assumes maximum

linear stress with an initial stress intercept, while that of the second equation postulates a zero-stress intercept. These two equations and the present equations in CSA S806 (2012) and ACI 440.1R (2015) design codes were assessed.

Equation (3.12) was developed after assessing all the parameters in the CSA S806 (2012) equation in the previous sections. An analysis was then performed on the specimens that failed due to splitting. The proposed Eq. (3.12) was developed by modifying the CSA S806 (2012) development length equation according to the type of test (beam end or splice). The proposed Eq. (3.12) was derived by considering the effect of the change in the embedment length on decreasing the maximum bond stress at failure by incorporating the initial stress intercept obtained indirectly through a linear regression analysis, as shown in Figure 3.10. The second proposed equation, Eq. (3.13), modified the present CSA S806 (2012) equation by assuming a linear zero bond stress intercept.

$$l_d = 1.75 \frac{k_1 k_2 k_3 k_4 k_5}{(d_{cs} + K_{tr} \frac{E_{FRP}}{E_s})} \frac{f_f}{\sqrt{f'_c}} A_b - 14.5 d_b \quad (3.12)$$

$$l_d = 1.25 \frac{k_1 k_2 k_3 k_4 k_5}{(d_{cs} + K_{tr} \frac{E_{FRP}}{E_s})} \frac{f_f}{\sqrt{f'_c}} A_b \quad (3.13)$$

where f_f is the design stress in GFRP tension reinforcement at the ultimate limit state in MPa; A_b is the cross-sectional area of the bar in mm²; k_1 is the bar location factor given as 1.3 for horizontal reinforcement placed where more than 300 mm of fresh concrete is cast below the development length or splice and 1.0 for other cases; k_2 is the concrete density factor taken as 1.3 for low-density concrete, 1.2 for semi-low-density concrete, and 1.0 for normal-density concrete; k_3 is the bar size factor taken as 0.9 for diameters #4, #5 and #6, and 1.1 for bar diameter #8; k_4 is the bar fibre factor proposed as 1.0 for carbon fibre-reinforced polymer (CFRP) and GFRP, and 1.25 for aramid fibre-reinforced polymer (AFRP); k_5 is the bar surface profile factor and shall not be taken as less than 0.5 and can be taken as 1.0 for sand-coated bars, and 1.05 for helically wrapped and ribbed bars; $\sqrt{f'_c}$ is the square root of the concrete compressive strength and shall not exceed 8; d_{cs} is the smaller value of the concrete cover (in mm) measured from the extreme tension fibres to the center of the tensile developed bars and two-thirds of the spacing between the center-to-center of the developed bars, and shall not exceed $2.5d_b$, where d_b is the bar diameter; and K_{tr} is the transverse reinforcement index and calculated using Eq. (3.2) with the same parameters, except

that f_y will be f_{frpu} in case of using FRP stirrups.

The development length in Eq. (3.12) and Eq. (3.13) should be multiplied by 1.3 to obtain the splice length. The following sections assess the two approaches to evaluate their reliability compared to other code equations.

3.7.1 Analysis of critical pullout and rupture failures

Proposed equations (3.12) and (3.13) were developed based on the splitting mode of failure of the beam end and splice specimens. However, some specimens that failed due to pullout and rupture of GFRP bars are of great concern and must be analyzed. These specimens are referred to as critical pullout and rupture failures. The critical pullout specimens are defined as those with the largest embedment lengths that failed by the GFRP bar pullout, as shown in Figure 3.11(a). The critical rupture specimens are those with the shortest embedment lengths that failed by the rupture of GFRP bars, as illustrated by Figure 3.11(b).

Figure 3.11(a) shows that most of the pullout failures occurred at relatively small embedment lengths with l_e/d_b less than or equal to 10. This was justified by Wambeke and Shield (2006), who found that when the bar was not embedded sufficiently into the concrete, the bar could attain its full bond strength with the generation of minor splitting forces. Out of 188 beam end specimens, 103 specimens (with $l_e/d_b \leq 10$) had f'_c ranging from 17.3 to 31 MPa. This demonstrates that the concrete beams did not fail by splitting, even at low concrete strengths. There were 22 critical pullout specimens that included 14 beam end specimens and eight confined splice specimens.

Regarding the specimens that failed by the rupture of GFRP bars, the critical rupture specimens are assumed to have embedment lengths less than $50d_b$. Out of 60 beam end specimens, 53 specimens are considered critical, with embedment lengths ranging from $10d_b$ to $40.5d_b$. For the four splice specimens that failed by the rupture of GFRP bars, three beams had embedment lengths of $31.4d_b$, $36.6d_b$, and $44d_b$. Notably, all the rupture specimens had f'_c greater than 30 MPa, so 19 specimens ranged from 30 to less than 40 MPa. The remaining 45 beams had f'_c greater than 40 and up to 55 MPa. This might be the reason for the rupture of GFRP bars in lieu of splitting since the bar reached its tensile strength, and the concrete did not split. Moreover, 14 beam end specimens had concrete covers to the center of the GFRP bar that were $2.5d_b$, while the rest of the specimens had concrete covers ranging from $3d_b$ to $9.8d_b$. The four splice specimens were

confined with transverse reinforcement. These results show that the confinement effect resulting from the concrete cover and transverse reinforcement might have assisted in achieving the bar tensile strength instead of pullout and splitting failures.

In this study, the proposed Eq. (3.12) was utilized to ensure that the computed development lengths covered the pullout and rupture critical specimens and were greater than the experimental embedment lengths. The development lengths were calculated using the experimental stress in the GFRP reinforcement at failure. Concerning the pullout specimens, the results showed that the average l_e/l_d values for the beam end and splice specimens were 0.44 and 0.83, respectively. For the rupture tests, the average l_e/l_d values for the beam end and splice specimens were 0.88 and 0.83, respectively. The results of the development lengths demonstrated that the proposed development length Eq. (3.12) provides a sufficient development length that would prevent critical pullout and rupture failures.

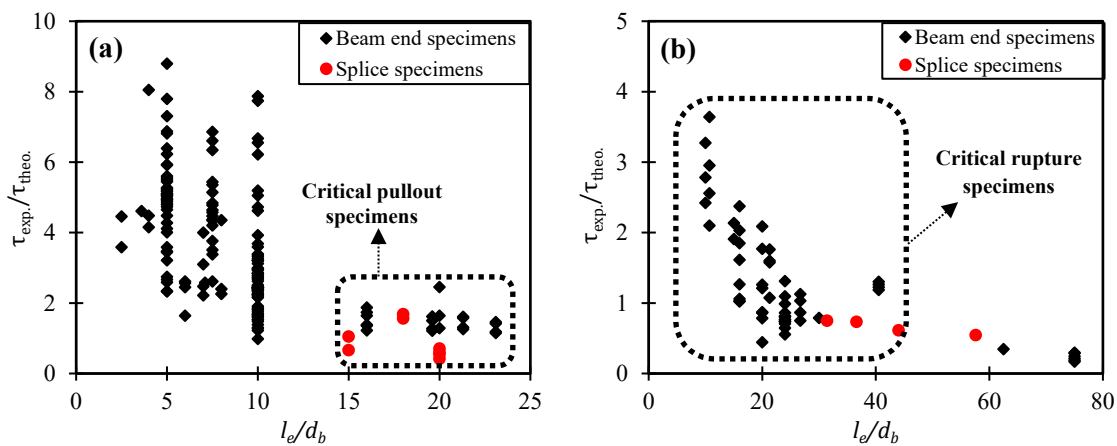


Figure 3.11 Comparison between the normalized experimental bond strength and normalized embedment length for beams failed by: (a) pullout; and (b) rupture of GFRP bar

3.7.2 Comparison of development length equations

This section provides a quantitative comparison of the development length equations proposed in this thesis and those currently used in CSA S806 (2012) and ACI 440.1R (2015) for the splice and beam end specimens failed by splitting failure. Several parameters affect the development length equations, including the concrete compressive strength, concrete cover thickness, bar location and diameter, confinement effect due to transverse reinforcement, and stress level in the GFRP reinforcement. The bar location effect is accounted for by multiplying the development

length equations by the bar location factor. The splice specimens included 49 beams confined with transverse reinforcement, whereas all the beam end specimens were unconfined. Accordingly, the unconfined spliced specimens were analyzed separately from the confined spliced specimens, and then both groups were analyzed together to discuss the sensitivity of the development length predictions to confinement by transverse reinforcement. The experimental embedment length was compared with the theoretical prediction for GFRP bars at the same stress level at failure in terms of the mean and standard deviation. The results are presented in Table 3.4.

Table 3.4 Comparison of the ratio of the experimental to theoretical embedment lengths between splitting failure specimens

	Beam End Specimens			
	Proposed Eq. (12)	Proposed Eq. (13)	CSA S806 (2012)	ACI 440.1R (2015)
Mean ± S.D. (All specimens)	0.89 ± 0.11	0.86 ± 0.11	0.75 ± 0.10	0.74 ± 0.14
Mean ± S.D. ($d_{cs}/d_b = 1.5$)	0.22 ± 0.02	0.23 ± 0.03	0.20 ± 0.03	0.12 ± 0.04
Mean ± S.D. ($d_{cs}/d_b = 2.5$)	0.96 ± 0.13	0.91 ± 0.11	0.78 ± 0.11	0.77 ± 0.16
Mean ± S.D. (d_{cs}/d_b from 3.1-3.5)	0.88 ± 0.10	0.87 ± 0.13	0.80 ± 0.08	0.81 ± 0.10
	Splice Test Specimens			
Mean ± S.D. (All specimens)	0.93 ± 0.22	0.93 ± 0.25	0.99 ± 0.29	1.47 ± 1.22
Mean ± S.D. (Unconfined specimens)	0.93 ± 0.24	0.93 ± 0.26	1.04 ± 0.31	1.22 ± 0.70
Mean ± S.D. (Confined specimens)	0.93 ± 0.20	0.94 ± 0.20	0.93 ± 0.22	1.71 ± 1.90

For the beam end specimens, 48 specimens had concrete compressive strengths ranging from 38 to 44 MPa, and the remaining beams ranged from 22.8 to 30 MPa. For the concrete cover thickness to the center of the GFRP bars, four specimens had d_{cs}/d_b values of 1.5, 41 had d_{cs}/d_b equal to 2.5, and 18 had d_{cs}/d_b ranging from 3.1 to 3.5. The concrete compressive strengths were normal-strength concrete, and the specimens were analyzed together. For the concrete cover thickness, the specimens were analyzed separately to discuss the effect of the concrete cover on the development length.

The mean ratios of the experimental to theoretical embedded lengths for the proposed Eq. (3.12) and Eq. (3.13) were 0.89 and 0.86, with standard deviations of 0.11 and 0.12, respectively. The CSA S806 (2012) equation had a mean of 0.75 with a standard deviation of 0.10, whereas the ACI 440.1R (2015) equation had a mean of 0.74 with a standard deviation of 0.14. The ACI 440.1R (2015) and CSA S806 (2012) equations overestimated the development length predictions compared to the proposed equations. The comparison between the l_{e-exp}/l_{e-theo} values presented in Table 3.4 for different concrete covers (d_{cs}/d_b) shows that all the equations provided similar predictions at different concrete covers; however, the degree of conservatism differed from one

equation to another. The proposed equations provided shorter development length values at the same stress level (failure stress) compared to the ACI 440.1R (2015) and CSA S806 (2012) equations, even though the CSA S806 (2012) was slightly more accurate than the proposed equations in terms of the standard deviation.

For the splice test specimens, 103 viable tests out of 118 tests were considered in the comparison due to the exclusion of outlier specimens. From the 103 tests, there were 61 unconfined specimens and 42 confined specimens. The concrete compressive strengths (f'_c) of 103 splitting beams varied from 23 to 52 MPa, and only three beams had an f'_c of 72 MPa. The specimens were not analyzed based on compressive strength.

The proposed equations provided a good prediction of the development lengths with a smaller standard deviation than the ACI 440.1R (2015) equation. The proposed Eq. (3.12) and Eq. (3.13) had mean ratios of $l_{e-exp}/l_{e-theo.}$ of 0.93 and 0.93 with standard deviations of 0.22 and 0.25, respectively. The CSA S806 (2012) equation yielded an average value of 0.99 with a corresponding standard deviation of 0.29. In contrast, the ACI 440.1R (2015) equation underestimated the development length prediction with a higher standard deviation than the proposed and CSA S806 (2012) (2012) equations. The comparison between the confined and unconfined specimens showed that the proposed equations could consider the effect of confinement due to transverse reinforcement. The confinement effect showed some sensitivity to the CSA S806 (2012) equation, although the equation provided a conservative mean of 0.93 ± 0.22 . The ACI 440.1R (2015) equation yielded nonconservative predictions for the confined and unconfined specimens. For the analysis of all splice specimens, the proposed equations provided good results compared to the ACI 440.1R (2015) equation and were more conservative than the CSA S806 (2012) equation in terms of the mean and standard deviation of the ratio $l_{e-exp}/l_{e-theo.}$.

Figure 3.12 shows the relationship between the experimental and theoretical embedment lengths at the same experimental failure stress for the equations proposed in this thesis, Eq. (3.12) and Eq. (3.13), and those in CSA S806 (2012), and ACI 440.1R (2015). The beam end specimens showed promising results for the proposed Equations (3.12) and (3.13), and the points tended to shift above the diagonal line toward the theoretical embedment lengths. Moreover, the data for the splice specimens were more closely distributed around the diagonal line compared to the predictions of the CSA S806 (2012) and ACI 440.1R (2015) equations. However, the results of

the CSA S806 (2012) and ACI 440.1R (2015) showed good distributions and predictions of the embedment lengths for the beam end specimens. Unlike the splice beam specimens, there was more scattered in the predictions of the two equations, particularly the ACI 440.1R (2015) equation. Figure 3.12(d) shows that the ACI 440.1R (2015) equation provided an uneven distribution for the predicted embedment lengths.

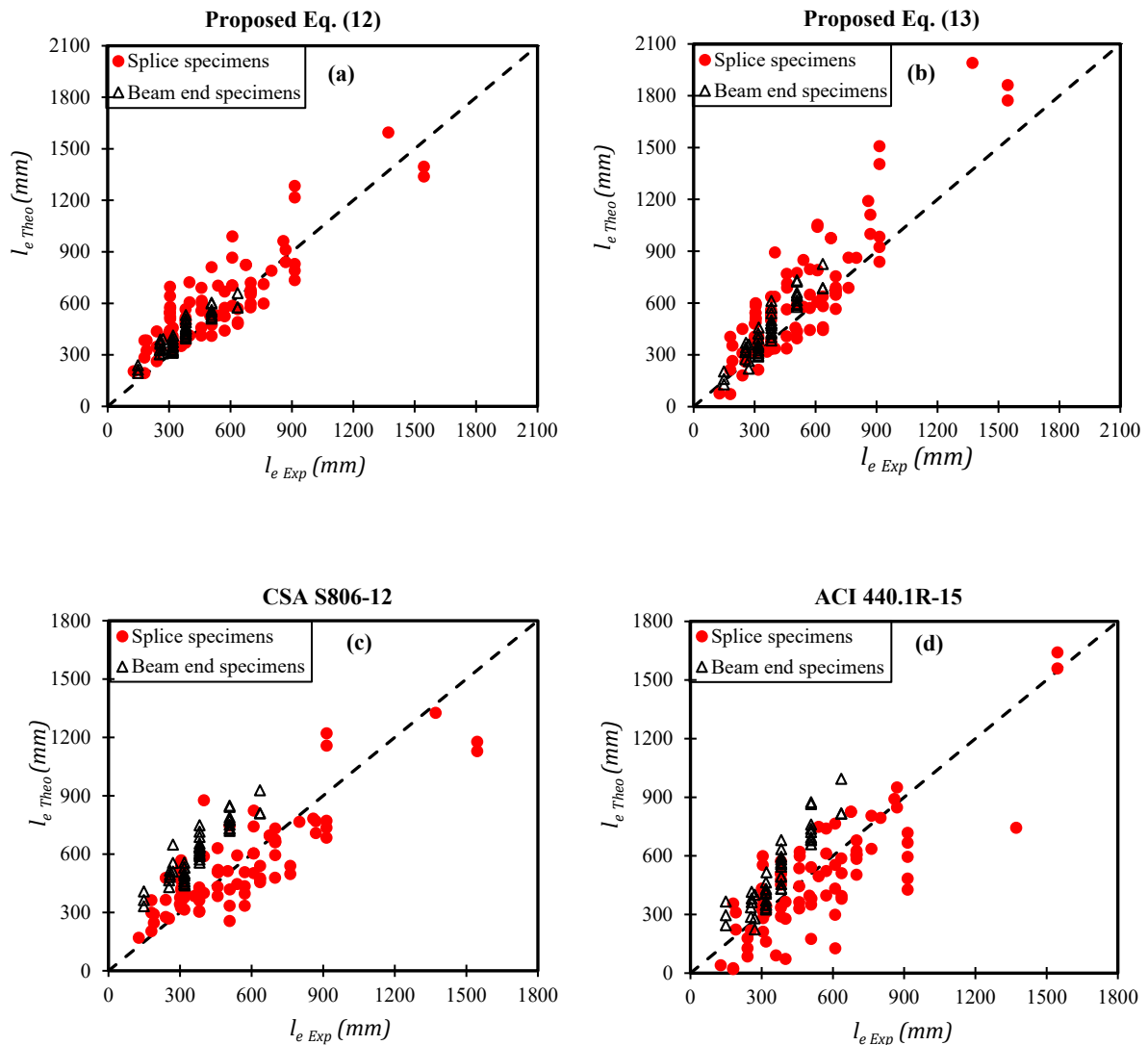


Figure 3.12 Relationships between the experimental embedment lengths and predicted embedment lengths

3.7.3 Failure mode prediction

This section compares the experimental failure modes with the failure modes predicted by the design equations to quantitatively check the accuracy of the different equations in capturing the

failure mode. Figure 3.13 presents the relationships of the beams that failed by splitting for the beam end and splice beam specimens. The maximum experimentally attained stress as a percentage of the ultimate tensile strength on the vertical axis was plotted vs. the embedment length as a percentage of the development length (l_d). Since the experimental tests were conducted on specimens at early ages, the environmental reduction coefficient C_E was assumed to be 1.0 for the guaranteed tensile strength calculation. Figure 3.13 shows a direct relationship between the bar stress and the embedment length for all the design equations. For the beam end specimens, two specimens that failed by splitting had embedment lengths longer than the estimated development length without achieving the ultimate strength of the bar from the CSA S806 (2012) equation. According to the ACI 440.1R (2015) equation and the two proposed equations, no specimens with embedment lengths were greater than the development length estimation. For the splice beam specimens, 15 specimens had embedment lengths greater than the development lengths according to the CSA S806 (2012) equation, while 13 beams did not attain the ultimate bar strength according to the CSA S6-14 (2014) equation. Two specimens did not attain the ultimate bar strength according to the proposed Eq. (3.13). Notably, ACI 440.1R (2015) and proposed Eq. (3.12) did not provide any (l_e/l_d) values greater than 100%. Hence, the results of the proposed Eq. (3.12) and ACI 440.1R (2015) equation were better than those of the proposed Eq. (3.13) and CSA S806 (2012) equation.

Table 3.5 presents a brief comparison of the results of the 431 beams that failed due to splitting, pullout, and tensile rupture of the bar (excluding beams that failed by other failure modes and outlier specimens). The comparison criteria were as follows: (a) if the embedment length is shorter than the development length, then the expected failure should be a bond failure; and (b) if the length of embedment is greater than the development length, then the failure should be a rupture in the bar unless the experimental stress attained in the GFRP bar happens to be greater than the ultimate tensile strength. In general, the two proposed equations yielded the best predictions among the other equations, along with the ACI 440.1R (2015) equation for the splitting specimens.

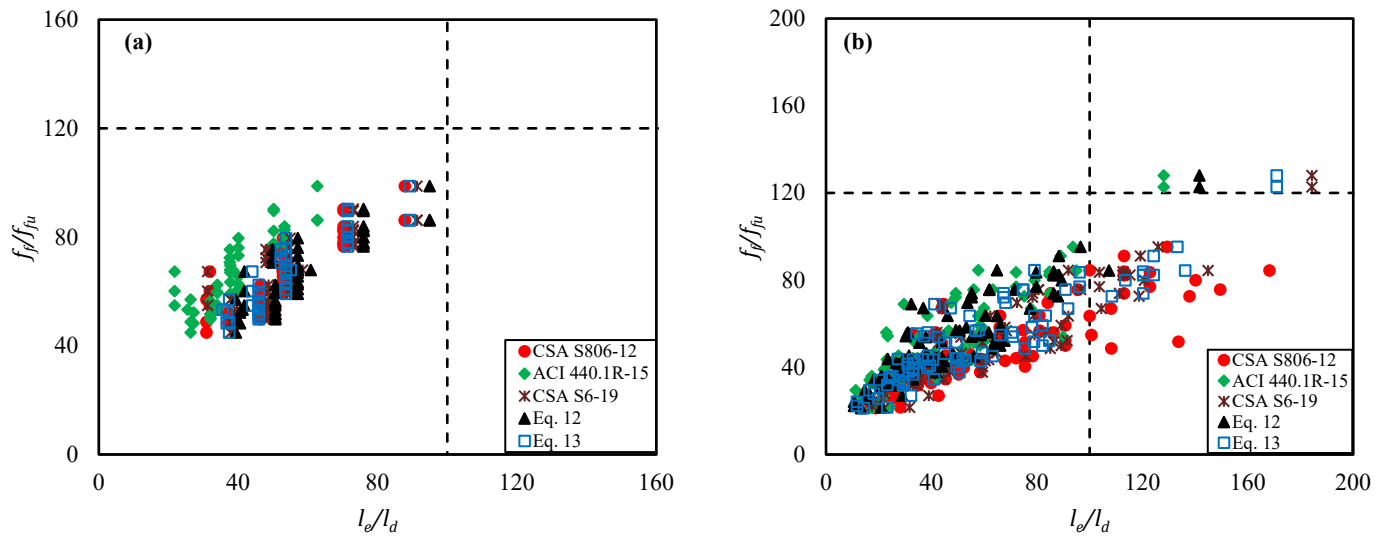


Figure 3.13 The effectiveness of different equations in the guidelines and standards in predicting the experimental embedment length of beams failed by splitting: (a) Beam end specimens; and (b) Splice specimens

Table 3.5 Evaluation of design development length equations for the entire test specimens at the ultimate stress

Equation		Number of pullout failures	Number of splitting failures	Number of Rupture failures
ACI 440.1R (2015)	$l_e < l_d$	178	179	56
	$l_e > l_d$	0	2	8
CSA S806-12 (CSA 2012)	$l_e < l_d$	178	160	56
	$l_e > l_d$	0	21	8
CSA S6-14 (CSA 2014)	$l_e < l_d$	178	166	51
	$l_e > l_d$	0	15	13
Proposed Eq. (12)	$l_e < l_d$	178	178	57
	$l_e > l_d$	0	3	7
Proposed Eq. (13)	$l_e < l_d$	178	179	57
	$l_e > l_d$	0	2	7

3.7.4 Comparison of bond strength equations

This section investigates the bond strength predictions of the proposed equations and the CSA S806 (2012) and ACI 440.1R (2015) equations. The average bond strength estimation from the proposed development length according to Eqs. (3.12) and (3.13) is obtained by substituting the

development length equations in Eq. (3.6). Figure 3.14 shows the relationship between the theoretical and experimental bond strengths for the various equations. The CSA S806 (2012) equation and the proposed Eq. (3.13) produced a flattened trend due to the assumption of maximum linear stress with a zero intercept. The proposed Eq. (3.12) and the ACI 440.1R (2015) equation exhibited an analogous sloping relation to the proportionality line. Table 3.6 displays the quantitative ratio between the theoretical and experimental bond strengths. The CSA S806 (2012) equation highly overestimated the bond strength with a ratio of 1.13 and a corresponding standard deviation of 0.4.

Table 3.6 Ratio between the theoretical and experimental bond strengths

	Proposed Eq. (3.12)	Proposed Eq. (3.13)	CSA S806 (2012)	ACI 440.1R (2015)
Mean	0.97	0.87	1.13	0.96
Standard deviation	0.24	0.20	0.40	0.37

However, the proposed Eq. (3.13) predictions were more conservative, with a lower standard deviation. The proposed Eq. (3.12) showed the best mean, 0.97, among the equations, followed by the ACI 440.1R (2015) equation, 0.96. However, the standard deviation for the proposed Eq. (3.12), 0.24, was smaller than that of the equation of the ACI 440.1R (2015), 0.37. Accordingly, the proposed Eq. (3.12) is better than the other equations, and the introduction of the nonzero intercept results in a better representation of the bond strength.

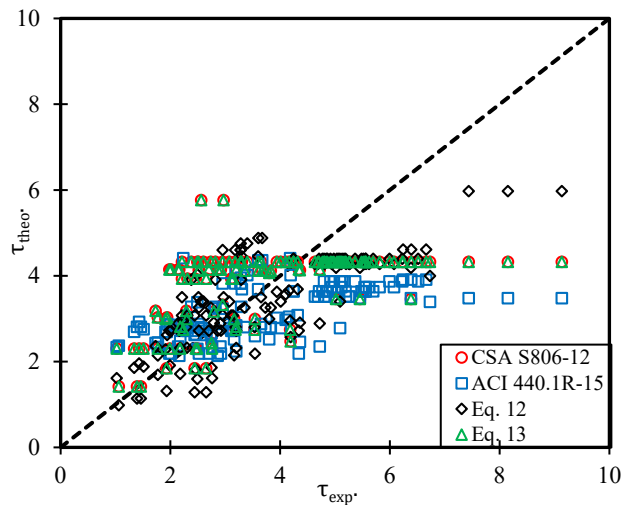


Figure 3.14 Proportionating the experimental and theoretical bond strength equations

3.8 Parametric study

A parametric study was conducted to assess the sensitivity of each equation with respect to the different parameters. The main parameters included in this study were the concrete cover to the center of the bars (from $1.5d_b$ to $3.5d_b$), GFRP tensile stress (f_f) (500 and 1000 MPa), GFRP elastic modulus (E_f) of 60 GPa, concrete compressive strength (35 and 65 MPa), and bar diameters (#3, #4, #5, #6, and #8). The study was conducted for splice beams while taking into consideration the resistance factor for GFRP reinforcement ($\phi_{GFRP} = 0.75$) for the CSA S806 (2012), CSA S806 (2002), CSA S6 (2014), and proposed equations. The resulting development length was multiplied by 1.3, as recommended by the code requirements. The value of C_E was assumed to be 0.85 for ACI 440.1R (2015).

For a GFRP tensile stress of 500 MPa, the graphs in Figure 3.15 show that at a concrete strength of 35 MPa, the proposed Eq. (3.12) usually provides shorter development lengths than the CSA S806 (2012) and ACI 440.1R (2015) equations, except at a concrete cover of $1.5d_b$. At the concrete cover of $2d_b$, the development lengths calculated with the proposed equations and the CSA S806 (2012) and ACI (2015) equations are almost the same. At bar diameter #8, the proposed Eq. (3.12) and the CSA S806 (2012) equation predict almost the same development lengths for concrete covers of $2d_b$ and greater. The CSA S806-12 (2012) equation requires shorter development lengths below this value. The proposed Eq. (3.13) and the ACI 440.1R (2015) equation yield slightly longer development lengths than the CSA S806 (2012) equation and the proposed Eq. (3.12). For bar diameter #8, for concrete covers less than $2.5d_b$, the ACI 440.1R (2015) equation provides shorter development lengths compared to Eq. (3.12), Eq. (3.13), and the CSA S806 (2012) equation.

The proposed Eqs. (3.12) and (3.13) require longer development lengths compared to the CSA S6 (2014) and CSA S806 (2002) equations. However, at a concrete strength of 65 MPa, the proposed Eq. (3.12) yields the shortest development lengths compared with the other equations in the standards and guidelines except at concrete covers of $2d_b$ and less and bar diameter #8, where the CSA S6 (2014) equation requires shorter development lengths. Notably, at a concrete strength of 65 MPa, the CSA S806 (2012) equation provided the longest development lengths compared to all the other equations for all the bar diameters. However, the proposed Eq. (3.13) requires shorter development lengths than the CSA S806 (2012) equation and longer lengths than that needed by

the CSA S6 (2014) and CSA S806 (2002) equations and the proposed Eq. (3.12).

For a GFRP tensile strength of 1000 MPa, the relationships presented in Figure 3.15 show that for a concrete strength of 35 MPa, the proposed Eqs. (3.12) and (3.13) typically require longer development lengths than the CSA S806 (2012), CSA S6 (2014), and CSA S806 (2002) equations for all bar diameters. The development lengths predicted by the proposed Eq. (3.12) are usually shorter than those predicted by ACI 440.1R (2015) equation, except at a concrete cover of $1.5d_b$ for bar diameters #3, #4, #5, and #6. By increasing the concrete strength to 65 MPa, the CSA S806 (2012) equation yielded longer development lengths than the proposed Eqs. (3.12) and (3.13).

Based on the conducted assessment and analyses, the authors recommend using proposed Eq. (3.12) for predicting the required development length for GFRP bars in flexural concrete members.

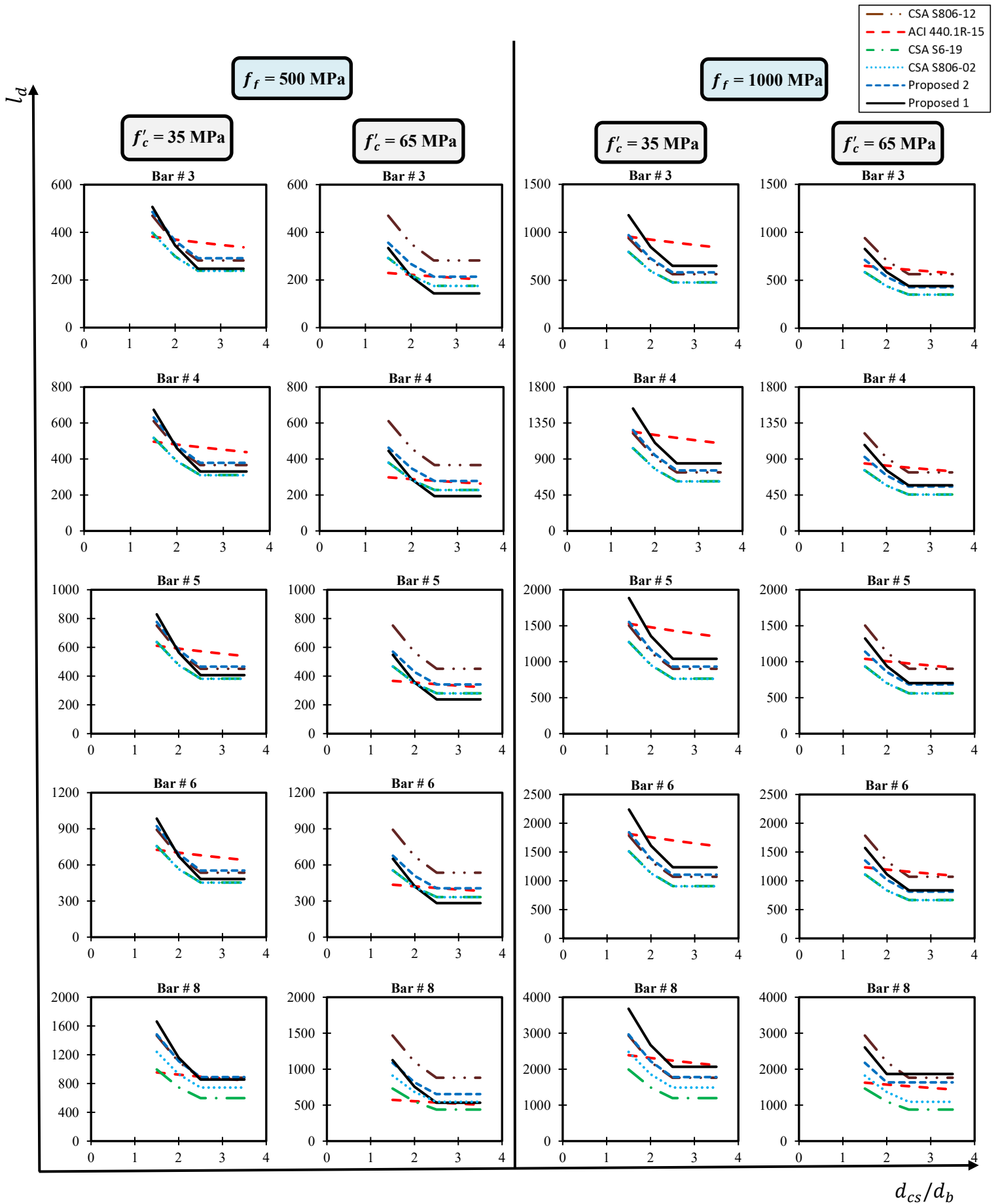


Figure 3.15 Comparison between different development length equations

3.9 Conclusions

In various standards, the current equations for the development length of GFRP bars embedded in flexural concrete members are based on a limited number of bond tests. The present study utilized an extensive database of recently conducted bond tests to optimize the development length equation of the CSA S806 (2012) design code. The study also quantified the effect of different parameters on the development length. The following conclusions were drawn from this study:

- The proposed Eq. (3.12) showed high reliability and effectiveness in predicting the development length by introducing the initial stress intercept based on a regression analysis of the beam end and splice beam test results.
- The proposed equations provided more accurate predictions of the mode of failure and the bond strength than the CSA S806 (2012) and the ACI 440.1R (2015) equations, and the standard deviation was the lowest for the proposed equations.
- Based on the available top bar splitting specimens, the coefficient (k_1) that accounts for the top bar effect is set to 1.3 for a horizontal reinforcement placed where more than 300 mm of fresh concrete is cast below the bar and 1.0 for other cases.
- The current study recommends increasing the limit of the square root of the concrete compressive strength to 8 based on a conservative limit for beams that failed by splitting and pullout of GFRP bars.
- The concrete cover significantly affected the estimation of the development length and depended on the bar size. To develop the bond strength of GFRP bars, the concrete cover to the center of the bar is recommended to be $2.5d_b$ for all bar diameters.
- The assessment of the bar size coefficient (k_3) showed that the coefficient has almost the same value, 0.9, for #3, #4, #5, and #6 bars and 1.1 for #8 bars due to shear lag and the effects of air entrainment underneath the bars.
- The enhancement in bond strength associated with transverse reinforcement confinement depended upon the type of bar surface configuration. The confinement had a negligible

effect on the bond strength for helically wrapped GFRP bars and increased the bond strength for ribbed and sand-coated surfaces. Accordingly, the term (K_{tr}) was incorporated into the development length equation to account for the confinement effect from transverse reinforcement.

- Estimates of the development length using the proposed equations decreased with increasing concrete compressive strength, unlike the predictions of CSA S806 (2012).
- Finally, the authors recommend utilizing the proposed Eq. (3.12) as a new design development length equation for GFRP reinforced concrete members.

Chapter 4

Investigation of different parameters affecting the crack width and k_b coefficient of GFRP-RC beams

4.1 Abstract

The crack width control is one of the parameters that affect the design of glass fibre-reinforced polymer (GFRP) reinforced concrete (RC) members. The crack width equations in the CSA S806 (2012) standard and ACI 440.1R (2015) guidelines account for the bond between the GFRP reinforcement and the surrounding concrete through the bond-dependent coefficient (k_b). According to the different standards and guidelines, each GFRP bar surface profile is assigned a k_b value obtained from the experimental tests. This chapter aims to experimentally investigate the main parameters that affect the crack width and k_b coefficient of GFRP bars by testing 16 beams. The primary purpose is to determine whether k_b is a fixed value that is solely dependent on the bar surface profile (as assumed by the above standard and guide) or that the k_b itself is a function of certain parameters. The studied parameters were the concrete cover, bar spacing, reinforcement ratio, confinement provided by transverse reinforcement, concrete compressive strength, and bar surface profile. The results showed that the k_b coefficient varies by changing the concrete type and the reinforcement configuration of the beam. Based on the results, design recommendations are proposed. Moreover, the k_b coefficient is recalibrated considering available experimental data in the literature.

4.2 Introduction

Glass fibre reinforced polymer (GFRP) reinforcement bars are used as an alternative to steel reinforcement due to their non-corrosive characteristics and high durability. GFRP manufacturers have mainly developed bars with various surface profiles to enhance their bond to concrete (Emparanza et al. 2017; Solyom and Balázs 2020). The available industrial GFRP bar surface profiles are ribbed, sand-coated, helically wrapped, grooved, and their combinations (Solyom and Balázs 2020).

The crack width and deflection of GFRP reinforced concrete (RC) members under service loads can dominate their design due to the lower elastic modulus of the GFRP reinforcement (El-Nemr et al. 2016; Esfahani et al. 2013). The bond behaviour of GFRP reinforcement with the surrounding concrete directly influences the crack width of the structural member (Baena et al. 2009). North American design standards and guidelines consider the bond of GFRP bars in the crack width equations through the bond-dependent (k_b) coefficient. The k_b coefficient significantly influences the crack width values and, consequently, the design of GFRP RC members (Benzecry et al. 2021; El-Nemr et al. 2016). The k_b of uncoated steel reinforcement is assumed to be 1.0, whereas that of GFRP bars differs depending on the surface profile. There is a disagreement between design standards and guidelines regarding the k_b value. The ACI 440.1R (2015), CSA S806 (2012) and ISIS Canada design manual (2012) recommend k_b values of 1.4, 1.2 and 1.2, respectively, in the case of a lack of experimental results. The k_b coefficient is determined following the adopted test method in Annex S of CSA S806 (2012) by correlating the k_b factor with the experimentally measured crack width through Eq. (4.1), as follows:

$$w = 2 \frac{f_f}{E_f} \beta k_b \sqrt{d_c^2 + (s/2)^2} \quad (\text{CSA S806 (2012)}) \quad (4.1)$$

where w is the maximum measured crack width and shall not exceed 0.7 mm; f_f is the stress in GFRP reinforcement in tension in MPa; E_f is the elastic modulus of the GFRP bar in MPa; β is the ratio of the distance from the neutral axis to the extreme tension fibre to the distance from the neutral axis to the center of the tensile reinforcement; k_b is the bond-dependent coefficient; d_c is the concrete cover thickness measured from the extreme tension fibre to the center of the outermost tension bar in mm; and s is the center to center spacing between the tensile bars in mm.

The experimental data available in the literature showed that k_b could vary from 0.6 to 1.72 (Benzecry et al. 2021). Furthermore, Shield et al. (2019) compiled and analyzed a total of 39 reliable crack widths. The results showed that the k_b values ranged from 0.69 and 1.57 for the sand-coated GFRP bars (Shield et al. 2019). They recommended that the k_b value in ACI 440.1R (2015) for sand-coated GFRP bars be reduced from 1.4 to 1.2. However, a k_b value of 1.4 was recommended for other surface types due to the lack of experimental data.

Although k_b was originally foreseen to be a unique value based on the surface profile, El-Nemr et al. (2016) found that other parameters affect k_b , including the bar diameter and concrete compressive strength. Accordingly, this study investigates the influence of different configurational parameters, including the concrete cover (30 mm, 38 mm, and 50 mm), bar spacing, bar diameter (13 mm, 15 mm, 20 mm, and 25 mm), reinforcement ratio, concrete strength (normal- and high-strength), bar surface profile (ribbed and sand-coated), and confinement effect due to transverse reinforcement in the middle constant moment zone on the k_b coefficient by testing 16 concrete beams reinforced with high-modulus (Grade III) GFRP bars.

4.3 Research significance

This study quantifies the influence of different configurational parameters on the crack width of GFRP reinforced concrete flexural, which contributes to a better understanding of the cracking behaviour of flexural members. It also investigates whether the k_b coefficient is a function of the GFRP bar surface profile only or it is a function of other parameters. Moreover, this study provides more experimental data on the crack width of concrete beams reinforced with ribbed and sand-coated GFRP bars, which supplements the available database of the ACI 440 committee.

4.4 Experimental program

4.4.1 Material properties

4.4.1.1 Concrete

Normal- and high-strength concrete (NSC and HSC) with specified 28-day compressive strengths of 35 MPa and 65 MPa, respectively, were utilized in this study. The actual concrete strength was quantified by testing five 100 × 200 mm concrete cylinders for each concrete batch following ASTM C39/C39M (2021) on the day of testing (\pm 1 week). The NSC beams were cast using two batches (NSC-1 and NSC-2). The measured compressive strengths for NSC-1, NSC-2,

and HSC were 35.75 ± 1.13 , 40.01 ± 1.44 MPa, and 70.84 ± 2.14 MPa, respectively. According to ASTM C143/C143M (2020), the concrete slump obtained was 101 mm and 165 mm for NSC and HSC, respectively. The concrete modulus of rupture (f_r) and cylinder splitting tests (T) were performed per ASTM C78/C78M (2021) and ASTM C496/C496M (2017), respectively. NSC-1, NSC-2, and HSC had f_r values of 4.97 ± 0.29 , 5.32 ± 0.38 , and 5.98 ± 0.27 and T values of 3.59 ± 0.21 , 3.79 ± 0.29 and 4.67 ± 0.19 MPa, respectively.

4.4.1.2 GFRP and steel reinforcement

High modulus Grade III GFRP bars were used as tensile reinforcement, and Grade 400 steel bars were used as compression reinforcement and stirrups. Canadian manufacturers supplied the ribbed and sand-coated GFRP bars. The steel bars were 10M deformed steel reinforcement with a nominal diameter of 11.3 mm, cross-sectional area of 100 mm^2 , and specified yield strength (f_y) of 400 MPa. The surface profiles of the GFRP and steel bars are presented in Figure 4.1. The designated diameters of the GFRP bars were #4 (13 mm), #5 (15 mm), #6 (20 mm), and #8 (25 mm). According to ASTM D7205/D7205M (2021), five specimens were tested for each bar diameter to determine the tensile strength, ultimate strain at failure, and modulus of elasticity. The mechanical and nominal cross-sectional properties of GFRP bars are presented in Table 4.1. The tensile strength and elastic modulus of the GFRP bars were calculated based on the nominal bar cross-sectional area as per ASTM D7957/D7957M (2017). The properties of the steel bars are nominal values taken from the datasheet provided by the supplier.

Table 4.1 Properties of GFRP bars

Bar type	Designated diameter	Nominal cross-sectional area (mm^2)	Nominal diameter (mm)	Tensile strength (MPa)	Elastic modulus (GPa)	Ultimate strain (%)
Ribbed	#4 (13 mm)	129	12.7	1049 ± 9.9	60.40 ± 0.38	1.74
GFRP	#5 (15 mm)	199	15.9	1087 ± 9.8	60.36 ± 0.46	1.80
	#6 (20 mm)	284	19.1	1052 ± 8.4	61.02 ± 0.91	1.72
	#8 (25 mm)	510	25.4	1090 ± 11.3	61.94 ± 0.36	1.76
Sand-coated GFRP	#6 (20 mm)	284	19.1	1473 ± 33.0	63.11 ± 0.86	2.33



Figure 4.1 The surface profile of steel, ribbed, and sand-coated Grade III GFRP bars

4.4.2 Design of the tested beams

The experimental work comprised 16 simply-supported concrete beams constructed and tested under four-point flexural loading. The beams were designed as per ACI 440.1R (2015). The beams were 200 mm wide and 400 mm high in cross-section. The total length of the beams was 4350 mm, and the distance between the centreline of the supports was 3750 mm. The beams were divided into two groups named A and B. Group A included 12 NSC beams, whereas group B comprised 4 HSC beams. The tensile reinforcement comprised a different number of GFRP bars. Two 10M deformed steel bars were used as compression reinforcement, and the stirrups were fabricated from 10M deformed steel bars. The elevation, cross-sectional dimensions, and reinforcement details for all the beams are shown in Figure 4.2.

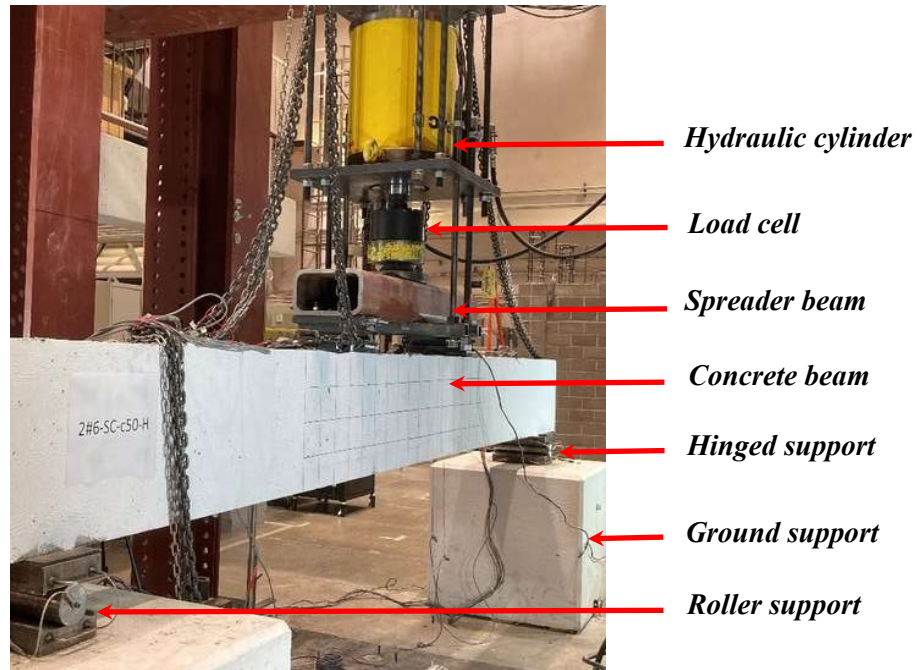
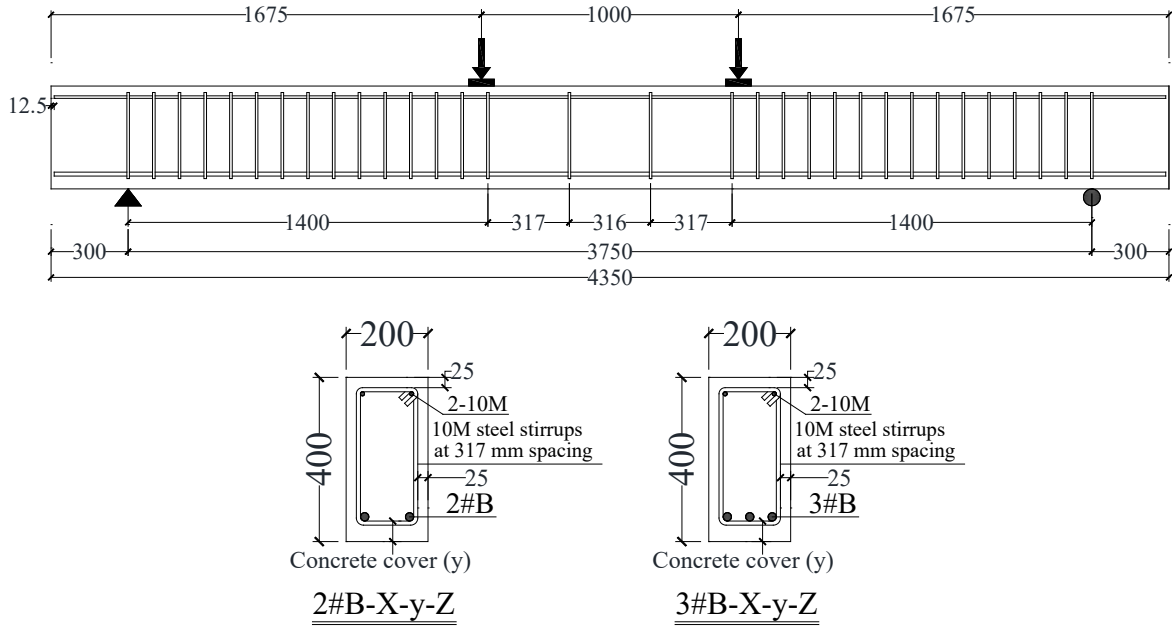


Figure 4.2 Elevation, cross-sectional details, and test setup of the beams (Note: all dimensions are in mm)

The specimen details are listed in Table 4.2. The notations in Table 4.2 are discussed through the following example: A#B-X-y-Z, where letter A stands for the total number of GFRP tensile reinforcements; letter B refers to the reinforcement diameter number; letter X denotes the surface profile of the GFRP bar: R for ribbed and S for sand-coated; letter y represents the clear concrete

cover to GFRP reinforcement in mm; and letter Z stands for the concrete type: N for NSC and H for HSC. It is important to note that the confinement effect due to transverse reinforcement in the bending zone was investigated as a parameter in beams 3#5-R-c50-s317-N, 3#5-R-c50-s200-N, and 3#5-R-c50-s100-N, where the three specimens have the same nomenclature as previously identified except for s317, s200, and s100, which represent the center-to-center spacing between the transverse reinforcement in the constant moment zone in mm. The clear concrete cover to the GFRP reinforcement was a parameter in this study and was chosen to be 30 mm, 38 mm, and 50 mm, whereas the side cover was 25 mm measured from the side of the stirrup to the concrete surface.

As per ACI 440.1R (2015), all specimens were designed as over-reinforced sections to fail in flexure by concrete crushing. The beams were provided with an adequate amount of 10M steel stirrups in the shear zone, spaced at 100 mm from center to center. At the middle flexural zone (zero shear), the stirrups were used as hangers for the top reinforcement, and the spacing was increased to 317 mm to preclude any confinement effect from the transverse reinforcement.

Table 4.2 Test matrix and details of the tested beams

Group	Beam Designation	f'_c	Clear cover	Bar spacing	d_b	ρ_f
		MPa	mm	mm	mm	%
A	3#4-R-c30-N	40.01	30	57.35	12.7	0.532
	3#4-R-c38-N	40.01	38	57.35	12.7	0.544
	3#4-R-c50-N	40.01	50	57.35	12.7	0.563
	2#5-R-c30-N	40.01	30	111.50	15.9	0.550
	2#5-R-c50-N	40.01	50	111.50	15.9	0.582
	2#6-R-c50-N	35.75	50	108.30	19.1	0.834
	2#8-R-c50-N	35.75	50	102.00	25.4	1.512
	3#6-R-c38-N	35.75	38	54.15	19.1	1.251
	3#6-R-c50-N	35.75	50	54.15	19.1	1.251
	3#5-R-c50-s317-N	35.75	50	55.75	15.9	0.873
	3#5-R-c50-s200-N	35.75	50	55.75	15.9	0.873
	3#5-R-c50-s100-N	35.75	50	55.75	15.9	0.873
	B	2#6-R-c50-H	70.84	50	108.30	19.1
3#6-R-c50-H		70.84	50	54.15	19.1	1.251
2#6-S-c50-H		70.84	50	108.30	19.1	0.834
3#6-S-c50-H		70.84	50	54.15	19.1	1.251

4.4.3 Test setup and instrumentation

The test setup and the recommended procedures in Annex S in the CSA S806 (2012) method were followed to determine the k_b coefficient of all the beams. All the specimens were simply-supported and tested under a four-point bending loading scheme. The distance between the point loads was 1000 mm. The test setup and instrumentations are illustrated in Figure 4.2 and Figure 4.3, respectively. The load was applied using a hydraulic cylinder and was measured by a 500 kN load cell with an accuracy of 0.05 kN. The load cell was directly attached to the hydraulic cylinder. The load was applied to a spherical platen attached to a rigid steel spreader beam to ensure a uniformly distributed load over the beam, as shown in Figure 4.2.

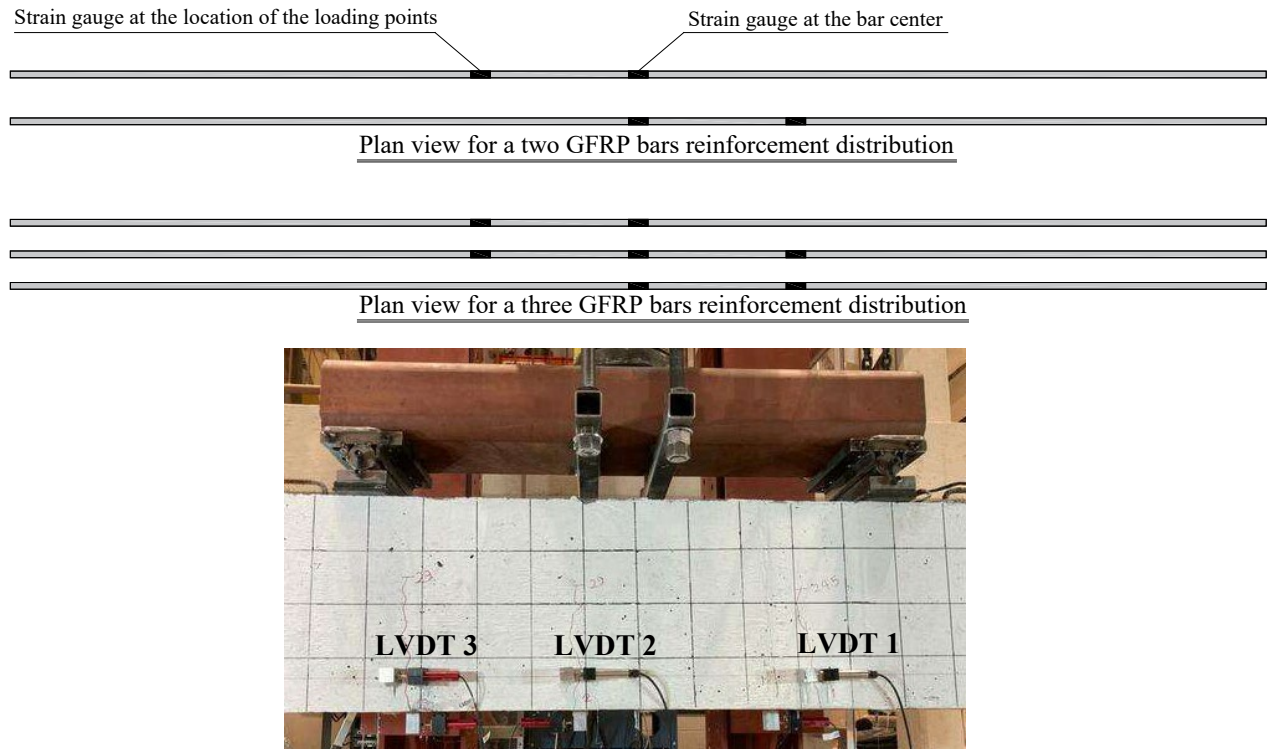


Figure 4.3 Instrumentation of the tested beams

The beams were loaded at a rate of 0.6 mm/min until the first crack appeared; then, the load was held constant, and the initial crack was measured using a hand-held microscope with a resolution of 0.01 mm. After that, a linear variable displacement transducer (LVDT) was installed at the level of the reinforcement to monitor the crack width until failure, as shown in Figure 4.3. The same procedure was followed for measuring the second and third cracks. In the HSC beams, the side and bottom crack widths of the first three cracks were measured using six LVDTs, as

shown in Figure 4.3. After installation of all LVDTs, the beams were loaded at 1.2 mm/min until failure. The strains in the GFRP reinforcement were measured using electrical strain gauges with a gauge length of 2 mm. As shown in Figure 4.3, a minimum of two strain gauges were utilized for each GFRP reinforcement, one gauge at the center of the bar and the other gauge at the location of the point loading.

4.5 Experimental results and discussions

4.5.1 Cracking observations

The first three flexural cracks were initiated in the mid-span and under the point loading. In general, the number of cracks slightly increased and crack spacing decreased by increasing the concrete cover thickness, bar diameter and reinforcement ratio. It was also observed that the HSC beams had higher cracking loads and wider initial crack widths than the NSC beams.

4.5.2 Crack widths of GFRP-RC beams

Figure 4.4 shows the maximum measured side crack width extrapolated to the tension face versus the theoretical tensile strains extrapolated to the tension face. The side crack width and theoretical tensile strains are extrapolated to the tension face using a factor β . Out of the measured cracks, the crack that reached 0.7 mm at the tension face at a lower strain was considered the maximum crack. To ease the comparisons for the serviceability range, the graphs show the trend up to the crack width of 0.8 mm.

Figure 4.4(a) compares the crack widths of beams with similar $\sqrt{d_c^2 + (s/2)^2}$ values. As shown the strains of beams 2#6-R-c50-N and 2#8-R-c50-N were very similar for the entire crack width range. However, beam 2#5-R-c50-N exhibited narrower crack widths under the same strain compared to the other two beams up to a crack width of 0.6 mm but wider crack widths for strains greater than approximately $6000 \mu\epsilon$. From Eq. (4.1), these beams were expected to have similar crack widths at the same strain level (i.e., the same βf_f).

Figures 4.4(b and c) compare the effect of the concrete cover (d_c) on the maximum crack width. From Eq. (4.1), the crack width is expected to decrease with a decrease in d_c . However, Figure 4.4(c and d) shows no trend for the effect of d_c on crack width. The maximum crack widths of beams 3#4-R-c30-N and 2#5-R-c30-N were smaller than those of the corresponding beams with

a cover of 50 mm. However, beams 3#4-R-c38-N and 3#6-R-c38-N exhibited narrower crack widths up to a crack width of approximately 0.4 mm than beams 3#4-R-c50-N and 3#6-R-c50-N but larger crack widths after that.

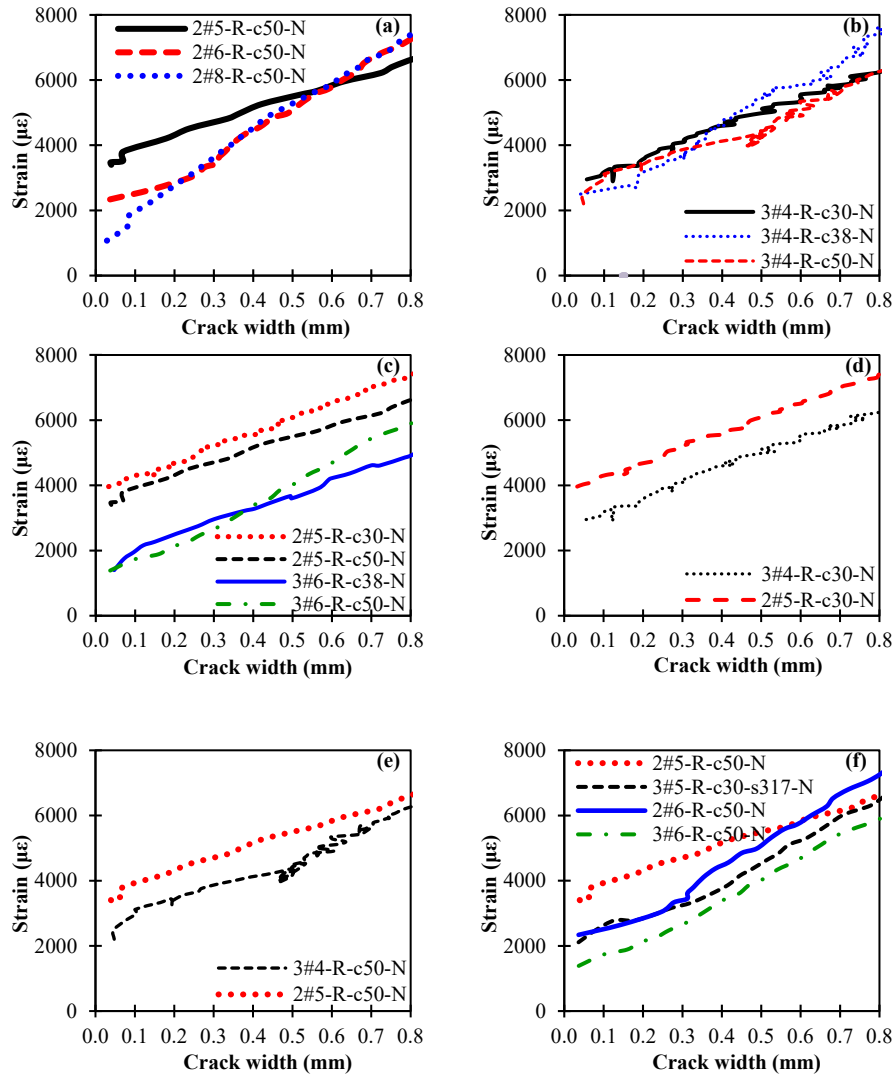
Figures 4.4(d and e) show the effect of reinforcement spacing at a similar reinforcement ratio on crack width. As shown, beams with the reinforcement at larger spacing (2#5-R-c30-N vs. 3#4-R-c30-N and 2#5-R-c50-N vs. 3#4-R-c50-N) demonstrated smaller crack widths at the same strain level. Moreover, Figure 4.4(f) shows that beams 3#5-R-c50-s317-N and 3#6-R-c50-N with smaller bar spacing had wider crack widths at the service stage than beams 2#5-R-c50-N and 2#6-R-c50-N, respectively. These observations do not agree with the expected relationship between crack width and bar spacing (see Eq. (4.1)), where for a given strain and d_c , the maximum crack width decreases by decreasing the bar spacing.

Figure 4.4(g) demonstrates the effect of the transverse reinforcement spacing on the crack width. As shown, beam 3#5-R-c50-s100-N exhibited smaller crack width values than beams 3#5-R-c50-s200-N and 3#5-R-c50-s317-N. Moreover, beams 3#5-R-c50-s200-N and 3#5-R-c50-s317-N manifested very close crack widths, which proves that spacings of 200 mm (i.e., approximately half of the beam depth) and 317 mm between the stirrups did not affect the crack width.

Figures 4.4 (h and i) show the effect of the bar surface profile on the maximum crack width of GFRP-reinforced HSC beams. It is worth mentioning that those graphs show the relationship between the extrapolated crack width and extrapolated strain. The effect of the surface profile on the maximum crack width measured at the soffit of the beam is discussed in a proceeding section. As shown in Figure 4.4(h), beam 2#6-R-c50-H reinforced with ribbed GFRP bars provided smaller crack width values at the same strain level than beam 2#6-S-c50-H reinforced with sand-coated bars. The beam reinforced with a sand-coated bar 3#6-S-c50-H (shown in Figure 4.4(i)) exhibited very similar cracking behaviour to the corresponding beam reinforced with ribbed GFRP bars (3#6-R-c50-H) up to a crack width of approximately 0.65 mm; subsequently, beam 3#6-R-c50-H exhibited smaller crack width values compared with beam 3#6-S-c50-H.

Based on ACI 440.1R (2015) and CSA S806 (2012), the effect of the concrete compressive strength is not considered for crack width calculations. Figure 4.4(j) compares the maximum crack width of the NSC and HSC beams. The HSC beams exhibited a considerably different crack width

trend than the corresponding NSC ones. Overall, the HSC beams exhibited larger cracks than the NSC beams at the same strain level. This might be attributed to the increase in the concrete tensile strength of HSC compared to NSC. The increase in the concrete tensile strength will delay the initiation of cracks, and hence, the cracking stabilization stage will be achieved at higher strains, resulting in wider crack widths and larger spacing between the cracks, particularly at service moments corresponding to crack widths up to 0.7 mm.



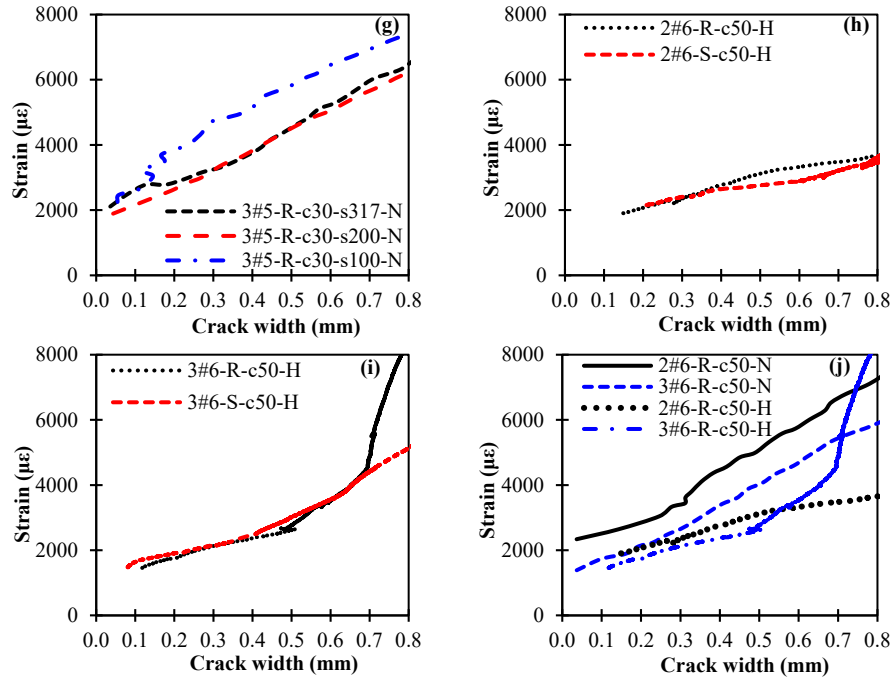


Figure 4.4 Extrapolated crack width to tension face versus GFRP extrapolated strain relations

4.5.3 Comparison between bottom and side crack widths

As mentioned, for the HSC beams, the side and bottom crack widths of the first three cracks were measured using six LVDTs; three on the beam's side and three at the beam soffit. It is important to indicate that the distance between the stroke of the LVDT used to measure the bottom crack widths and the beam bottom soffit was 25.4 mm; accordingly, the measured bottom crack widths were corrected by multiplying the measured bottom crack widths by the ratio $(h-c)/(h+25.4-c)$. The relationships in Figure 4.5 compare the maximum side crack widths and their corresponding bottom ones. It can be clearly seen that the bottom crack widths are always wider than the side crack widths. Comparing the bottom measured crack widths of the sand-coated and ribbed GFRP bars shows that the ribbed GFRP bars demonstrated consistently smaller crack widths than the sand-coated GFRP bars, especially at higher crack widths.

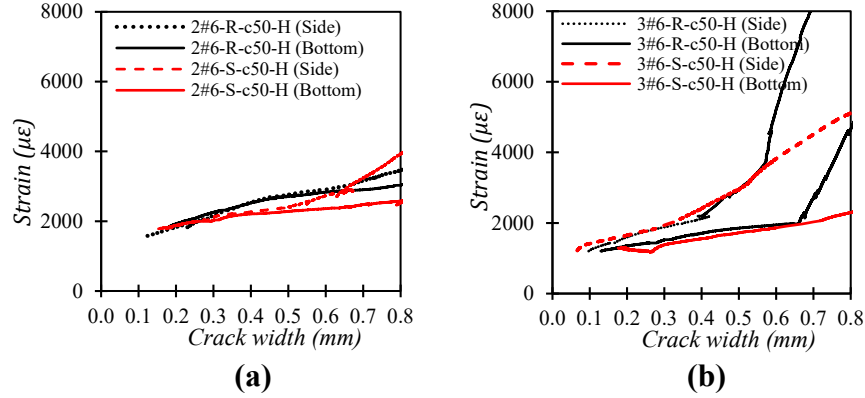


Figure 4.5 Comparison between side and bottom crack widths for high-strength beams.

The factor β in the crack width equation in CSA S806 (2012) is defined as the ratio of the distance from extreme tension fibres to the neutral axis to the distance from the centre of tension reinforcement to the neutral axis. In other words, the factor β can be defined as the ratio between the bottom and side crack widths of the same crack at the same strain level. The width of the critical crack in most experimental studies available in the literature is measured at the level of reinforcement. Figure 4.6 shows the relation between the experimental and theoretical β values versus the bottom crack widths for the high-strength beams. The experimental β values were computed by taking the ratio between the bottom and side crack widths for the maximum of the first three flexural cracks. As shown in Figure 4.6, the beams reinforced with sand-coated bars provide noticeably higher β values than those reinforced with ribbed bars. The experimental β values for the beams reinforced with sand-coated bars range between 1.30 and 1.97 at a crack width of 0.7 mm. These β values are higher than the theoretical values for the tested beams, which is approximately 1.2. However, for the beams reinforced with ribbed GFRP bars, the experimental β values range between 1.12 and 1.23. The results show that the theoretical β values used to extrapolate the side crack width for the beams reinforced with sand-coated bars are highly unconservative and provide lower extrapolated crack width values at the service stage than the experimental values; hence, using side crack values extrapolated to the tension face of the beam in the calculation of the bond-dependent coefficient may result in unconservative k_b values and thus unrealistic maximum crack width predictions. This could be attributed to the fact that the neutral axis at the service stage moves upwards as the load increases until it reaches the neutral axis location that is used in calculating the theoretical value, β . At lower loads, the ratio between the bottom crack width and the side crack width will be higher than the theoretical value, β . More

investigations are required to focus on measuring the bottom crack widths and comparing them to the side crack widths for different bar surface profiles to assess the theoretical β values. It is also recommended that the code committees develop a standard test method for crack width evaluations of members reinforced with GFRP bars.

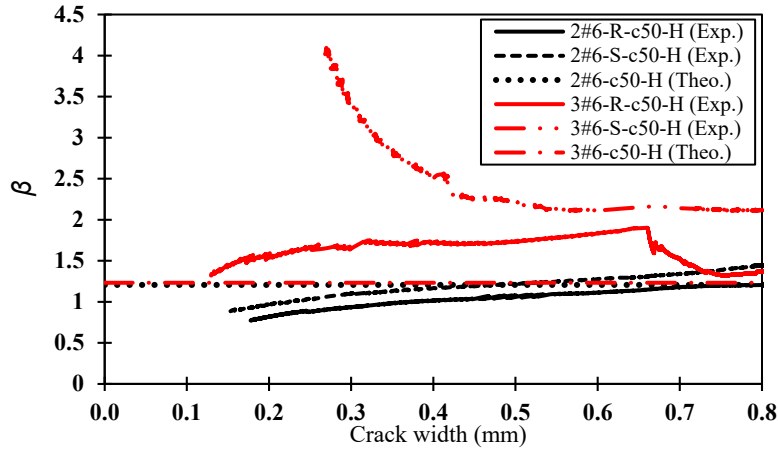


Figure 4.6 Relationship between the factor β and the bottom measured crack width.

4.5.4 The bond-dependent coefficient, k_b , of GFRP-RC beams

Based on the current CSA S806 (2012), the k_b coefficient is determined by measuring the experimental crack width at the specified service load. Rearranging Eq. (4.1), the k_b coefficient can be computed from Eq. (4.2).

$$k_b = w \frac{E_f}{2f_f} \frac{1}{\beta} / \sqrt{d_c^2 + (s/2)^2} \quad (4.2)$$

As the only standard available in North America, CSA S806 (2012), Annex S specifies that the k_b coefficient should be determined for the maximum measured crack width that does not exceed 0.7 mm. The term service load is defined as the load that should not be exceeded in the GFRP reinforcement to maintain the serviceability of the flexural member within acceptable limits. Several researchers (Yost and Gross 2003; Kassem et al. 2011; and El-Nemr et al. 2013, 2016, 2018) used 30% (or 33%) of the nominal moment as a service limit for crack width measurements. The ACI 440.1R (2015) sets an acceptable range for crack widths between 0.4 mm and 0.7 mm. CSA S6 (2014) limits the crack width to 0.5 mm for structural members subjected to aggressive environments and 0.7 mm for other members for bridge serviceability. The ISIS Canada design manual (2012) limits the strain in the GFRP reinforcement to 2000 $\mu\epsilon$ under service loads to

maintain a crack width less than or equal to 0.5 mm. AASHTO LRFD GRFP (2018) has a crack width limit of 0.7 mm for GFRP-RC members.

In this section, the k_b coefficient is computed at 0.5, 0.6, and 0.7 mm by taking the maximum of the first three measured flexural crack widths extrapolated to the tension face of the beams, as presented in Table 4.3. The effect of using the average crack width and maximum crack width measured at the soffit of the beam is also considered and discussed. It is worth noting that the k_b values are calculated using applied moments that include the self-weight of the beam.

The results of the average k_b values show that the k_b coefficient increases for NSC beams as the crack width increases. However, there is no trend for the effect of crack width on the k_b coefficient of HSC beams. Moreover, the k_b value changes from one rebar configuration to another. Comparing the results of NSC with HSC beams shows that the k_b values calculated for the HSC beams reinforced with ribbed GFRP bars are different from those of the corresponding NSC beams.

In Table 4.3, the average k_b values in the last column are computed based on the three values for each specimen (at 0.5, 0.6, and 0.7 mm extrapolated crack widths). The average k_b value for the NSC beams from 36 k_b values is 0.87 ± 0.22 (COV of 25%), whereas for the HSC reinforced with ribbed bar and sand-coated GFRP bars, the k_b values are 1.18 ± 0.07 (COV of 6%) and 1.26 ± 0.01 (COV of 0.6%). The average k_b value for the ribbed GFRP bars from the NSC and HSC beams using 42 available k_b values is 0.91 ± 0.23 (COV of 26%).

The following section discusses the effect of different parameters on the k_b values. The approach followed to compare the k_b values of the different specimens for the same test parameter was based on the maximum crack width of 0.7 mm (measured experimentally at the level of reinforcement and extrapolated to the tension face for determining k_b). Figure 4.7 shows the relation between the k_b values versus the extrapolated strain of the ribbed and sand-coated specimens to the outer tension fibres. The relations in Figure 4.7 show a decreasing trend in the k_b values by increasing the extrapolated strains with a good correlation between the k_b values and strains. This reduction in the k_b values is in agreement with Eq. (4.1).

Table 4.3 Test results

Beam	Moment (kN-m)			Theoretical strain extrapolated to the tension face ($\mu\epsilon$)			k_b			Average
	0.5 mm	0.6 mm	0.7 mm	0.5 mm	0.6 mm	0.7 mm	0.5 mm	0.6 mm	0.7 mm	
3#4-R-c30-N	37.1	40.4	42.4	5115	5560	5839	1.06	1.17	1.30	1.17
3#4-R-c38-N	38.4	40.5	44.4	5550	5855	6423	0.85	0.97	1.03	0.95
3#4-R-c50-N	30.9	36.0	37.7	4808	5610	5871	0.82	0.84	0.94	0.87
2#5-R-c30-N	44.8	48.1	51.2	6071	6517	6936	0.60	0.69	0.75	0.68
2#5-R-c50-N	35.5	38.0	40.4	5443	5817	6197	0.58	0.64	0.70	0.64
2#6-R-c50-N	47.9	53.7	60.4	5228	5857	6598	0.60	0.64	0.66	0.63
2#8-R-c50-N	84.1	92.5	105.8	5308	5841	6679	0.59	0.63	0.65	0.62
3#6-R-c38-N	52.4	61.4	67.2	3600	4211	4612	1.26	1.30	1.39	1.31
3#6-R-c50-N	53.6	63.9	72.6	3982	4745	5394	0.95	0.97	1.00	0.97
3#5-R-c50-s317-N	43.0	50.2	56.4	4479	5221	5870	0.87	0.89	0.93	0.90
3#5-R-c50-s200-N	44.1	48.4	55.9	4586	5043	5816	0.85	0.92	0.94	0.90
3#5-R-c50-s100-N	53.5	62.3	63.7	5571	6487	6635	0.70	0.73	0.82	0.75
2#6-R-c50-H	29.1	31.0	32.4	3137	3336	3484	1.00	1.13	1.26	1.13
3#6-R-c50-H	38.6	49.0	72.0	2817	3575	5252	1.37	1.29	1.03	1.23
2#6-S-c50-H	26.5	27.9	31.0	2766	2905	3226	1.13	1.29	1.35	1.26
3#6-S-c50-H	43.1	50.7	63.1	3045	3585	4462	1.27	1.29	1.21	1.25
All NSC ^a	Average			4978	5564	6073	0.81	0.87	0.93	0.87
	Standard Deviation			714	672	649	0.21	0.22	0.24	0.22
	Coefficient of Variation			14%	12%	11%	26%	25%	26%	25%
HSC-R ^b	Average			2977	3456	4368	1.19	1.21	1.15	1.18
	Standard Deviation			226	169	1250	0.26	0.11	0.16	0.07
	Coefficient of Variation			8%	5%	29%	22%	9%	14%	6%
HSC-S ^c	Average			2906	3245	3844	1.20	1.29	1.28	1.26
	Standard Deviation			197	481	874	0.10	0.00	0.10	0.01
	Coefficient of Variation			7%	15%	23%	8%	0%	8%	0.6%
All R ^d	Average			4693	5263	5829	0.86	0.92	0.96	0.91
	Standard Deviation			981	985	927	0.25	0.24	0.24	0.23
	Coefficient of Variation			21%	19%	16%	29%	26%	25%	26%
All HSC ^e	Average			2941	3350	4106	1.19	1.25	1.21	1.22
	Standard Deviation			178	318	931	0.16	0.08	0.13	0.06
	Coefficient of Variation			6%	10%	23%	14%	6%	11%	5%

a. All NSC beams reinforced with ribbed GFRP bars.

b. HSC beams reinforced with ribbed GFRP bars.

c. HSC beams reinforced with sand-coated GFRP bars.

d. NSC and HSC beams reinforced with ribbed GFRP bars.

e. All HSC beams reinforced with ribbed and sand-coated GFRP bars.

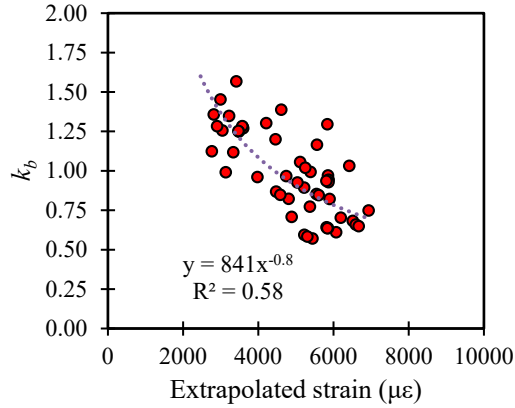


Figure 4.7 Relation between the k_b coefficient and the extrapolated strains for all the specimens

Figure 4.8 shows the k_b values versus the clear concrete cover to the GFRP bar surface. The relations in Figure 4.8 show a decreasing trend in the k_b values by increasing the concrete cover. However, the change in the k_b values with respect to the change in the concrete cover was different between the specimens. The k_b of beams reinforced with 3#6 showed the highest sensitivity to the change in clear cover. This reduction in the k_b values might be because the area of the concrete surrounding the GFRP bar increases by increasing the thickness of the concrete cover. This enhances the bond performance of the embedded bar with concrete, which decreases the k_b values.

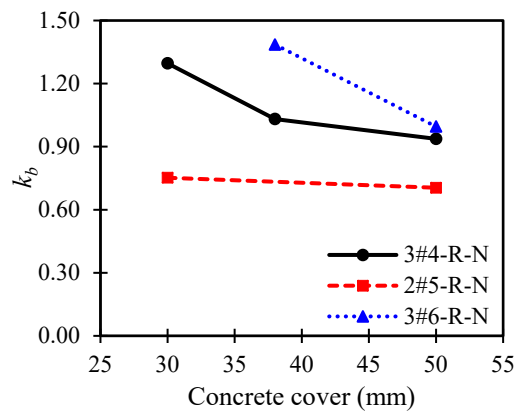


Figure 4.8 Relation between the k_b coefficient and the clear concrete cover to the GFRP bar surface.

Comparing the results of beams with similar $\sqrt{d_c^2 + (s/2)^2}$ (i.e., 2#5-R-c50-N, 2#6-R-c50-N, and 2#8-R-c50-N) as presented in Table 4.3 shows that the k_b value is not sensitive to the bar

diameter, as long as $\sqrt{d_c^2 + (s/2)^2}$ remains the same.

The trends in Figure 4.9 illustrate the relations between the k_b values and the center-to-center spacing between the GFRP bars at the same reinforcement ratio. In this figure, Group A includes beams 3#4-R-c30-N and 2#5-R-c30-N (ρ_f of 0.532 and 0.550%, respectively), Group B comprises beams 3#4-R-c50-N and 2#5-R-c50-N (ρ_f of 0.563 and 0.582%, respectively), and Group C involves beams 3#5-R-c50-s317-N and 2#6-R-c50-N (ρ_f of 0.873 and 0.834%, respectively). As shown in Figure 4.9, there is a significant reduction in the k_b values by increasing the bar spacing. The k_b values decreased for Groups A and B beams by 42% and 25%, respectively, by increasing the bar spacing from 57.4 mm to 111.5 mm. For Group C, the k_b value decreased by 29% by increasing the bar spacing from 55.8 mm to 108.3 mm. When the bar spacing decreases, the effective concrete area surrounding each bar reduces, and the concrete confinement becomes lower. This reduces the bond between the bar and concrete; hence, k_b decreases.

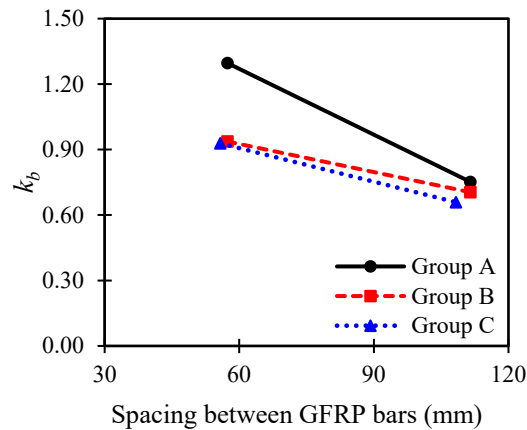


Figure 4.9 Relation between the k_b coefficient and bar spacing.

The relations presented in Figure 4.10 show that the concrete strength affects the k_b coefficient of one out of two sets of specimens with the same reinforcement configuration. For beams reinforced with 2#6-R-c50, and 3#6-R-c50, the k_b values increased by 91% and 3%, respectively, by increasing the concrete strength from 35.75 MPa to 70.84 MPa. This could be attributed to the high concrete tensile strength delaying the initiation of the secondary cracks in the vicinity of the primary cracks. The secondary cracks reduce the crack spacings between the primary cracks,

resulting in narrower primary crack widths and hence lower k_b values at high service moments. It is important to note that the k_b value of beams 3#6-R-c50-H decreased to a lower value of 0.67 at higher crack width of 0.95 mm, which shows that the stabilization of cracks happens at higher crack widths in HSC.

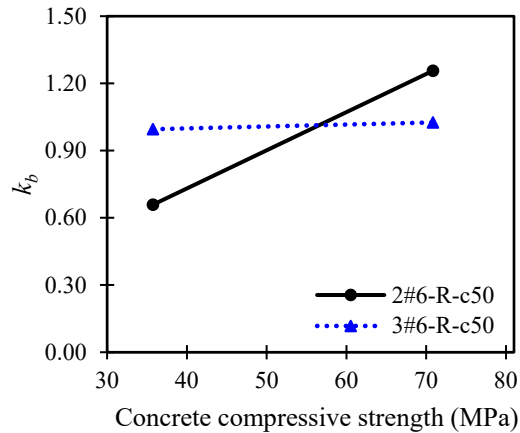


Figure 4.10 Relation between the k_b coefficient and concrete compressive strength.

The confinement effect due to the closely spaced stirrups in the middle constant flexure zone was investigated in beams 3#5-R-c50-s317-N, 3#5-R-c50-s200-N, and 3#5-R-c50-s100-N. The results presented in Figure 4.11 show that k_b was reduced by decreasing the spacing between stirrups in the flexural zone, particularly from 317 mm to 100 mm, whereas decreasing the spacing from 317 mm to 200 mm resulted in a negligible change in the k_b coefficient. This reduction in k_b by decreasing the spacing from 317 mm to 100 mm was attributed to the uniformly distributed cracks that developed in the middle bending zone at the service stage due to the concentration of stirrups with small spacing that resulted in more confinement and higher moments, thus reducing the k_b value.

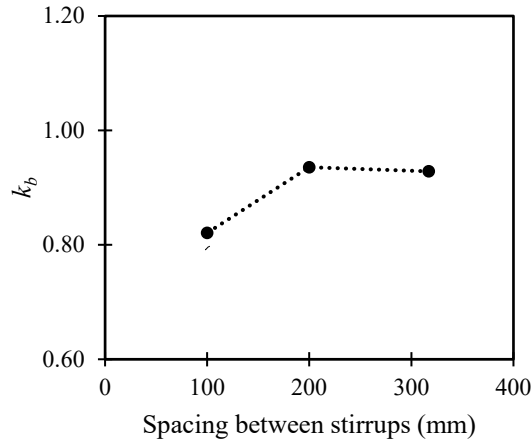


Figure 4.11 Relation between the k_b coefficient and spacing between stirrups.

The results of the ribbed and sand-coated GFRP RC beams are presented in the bar chart in Figure 4.12. The surface profile of the ribbed and sand-coated bars controls the bond performance of each bar with concrete. The results in Figure 4.12 show that the bar surface profile affects the k_b values for the beams with the same reinforcement configuration. The k_b values from the extrapolated side crack widths indicate that the k_b value of beams 2#6-R-c50-H is 8% lower than the k_b of beams 2#6-S-c50-H. Moreover, beam 3#6-R-c50-H reinforced with ribbed bars had a lower k_b value than beam 3#6-S-c50-H by 18%. The k_b results from the bottom measured crack widths demonstrate that the ribbed GFRP bars consistently have lower k_b at 0.7 mm values than the sand-coated bars. The average k_b value of the HSC beams reinforced with ribbed GFRP bars using the bottom measured crack width is 1.41 ± 0.23 , while the average k_b value of the sand-coated GFRP-RC beams is 1.81 ± 0.51 . The comparison shown in this figure shows that based on the experimental results, the extrapolated side crack widths provide lower k_b values than the bottom measured crack widths.

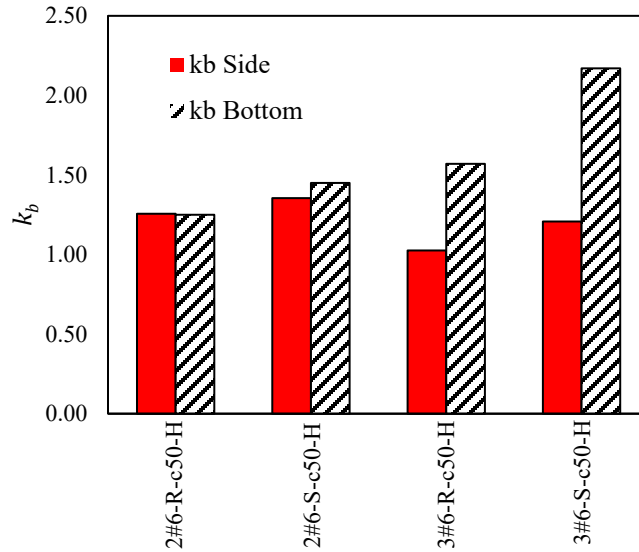


Figure 4.12 The k_b comparison between the ribbed and sand-coated GFRP bars

4.5.5 Effect of the critical crack on the k_b values

The definition of a critical crack to be considered in calculating the k_b value varies from one research study to another. Some researchers reported the data and calculated the crack width for the maximum of three cracks measured at the level of reinforcements (El-Nemr et al. 2016; and Abdelkarim et al. 2019); others considered the maximum of two measured cracks (Kassem et al. 2011; and Benzecry et al. 2021), and some measured and used the first initiated crack (El-Nemr et al. 2013, 2016; Mehany et al. 2022). Gross et al. (2009) monitored crack widths by measuring them at the bottom of the side face. Moreover, McCallum (2013) conducted a series of tests and measured the crack width at the level of reinforcement and the bottom soffit of the beam. This inconsistency in the critical crack width definition is one of the reasons for the large variation in k_b values available in the literature.

To investigate how the selection of the critical crack can affect the results, the k_b values are calculated at 0.7 mm crack width for the average of the three measured side cracks, the first side crack, the first side crack close to the centreline of the beam and the maximum measured crack at the tension face crack and are compared with the k_b value of the maximum crack measured on the side of the beam, as presented in Table 4.4.

As demonstrated in Table 4.4, k_b values differ depending on the critical crack width used in

calculations. The results demonstrate that the first flexural crack, in most cases, is the critical crack among the other flexural cracks. Although in this study, the maximum crack width was considered in the calculations of k_b values to be on the conservative side, the consideration of the maximum crack width might be over-conservative. The results show that the k_b values calculated using the average value of the first three crack widths provided less variation (lower coefficient of variation) compared to the maximum and first crack widths. Moreover, the k_b values calculated based on the average crack width are approximately 10% lower than those calculated based on the maximum crack width. Notably, based on visual observations during the test, the first three cracks were wider than the other cracks developed within the 1000 mm constant moment span of the beams. Moreover, the results demonstrate that the k_b values computed from the extrapolated side crack widths give smaller values than the calculated k_b values from the measured bottom crack widths. Furthermore, the average k_b value of the ribbed bars computed based on the crack measured at the soffit of the beam is less than that of the sand-coated bars, while those computed from extrapolated side crack widths are very similar. It can be concluded that there is a difference between the crack width of the sand-coated and ribbed GFRP bars when the cracks are measured at the tension face. More experimental data are required to confirm this conclusion.

Table 4.4 k_b values for the tested beams using the theoretical strains

Beam	Side crack widths extrapolated to the tension face				Bottom crack	
	Maximum crack	Average of three cracks	First crack	First crack close to the center of the beam	Maximum crack	
3#4-R-c30-N	1.30	1.05	1.30	1.30	-	
3#4-R-c38-N	1.03	0.94	1.03	0.98	-	
3#4-R-c50-N	0.94	0.88	0.90	0.90	-	
2#5-R-c30-N	0.75	0.69	0.61	0.75	-	
2#5-R-c50-N	0.70	0.60	0.53	0.53	-	
2#6-R-c50-N	0.66	0.63	0.66	0.59	-	
2#8-R-c50-N	0.65	0.63	0.65	0.65	-	
3#6-R-c38-N	1.39	1.22	1.39	1.25	-	
3#6-R-c50-N	1.00	0.97	0.99	0.99	-	
3#5-R-c50-s317-N	0.93	0.77	0.93	0.93	-	
3#5-R-c50-s200-N	0.94	0.91	0.94	0.88	-	
3#5-R-c50-s100-N	0.82	0.79	0.82	0.82	-	
2#6-R-c50-H	1.26	1.12	1.26	1.26	1.17	
3#6-R-c50-H	1.03	0.97	1.03	1.00	1.46	
2#6-S-c50-H	1.35	1.26	1.35	1.28	1.35	
3#6-S-c50-H	1.21	1.14	1.21	1.11	2.02	
All NSC ^a	Avg.	0.93	0.84	0.90	0.88	-
	SD	0.24	0.19	0.27	0.24	-
	C.O.V.	25%	23%	30%	27%	-
HSC-R ^b	Avg.	1.15	1.05	1.15	1.13	1.31
	SD	0.16	0.11	0.16	0.18	0.21
	C.O.V.	14%	10%	14%	16%	16%
HSC-S ^c	Avg.	1.28	1.20	1.28	1.20	1.69
	SD	0.10	0.08	0.10	0.12	0.47
	C.O.V.	8%	7%	8%	10%	28%
All R ^d	Avg.	0.96	0.87	0.93	0.92	1.31
	SD	0.24	0.19	0.26	0.24	0.21
	C.O.V.	25%	22%	28%	26%	16%

a. All NSC beams reinforced with ribbed GFRP bars.

b. HSC beams reinforced with ribbed GFRP bars.

c. HSC beams reinforced with sand-coated GFRP bars.

d. NSC and HSC beams reinforced with ribbed GFRP bars.

4.6 Recalibration of k_b values

Shield et al. (2019) recalibrated the k_b values of GFRP bars by applying a rigorous set of criteria to the available database from the literature (Gross et al. 2009; Kassem et al. 2011;

McCallum 2013; and El-Nemr et al. 2013, 2018). Out of more than 200 specimens, only 39 tests were considered. These criteria and the details of the specimens are reported in Shield et al. (2019). Based on the analytical study, they recommended a k_b value of 1.2 for sand-coated bars, and a conservative k_b value of 1.4 was proposed for the ribbed and grooved bars due to the shortage of data.

To recalibrate the k_b values, the experimental results of this study were added to the database of Shield et al. (2019). The results of beam 3#5-R-c50-s100-N are excluded to avoid the effect of the confinement provided by closely spaced stirrups on k_b values. Moreover, one specimen (2#5-c38) taken from Gouda et al. (2022) is added to the database. This specimen developed service moments of 34.4 kN-m, 37.8 kN-m, and 41.5 kN-m at extrapolated crack widths of 0.5, 0.6, and 0.7 mm, respectively (Gouda et al. 2022).

To analyze the data, helically wrapped bars covered with sand-coated bars were treated as sand-coated bars (same as Shield et al. 2019); while the grooved and ribbed bars were analyzed separately (unlike Shield et al. 2019). The new database comprises a total of 91 k_b results, including 39 sand-coated, 46 ribbed, and six grooved results. The k_b values of the 91 data points were computed using the strains from the cracked section analysis. The crack widths measured or extrapolated to the tension face of the beam and k_b values of the tests are presented in Table 4.5.

The results show that sand-coated bar GFRP bars have an average k_b value of 1.16 ± 0.26 (COV of 22%), with a 70th percentile (i.e. average \pm 1.0 standard deviation) k_b value of 1.26. On the other hand, ribbed GFRP bars have an average k_b value of 0.94 ± 0.24 (COV of 26%), with a 70th percentile k_b value of 1.04. Moreover, based on a limited amount of data available, grooved GFRP bars have an average k_b value of 1.32 ± 0.20 (COV of 16%), with a 70th percentile k_b value of 1.48. The results demonstrate that the ribbed bars had a lower k_b value than the sand-coated and grooved GFRP bars. The standard deviation was close and high for the three types of bars. More experimental data are required to provide a reliable k_b value for the GFRP rebar.

Table 4.5 Crack widths and k_b values of the database

Ref.	Surface	Beam ID	Extrapolated crack widths	k_b	Ref.	Surface	Beam ID	Extrapolated crack widths	k_b
A	Sc	G1-6	0.57	1.13	F	Ri	3#4-R-c50-N	0.50	0.82
A	Sc	G1-8	0.47	1.17	F	Ri	2#5-R-c30-N	0.50	0.61
B	Sc	N5#15G2	0.86	1.19	F	Ri	2#5-R-c50-N	0.50	0.57
B	Sc	N6#15G1	0.53	0.68	F	Ri	2#6-R-c50-N	0.50	0.59
B	Sc	H5#15G2	0.69	0.72	F	Ri	2#8-R-c50-N	0.50	0.58
B	Sc	H6#15G1	0.54	1.04	F	Ri	3#6-R-c38-N	0.50	1.27
C	Sc	4#15G1	0.49	0.99	F	Ri	3#6-R-c50-N	0.50	0.96
C	Sc	2#20G1	0.88	1.22	F	Ri	3#5-R-c50-s317-N	0.50	0.87
C	Sc	3#20G1	0.62	1.20	F	Ri	3#5-R-c50-s200-N	0.50	0.85
C	Sc	2#22G1	0.62	0.90	F	Ri	2#6-R-c50-H	0.50	0.99
C	Sc	3#20G2	0.80	1.39	F	Ri	3#6-R-c50-H	0.50	1.36
C	Sc	2#25G1	0.68	1.19	F	Ri	3#4-R-c30-N	0.60	1.17
C	Sc	2#25G2	0.45	0.94	F	Ri	3#4-R-c38-N	0.60	0.97
C	Sc	5#13G1	0.55	0.84	F	Ri	3#4-R-c50-N	0.60	0.85
D	Sc	GX3A	0.69	1.60	F	Ri	2#5-R-c30-N	0.60	0.68
D	Sc	GY3A	0.48	1.26	F	Ri	2#5-R-c50-N	0.60	0.64
D	Sc	GX4A	0.48	1.54	F	Ri	2#6-R-c50-N	0.60	0.64
E	Sc	B1	0.67	1.42	F	Ri	2#8-R-c50-N	0.60	0.64
E	Sc	B1	0.77	1.49	F	Ri	3#6-R-c38-N	0.60	1.30
E	Sc	B6	0.69	1.26	F	Ri	3#6-R-c50-N	0.60	0.97
E	Sc	B6	0.75	1.27	F	Ri	3#5-R-c50-s317-N	0.60	0.89
E	Sc	B1V5	0.77	1.04	F	Ri	3#5-R-c50-s200-N	0.60	0.93
E	Sc	B1V5	0.70	0.95	F	Ri	2#6-R-c50-H	0.60	1.12
E	Sc	B2V5	0.68	1.04	F	Ri	3#6-R-c50-H	0.60	1.28
E	Sc	B2V5	0.74	1.13	F	Ri	3#4-R-c30-N	0.70	1.30
E	Sc	B3V5	0.55	0.96	F	Ri	3#4-R-c38-N	0.70	1.03
E	Sc	B3V5	0.73	1.11	F	Ri	3#4-R-c50-N	0.70	0.94
E	Sc	B4V5	0.78	1.06	F	Ri	2#5-R-c30-N	0.70	0.75
E	Sc	B4V5	0.73	1.11	F	Ri	2#5-R-c50-N	0.70	0.70
E	Sc	B5V5	0.69	0.94	F	Ri	2#6-R-c50-N	0.70	0.66
E	Sc	B5V5	0.55	0.75	F	Ri	2#8-R-c50-N	0.70	0.65
F	Sc	2#6-S-c50-H	0.50	1.12	F	Ri	3#6-R-c38-N	0.70	1.39
F	Sc	3#6-S-c50-H	0.50	1.26	F	Ri	3#6-R-c50-N	0.70	0.99
F	Sc	2#6-S-c50-H	0.60	1.28	F	Ri	3#5-R-c50-s317-N	0.70	0.93
F	Sc	3#6-S-c50-H	0.60	1.28	F	Ri	3#5-R-c50-s200-N	0.70	0.94
F	Sc	2#6-S-c50-H	0.70	1.35	F	Ri	2#6-R-c50-H	0.70	1.25
F	Sc	3#6-S-c50-H	0.70	1.20	F	Ri	3#6-R-c50-H	0.70	1.02
F	Sc	2#6-S-c50-H	0.70	1.35	F	Ri	2#6-R-c50-H	0.70	1.17
F	Sc	3#6-S-c50-H	0.70	2.02	F	Ri	3#6-R-c50-H	0.70	1.46
A	Ri	G2-6	0.62	1.08	B	Gr	N5#15G3	0.84	1.19
A	Ri	G2-8	0.51	1.06	B	Gr	H5#15G3	0.75	1.42
G	Ri	2#5-c38	0.50	0.71	B	Gr	H2#25G3	0.66	1.13
G	Ri	2#5-c38	0.60	0.77	C	Gr	5#15G3	0.49	1.54
G	Ri	2#5-c38	0.70	0.82	C	Gr	2#15G3	0.76	1.09
F	Ri	3#4-R-c30-N	0.50	1.06	C	Gr	2#25G3	0.56	1.53
F	Ri	3#4-R-c38-N	0.50	0.85					

Sc stands for bars with sand-coated, Ri stands for ribbed bars, and Gr stands for grooved bars.

A is (Kassem et al. 2011)

B is (El-Nemr et al. 2013)

C is (El-Nemr et al. 2018)

D is (Gross et al. 2009)

E is (McCallum 2013)

F is Current study

G is (Gouda et al. 2022)

4.7 Conclusions

In this study, a total of 16 GFRP RC beams were tested under four-point loading. The tested beams cover several parameters, including the concrete cover thickness, bar spacing,

reinforcement ratio (bar diameter), confinement effect due to closely spaced transverse reinforcement, concrete strength, and bar surface profile. The k_b coefficient for the tested beams was determined. Based on the experimental and analytical study performed in this study, the following conclusions can be drawn:

- The change in the spacing between the transverse reinforcements in the flexural zone from 317 to 200 mm did not affect the crack width and k_b values of the GFRP RC beams. However, the beams with 100 mm stirrup spacing showed narrower cracks and smaller k_b values than those with 200 mm and 317 mm stirrup spacing.
- Overall, the bar surface profile of the sand-coated or ribbed had a minor effect on the maximum crack width of the beams at the level of reinforcement. However, beams reinforced with ribbed GFRP bars showed narrower cracks than those reinforced with sand-coated GFRP bars.
- Using theoretical β values to extrapolate the crack width of GFRP RC beams may result in unconservative crack width predictions. The level of un-conservatism is higher in the case of sand-coated GFRP bars.
- The k_b values at a 0.7 mm crack width are affected by several cross-sectional parameters, including the concrete cover, reinforcement ratio (bar diameter), and bar spacing. It is also a function of crack width. The higher the crack width is, the higher the k_b value. The k_b value at a 0.7 mm crack width showed a decreasing trend by increasing the concrete cover and bar spacing, while it showed a slight increasing trend in one specimen and significant increasing trend in other specimens by increasing the concrete compressive strength. However, the change in the k_b values with respect to the change in those parameters was different between the specimens. Moreover, the stabilization of cracks happens at higher crack widths in the HSC beams.
- The experimental results show that the k_b values depend on the definition of the critical crack used in the analysis.
- The crack widths of this study and those available in the literature were analyzed to recalibrate the k_b values. The results show that sand-coated bar GFRP bars have an average k_b value of 1.16 ± 0.26 (COV of 22%), with a 70th percentile k_b value of 1.26. On the other hand, ribbed GFRP bars have an average k_b value of 0.94 ± 0.24 (COV of 26%), with a

70th percentile k_b value of 1.04. Moreover, based on a limited amount of data available, grooved GFRP bars have an average k_b value of 1.32 ± 0.20 (COV of 16%), with a 70th percentile k_b value of 1.48.

It should be noted that the above conclusions are based on the limited data available in the literature and the tests performed in this research. More experimental studies are recommended to focus on the effect of different parameters, including the concrete cover, number of reinforcement layers, concrete strength, and bar surface profiles on the k_b values. It is also recommended that the code committees develop a standard test method to evaluate the crack width of GFRP-RC elements. More experimental results are required to verify the conclusions of this research.

Chapter 5

Flexural and serviceability behaviour of concrete beams reinforced with ribbed GFRP bars

5.1 Abstract

Glass fibre-reinforced polymer (GFRP) bars are used as internal reinforcement in many structural applications. The structural performance of GFRP reinforced concrete elements is dependent on the physical and mechanical properties of GFRP reinforcement. There is a lack of experimental data on the flexural behaviour of concrete beams reinforced with ribbed GFRP bars. This study evaluates the flexural strength and serviceability performance of concrete beams reinforced with ribbed GFRP bars. A total of 11 GFRP reinforced concrete beams with dimensions of 4350×400×200 mm (length×height×width) were constructed and tested under a four-point loading test setup. The main test parameters were the concrete cover, reinforcement ratio, bar spacing, and confinement due to the transverse reinforcement in the bending zone. The results quantify the effect of increasing the reinforcement ratio on the increase in the ultimate capacity and the reduction in deflection at the service and ultimate stages. In addition, the results showed that the increase in the confinement in the bending zone due to closely spaced stirrups resulted in a higher ductility index and ultimate capacity with no considerable effect on the post-cracking stiffness of the beams. Moreover, based on the experimental results, the accuracy of deflection equations available in design codes and guidelines is evaluated and discussed.

5.2 Introduction

One of the significant shortcomings of steel reinforcing bars is their susceptibility to corrosion, which reduces the service life of reinforced concrete (RC) structures subjected to aggressive environments such as bridges, marine structures, and tunnels. The use of glass fibre-reinforced polymer (GFRP) bars in such structures provides several advantages because of their superior durability and lower strength-to-weight ratio than steel rebars.

GFRP bars are produced with different physical and mechanical properties. They have several types of surface profiles, such as helically wrapped, sand-coated, grooved, and ribbed (Solyom and Balázs 2020). Many studies have shown that the surface profile significantly affects the bond performance and cracking behaviour of GFRP RC members (Kassem et al. 2011, McCallum 2013, and El-Nemr et al. 2016). Nonetheless, El-Nemr et al. (2018) stated that the bar surface profile has no effect on the flexural strength and deflection behaviour of GFRP-RC members.

The design of GFRP-RC members is primarily based on fulfilling the serviceability requirements comprising the crack width and deflection, as well as creep rupture limits rather than the ultimate limit states due to the lower elastic modulus of GFRP bars compared with steel reinforcement (Baena et al. 2009, El-Nemr et al. 2016, and Benzecry et al. 2021). El-Nemr et al. (2018) found that manufacturing GFRP bars with an elastic modulus greater than 60 GPa was efficient in obtaining an optimum design with the lowest production cost.

Another concern in designing GFRP-RC members is the lack of ductility due to the linear elastic behaviour of the GFRP material up to failure without prominent plastic deformation or considerable energy absorption (ACI 440.1R (2015), and Solyom and Balázs 2018). Vijay and GangaRao (2001) stated that at the service stage, over-reinforced beams demonstrated lower deflections than under-reinforced beams because of the increase in FRP bar stiffness and reduced strains. They deduced that the reinforcement ratio in the GFRP-RC beams should be greater than 1.4 times the balanced reinforcement ratio (ρ_b) to fulfill the serviceability requirements. Xue et al. (2016) performed a statistical analysis on 173 GFRP-RC flexural beams and concluded that the upper limit for the reinforcement ratio in the transition zone should be taken as $1.5\rho_b$.

To quantify the flexural ductility of FRP-RC beams, Jaeger et al. (1997) defined the deformability index by computing the curvature ratio at the ultimate stage to that at the service

stage. The Canadian Highway Bridge Design Code CSA S6 (2014) adopted the concept of deformability and set a lower limit of 4.0 for rectangular sections and 6.0 for T-sections.

Few studies have investigated the effect of using non-sand-coated GFRP bars on the flexural and serviceability performance of RC members (Kassem et al. 2011 and Abdelkarim et al. 2019). Kassem et al. (2011) found that the sand-coated bars had a superior cracking performance by having a greater number of cracks than the deformed bars. Abdelkarim et al. (2019) investigated the effect of the reinforcement ratio, bar diameter, and change in concrete strength on the flexural behaviour of eight concrete beams reinforced with ribbed GFRP bars. The results showed that the ribbed bars provided moment resistance in agreement with CSA S806 (2012) and ACI 440.1R (ACI 2015). In addition, the normal-strength concrete beams exhibited higher curvatures than the high-strength concrete beams. Abdelkarim et al. (2019) proposed a curvature-based method for calculating the ductility indices of GFRP-RC beams.

However, the effect of other parameters, including the change in bar spacing, confinement from transverse reinforcement, and concrete cover on the flexural strength, ductility, curvatures, moment capacity, and deflection behaviour of the concrete beams reinforced with ribbed GFRP bars, need to be investigated.

Thus, this research aims to quantify the effect of different parameters, including the clear concrete cover to GFRP reinforcement (30, 38, and 50 mm), bar spacing, bar diameter (13, 15, 20, and 25 mm), reinforcement ratio, and confinement from transverse reinforcement on the flexural strength, serviceability performance, and deformability of RC beams. The results of this research may enrich the experimental dataset available on GFRP-RC beams and provide a better understanding of the behaviour of ribbed GFRP bars.

To achieve the objectives of this research, several concrete beams reinforced with ribbed GFRP bars have been constructed and tested. The test results are presented and discussed in terms of failure mode, moment capacity, deflection, curvatures, concrete and GFRP reinforcement strains, and deformability.

5.3 Experimental program

In this study, a total of 11 RC beams were constructed and tested monotonically up to failure. The beams were designed to cover several parameters that would provide sufficient data for investigating their effect on the behaviour of GFRP-RC beams and help in assessing the limits and design provisions proposed by the codes and standards.

5.3.1 Materials

All the beams were cast using two batches of ready-mix normal-strength concrete with a target 28-day compressive strength of 35 MPa. The concrete mix proportions are presented in Table 5.1. The concrete compressive strength (f'_c) was measured at the testing day of the beams (± 1 week) by testing five 100×200 mm concrete cylinders per ASTM C39/C39M (ASTM 2021). In addition, three 150×150×500 mm concrete prisms and five 100×200 mm concrete cylinders were tested to determine the modulus of rupture (f_r) as per ASTM C78/C78M (ASTM 2021) and splitting tensile strength (T) as per ASTM C496/C496M (ASTM 2017), respectively. The concrete characteristics are listed in Table 5.2. The measured compressive strength was 40.0 ± 1.44 MPa, and 35.8 ± 1.13 MPa for the two concrete batches. The concrete slump of both concrete batches was measured to be 101 mm according to ASTM C143/C143M (ASTM 2020).

Table 5.1 Concrete mix design

Target concrete strength	Ordinary Portland cement	Fine sand	Coarse aggregate	Free water	W/C ratio
MPa	kg/m ³	kg/m ³	kg/m ³	liter/m ³	%
32	405	839	937	166	0.41
32	377	862	942	171	0.45

High modulus (Grade III) ribbed GFRP bars were utilized as tensile reinforcing bars. The GFRP bars had a ribbed surface profile and were manufactured by a Canadian producer. The ribbed profile of the GFRP bars aims to simulate an interlocking behaviour similar to the steel bars that would provide high bond performance between the GFRP bars and the surrounding concrete. The GFRP bar diameters utilized in reinforcing the beams were #4 (13 mm), #5 (15 mm), #6 (20 mm), and #8 (25 mm). Figure 5.1 shows the surface profile of the GFRP rebar along with a representative closeup of a representative bar for each size, with a ruler near the cross-section. Notably, the

diameters shown in Figure 5.1 include the rib height. According to ASTM D7205/D7205M (2021), five GFRP bars per diameter were tested to obtain the tensile strength, ultimate elongation, and modulus of elasticity. The ultimate stress and elastic modulus of the GFRP bars were calculated based on the nominal bar cross-sectional area, ASTM D7957/D7957M (2017). The measured mechanical properties and nominal cross-sectional properties of GFRP bars are presented in Table 5.3.

Table 5.2 Details of the tested beams

Beam Designation	f'_c	f_r	T	Clear cover to GFRP bar	Center-to-center bar spacing	GFRP total area (A_f)	Reinforcement ratio (ρ_f)	Balanced reinforcement ratio (ρ_{fb})*
	MPa	MPa	MPa	mm	mm	mm ²	%	%
3#4-c50	40.0	5.3	3.8	50	57.4	387	0.563	0.384
2#5-c30	40.0	5.3	3.8	30	111.5	398	0.550	0.370
2#5-c38	40.0	5.3	3.8	38	111.5	398	0.562	0.370
2#5-c50	40.0	5.3	3.8	50	111.5	398	0.582	0.370
2#6-c50	35.8	5.0	3.6	50	108.3	568	0.835	0.366
2#8-c50	35.8	5.0	3.6	50	102.0	1020	1.511	0.360
3#6-c38	35.8	5.0	3.6	38	54.2	852	1.217	0.366
3#6-c50	35.8	5.0	3.6	50	54.2	852	1.253	0.366
3#5-c50-s317	35.8	5.0	3.6	50	55.8	597	0.873	0.352
3#5-c50-s200	35.8	5.0	3.6	50	55.8	597	0.873	0.352
3#5-c50-s100	35.8	5.0	3.6	50	55.8	597	0.873	0.352

*Balanced reinforcement ratio (ρ_{fb}) is calculated as per ACI 440.1R (2015).

Grade 400 steel bars were used as top compression reinforcement and transverse stirrups. The steel bars were 10 M deformed steel with a nominal diameter of 11.3 mm, cross-sectional area of 100 mm², and yield strength (f_y) of 400 MPa. The properties of the steel bars were obtained from the datasheet provided by the supplier.

Table 5.3 Properties of ribbed GFRP bars

Bar type	Designated diameter	Nominal cross-sectional area	Nominal diameter	Tensile strength	Elastic modulus	Ultimate strain
		mm ²	mm	MPa	GPa	%
GFRP	#4	129	12.7	1049 ± 10	60.4 ± 0.4	1.74
	#5	199	15.9	1087 ± 10	60.4 ± 0.5	1.80
	#6	284	19.1	1052 ± 8	61.0 ± 0.9	1.72
	#8	510	25.4	1090 ± 11	61.9 ± 0.4	1.76
Steel	10 M	100	11.3	400	200	-

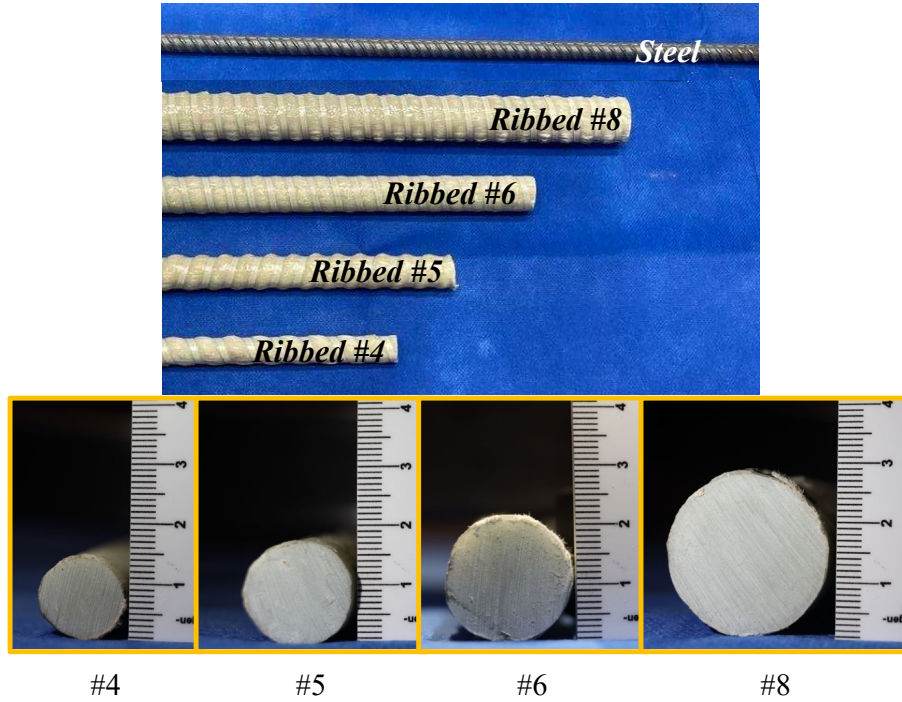


Figure 5.1 Surface deformation of Grade III ribbed GFRP bars and 10M steel bars

5.3.2 Design of test specimens

In this study, a total of 11 simply-supported RC beams were tested up to failure under a four-point bending scheme. The total length of the beams was 4350 mm, and the width and height of the cross-section were 200 mm and 400 mm, respectively.

The beams were designed according to ACI 440.1R (2015) to fail by concrete crushing before tensile rupture of the GFRP bars. The ACI 440.1R (2015) design of the over-reinforced sections requires that the reinforcement ratio (ρ_f) be 1.4 times the balanced reinforcement ratio (ρ_{fb}). ρ_f and ρ_{fb} can be calculated from Eq. (5.1) and (5.2), as follows:

$$\rho_f = \frac{A_f}{b d} \quad (5.1)$$

$$\rho_{fb} = \alpha_1 \beta_1 \frac{f'_c}{f_{fu}} \frac{E_f \epsilon_{cu}}{E_f \epsilon_{cu} + f_{fu}} \quad (5.2)$$

where A_f is the total area of the GFRP bars in mm²; b is the width of the rectangular cross-section in mm; d is the distance from the extreme compression fibres to the center of the tensile reinforcement in mm; α_1 is the ratio of the average of the equivalent stress block to the concrete

compressive strength, taken as 0.85; and β_1 is a factor converting the actual stress diagram along the cross-section to an equivalent rectangular stress block. β_1 is taken as 0.85 for concrete strengths up to 28 MPa, and reduces by 0.05 for each 7 MPa increment in f'_c , and shall not be less than 0.65; f'_c is the specified compressive strength of the concrete in MPa; E_f is the GFRP reinforcement elastic modulus in MPa; f_{fu} is the GFRP bars design tensile strength in MPa, and calculated by multiplying the guaranteed tensile strength (defined as the mean tensile strength of a sample of test specimens minus three times the standard deviation) of the GFRP bars by the environmental reduction factor ($C_E = 1$, in this study); and $\varepsilon_{cu} = 0.003$ is the ultimate concrete strain in the compression.

The balanced reinforcement ratio in CSA S806 (2012) is calculated by using Eq. (5.2) with minor differences from ACI 440.1R (2015). The ε_{cu} in CSA S806 (2012) is taken as 0.0035; in addition, α_1 and β_1 are calculated by Eq. (5.3) and (5.4),

$$\alpha_1 = 0.85 - 0.0015f'_c \geq 0.67 \quad (5.3)$$

$$\beta_1 = 0.97 - 0.0025f'_c \geq 0.67 \quad (5.4)$$

The beams were reinforced in the shear span by 10M steel stirrups spaced at 100 mm on the center to preclude any shear failure before flexural failure. The confinement effect from the transverse reinforcement was avoided in the middle bending zone of the beam by placing the stirrups at 317 mm and 316 mm spacing. The stirrups in this zone act as hangers for the top reinforcement.

Table 5.2 presents the beams with their properties and reinforcement ratios. The clear concrete covers from the concrete bottom fibres to the edge of the GFRP reinforcement were taken as 30, 38, and 50 mm. The side and top covers measured from the concrete surface to the edge of the stirrups were 25 mm for all the beams. The elevation, cross-sectional dimensions, and reinforcement details of the beams are shown in Figure 5.2. The nomenclatures of the beams are in the form of A#B-c, where letter A stands for the total number of GFRP tensile reinforcements; letter B refers to the reinforcement size; and letter c denotes the clear concrete cover to the GFRP bar in millimetres. Beams 3#5-c50-s317, 3#5-c50-s200, and 3#5-c50-s100 have the same nomenclature as the other beams except for the notations s317, s200, and s100, which represent the center-to-center spacing between the transverse reinforcement in the constant moment zone.

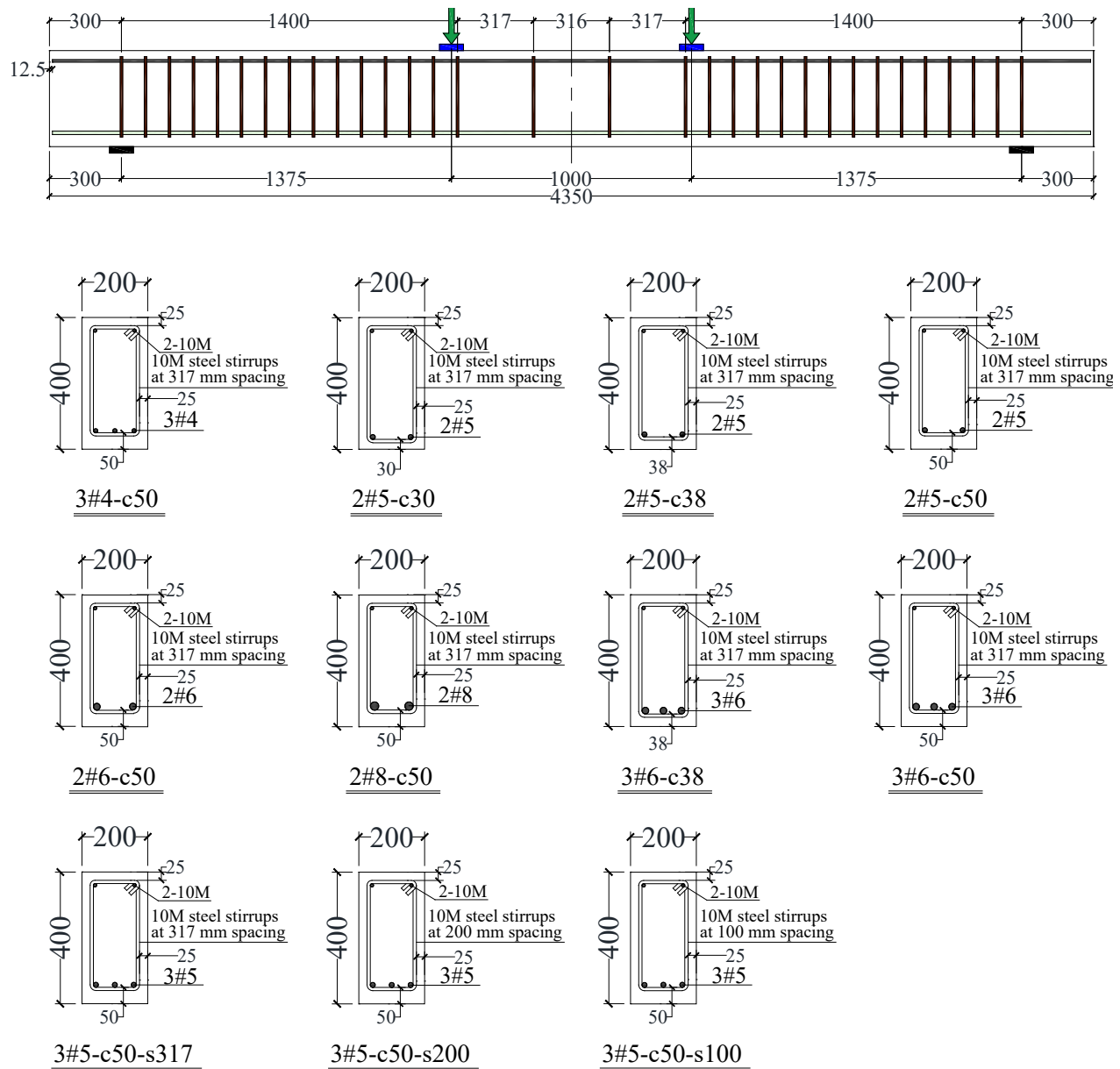


Figure 5.2 Elevation and cross-sectional details of the beams (Note: all dimensions are in mm)

5.3.3 Test procedure, setup and instrumentation

The beam tests started four months after concrete pouring and lasted for a total of four weeks. The concrete beams, cylinders, and prisms were cured by wetting their external surfaces for one week. The specimens were kept under the same laboratory environmental conditions until the day of testing. The beams were loaded at a rate of 0.6 mm/min until the initiation of the first flexural crack to facilitate visual crack initiation monitoring. After that, the loading rate was increased to 1.2 mm/min until failure.

The test setup and the locations of the instrumentation and strain gauges are presented in Figure 5.3. The beams were tested under a four-point loading scheme. The beams were simply-supported with a span of 3750 mm between the centreline of the supports and 1000 mm between the centerline of the loading points. The shear span to depth ratio (a/h) was 3.44. The load was applied by a hydraulic cylinder under displacement control. The load values were measured by a 500 kN load cell with an accuracy of ± 0.05 kN. The test setup consisted of a compression platen directly connected to a strong steel distributor beam. The loading points were steel rods and rested on rubber sheets to prevent load concentration on the concrete surface.

The deflection was measured using five potentiometers placed at the center of the beams (2 potentiometers), under the loading points, and at the midpoint between the loading point and the hinged support, as shown in Figure 5.3. The potentiometers had a total stroke of 500 mm with a nonlinearity of less than $\pm 0.1\%$ at their full stroke.

The strains in the GFRP bars and top concrete compression fibres were measured using strain gauges, as depicted in Figure 5.3: at least two strain gauges with 2 mm gauge length were installed on each GFRP reinforcement, one gauge at the center of the bar and another gauge at the location of the loading point; and two concrete strain gauges with 84 mm gauge length were attached at the mid-span section and in the vicinity of one of the loading points. The bars were ground using two grades of grinding discs with a diameter of 20 mm. After that, the surface was neutralized and cleaned according to the instructions provided by the strain gauge manufacturer. The strain gauges were bonded to the GFRP bar surface using a compatible adhesive following the instructions of the strain gauge manufacturer. Special care was taken to prevent any over-grinding that would affect the longitudinal mechanical properties of the bar, as shown in Figure 5.3.

During the testing, the width of the first three flexural cracks was measured until failure. For each crack, the initial crack width was measured using a handheld microscope, and then an LVDT was installed to measure the progress of crack width with the load. Moreover, certain steps were undertaken to facilitate the visual observations of cracking and crack mapping, where the beam was checked before testing for any pre-existing cracks (no pre-existing cracks were found). In addition, before cracking, the beams were loaded at 0.6 mm/min, which is one-half of the recommended rate by CSA S806 (2012). This loading rate helped two persons in front of the beam to better observe the initiation of the flexural cracks.

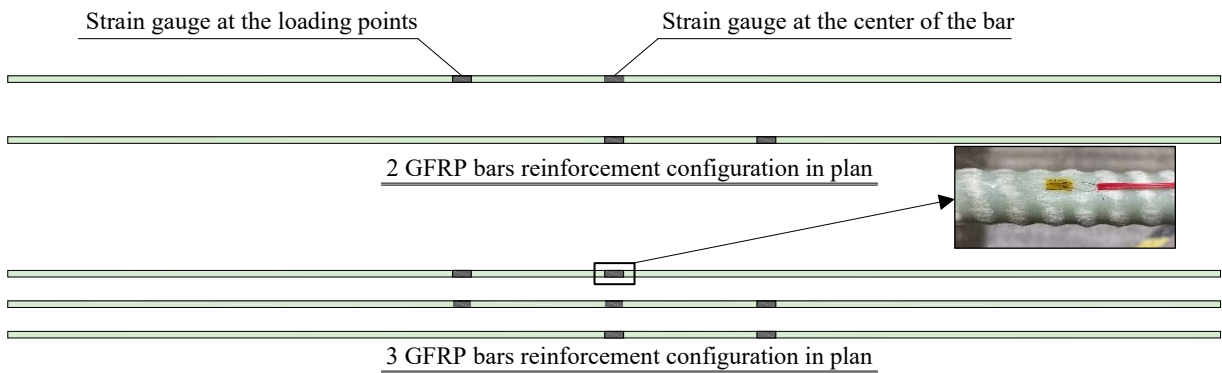
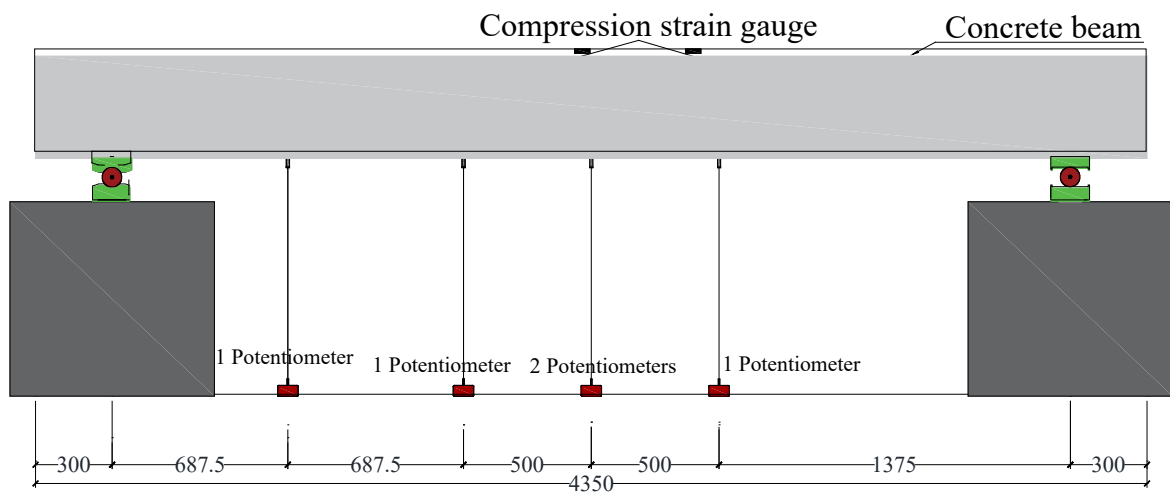
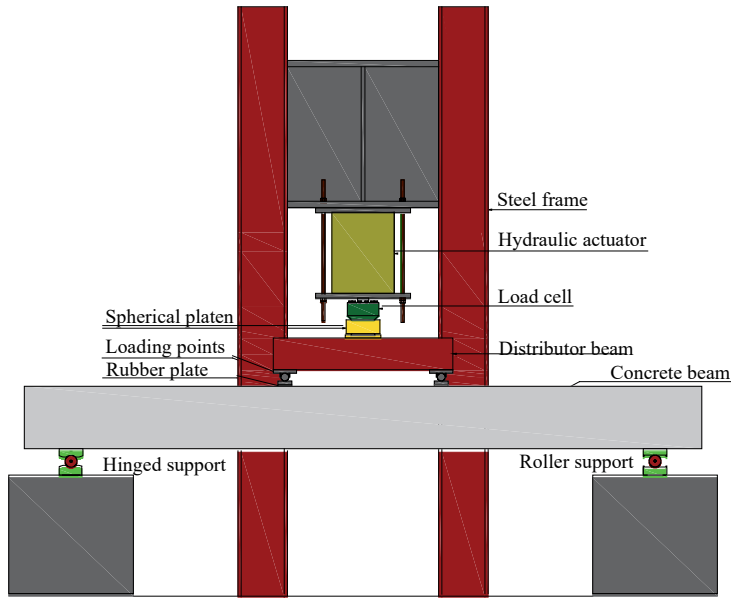


Figure 5.3 The test setup and instrumentations (Note: all dimensions are in mm)

5.4 Discussion of results

In this section, the results of the tested GFRP-RC beams are presented. Different parameters are discussed separately to quantify their influence on the flexural behaviour of the beams at the serviceability and ultimate states.

5.4.1 Cracking moments and moments at different serviceability limits

From the moment-deflection relationships, the stiffness of the beams was linear and approximately constant up to the cracking load. The cracking load was recorded during the test and was validated from the drop in the load and the change in the slope of the moment-deflection graphs. The experimental cracking moment was calculated based on the applied load and the moment due to the self-weight of the beam (3.375 kN-m). The results showed that the cracking moments of the beams varied from 14.47 to 19.58 kN-m. The theoretical cracking moment is directly related to the concrete tensile strength, which is a function of the concrete compressive strength (f'_c), as shown in Eq. (5.5) and Eq. (5.6):

$$M_{cr} = f_r I_g / y_b \quad (5.5)$$

$$f_r = 0.6 \sqrt{f'_c} \quad \text{CSA S806 (2012)} \quad (5.6a)$$

$$f_r = 0.62 \sqrt{f'_c} \quad \text{ACI 440.1R (2015)} \quad (5.6b)$$

$$f_r = 0.4 \sqrt{f'_c} \quad \text{CSA S6 (2014)} \quad (5.6c)$$

where M_{cr} is the cracking moment in N-mm; f_r is the concrete tensile strength in MPa; y_b is the distance from the extreme tensile concrete fibres to the neutral axis ($h/2$) in mm; and I_g is the gross moment of inertia of the cross-section of the beam in mm⁴.

The experimental and predicted cracking moments are presented in Table 5.4. The results show that CSA S806 (2012) and ACI 440.1R (2015) had mean experimental-to-predicted cracking moment ratios ($M_{cr-exp}/M_{cr-Theo.}$) of 0.89 ± 0.09 and 0.86 ± 0.09 , respectively. These results illustrate that CSA S806 (2012) and ACI 440.1R (2015) are slightly greater than the experimental results. The reduction in the experimental cracking moment might be attributed to the strains developed in concrete because of the restraints due to shrinkage from the internal reinforcement and the natural variation in the actual modulus of rupture (Bischoff and Gross 2011a). CSA S6 (2014), on the other hand, showed highly conservative results with an average

$M_{cr-exp}/M_{cr-Theo}$ of 1.34 ± 0.14 .

A comparison was conducted between the moments at the serviceability limits proposed by the different studies, as well as design guidelines and standards. Bischoff et al. (2009) used a service load limit as one-third of the beam nominal flexural moment capacity to evaluate deflection equations. Yost et al. (2003), Kassem et al. (2011), El-Nemr et al. (2013), El-Nemr et al. (2016), and El-Nemr et al. (2018) utilized 30% of the nominal moment ($0.3M_n$) as a service limit. The serviceability limits are defined in the standards and guidelines to maintain the serviceability of the GFRP-RC flexural members within acceptable margins. ACI 440.1R (2015) sets a crack width acceptable range between 0.4 mm and 0.7 mm. For bridge applications, CSA S6 (2014) limits the crack width to 0.5 mm for members subjected to aggressive environments and 0.7 mm for other members, while AASHTO LRFD for GFRP (2018) has a crack width limit of 0.7 mm. The design manual of ISIS Canada, ISIS-M03 (2007), recommends a strain limit of 2000 $\mu\epsilon$ under service loads to keep the crack width less than or equal to 0.5 mm. The CSA S806 (2012) standards and ACI 440.1R (2015) guidelines limit the stress in the GFRP reinforcement under sustained loads to $0.25f_{fu}$ and $0.20f_{fu}$, respectively, to prevent creep rupture of GFRP bars. Recent research by Benmokrane et al. (2019) proposed a creep rupture limit for GFRP bars of $0.30f_{fu}$.

Table 5.4 Results of the tested beams

Designated beam	CSA S806 (2012)						ACI 440.1R (2015)				CSA S6 (2014)	
	Experimental		Theoretical		$M_{cr-exp.} / M_{cr-theo.}$	M_n / M_r	Theoretical		$M_{cr-exp.} / M_{cr-theo.}$	M_n / M_r	Theoretical	$M_{cr-exp.}$
	M_{cr}	M_n	M_{cr}	M_r			M_{cr}	M_r			M_{cr}	$M_{cr-theo.}$
kN-m	kN-m	kN-m	kN-m			kN-m	kN-m			kN-m		
3#4-c50	17.7	118	20.2	112	0.88	1.06	20.9	101	0.85	1.16	13.5	1.31
2#5-c30	16.4	125	20.2	123	0.81	1.02	20.9	111	0.78	1.12	13.5	1.21
2#5-c38	14.5	119	20.2	118	0.71	1.01	20.9	108	0.69	1.11	13.5	1.07
2#5-c50	16.4	104	20.2	112	0.81	0.93	20.9	102	0.78	1.02	13.5	1.21
2#6-c50	16.4	115	19.1	121	0.86	0.95	19.8	113	0.83	1.02	12.8	1.29
2#8-c50	19.6	138	19.1	148	1.02	0.93	19.8	139	0.99	0.99	12.8	1.54
3#6-c38	17.1	149	19.1	148	0.89	1.01	19.8	138	0.86	1.08	12.8	1.34
3#6-c50	18.1	133	19.1	141	0.95	0.94	19.8	132	0.92	1.00	12.8	1.42
3#5-c50-s317	19.3	128	19.1	124	1.01	1.03	19.8	116	0.98	1.10	12.8	1.52
3#5-c50-s200	17.8	124	19.1	124	0.93	1.00	19.8	116	0.90	1.07	12.8	1.40
3#5-c50-s100	17.6	143	19.1	124	0.92	1.15	19.8	116	0.89	1.23	12.8	1.38
Average					0.89	1.00			0.86	1.08		1.34
Standard Deviation					0.09	0.07			0.09	0.07		0.14
Coefficient of variation (%)					10.11	6.57			10.46	6.82		10.45

- M_{cr} is the cracking moment in kN-m; M_n is the experimental nominal moment capacity of the beams based on applied load; and M_r is the theoretical resistance moment of the beams.

- The self-weight of the beams was included in computing the experimental and theoretical cracking moments.

- The experimental and theoretical failure moments (M_n and M_r) were provided by excluding the moment due to self-weight.

- The theoretical failure moments of the CSA S6 (2014) are the same as computed by CSA S806 (2012).

Table 5.5 presents the moments at different serviceability limits, including the beam self-weight. Figure 5.4 shows the relation between the reinforcement ratio (ρ_f) on the horizontal axis and the moment (M_s) on the vertical axis. As illustrated, the moments at different serviceability limits increased with increasing reinforcement ratio, which is in agreement with the mechanics of reinforced concrete sections. The rate of moment increase at $0.3M_n$ was significantly less than the other moments at the different serviceability limits. Moreover, the $2000 \mu\epsilon$ service limit provided the most conservative moments for all the beams. For the beams with a concrete cover of 30 mm, it was found that the moments monitored at $0.3M_n$ and $0.20f_{fu}$ were slightly higher than the moments recorded at 0.5 mm crack width. On the other hand, increasing the concrete cover to 50 mm resulted in conservative moments at $0.20f_{fu}$ and $0.3M_n$ compared with the monitored moments at the 0.5 mm limit. Figure 5.4 also shows that the moments recorded at $0.30f_{fu}$ provided the highest value among the other limits. Given that in most design cases, the bending moments due to the sustained loads are lower than those of the service loads, it can be concluded that for the beams tested in this study, the creep rupture stress limit of $0.30f_{fu}$ will not govern the design if the crack width limit of 0.5 mm is to be checked.

The relationships in Figure 5.5 illustrate that the experimental moments at $0.3M_n$, $2000 \mu\epsilon$, and $0.25f_{fu}$ serviceability limits showed good agreement with the predicted moments with a decreasing trend by increasing the concrete cover. It is important to note that the strains measured using strain gauges are affected by their position with respect to the nearby cracks. This might be one of the reasons for the difference between the experimental and predicted moments at the serviceability limits, as shown in Figure 5.5.

Table 5.5 Moments of the beams at different serviceability limits

Designated beam	Moments (kN-m)						<i>c/d</i>				
	$0.3M_n$	$2000\mu\epsilon$	$0.20f_{fu}$	$0.25f_{fu}$	$0.30f_{fu}$	0.5 mm	Exp.	CSA (2012)	ACI (2015)	Exp./CSA	Exp./ACI
3#4-c50	38.7	28.8	34.9	37.8	43.8	30.9	0.172	0.187	0.180	0.92	0.96
2#5-c30	40.8	18.6	27.7	32.5	37.7	44.8	0.207	0.185	0.179	1.12	1.16
2#5-c38	39.1	17.8	30.2	37.0	43.2	34.4	0.175	0.187	0.180	0.94	0.97
2#5-c50	34.5	17.7	28.1	33.2	38.9	35.5	0.202	0.190	0.183	1.06	1.10
2#6-c50	38.0	25.8	37.4	46.2	55.6	47.9	0.200	0.232	0.220	0.86	0.91
2#8-c50	44.7	41.1	64.9	83.6	98.5	84.1	0.267	0.298	0.283	0.90	0.94
3#6-c38	48.0	34.0	57.4	72.3	86.6	52.4	0.282	0.272	0.258	1.04	1.09
3#6-c50	43.1	30.8	48.8	60.3	72.8	53.6	0.258	0.276	0.262	0.93	0.98
3#5-c50-s317	41.6	28.5	45.25	55.5	66.9	43.0	0.175	0.236	0.224	0.74	0.78
3#5-c50-s200	40.5	24.2	39.95	49.9	58.6	44.1	0.202	0.236	0.224	0.86	0.90
3#5-c50-s100	46.3	23.2	32.6	41.0	48.5	53.5	0.205	0.236	0.224	0.87	0.92
Average										0.93	0.97
Standard deviation										0.11	0.11
Coefficient of variation (%)										11.6	11.0

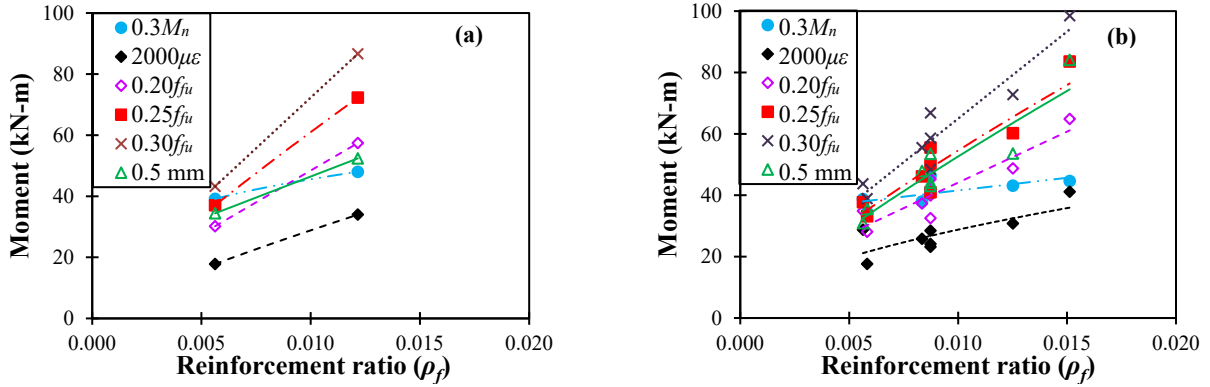


Figure 5.4 Relationship between moments at different serviceability limits and reinforcement ratio at the concrete cover of (a) 30 mm and (b) 50 mm

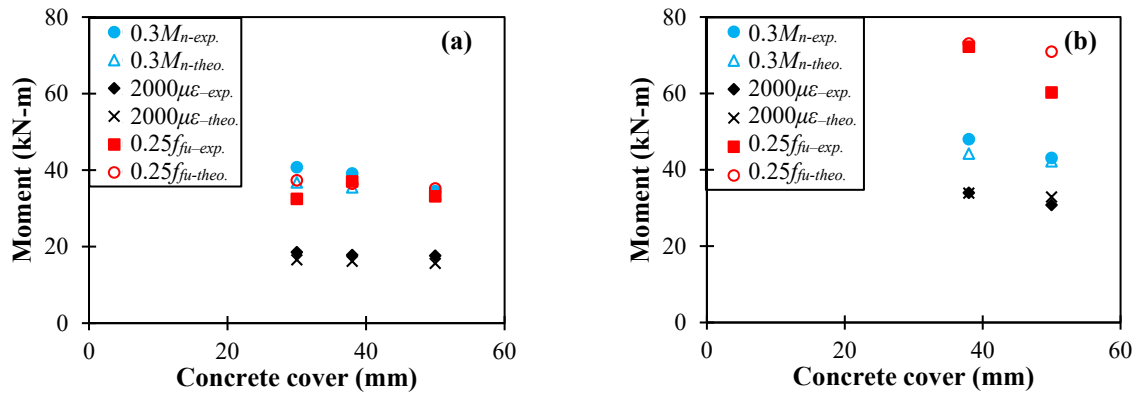


Figure 5.5 Relation between experimental and theoretical moments at different serviceability limits and concrete cover for beams reinforced with (a) 2#5 and (b) 3#6

5.4.2 Failure modes and flexural resistance

As expected, all the beams failed by the crushing of top concrete fibres. As shown in Figure 5.6, it was observed that the depth of the crushed compression concrete block increased by increasing the reinforcement ratio, as monitored in beams 3#5-c50-s317 and 2#8-c50.

The top steel bars were subjected to buckling at the concrete crushing stage, as shown in Figure 5.6. This was attributed to inadequate lateral support for compression reinforcements due to the wide spacing between the stirrups in the middle bending zone. The influence of confinement and lateral support provided by stirrups appeared in beam 3#5-c50-s100, where the concrete crushing occurred gradually with an imperceptible loss in energy without premature failure of compression reinforcements. The strain in the GFRP bottom bars increased until compression

The theoretical nominal flexural resistance, without considering reduction factors, predictions by CSA S806 (2012) and ACI 440.1R (2015) are presented in Table 5.4. The results show that the moment capacities anticipated by CSA S806 (2012) and ACI 440.1R (2015) agree well with the experimental results. The average ratio between the experimental and theoretical capacities for CSA S806 (2012) and ACI 440.1R (2015) were 1.00 and 1.08, with standard deviations of 0.07 and 0.07, respectively. Even though the two anticipations were close to the experimental moment capacities, the CSA S806 (2012) predictions were more accurate than the ACI 440.1R (2015). The difference in the capacity predictions arises from the difference in the ultimate concrete strains, 0.0035 for CSA S806 (2012) and 0.003 for ACI 440.1R (2015), and the variation in the α_1 and β_1 factors.

Figure 5.7(a) shows the relationship between the ratio of the neutral axis depth to the depth of tension reinforcement (c/d) versus the developed theoretical stress in the GFRP reinforcement at failure calculated using the CSA S806 (2012) and ACI 440.1R (2015) equations. It is clear from Figure 5.7(a) that as the c/d ratio increases, the stress in the GFRP bars at failure decreases. The reason behind this was that when the reinforcement ratio increases, the height of the compression block increases, and the stresses in the GFRP bars decrease accordingly. This observation agreed with the experimental observations of this study and was also reported by Kassem et al. (2011) and El-Nemr et al. (2018). Figure 5.7(a) shows that the developed stress at failure from CSA S806 (2012) at the same c/d was higher than the maximum calculated stress using ACI 440.1R (2015). In addition, as the c/d ratio increases, the moment capacity increases, as depicted in Figure 5.7(b). Table 5.5 shows good agreement between the theoretical and experimental results of the c/d ratios. The mean experimental to theoretical c/d ratio was 0.93 ± 0.11 for CSA S806 (2012) and 0.97 ± 0.11 for ACI 440.1R (2015). The experimental and theoretical results are very close, with a difference of less than 10.0%. Nonetheless, the ACI 440.1R (2015) showed a slightly closer prediction than CSA S806 (2012).

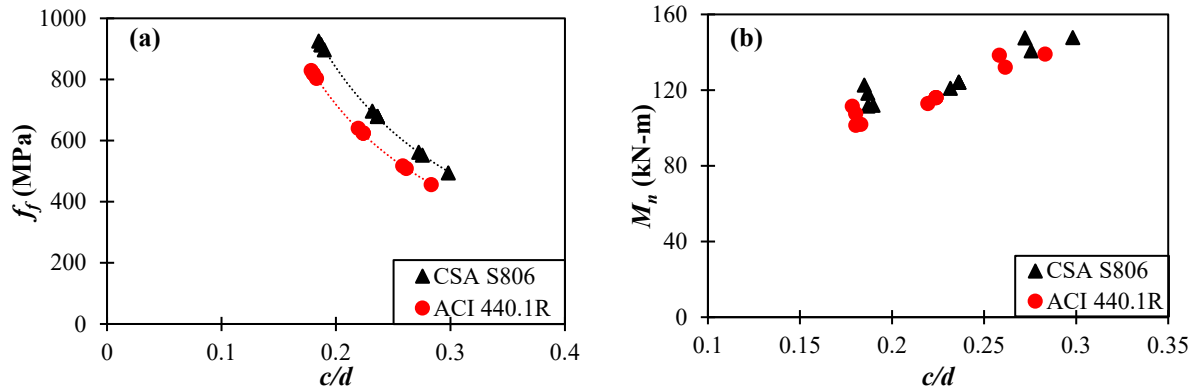


Figure 5.7 Relation between the ratio of the theoretical values of c/d and (a) maximum theoretical stress in the GFRP reinforcement and (b) theoretical moment resistance

5.4.3 Strains in reinforcement and concrete

The moment versus maximum GFRP bar tensile strain and moment versus maximum concrete compression strain relationships are shown in Figure 5.8(a-c). Table 5.6 provides the experimental GFRP bar tensile strains at failure, if recorded, and at 90% of the ultimate loads for all the tested beams. It should be noted that the GFRP strain values are the mean value of the two strain gauge readings in the mid-span section for two different bars.

In general, the moment strain relations were bilinear with a proportional increment with the applied moment. The concrete and GFRP strains started initially with a sharp linear trend in all the beams until the initiation of the first flexural crack. After that, the strains increased with a lower plateau slope. It was noticed that there was a sudden jump in strain in some beams after the first crack, which is attributed to the formation of the crack in the vicinity of the strain gauge. The experimental measurements listed in Table 5.6 confirm that the measured concrete strains at failure, if recorded, were greater than the ACI 440.1R (2015) and CSA S806 (2012) limits (3000 and 3500 $\mu\epsilon$, respectively).

The results showed that the GFRP reinforcement tensile strains decreased by increasing the reinforcement ratio at the same load level. Furthermore, the moment-strain relations in Figure 5.8(c) illustrate that beams 3#5-c50-s317 and 2#6-c50 were close, which shows that maintaining the reinforcement ratio and changing the bar spacing provides similar strains at the same load levels. Beam 3#5-c50-s100 reached $\epsilon_{f-90\%}$ of 18739 $\mu\epsilon$, close to the ultimate strain of the bar. This beam failed by concrete crushing, followed by GFRP bar rupture. This is explained by the effect

of confinement in the middle bending zone that enhanced the beam capability for energy absorption and increased the compression block capacity in parallel with depleting the bar tensile capacity until the bar ruptured. In comparison, beam 3#5-c50-s317 attained a strain ($\epsilon_{f-90\%}$) of 9794 $\mu\epsilon$, reaching approximately 50% of the bar ultimate strength.

The comparison in Figure 5.8(d) illustrates that the experimental strain readings for the three sample beams (2#5-c50, 2#6-c50, and 2#8-c50) are in good agreement with the theoretical values at the service stage. This validation can provide a good indication that the experimental strains could be reliable in the computation of the ductility indices for deformability. It should also be noted that the recorded strains of GFRP bars are dependent on the position of the strain gauge with respect to nearby cracks, which could justify the discrepancies between the experimental and theoretical strains.

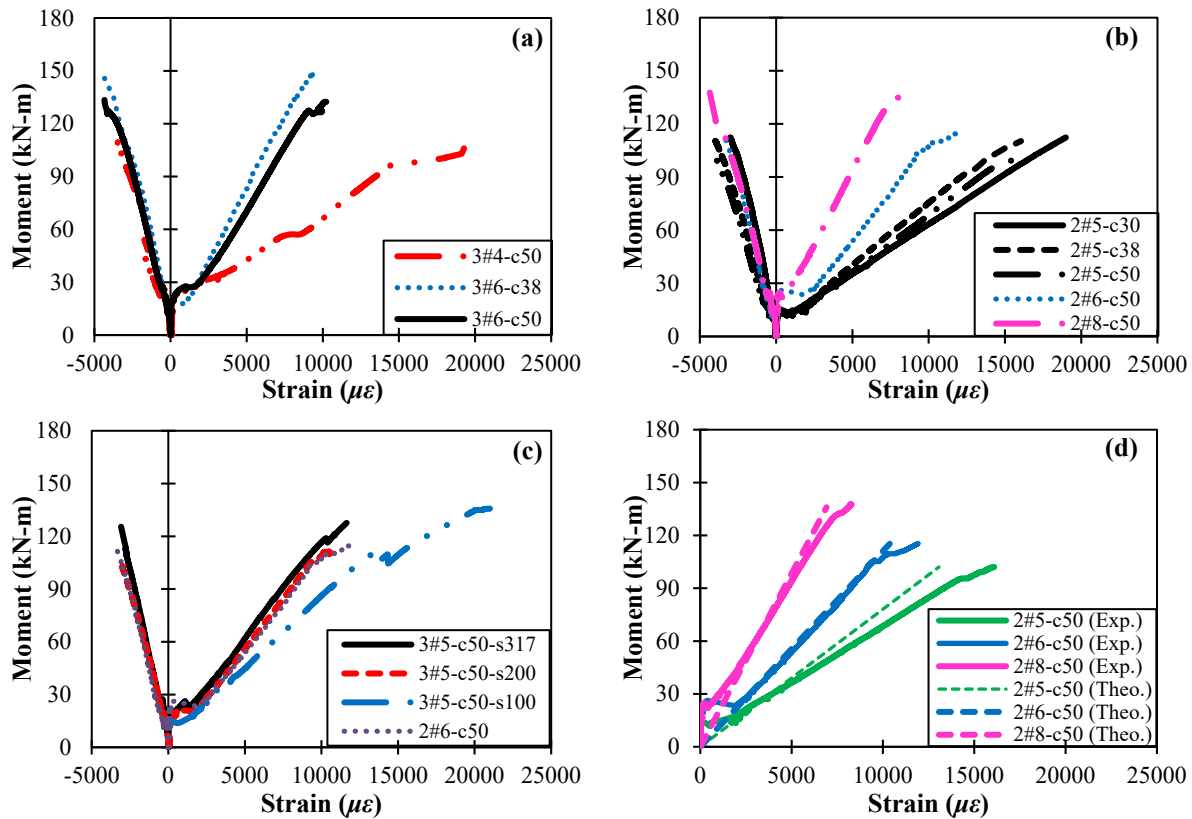


Figure 5.8 Concrete and GFRP reinforcement strains of the tested beams: (a-c) measured concrete and GFRP strains; and (d) comparison between the experimental and theoretical GFRP strains for beams 2#5-c50, 2#6-c50, and 2#8-c50

Table 5.6. Curvature and strains of the tested beams

Beam	$\varphi_{0.3M_n}$ (rad/mm)	$\varphi_{0.5mm}$ (rad/mm)	φ_{2000} (rad/mm)	$\varphi_{0.25f_{fu}}$ (rad/mm)	φ_{1000} (rad/mm)	$\varphi_{0.20f_{fu}}$ (rad/mm)	$\varphi_{90\%}$ (rad/mm)	φ_u (rad/mm)	$\varepsilon_{c,90\%}$ $\mu\varepsilon$	$\varepsilon_{f,90\%}$ $\mu\varepsilon$	ε_{cu} $\mu\varepsilon$	ε_{fu} $\mu\varepsilon$
3#4-c50	1.52E-05	8.25E-06	9.77E-06	1.60E-05	8.93E-06	1.50E-05	6.59E-05	-	-3377	19276	-	-
2#5-c30	1.70E-05	1.92E-05	6.52E-06	1.43E-05	2.26E-05	1.16E-05	6.07E-05	-	-3004	18989	-	-
2#5-c38	1.57E-05	1.35E-05	7.46E-06	1.63E-05	1.24E-05	1.31E-05	5.37E-05	-	-3816	15200	-	-
2#5-c50	1.58E-05	1.65E-05	6.51E-06	1.71E-05	1.15E-05	1.44E-05	5.11E-05	5.88E-05	-3598	13871	-4017	16085
2#6-c50	1.23E-05	1.58E-05	8.09E-06	1.64E-05	1.22E-05	1.33E-05	3.61E-05	4.52E-05	-3020	9265	-3463	11920
2#8-c50	8.84E-06	1.91E-05	8.64E-06	1.98E-05	7.77E-06	1.49E-05	3.21E-05	3.72E-05	-3996	6821	-4323	8214
3#6-c38	1.02E-05	1.14E-05	7.67E-06	1.69E-05	1.11E-05	1.33E-05	3.39E-05	3.94E-05	-3742	8143	-4487	9338
3#6-c50	1.12E-05	1.43E-05	8.15E-06	1.72E-05	1.08E-05	1.39E-05	3.47E-05	-	-3462	8362	-	-
3#5-c50-s317	1.12E-05	1.17E-05	7.74E-06	1.71E-05	1.28E-05	1.35E-05	3.69E-05	4.31E-05	-2830	9794	-3085	11641
3#5-c50-s200	1.24E-05	1.37E-05	7.33E-06	1.68E-05	1.40E-05	1.34E-05	3.88E-05	-	-3031	10227	-	-
3#5-c50-s100	-	-	-	-	-	-	-	-	-	18739	-	-

- $\varphi_{0.3M_n}$, $\varphi_{0.5mm}$, φ_{2000} , $\varphi_{0.25f_{fu}}$, φ_{1000} , $\varphi_{0.20f_{fu}}$, $\varphi_{90\%}$ and φ_u are the curvatures at $0.3M_n$, 0.5 mm crack width, 2000 $\mu\varepsilon$ in GFRP reinforcement, 0.25 f_{fu} , 1000 $\mu\varepsilon$ in concrete top fibres, 0.20 f_{fu} , 90% of the ultimate load of the beam, and failure.
- $\varepsilon_{c,90\%}$ is the concrete strain at 90% of the beam ultimate load; $\varepsilon_{f,90\%}$ is the GFRP reinforcement strain at 90% of the beam ultimate load; ε_{cu} is the concrete ultimate strain; and ε_{fu} is the GFRP reinforcement ultimate strain.

5.4.4 Curvature

Figure 5.9 displays the relationship between the moment and curvature for some tested beams. The graphs illustrate the maximum curvature each beam attained at the midspan section. The curvature was calculated by Eq. (5.7)

$$\varphi_m = \frac{\varepsilon_c + \varepsilon_f}{d} \quad (5.7)$$

where φ_m is the curvature of the beam at an applied moment; ε_c is the concrete strain at the same moment; ε_f is the corresponding GFRP tensile strain; and d is the distance from the extreme compression fibres to the centroid of the GFRP tension reinforcement in mm. It is worth noting that the concrete and GFRP strain gauges in some beams stopped reading before beam failure. Accordingly, to unify the comparisons, the curvature for all the beams was calculated at 90% of the failure load. Table 5.6 represents the curvature for the tested beams at failure (M_n), $0.9M_n$, $0.3M_n$, and 0.5 mm crack width.

It was observed that by increasing the reinforcement ratio from beam 2#5-c50 to beams 2#6-c50 and 2#8-c50, the maximum curvature decreased with a stiffer behaviour, as shown in Figure 5.9. Furthermore, comparing beams 2#5-c30 and 2#5-c50, it was found that the curvature slightly decreased by decreasing the concrete cover. The reason behind this might be that at the same load level, as the distance from the extreme concrete compression fibres to the center of the reinforcement increases, the induced strains in the GFRP reinforcement increase. Hence, the resulting ratio ε_c/c becomes greater for beams with a larger concrete cover.

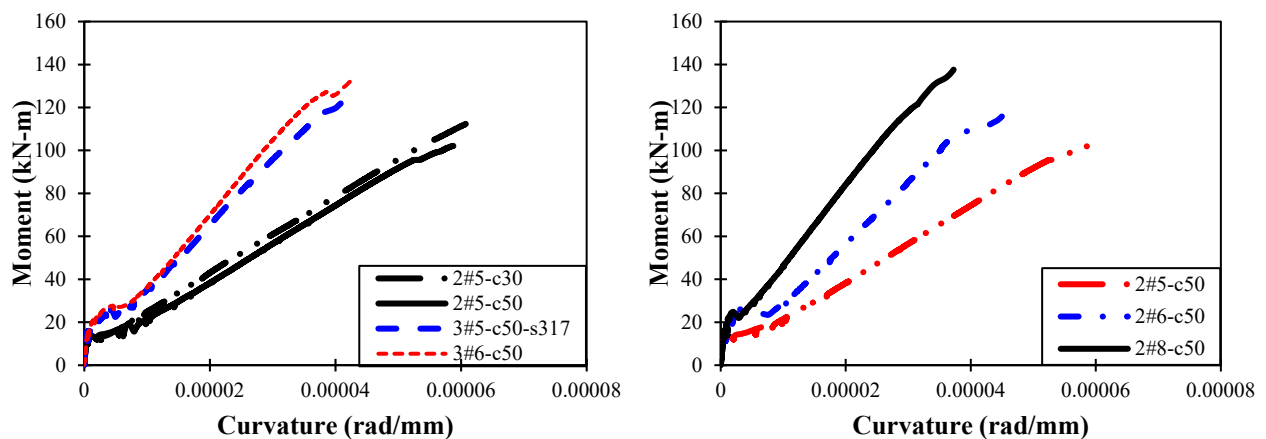


Figure 5.9 Moment-curvature relationships of the tested beams

5.4.5 Evaluation of Deformability

The ductility of the GFRP-RC beams cannot be defined by the conventional approaches for steel-RC beams since the GFRP bars perform linearly elastic up to failure without any yielding sign. Consequently, two main approaches, namely, energy-based and deformation-based approaches, are used in the literature for predicting ductility.

3.4.5.1 Energy-based approach

In this approach, ductility is defined as the capacity of flexural members to absorb energy. Naaman and Jeong (1995) proposed that the ductility index (μ_e) can be defined as the ratio between the total energy and the elastic energy, as illustrated in Figure 5.10, using Eq. (5.8),

$$\mu_e = \frac{1}{2} \left(\frac{E_t}{E_e} + 1 \right) \quad (5.8)$$

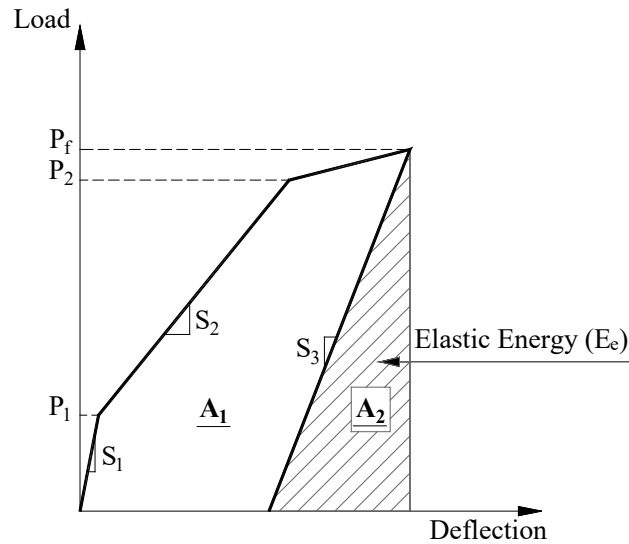


Figure 5.10 Energy-based approach for ductility computation

where E_t is the total absorbed energy calculated as the entire area under the load-deflection relationship ($A_1 + A_2$) and E_e is the elastic absorbed energy computed as the area in the elastic zone below line S_3 drawn from the failure load (P_f) to the line intersection with the deflection axis (represents A_2), as displayed in the idealized load-deflection relation in Figure 5.10. The slope of the line S_3 is defined through the points P_1 , P_2 , S_1 , and S_2 and can be calculated from Eq. (5.9),

$$S_3 = [P_1 S_1 + (P_2 - P_1) S_2] / P_2 \quad (5.9)$$

where S_3 is the unloading slope of the elastic region from the failure point; P_1 is the cracking load;

S_1 is the initial slope of the loading curve; P_2 is theoretically the load at the beginning of concrete compression crushing in the case of over-reinforced sections; and S_2 is the secant slope of the moment-deflection curve after cracking. The moment-deflection relation of some beams is bilinear; in that case, P_2 can be taken as P_f . The ductility index (μ_e) values are summarized in Table 5.7, and the results are displayed in Figure 5.11.

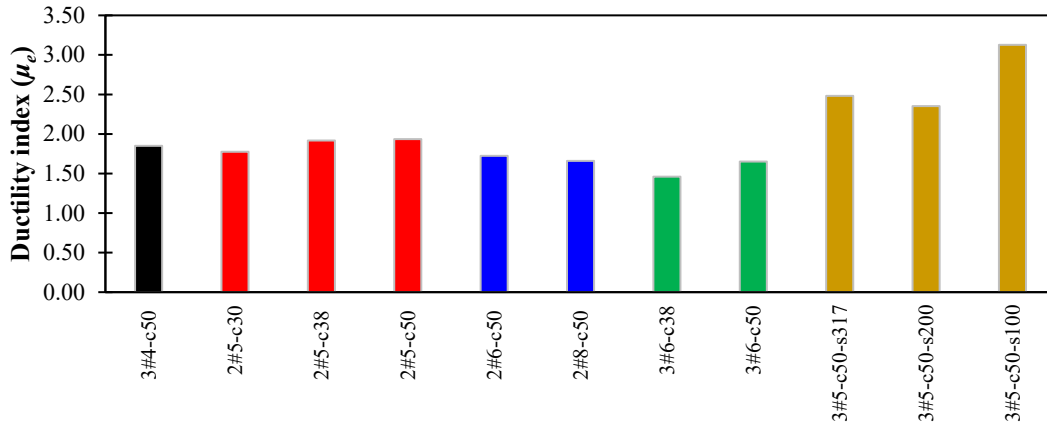


Figure 5.11 Ductility indices using the energy-based approach

3.4.5.2 Deformation-based approach

In this approach, introduced by Jaeger et al. (1997), the strength is defined through the strength factor C_s , whereas the deformability is introduced by the deflection or curvature factors (C_d or C_c , respectively). The factors C_s , C_d , and C_c are calculated by Equations 5.10(a), (b), and (c). These factors are expressed as the ratio of the ultimate moment, deflection, and curvature, respectively, to the corresponding values at the concrete compressive strain of $1000 \mu\epsilon$, which is considered nearly the beginning of the concrete inelastic deformation (Jaeger et al., 1997). The deformability index can be computed from Eq. (5.11).

$$C_s = \frac{M_{ult}}{M_{\epsilon=0.001}} \quad (5.10a)$$

$$C_d = \frac{\Delta_u}{\Delta_{\epsilon=0.001}} \quad (5.10b)$$

$$C_c = \frac{\varphi_u}{\varphi_{\epsilon=0.001}} \quad (5.10c)$$

$$\mu_d = C_s \times C_d \text{ (or } C_c) \quad (5.11)$$

The CSA S6 (2014) standard adopted this approach and defined the deformability by factor J as expressed by Eq. (5.12), as follows:

$$J = \frac{M_{ult} \psi_{ult}}{M_c \psi_c} \quad (5.12)$$

where M_{ult} is the ultimate moment capacity; ψ_{ult} is the curvature at M_{ult} ; M_c is the moment at a concrete compressive strain of 0.001; and ψ_c is the curvature at M_c . In this study, the deflection and curvature ductility indices were computed at 2000 $\mu\epsilon$, 0.5 mm crack width, 1000 $\mu\epsilon$, $0.25f_{frrpu}$, and $0.20f_{frrpu}$. It is important to note that the ultimate curvature of 6 out of 11 beams could not be calculated, as some strain gauges stopped working before beam failure. To unify the comparisons, the deformation-based ductility index utilizing the curvature factor of all beams is calculated for curvature at $0.9M_n$. The results are illustrated in Figure 5.12 and summarized in Table 5.7.

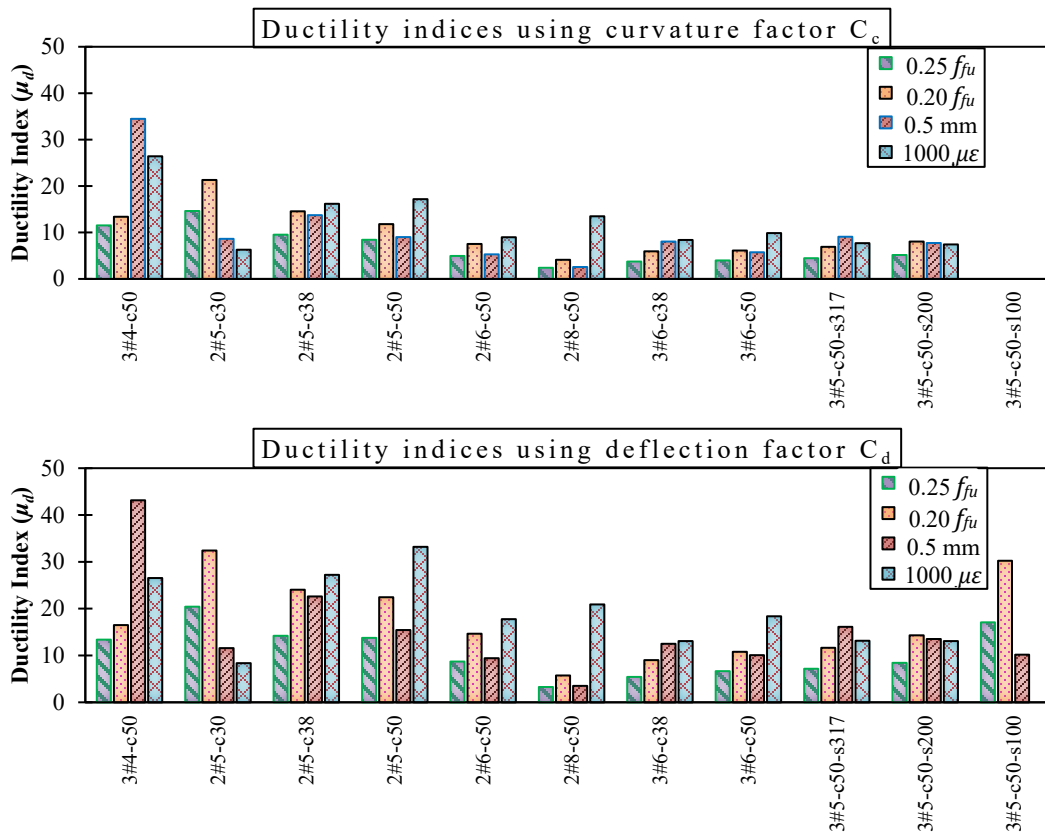


Figure 5.12 Ductility indices using the deformation-based approach

3.4.5.3 Discussion of deformability results

The deformability predictions using the energy-based method showed a clear trend for some parameters, as revealed in Figure 5.11 and Table 5.7. The ductility index slightly increased with increasing concrete cover, as demonstrated by comparing beams (2#5-c30, 2#5-c38, and 2#5-c50) and (3#6-c38 and 3#6-c50). This might be attributed to the slight decrease in deflection for beams

with larger concrete cover. This resulted in a corresponding lower elastic energy, hence a higher ratio of E_t/E_e and greater deformability by increasing the concrete cover. Moreover, the ductility index using the energy-based method decreased when the reinforcement ratio and the bar diameter increased, which can be observed in beams (2#5-c50, 2#6-c50, and 2#8-c50) and (3#4-c50 and 2#8-c50). It was evident that increasing the confinement in the bending zone provided higher ductility indices than the less confined beams, as demonstrated by beam 3#5-c30-s100. It is worth mentioning that beam 3#5-c30-s100 manifested the highest ductility indices among the other beams using the energy-based method with a value of 3.13 due to the influence of transverse reinforcement confinement in the flexural zone that resulted in increasing the amount of absorbed energy before failure. However, comparing beams with a similar reinforcement ratio but different bar spacing shows no clear trend. Although the ductility index of beam 2#6-c50 was considerably lower than that of 3#5-c50-s317 (1.72 and 2.48, respectively), there was no significant difference between the ductility indices of beams 2#5-c50 and 3#4-c50 (1.94 and 1.85, respectively).

Comparisons conducted between the ductility indices calculated using the deformation-based method in Figure 5.12 show that this ductility index is sensitive to the level of stress of GFRP bars. In other words, for a given cross-section, this ductility index will change depending on the member geometry and loading conditions. The deformation-based approach is the product of factors C_s and C_c (or C_d). These factors are calculated as the ratio of the moment and curvature (or deflection) at the ultimate stage to the corresponding moment and curvature (or deflection) at the service stress level. Therefore, an increase in the service load level (GFRP stress) will reduce the ductility index.

In general, the deformation-based ductility index utilizing the curvature or deflection factor showed no clear trend for different parameters. The comparison between the different ductility indices using the curvature approach at $2000 \mu\epsilon$, 0.5 mm , $0.25f_{fu}$, and $1000 \mu\epsilon$, as illustrated in Figure 5.12, indicates that the $2000 \mu\epsilon$ limit provided the most consistent ductility indices with a trend for some parameters compared to the other limits. The results showed that for the beams tested in this study, the service load at a GFRP strain of $2000 \mu\epsilon$ was conservative at all reinforcement ratios and lower than the moments at a 0.5 mm crack width.

Table 5.7 Ductility indices calculated using the energy and deformation-based approaches

Beam	Energy-based approach (μ_e)	Curvature factor (C_c)					Deflection factor (C_d)				
		0.5 mm	2000 $\mu\epsilon$	0.25 f_{fu}	1000 $\mu\epsilon$	0.20 f_{fu}	0.5 mm	2000 $\mu\epsilon$	0.25 f_{fu}	1000 $\mu\epsilon$	0.20 f_{fu}
3#4-c50	1.85	34.5	24.9	11.5	26.4	13.4	43.1	29.4	13.4	26.5	16.5
2#5-c30	1.78	8.6	56.4	14.6	6.3	21.3	11.6	148.2	20.4	8.4	32.4
2#5-c38	1.92	13.7	43.4	9.5	16.2	14.6	22.6	107.7	14.2	27.2	24.1
2#5-c50	1.94	9.0	41.5	8.4	17.2	11.8	15.5	82.0	13.8	33.2	22.5
2#6-c50	1.72	5.3	17.9	4.9	9.0	7.5	9.4	42.5	8.7	17.8	14.7
2#8-c50	1.66	2.6	11.2	2.4	13.5	4.1	3.5	16.9	3.3	20.9	5.8
3#6-c38	1.46	8.0	17.4	3.7	8.4	5.9	12.5	24.5	5.4	13.1	9.0
3#6-c50	1.65	5.8	16.5	4.0	9.9	6.1	10.1	31.9	6.7	18.4	10.8
3#5-c50-s317	2.48	9.1	19.2	4.5	7.7	6.9	16.1	36.9	7.2	13.2	11.7
3#5-c50-s200	2.35	7.8	24.4	5.2	7.4	8.1	13.5	56.0	8.4	13.1	14.3
3#5-c50-s100	3.13	-	-	-	-	-	10.2	86.6	17.1	-	30.3

3.4.5.4 Comparison with steel RC beams

The steel design provisions generally recommend designing the flexural members as under-reinforced sections to allow the members to achieve relatively large curvatures before failure due to the yielding of steel reinforcement in tension. Newhook et al. (2002) showed that the deformability indices of rectangular concrete sections reinforced with Grade 400 steel bars calculated using the curvature deformation-based approach range from 50 at low reinforcement ratios to less than 4 at the balanced reinforcement ratio. The study showed that the deformability index values decreased as the reinforcement ratio increased. The deformability indices of the steel RC sections reached a value of 4 at approximately 85% of the balanced reinforcement ratio. CSA S6 (2014) defined the deformability as the curvature deformation-based approach (J) at a concrete strain of $1000 \mu\epsilon$ that shall be at least 4.0 for rectangular sections. It is clear from Table 5.7 that the deformability values using the curvature deformation-based approach for the tested beams were greater than 4.0, with minimum and maximum values of 6.30 and 26.42, respectively.

5.4.6 Deflection behaviour

The moment versus mid-span deflection relations are displayed in Figure 5.13, and the maximum deflection values for the tested beams are provided in Table 5.8. All the graphs included the moment due to the self-weight of the beams. The mid-span deflection represents the average readings of the two mounted potentiometers. The deflection relations commenced with a relatively high stiffness up to the first crack; after that, there was a drop in the load at the instant of crack initiation accompanied by a decrease in the beam stiffness. The moment-deflection curves illustrate that the flexural stiffness of the beam after cracking increases by increasing the reinforcement ratio (ρ_f). In addition, comparing specimens 2#5-c50 and 2#8-c50 and specimens 3#4-c50 and 3#6-c50 confirms that the maximum deflection at failure decreases by increasing the reinforcement ratio.

In general, it was observed that the behaviour of the beams with a lower reinforcement ratio was bilinear (approximately $\leq 0.80\%$), whereas the higher reinforcement ratio beams exhibited trilinear behaviour up to failure, as depicted in Figure 5.13(a) and (c) for beams 3#6-c50, 2#6-c50, and 2#8-c50. In beams with higher reinforcement ratios, the deflection became nonlinear after the appearance of compression microcracks until the cracks in the top fibres merged and a block of

compression concrete was disintegrated.

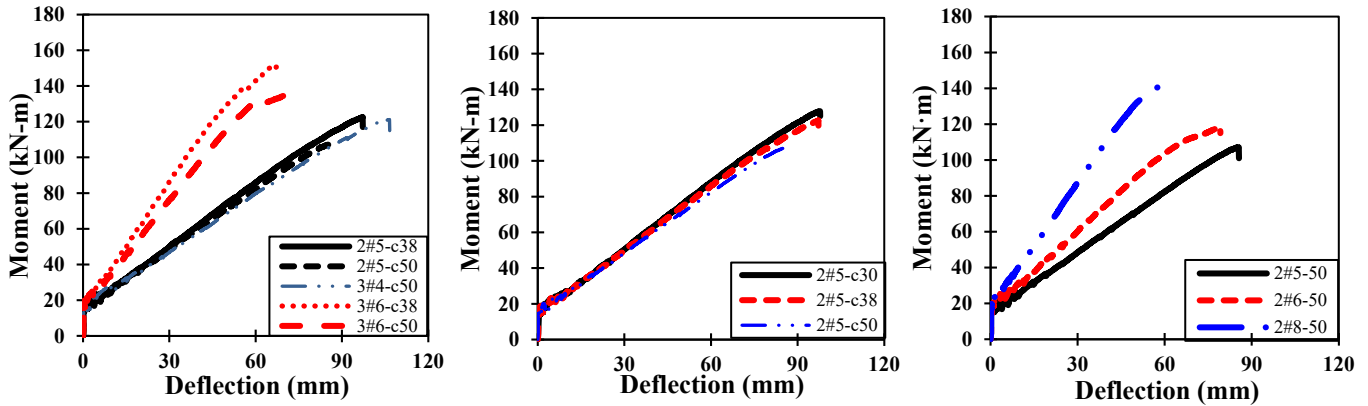


Figure 5.13 Deflection versus applied moment for all GFRP-RC beams (note: the graphs shown are considering the moment due to the self-weight)

5.4.6.1 Evaluation of theoretical deflection equations

The CSA S806 (2012) and ACI 440.1R (2015) deflection predictive equations are shown in Eq. 5.13 and Eq. 5.14, respectively. Table 5.8 provides the experimental and theoretical deflections at the service limit of $0.33M_n$, including the self-weight of the beams. The theoretical deflections were calculated using M_{cr} and $0.8M_{cr}$. The $0.8M_{cr}$ was chosen by ACI 440.1R-06 (2006) to provide a reasonable fit with the experimental data (Bischoff et al. 2009). Furthermore, Bischoff et al. (2009) recommended $0.8M_{cr}$ to provide a safety factor against the possibility of cracking due to temperature and shrinkage over the long term for load cases where the values of the moment at the service stage are marginally less than the unrestrained cracking moment.

CSA S806 (2012)

$$\delta_{max} = \frac{PL^3}{24E_c I_{cr}} \left[3\left(\frac{a}{L}\right) - 4\left(\frac{a}{L}\right)^3 - 8\eta\left(\frac{L_g}{L}\right)^3 \right] \quad 5.13(a)$$

$$I_{cr} = \frac{bd^3}{3} k^3 + n_f A_f d^2 (1 - k)^2 \quad 5.13(b)$$

$$\eta = 1 - \frac{I_{cr}}{I_g} \quad 5.13(c)$$

$$L_g = a \frac{M_{cr}}{M_a} \quad 5.13(d)$$

ACI 440.1R (2015)

$$\delta_{max} = \frac{Pa}{24E_c I_e} [3L^2 - 4a^2] \quad 5.14(a)$$

$$I_e = \frac{I_{cr}}{1 - \gamma \left(\frac{M_{cr}}{M_a}\right)^2 \left[1 - \frac{I_{cr}}{I_g}\right]} \leq I_g \quad 5.14(b)$$

$$\gamma = 1.72 - 0.72 \left(\frac{M_{cr}}{M_a}\right) \quad 3.14(c)$$

where P is the acting load in kN; M_a is the applied moment at the acting load in kN-m; δ_{max} is the maximum mid-span deflection at the applied load in mm; L is the support-to-support span in mm; E_c is the concrete modulus of elasticity in MPa, taken as $4500\sqrt{f'_c}$ per CSA S806 (2012) and $4700\sqrt{f'_c}$ per ACI 318-19 (ACI 2019); I_e is the effective moment of inertia in mm^4 ; a is the shear span measured from the center of the support to the point load in mm; I_{cr} is the transformed moment of inertia of the equivalent cracked concrete section in mm^4 ; and b and d are defined before in Eq. (5.1); k is the ratio between the neutral axis and reinforcement depths; n_f is the ratio between the GFRP and the concrete elastic modulus; A_f is defined previously in Eq. (5.1); η is the ratio of the difference between the gross and cracked moment of inertia to the gross moment of inertia; L_g is the distance measured from the support to the M_{cr} point in a simply supported beam in mm; I_g and M_{cr} are defined in Eq. (5.5); and γ is the factor accounting for the variation in stiffness along the member length.

Table 5.8 presents the ratio of experimental-to-predicted deflections ($\delta_{exp.}/\delta_{pred.}$) for CSA S806 (2012) and ACI 440.1R (2015) at $0.33M_n$. The results indicate that the CSA S806 (2012) equation manifests good agreement with the experimental service deflections with a mean $\delta_{exp.}/\delta_{pred.}$ of 0.99 ± 0.04 . The ACI 440.1R (2015) equation underestimates the deflection prediction with a mean $\delta_{exp.}/\delta_{pred.}$ of 1.29 ± 0.09 .

Bischoff and Gross (2011b) highlighted that the variations in the concrete elastic modulus have a minimal influence on the computed deflection in contrast to the reduction in the M_{cr} due to the shrinkage and temperature effects. They also pointed out that the restrained cracking moment could vary from 90% to 60% of M_{cr} depending on the reinforcement ratio and amount of free shrinkage. As expected, reducing the cracking moment to $0.8M_{cr}$ showed a marginal change for the results of the CSA S806 (2012) equation with a mean $\delta_{exp.}/\delta_{pred.}$ of 0.97 ± 0.04 . In contrast, the ACI 440.1R (2015) equation was noticeably affected by such a reduction, providing a yet unconservative mean $\delta_{exp.}/\delta_{pred.}$ of 1.16 ± 0.06 . Using I_{cr} instead of the effective moment of inertia, the ACI 440.1R (2015) deflection predictions showed conservative results with a mean $\delta_{exp.}/\delta_{pred.}$ of 0.95 ± 0.04 .

Table 5.8 Experimental and theoretical deflection of the tested beams

Beam	Measured deflection (mm)	CSA (2012)			ACI (2015) (Eq. 5.14(b))			ACI (2015) (Eq. 5.15 for $m = 2$)		ACI (2015) (Eq. 5.15 for $m = 3$)	
		$\delta_{exp.}/\delta_{pred.}$ at $0.33M_n$			$\delta_{exp.}/\delta_{pred.}$ at $0.33M_n$			$\delta_{exp.}/\delta_{pred.}$ at $0.33M_n$		$\delta_{exp.}/\delta_{pred.}$ at $0.33M_n$	
		Failure	$0.33M_n$	M_{cr}	$0.8M_{cr}$	M_{cr}	$0.8M_{cr}$	I_{cr}	M_{cr}	$0.8M_{cr}$	M_{cr}
3#4-c50	107	25.7	1.00	0.98	1.39	1.22	0.95	1.14	1.05	1.04	1.00
2#5-c30	98	25.5	1.06	1.04	1.42	1.26	1.02	1.18	1.10	1.09	1.05
2#5-c38	97	24.1	1.00	0.98	1.38	1.21	0.96	1.13	1.05	1.04	1.00
2#5-c50	86	20.9	0.94	0.91	1.41	1.19	0.88	1.11	1.00	1.00	0.93
2#6-c50	79	17.4	0.93	0.92	1.25	1.11	0.89	1.04	0.97	0.96	0.93
2#8-c50	59	13.8	0.98	0.97	1.20	1.11	0.94	1.05	1.01	1.00	0.98
3#6-c38	68	15.8	0.99	0.98	1.18	1.11	0.96	1.05	1.02	1.01	0.99
3#6-c50	72	16.0	1.06	1.05	1.32	1.21	1.02	1.14	1.09	1.08	1.06
3#5-c50-s317	83	18.4	0.94	0.92	1.19	1.08	0.91	1.02	0.97	0.96	0.93
3#5-c50-s200	80	18.2	0.96	0.94	1.23	1.11	0.92	1.05	0.99	0.98	0.95
3#5-c50-s100	117	21.8	0.99	0.98	1.21	1.12	0.97	1.06	1.02	1.01	0.99
Average (mm)			0.99	0.97	1.29	1.16	0.95	1.09	1.02	1.01	0.98
Standard deviation (mm)			0.04	0.04	0.09	0.06	0.04	0.05	0.04	0.04	0.04
Coefficient of variation (%)			4.31	4.50	6.98	4.90	4.74	4.69	4.17	4.14	4.35

Note:

- The experimental and theoretical deflections were monitored and computed at failure and $0.33M_n$ by considering the self-weight of the beams.
- The deflections due to the self-weight of the beams are 0.26 mm and 0.25 mm based on the gross moment of inertia for CSA S806 (2012) and ACI 440.1R (2015), respectively.
- The deflection of the beams at the beam supports was not measured. The measured deflections might include any shortening of the supports.

5.4.6.2 Assessment of the ACI 440.1R (2015) deflection equations

As discussed, the results presented in Table 5.8 show that the mean $\delta_{exp.}/\delta_{pred.}$ ratios at $0.33M_n$ of all tested ribbed GFRP-RC beams are greater than one when the theoretical value of M_{cr} or $0.8M_{cr}$ is used, which demonstrates that the ACI 440.1R (2015) equation underestimates the deflection at the service stage. Kassem et al. (2011), Al-Sunna et al. (2012), Miàs et al. (2013), and El-Nemr et al. (2013) concluded that the ACI 440.1R-06 (ACI 2006) deflection equation that was based on Branson's (1965) effective moment of inertia equation underestimated the deflection values at the service stage. Moreover, El-Nemr et al. (2018) and Mousa et al. (2020) found that the ACI 440.1R (2015) deflection equation underestimated the predicted deflections at an applied moment of $0.3M_n$. This might be attributed to the overestimation of the effective moment of inertia (I_e) that resulted in reducing the values of the predicted deflection.

To further investigate the accuracy of the ACI 440.1R (2015) deflection equation, the $\delta_{exp.}/\delta_{pred.}$ values based on M_{cr} and $0.8M_{cr}$ at four load levels of $0.20M_n$, $0.25M_n$, $0.33M_n$, and $0.40M_n$ for all the beams are calculated. Figure 5.14 shows the scatter of the $\delta_{exp.}/\delta_{pred.}$ deflection ratios versus the I_g/I_{cr} and M_a/M_{cr} ratios. From Figure 5.14(a-b), it is apparent that the ACI 440.1R (2015) equation underestimates the deflection of all the tested beams for the four load levels when the theoretical M_{cr} is used. In this case, the mean value of $\delta_{exp.}/\delta_{pred.}$ for the four load levels was 1.33 with a standard deviation of 0.19.

Figure 5.14(a) shows that the deflection predictions of the ACI 440.1R (2015) equation are a function of the I_g/I_{cr} ratio. It also shows that data variation increases when the I_g/I_{cr} ratio exceeds 12. Moreover, Figure 5.14(b) shows a considerable data variation when the service moment is approximately less than $1.7M_{cr}$. Figure 5.14(c-d) illustrates that considering $0.8M_{cr}$ in the calculations of the deflection improves the code predictions and reduces the dependency of $\delta_{exp.}/\delta_{pred.}$ ratios on I_g/I_{cr} and M_a/M_{cr} . However, the majority of data points had experimental deflection less than the predicted deflection. In this case, the mean $\delta_{exp.}/\delta_{pred.}$ at the four load levels was 1.13 with a standard deviation of 0.10. It is worth mentioning that the results showed that the experimental-to-predicted cracking moments ($M_{cr-exp.}/M_{cr-Theo.}$) of the beams tested in this study have a mean of 0.86 ± 0.09 (see Table 5.8). This is close to the ratio recommended to be considered in the calculation of deflection based on the ACI 440.1R (2015) equation, as

highlighted by Bischoff et al. (2009).

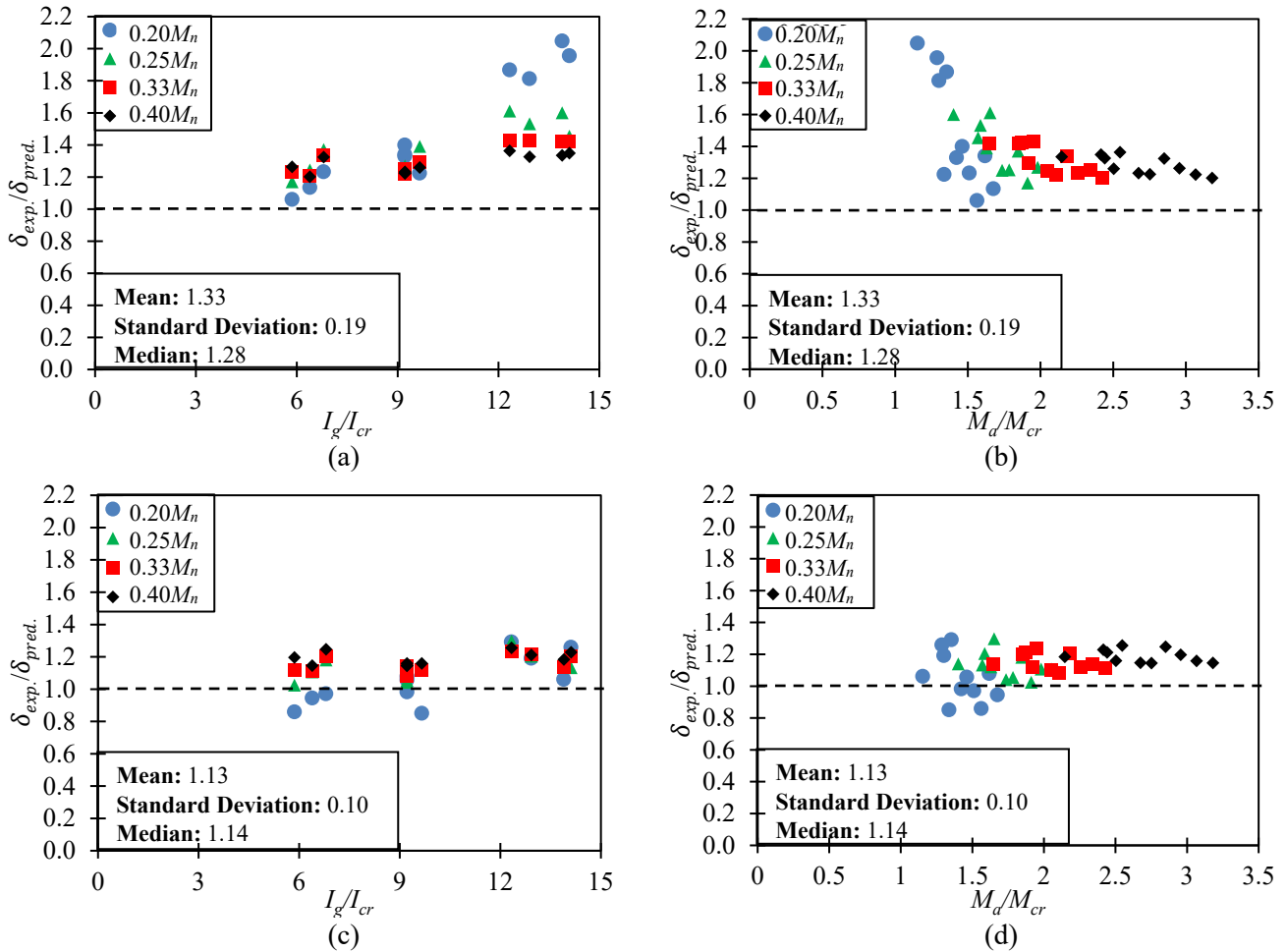


Figure 5.14 Distribution of $\delta_{exp}/\delta_{pred}$ values of ACI 440.1R-15 (ACI 2015) equation versus: (a) I_g/I_{cr} where δ_{pred} is calculated using M_{cr} ; (b) M_d/M_{cr} where δ_{pred} is calculated using M_{cr} ; (c) I_g/I_{cr} where δ_{pred} is calculated using $0.8M_{cr}$; and (d) M_d/M_{cr} where δ_{pred} is calculated using $0.8M_{cr}$

The experimental results show that the ACI 440.1R (2015) equation provides a stiffer beam response at the service stage than the real behaviour. The underestimation of the theoretical deflections by Eq. (5.14-a) might be attributed to the overestimated tension stiffening effect in the I_e equation. Eq. (5.14-b) can be rewritten in general terms as in Eq. (5.15) (Bischoff, 2005):

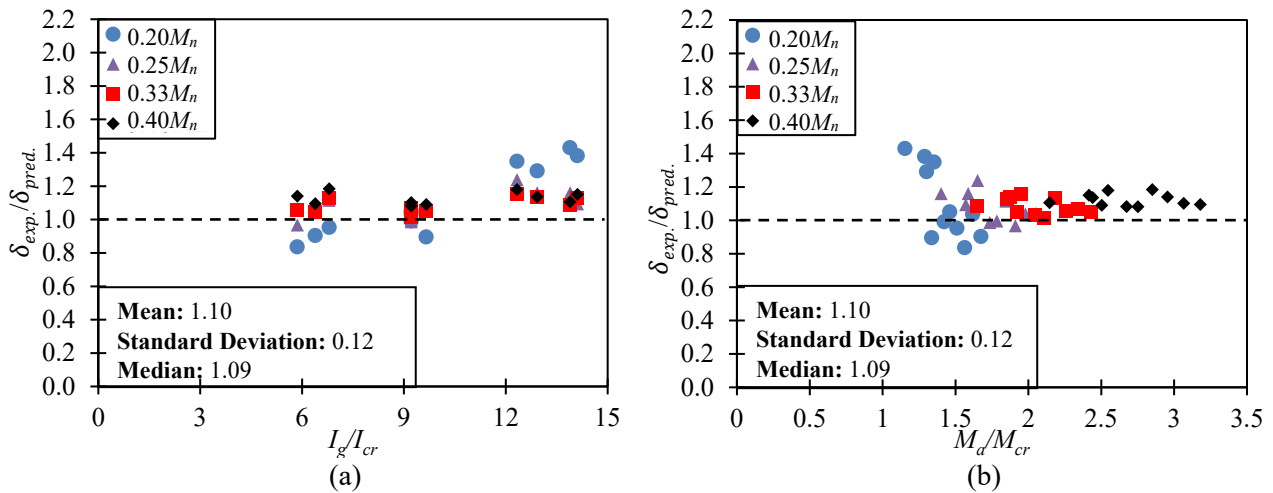
$$I_e = \frac{I_{cr}}{1 - \gamma \beta_c \left(\frac{M_{cr}}{M_d} \right) \left[1 - \frac{I_{cr}}{I_g} \right]} \leq I_g \quad (3.15)$$

where β_c is the tension stiffening factor. Bischoff et al. (2005) assumed that the tension stiffening factor (β_c) is equal to M_{cr}/M_d based on the assumption proposed by Rao (1966) that the tension

stiffening strain at the crack locations varies inversely with the bar stress. This results in β_c values that vary from 1 (full tension stiffening) at $M_a = M_{cr}$ to almost 0 (no tension stiffening) at high service loads ($M_a \gg M_{cr}$).

In this study, to reduce the effect of tension stiffening after cracking in the I_e equation, the tension stiffening factor (β_c) was defined as $(M_{cr}/M_a)^m$, and the power m was increased to 2 and 3 to obtain the optimal fit to the experimental data.

Figure 5.15 shows the scatter of $\delta_{exp.}/\delta_{pred.}$ deflection ratios versus I_g/I_{cr} and M_a/M_{cr} ratios when the tension stiffening factor is set to be $(M_{cr}/M_a)^2$. As shown, the mean $\delta_{exp.}/\delta_{pred.}$ for the four load levels decreased to 1.10 ± 0.12 and 0.96 ± 0.11 when M_{cr} and $0.8M_{cr}$ were used in the calculations, respectively. Moreover, at $0.33M_n$, the mean $\delta_{exp.}/\delta_{pred.}$ ratios were 1.09 ± 0.05 and 1.02 ± 0.04 , respectively (as listed in Table 5.8), which are lower than the corresponding mean $\delta_{exp.}/\delta_{pred.}$ at $0.33M_n$ for $\beta_c=M_{cr}/M_a$. Figure 5.15(a-b) shows that when M_{cr} is used in the calculations, there is a data variation for I_g/I_{cr} ratios less than 12 and M_a/M_{cr} ratios less than 1.7. The variation is, however, reduced compared to Figure 5.15(a-b). In this case, the $\delta_{exp.}/\delta_{pred.}$ ratios have a median value of 1.09, and thus, the majority of experimental deflections are greater than predicted deflections. Considering a reduced value of $0.8M_{cr}$ in the deflection calculations, the majority of $\delta_{exp.}/\delta_{pred.}$ are less than 1.00 (median of 0.98). Moreover, as shown in Figure 5.15(c), the dependency of $\delta_{exp.}/\delta_{pred.}$ ratios on I_g/I_{cr} is reduced. However, Figure 5.15(d) shows that the accuracy of the deflection predictions ($\delta_{exp.}/\delta_{pred.}$) is becoming a function of M_a/M_{cr} .



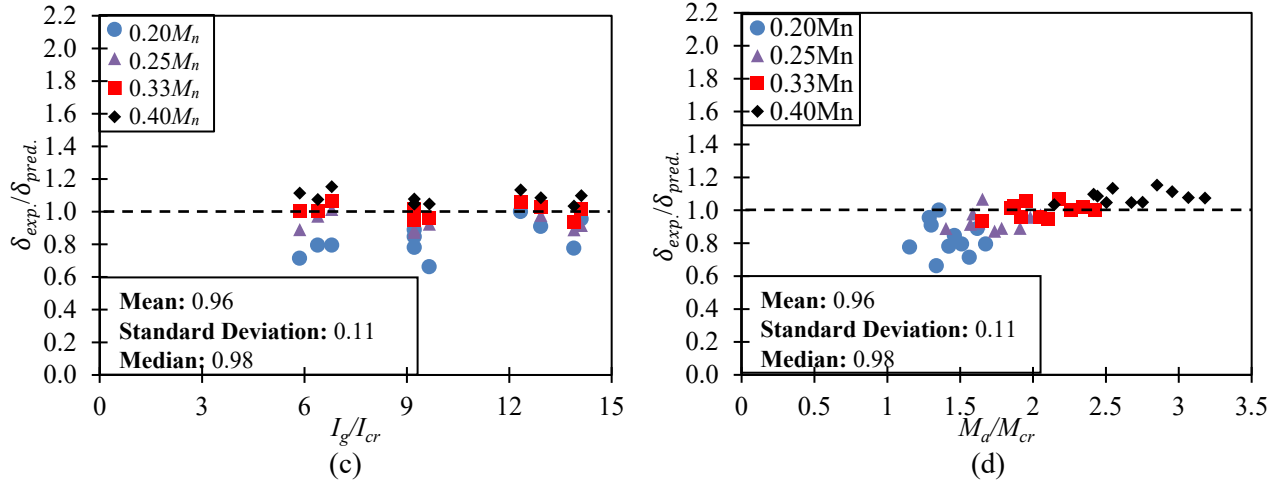


Figure 5.15 Distribution of $\delta_{exp.}/\delta_{pred.}$ values calculated assuming $\beta_c = (M_{cr}/M_a)^2$ versus: (a) I_g/I_{cr} where $\delta_{pred.}$ is calculated using M_{cr} ; (b) M_a/M_{cr} where $\delta_{pred.}$ is calculated using M_{cr} ; (c) I_g/I_{cr} where $\delta_{pred.}$ is calculated using $0.8M_{cr}$; and (d) M_a/M_{cr} where $\delta_{pred.}$ is calculated using $0.8M_{cr}$

Figure 5.16 displays the scatter of $\delta_{exp.}/\delta_{pred.}$ deflection ratios versus I_g/I_{cr} and M_a/M_{cr} ratios when the tension stiffening factor is set to be $(M_{cr}/M_a)^3$. As shown, the mean $\delta_{exp.}/\delta_{pred.}$ ratios for the four load levels decreased to 0.99 ± 0.10 and 0.91 ± 0.13 when M_{cr} and $0.8M_{cr}$ were used in the calculations, respectively. Comparing Figure 5.16(a-b) and Figure 5.16(a-b) shows that when M_{cr} is used in the calculations, there is less variation in the $\delta_{exp.}/\delta_{pred.}$ ratios for the range of the I_g/I_{cr} and M_a/M_{cr} ratios of the beams tested in this study. The $\delta_{exp.}/\delta_{pred.}$ ratios have a median value of 1.01, and thus, the majority of experimental deflections are greater than predicted deflections. Considering a reduced value of $0.8M_{cr}$ in deflection calculations, the majority of $\delta_{exp.}/\delta_{pred.}$ are less than 1.00 (median of 0.91). However, Figure 5.16(d) shows that the accuracy of deflection predictions ($\delta_{exp.}/\delta_{pred.}$) is a function of M_a/M_{cr} .

Figure 5.17 shows a comparison between the experimental and theoretical I_e for $(M_{cr}/M_a)^m$ with m equal to 1, 2, and 3 of all tested beams for the four load levels. It is apparent that there is an overestimation in I_e values using the current equation in ACI 440.1R (2015) (i.e., $m = 1$). In addition, by reducing the tension stiffening by increasing the power m in Eq. (5.15), Figure 5.17(b-c) show that the theoretical I_e results become closer to the experimental I_e . Moreover, the effect of reducing the cracking moment by 20% on the theoretical deflections appears to be lesser by decreasing the tension stiffening effect.

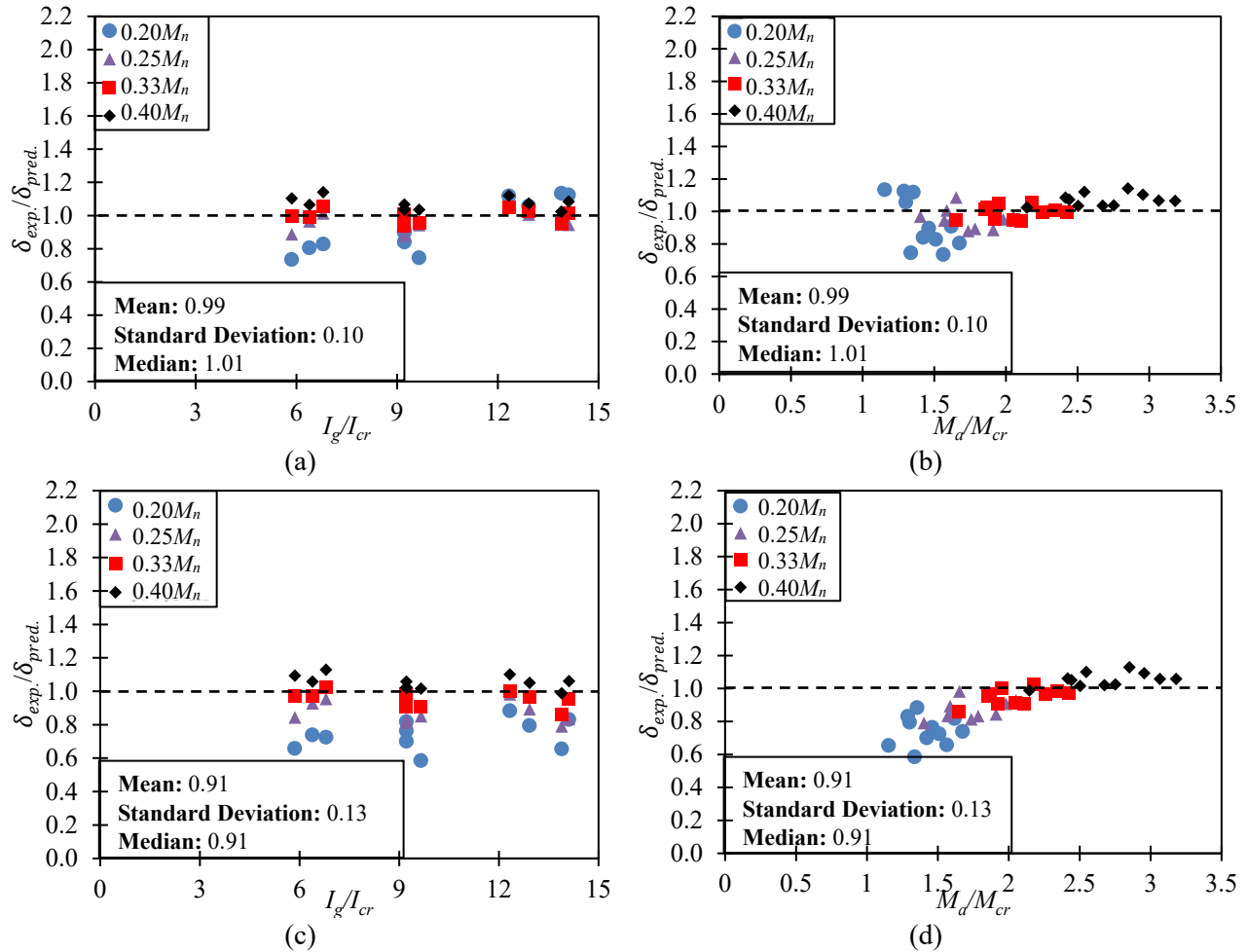


Figure 5.16 Distribution of $\delta_{exp}/\delta_{pred}$ values calculated assuming $\beta_c = (M_{cr}/M_a)^3$ versus: (a) I_g/I_{cr} where δ_{pred} is calculated using M_{cr} ; (b) M_a/M_{cr} where δ_{pred} is calculated using M_{cr} ; (c) I_g/I_{cr} where δ_{pred} is calculated using $0.8M_{cr}$; and (d) M_a/M_{cr} where δ_{pred} is calculated using $0.8M_{cr}$

North American design codes and guidelines set two limits on the deflections: 1) limits on the immediate deflection from live load and 2) limits on the incremental deflection occurring after attachment of nonstructural elements over the long term. The immediate deflection from the live load is calculated as the difference between the deflection due to dead plus live loads and the deflection due to dead load. In this case, the deflection due to dead plus live loads is estimated based on the corresponding effective moment of inertia (i.e., $I_{e,DL+LL}$), while the deflection due to dead load is estimated based on deflection $I_{e,DL}$. For most conservative cases, all the terms in the calculation of the incremental deflection occurring after attachment of nonstructural elements are calculated based on the effective moment of inertia due to dead plus live load ($I_{e,D+L}$).

Accordingly, the deflection equations should not only provide a reasonable accuracy at a given moment level but also should the predictions be independent of the moment level.

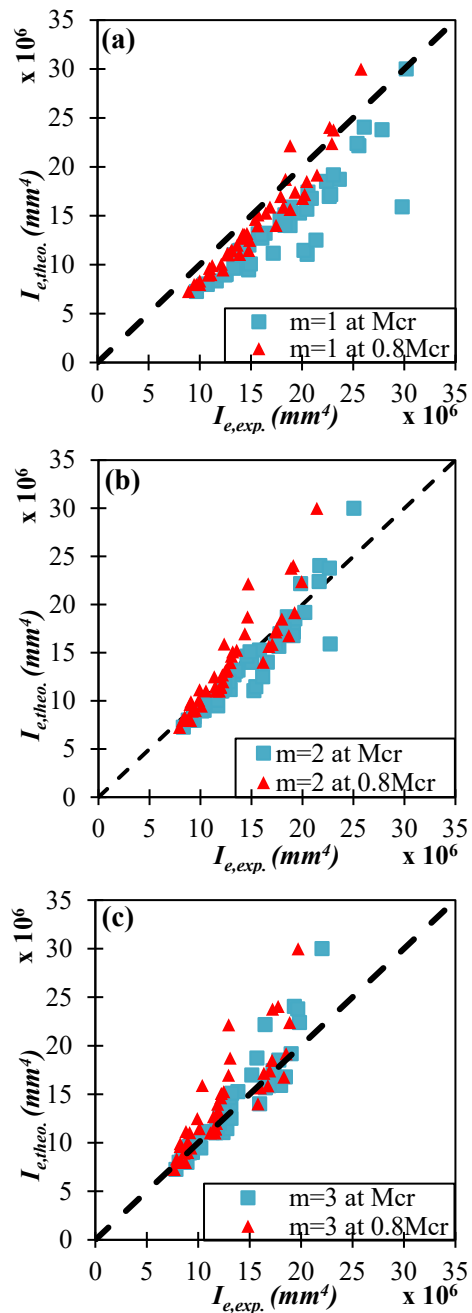


Figure 5.17 Relationship between the experimental and theoretical I_e for: (a) Eq. 5.14(b), (b) Eq. 5.15 with $m = 2$, and (c) Eq. 5.15 with $m = 3$

The discussion made in this section shows that the ACI 440.1R (2015) deflection equation provides unconservative deflection predictions with high data scatter when M_{cr} is used. Using $0.8M_{cr}$ improves the deflection predictions and data scatter; however, the equation still gives

stiffer beam behaviour than the experimental measurements. Decreasing the tension stiffening factor in the I_e equation by increasing the power m in Eq. (5.15) shifts the $\delta_{exp.}/\delta_{pred.}$ ratios toward the conservative side. However, the deflection predictions become a function of M_a/M_{cr} . The dependency of the deflection predictions on M_a/M_{cr} can result in unconservative immediate deflection from live load, even though the deflection predictions are conservative at any given acting moment. Although the experimental results of this study support the use of $\beta_c = (M_{cr}/M_a)^2$ in Eq. (5.15) at $0.8M_{cr}$ for deflection predictions, more investigations are required to closely examine the serviceability issues related to deflection and cracking in GFRP-reinforced concrete elements.

5.5 Summary and conclusions

This chapter investigated the flexural behaviour of 11 full-scale concrete beams reinforced with ribbed GFRP bars under a four-point loading scheme until failure. Based on the experimental results and discussions presented in this chapter, the following conclusions can be drawn:

- The tested beams failed by concrete crushing at the extreme compression fibres as designed. The beams with a low reinforcement ratio ($\leq 0.85\%$) exhibited bilinear load-deflection behaviour, whereas beams with a higher reinforcement ratio showed trilinear behaviour.
- An increase in the reinforcement ratio led to a considerable decrease in the deformability using energy- and deformation-based approaches (except for $1000 \mu\epsilon$) of the beams. Moreover, for the same increase in the reinforcement ratio, the serviceability moment capacity increased more than the ultimate moment capacity.
- The CSA S806 (2012) and ACI 440.1R (2015) provided moment capacity predictions close to the experimental results.
- Deflections calculated by the CSA S806 (2012) equation at $0.33 M_n$ provided a conservative prediction of the experimental results and were insensitive to the cracking moment.
- ACI 440.1R (2015) deflection equation provides unconservative deflection predictions

with high data scatter when M_{cr} is used. Using $0.8M_{cr}$ improves the deflection predictions and data scatter; however, the equation still gives slightly stiffer beam behaviour than the experimental measurements.

- The experimental results of this study support the use of $\beta_c = (M_{cr}/M_a)^2$ and $0.8M_{cr}$ for deflection predictions. However, the deflection predictions showed dependency on the level of loading as the power m in the tension stiffening factor (β_c) increased. More investigations are required to closely examine the serviceability issues related to deflection and cracking in GFRP-RC elements.
- The deformability calculated using the energy-based approach yielded more reasonable results with a clear trend than the deformation-based method for some parameters, including the concrete cover, reinforcement ratio (bar diameter), and confinement due to transverse reinforcement. However, this finding is different from the conclusions of Wang and Belarbi (2011) and Abdelkarim et al. (2018).
- The use of closely spaced stirrups in the middle flexural zone (100 mm spacing between stirrups) showed a considerable enhancement in the load-carrying capacity and ductility indices using the energy-based approach compared with the widely spaced stirrups (317 mm spacing between stirrups).
- The results of this study showed that for the beams tested in this study, the crack width limit of 0.5 mm governs other serviceability limits on stress in GFRP bars. It is recommended that the GFRP RC elements be designed for crack width and deflection requirements and then checked to satisfy other requirements.

It is important to note that the above conclusions are preliminary and pertinent to ribbed GFRP-RC beams with the abovementioned parameters. The number of samples tested in this research is limited and may not provide statistically sufficient evidence to generalize the conclusions. Moreover, only one sample was used for each design; thus, more tests need to be conducted to verify the repeatability of the test results. It is recommended that the GFRP-RC flexural elements be designed for crack width and deflection requirements and then checked to satisfy other requirements. The proposed deflection equation provided conservative results

compared to the ACI 440.1R (2015) equation, and it is recommended to compute the effective moment of inertia using $\beta_c = (M_{cr}/M_a)^2$. The confinement provided a considerable enhancement in terms of the deformability and ultimate capacity

Chapter 6

Experimental and numerical study on the deflection performance of GFRP reinforced concrete beams

6.1 Abstract

The design of glass fibre reinforced polymer (GFRP)-reinforced concrete (RC) structures is often governed by the serviceability limit states due to the low elastic modulus of GFRP compared to steel. Limited studies investigated the effect of changing the concrete compressive strength on the deflection behaviour of GFRP-RC beams. This study investigates, experimentally, by testing 11 GFRP-RC beams, the effect of different parameters, including the concrete compressive strength, clear concrete cover to GFRP reinforcement, and the number of GFRP reinforcement layers on the ultimate capacity and deflection behaviour. Moreover, a numerical parametric study was conducted to investigate the effect of varying the concrete strength from 25 MPa to 95 MPa on the cracking propagation and deflection performances of the GFRP-RC beams. The developed numerical model simulated the experimental behaviour of the beams with high accuracy. The experimental results provided insights into how the investigated parameters impact the deflection behaviour. It was also found that the ACI 440.1R (2015) deflection equation provides unconservative prediction at different concrete compressive strength values compared to the CSA S806 (2012).

6.2 Introduction

Glass fibre reinforced polymer (GFRP) reinforcement is currently used to replace steel reinforcement in structural applications, especially where corrosion is a concern. The design of the GFRP-reinforced elements is controlled by the serviceability limit states rather than the ultimate limit states due to the high tensile strength and low modulus of elasticity of the GFRP material (Barris et al. 2009). Therefore, it is crucial to fully understand the cracking and deflection behaviour of the GFRP-reinforced concrete elements.

Many research studies investigated the effect of concrete compressive strength on the flexural behaviour of GFRP-reinforced concrete beams. In general, higher-strength concrete allows taking advantage of the high tensile strength of GFRP bars by enhancing the load-carrying capacity and reducing the mid-span deflection at the service stage (Ashour 2006; Kalpana and Subramanian 2011; El-Nemr et al. 2013; Adam et al. 2015; Goldston et al. 2016; and El-Nemr et al. 2018). However, there is a lack of studies that covered the effect of varying the concrete compressive strength through a wide concrete strength spectrum and changing the tensile reinforcement configuration (Kassem et al. 2011; El-Nemr et al. 2013; and 2018) by placing the bars in different layers on the GFRP-RC serviceability performance.

This chapter addresses the influence of changing material and cross-sectional parameters on the flexural and serviceability performance of GFRP-RC beams through experimental and numerical work. This objective was achieved by constructing and testing 11 full-scale reinforced concrete beams. The investigated parameters include the concrete compressive strength, the clear concrete cover to GFRP reinforcement, and the number of tensile reinforcement layers. Furthermore, a nonlinear finite element simulation was performed using the experimental results for validation to extend the experimental study through a parametric investigation. The numerical parametric investigation discusses the effect of different concrete compressive strengths ranging from 25 MPa -incrementing 10 MPa- to 95 MPa on the deflection values at the service and ultimate stages, cracking propagation, and ultimate capacities. The deflection equations in the CSA S806 (2012) standard and ACI 440.1R (2015) guideline were evaluated to discuss the capability of these equations to predict the deflection values for higher concrete strengths.

6.3 Experimental program

6.3.1 Test specimens

In order to study the effect of different parameters on the deflection behaviour, a total of 11 full-scale reinforced concrete beams were tested, measuring 200 mm × 400 mm × 4350 mm. The shear span to depth ratio (a/h) was 3.44, and the span between the centerline of the supports was 3750 mm. The beams were reinforced with ribbed GFRP bars as the primary flexural reinforcement. The parameters included in this study are the concrete strength: normal-strength and high-strength with a target strength of 35 MPa and 65 MPa, respectively; reinforcement layer placement (one and two layers); and concrete cover (30 mm, 38 mm, and 50 mm). The test matrix is summarized in Table 6.1.

Table 6.1 Test matrix of the tested beams.

#	Beam Id*	Targeted concrete strength (MPa)	Actual concrete strength (MPa)	Number of reinf. Layers**	Bar diameter (mm)	Total number of bars	Clear concrete cover (mm)	Total reinf. area (mm ²)	Reinf. ratio ($\rho_f\%$)	Reinf. ratio ($\rho_{fb}\%$)
1	N-3#5-c30	35	40.0	1	15.9	3	30	597	0.82	0.45
2	N-4#5-c30	35	40.0	2	15.9	4	30	796	1.10	0.45
3	N-3#6-c38	35	35.8	1	19.1	3	38	852	1.21	0.42
4	N-3#6-c50	35	35.8	1	19.1	3	50	852	1.25	0.42
5	N-2#8-c50	35	35.8	1	25.4	2	50	1020	1.51	0.42
6	N-3#5-c50	35	35.8	1	15.9	3	50	597	0.87	0.41
7	N-5#5-c50	35	35.8	2	15.9	5	50	995	1.45	0.41
8	H-5#5-c50	65	70.8	2	15.9	5	50	995	1.45	0.68
9	H-3#6-c38	65	70.8	1	19.1	3	38	852	1.21	0.70
10	H-3#6-c50	65	70.8	1	19.1	3	50	852	1.25	0.70
11	H-2#8-c50	65	70.8	1	25.4	2	50	1020	1.51	0.69

*The first letter (N/H) indicates the concrete strength type, N for normal and H for high; the second number (2, 3, 4, or 5) indicates the number of reinforcing bars; the third number (#5, #6, #8) indicates the bar size, the following letter “c” is for cover, and the last number indicates the clear cover (in millimeters).

** The word “reinf.” stands for reinforcement.

The reinforcement configuration of the bars in the beam is shown in Figure 6.1. The GFRP-reinforced concrete beams were designed to fail by concrete crushing; this was achieved by designing the beams as over-reinforced sections ($\rho_f > 1.4\rho_{fb}$), as shown in Table 6.1. The balanced reinforcement ratio (ρ_{fb}) was calculated considering the actual concrete strength.

6.3.2 Material properties

6.3.2.1 Reinforcing Bars

The beams were reinforced using three sizes of ribbed GFRP bars as a longitudinal tensile reinforcement, #5, #6, and #8. Figure 6.2 illustrates the surface configuration of the ribbed GFRP bars. The ultimate tensile strength and modulus of elasticity were determined by testing five representative specimens of each diameter following the ASTM D7205/D7205M (ASTM D7205 2021) specifications.

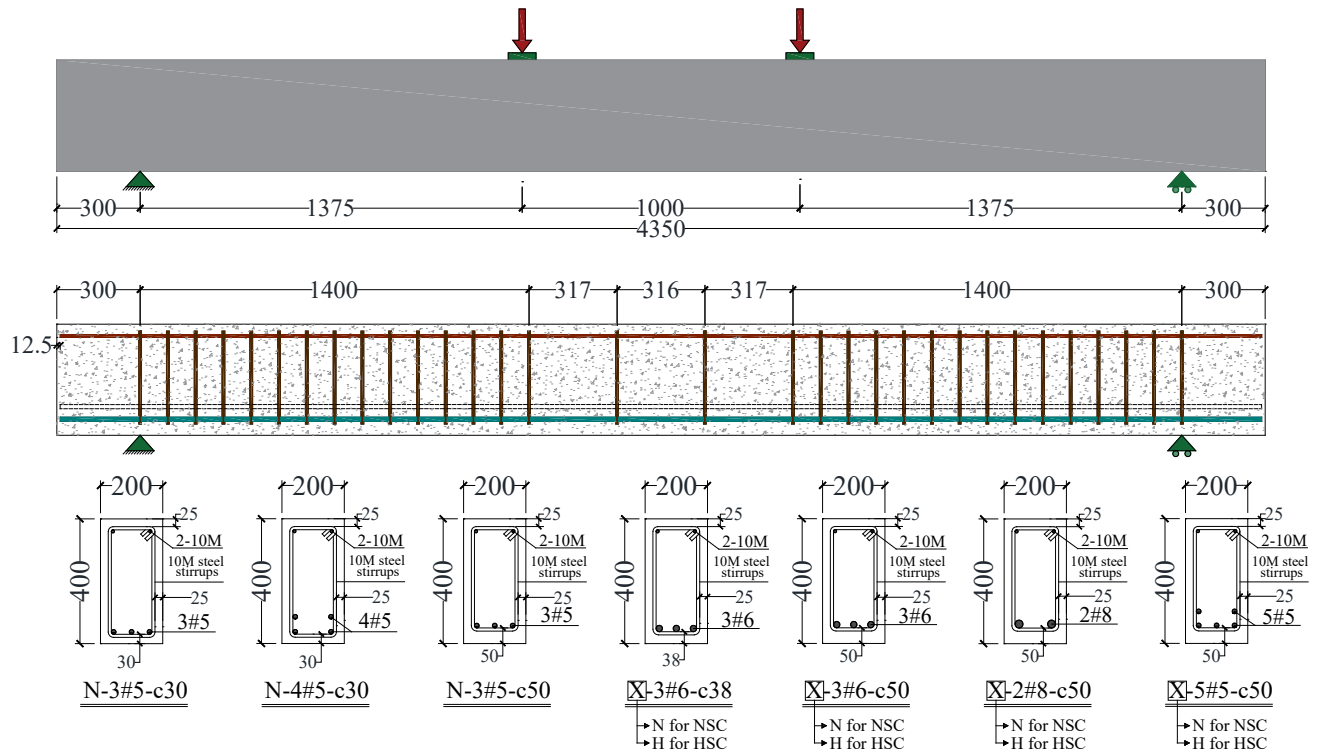


Figure 6.1 Test setup, specimens' cross section details and reinforcement configuration



Figure 6.2 GFRP reinforcement surface configuration

Table 6.2 summarizes the mechanical properties of the GFRP bars. The actual cross-sectional diameter was measured and used to calculate the mechanical properties. The top compression reinforcement and closed transverse stirrups were 10M steel rebars with a nominal diameter of 11.3 mm, a cross-sectional area of 100 mm², and a yield strength of 400 MPa. The steel mechanical properties were obtained from the manufacturer datasheet. In order to ensure a flexural-dominated failure and avoid shear failure, the stirrups were spaced at 100 mm in the shear span. In the middle bending zone between the two-point loads, the stirrups were spaced at 317 mm to reduce the confinement effect.

Table 6.2 Mechanical properties of GFRP reinforcing bars

Bar type	Designated diameter	Nominal cross-sectional area (mm ²)	Nominal diameter (mm)	Tensile strength (MPa)	Elastic modulus (GPa)	Ultimate strain (%)
GFRP	#5 (15 mm)	199	15.9	1087 ± 9.8	60.4 ± 0.46	1.80
	#6 (20 mm)	284	19.1	1052 ± 8.4	61.0 ± 0.91	1.72
	#8 (25 mm)	510	25.4	1090 ± 11.3	61.9 ± 0.36	1.76

6.3.2.2 Concrete

The beams were constructed using ready-mixed concrete with a target compressive strength of 35 MPa for the normal-strength concrete “NSC” specimens and 65 MPa for the high-strength concrete “HSC” specimens. The concrete mix design is presented in Table 6.3. The normal-strength specimens were cast in two patches, NSC1 and NSC2. The compressive strength was determined by testing five 100×200mm concrete cylinders per ASTM C39/C39M (2021) on the testing day of the beams (± one week). The measured compressive strength for the NSC1, NSC2, and HSC were 35.8 ± 1.13, 40.0 ± 1.44 MPa, and 70.8 ± 2.14 MPa, respectively. The modulus of rupture was determined by testing three 150×150×500 mm concrete prisms per ASTM C78/C78M (2022). The splitting tensile strength was determined by testing five 100×200 mm concrete cylinders as per ASTM C496/C496M (2017). The measured values of the concrete modulus of rupture (f_r) for the NSC1, NSC2, and HSC were: 4.97 ± 0.29, 5.32 ± 0.38, and 5.98 ± 0.27 MPa, respectively. The measured splitting strengths (T) were: 3.59 ± 0.21, 3.79 ± 0.29 and 4.67 ± 0.19 MPa, respectively.

Table 6.3 Concrete mix design.

Target concrete strength	Ordinary Portland cement	Fine sand	Coarse aggregate	Free water	W/C ratio
MPa	kg/m ³	kg/m ³	kg/m ³	liter/m ³	%
32	405	839	937	166	0.41
32	377	862	942	171	0.45
65	450	838	983	145	0.32

6.3.3 Test Procedure, setup, and instrumentation

All the beams were simply-supported and tested under the four-point loading scheme, as shown in Figure 6.3. The load was applied under a displacement-control procedure with a loading rate of 0.6 mm/min until the initiation of the first three flexural cracks, recognized by the reduction in stiffness in the load-displacement curve and visual observation. After the first three cracks initiation, the loading rate was increased to 1.2 mm/min up to failure as per CSA S806 (2012). The test setup consists of a hydraulic cylinder fixed at a strong steel frame and a 500kN load cell with ± 0.05 kN accuracy. A steel spreader beam was used to distribute the load using two steel rods on steel plates at the top of the beam.

Five linear potentiometers were placed under the beams and used to measure the deflection at different points, as shown in Figure 6.4(a). Two potentiometers were mounted at the mid-span, another two under the loading points, and the remaining one at the midpoint between the hinged support and the loading point. The strain gauges of the GFRP bars and concrete are illustrated in Figure 6.4(b).



Figure 6.3 Typical test setup for the tested beams

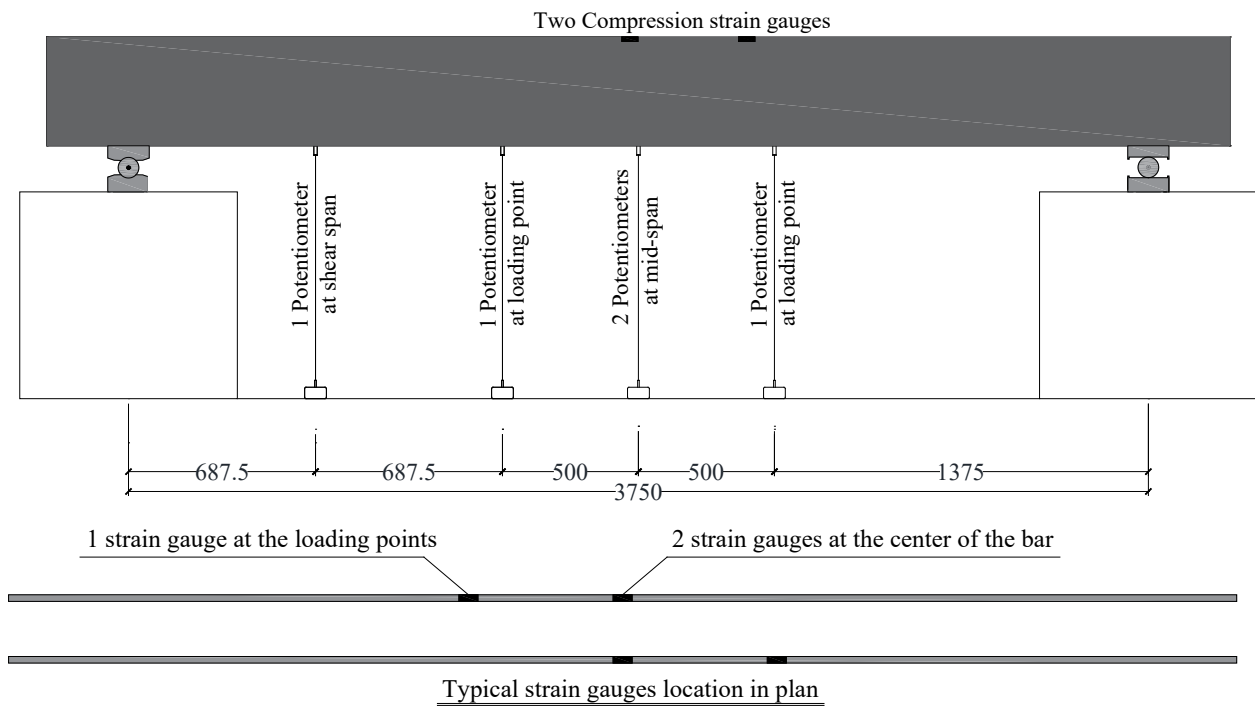


Figure 6.4 Typical beam instrumentation

6.4 Test results and discussion

6.4.1 General observations

The parameters under consideration in this study were the concrete compressive strength, clear concrete cover to GFRP reinforcement, and the number of GFRP reinforcement layers. The influence of these parameters on the deflection, flexural capacity, and mode of failure was investigated. Only the moment capacities and deflection results of beams N-3#5-c50, N-3#6-c38, N-3#6-c50, and N-2#8-c50 were obtained from Gouda et al. (2022) for the comparison purpose with the other beams. Table 6.4 presents the monitored cracking and ultimate moments (including the moment due to self-weight) and the observed failure mode. The deflection comparison was held at a service level taken as one-third of the beams' nominal flexural moment capacity ($0.33M_n$), as proposed by Bischoff et al. (2009) to evaluate deflection equations. This $0.33M_n$ was utilized after that by Kassem et al. (2011), El-Nemr et al. (2013), El-Nemr et al. (2016), and El-Nemr et al. (2018). Besides, the deflection relations were compared at the same moment level.

Table 6.4 Beams' moment, deflection, and failure mode

#	Beam Id	Cracking moment (kN.m)	Ultimate moment (kN.m)	Deflection at $0.33M_n$ (mm)	Ultimate deflection (mm)	Failure mode
1	N-3#5-c30	17.4	153	23.5	84	Concrete crushing
2	N-4#5-c30	18.2	165	20.2	77	Concrete crushing
3	N-3#6-c38	17.1	152	15.8	68	Concrete crushing
4	N-3#6-c50	18.1	136	16.0	72	Concrete crushing
5	N-2#8-c50	19.6	142	13.8	59	Concrete crushing
6	N-3#5-c50	19.3	131	18.4	83	Concrete crushing
7	N-5#5-c50	18.5	148	15.7	69	Concrete crushing
8	H-5#5-c50	22.7	186	20.8	76	Concrete crushing
9	H-3#6-c38	20.0	204	22.8	81	Concrete crushing
10	H-3#6-c50	21.6	187	23.7	83	Concrete crushing
11	H-2#8-c50	21.0	195	21.7	75	Concrete crushing

Note: The cracking and ultimate moments include the moment due to self-weight.

In general, the failure of all beams was identified as compression failure by concrete crushing of the top concrete fibre at the mid-span section and in the vicinity of the loading points. The crack propagation in the tested beams followed the typical flexural-cracking patterns in simply supported beams, as shown in Figure 6.5. The first crack was initiated in the constant-moment region at the soffit of the beam and extended vertically toward the compression zone. The cracks initiated

further away from the flexure zone towards the supports by increasing the acting loads. The flexure-shear cracks were observed at high load levels greater than $0.5M_n$, since the shear capacity of the cross-section was much higher than the applied load causing the delay of the shear cracks. Generally, the cracks propagation followed a similar trend in all the beams; however, increasing the reinforcement ratio, the number of layers, concrete cover, and concrete strength affected the distribution of the cracks over the span, as discussed in the following sections.

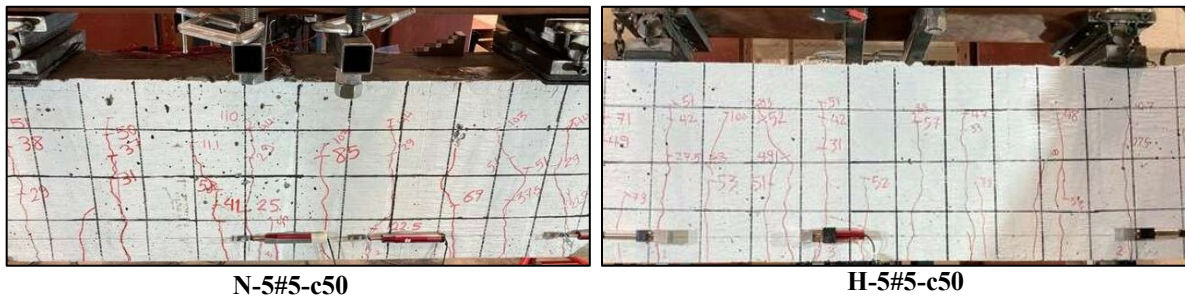


Figure 6.5 The typical crack pattern of the tested specimens at $0.33M_n$ crack width

6.4.2 Effect of concrete strength level

Two types of concrete strengths were used in this study, high-strength concrete (HSC) and normal-strength concrete (NSC). Figures 6.6(a) and (b) show the moment-deflection relationships for identical specimens with only the concrete strength as a variable. It was observed that the HSC specimens achieved higher ultimate moments than the corresponding NSC beams. Notably, the HSC specimens behaved linearly with no stiffness reduction up to failure. The observed failure was more brittle and occurred in a sudden manner compared to the NSC specimens. On the other side, the NSC specimens behaved linearly up to 70%-80% of the ultimate load. After this point, the stiffness started to degrade, leading the slope of the moment-deflection curve to reduce up to failure; this zone could be named a reduced-stiffness zone. This reduced-stiffness zone is attributed to the plastic deformation in the extreme compression fibres' zone. These plastic deformations were visually observed at the same load level as compression cracks started to develop in the extreme compression fibres, resulting in top cover splitting. Likewise, the concrete strength had a noticeable influence on the beams' deformation by reducing the mid-span deflection at the same moment level in the service stage, as shown in Figures 6.6(a) and (b); this is because the beams are over-reinforced, and the failure is controlled by the concrete strength. However, at $0.33M_n$, the

recorded deflections for the HSC beams were much higher than the deflections of the NSC beams, which is attributed to the higher moment capacity for the HSC beams than the NSC ones resulting in higher moments at the service stage and higher deflection values. The deflection comparisons show that comparing the beams at a service level of $0.33M_n$ provides different results to those compared at the same moment level.

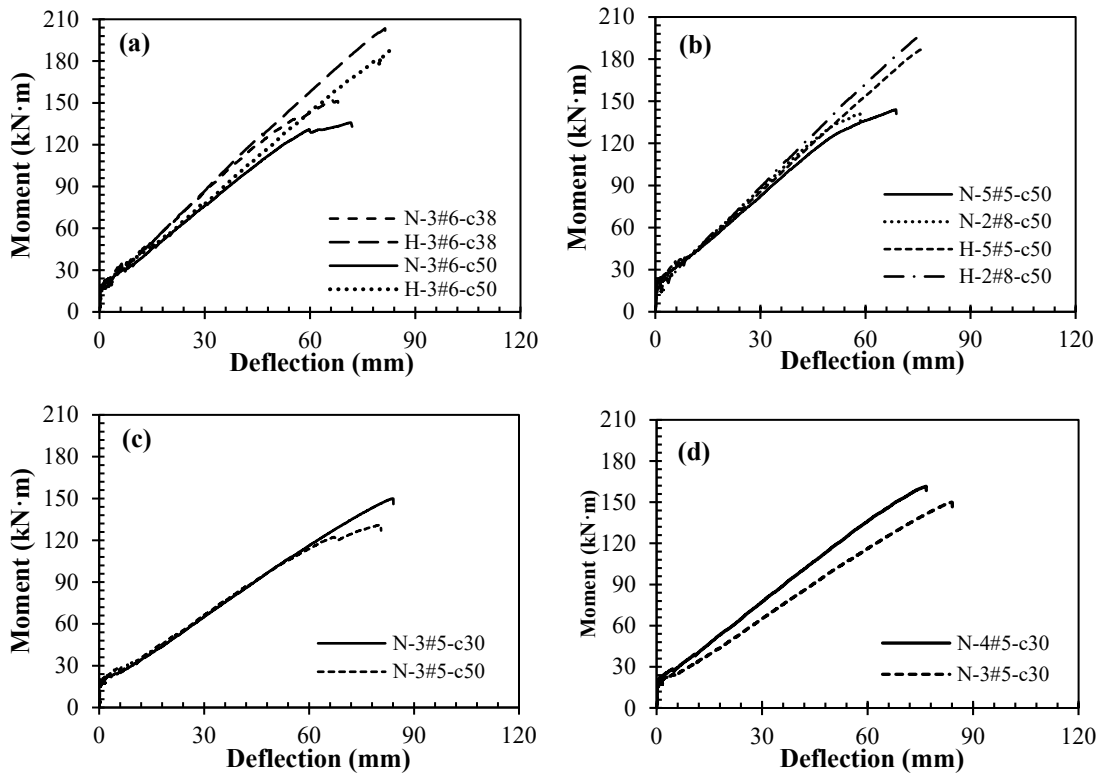


Figure 6.6 Moment-deflection for the tested beams specimens

6.4.3 Effect of concrete cover

As shown in Figure 6.6(a) and Table 6.4, all beams with a clear concrete cover of 38 mm exhibited lower deflection values at the same moment level and a service stage of $0.33M_n$ than beams with a clear cover of 50 mm. Beam N-3#6-c38 achieved 12% more load capacity compared to beam N-3#6-c50, whereas beam N-3#6-c50 achieved higher deflection levels at $0.33M_n$ and at the ultimate stage through a similar curve trend than beam N-3#6-c38 by 1% and 6%. Moreover, beam H-3#6-c38 achieved 9% higher load capacity compared to beam H-3#6-c50, while beam H-3#6-c50 attained 4% and 2% higher deflection values at $0.33M_n$ and at the ultimate stage than beam H-3#6-c38, respectively, as listed in Table 6.4. By increasing the clear concrete cover from

30 mm to 50 mm, beam N-3#5-c30 achieved 17% higher load capacity and 28% higher deflection at $0.33M_n$ than beam N-3#5-c50. While at the same moment level, the two beams achieved similar approximate deflection values up to around 80% of the ultimate loads, after that, beam N-3#5-c30 exhibited lower deflection values than beam N-3#5-c50 at the same moment level, as shown in Figure 6.6(c).

6.4.4 Effect of number of tensile reinforcement layers

In order to examine the effect of the number of tensile reinforcement layers on the deflection behaviour, two reinforcement configurations were investigated having similar reinforcement ratios; five GFRP bars #5 in two layers and two GFRP bars #8 in one layer. Another two configurations were studied with different reinforcement ratios, including four GFRP bars #5 in two layers and three GFRP bars #5 in one layer. It can be observed in Figure 6.6(b) that the one- and two-layer specimens approximately had the same moment capacities for both NSC and HSC beams. Moreover, at the same moment level, beams N-2#8-c50 and H-2#8-c50 had lower deflection values than beams N-5#5-c50 and H-5#5-c50, respectively. Similarly, at $0.33M_n$, it was noticed that the deflection of beam N-5#5-c50 was higher than that in beam N-2#8-c50 by 14%. In contrast, beam H-5#5-c50 had a slightly lower deflection than beam H-2#8-c50 by 4% at $0.33M_n$. As illustrated in Figure 6.6(d), even though beam N-3#5-c30 had a reinforcement ratio of 0.82%, lower than beam N-4#5-c30 with a reinforcement ratio of 1.10%, the two-layer specimen had a slightly higher moment capacity than the one-layer specimen by 8%. However, for the deflection behaviour, beam N-4#5-c30 had lower deflection values at the same moment levels, at $0.33M_n$, and at the ultimate stage than beam N-3#5-c30, as shown in Figure 6.6(d).

6.5 Numerical investigation

6.5.1 FE modelling

ATENA software-GID solver (Červenka and Červenka 2013) was used to develop a numerical simulation for the tested GFRP-RC beams. ATENA software is specialized in modelling concrete structures reinforced with steel and FRP reinforcement. The software can simulate the concrete material properties, including the compressive and tensile behaviour before and after cracking, post-peak behaviour, cracking behaviour, and tension stiffening in the cracked concrete. In addition, the software can simulate material and geometric nonlinearities. ATENA software

(Červenka and Červenka 2013) can capture the failure progression for different elements, including FRP rupture and concrete crushing. Furthermore, the software can provide a deformed shape and cracking pattern.

The numerical model is validated with the experimental results to check its accuracy in capturing the behaviour of the experimentally tested beams. Six beams were used to validate the numerical model; three NSC beams, N-5#5-c50, N-3#6-c50, and N-2#8-c50; the remaining three were the corresponding HSC beam, H-5#5-c50, H-3#6-c50, and H-2#8-c50. The main objective is to ensure the model's capability to capture the flexural and serviceability behaviour of the normal- and high-strength concrete beams.

6.5.2 Geometric models

The geometric elements in ATENA software (Červenka and Červenka 2013) are developed using linear or quadratic interpolation of one, two, and three-dimensional iso-parametric functions that can be extended to a higher order. The elements are integrated at the integration points using Gauss's integration rule.

The concrete beam is modelled using a 20-node 3D solid brick element. There are three translational degrees of freedom for each node in the x, y, and z directions, as illustrated in Figure 6.7(a). The 3D solid brick element can be subject to elastic and plastic deformations, cracking in three orthogonal directions, and crushing. The steel supporting and loading plates are modelled using 30 mm-thickness eight-node tetrahedral elements due to the small thickness of the steel plates compared to the concrete element, as presented in Figure 6.7(b).

The GFRP reinforcement, top steel bars, and transverse stirrups are modelled using discrete 2D truss elements, as illustrated in Figure 6.7(c). The truss elements are modelled in a two-dimensional state by applying the axial forces along the axis of the element. The two-node truss elements undergo a linear interpolation for the position and displacement with constant stress along the element length. The material and cross-sectional properties are defined in the material definition section and then assigned to the truss element.

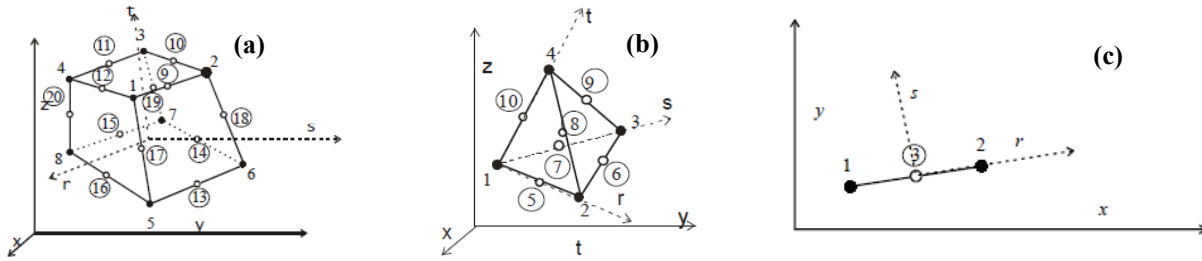


Figure 6.7 Geometric models of (a) brick element, (b) tetrahedral elements, and (c) truss element (Červenka and Červenka 2013)

6.5.3 Material Models

The concrete material nonlinearity results from various aspects, including the concrete cracking in tension, the nonlinear interaction between the GFRP reinforcement and concrete beam during loading, and the compression behaviour before crushing. ATENA software (Červenka and Červenka 2013) accounts for the concrete material nonlinearity through fracture-plastic constitutive models; steel and GFRP reinforcement stress-strain relations.

The concrete is modelled using a “Cementitious2” material based on fracture-plastic constitutive laws. The fracture-plastic constitutive model combines the compression and tension models in plasticity and fracturing, respectively. The fracture model is based on classical orthotropic smeared crack formulation and crack band model. The concrete “Cementitious2” material considers the concrete nonlinear hardening and softening behaviour in compression, concrete fracture in tension based on fracture mechanics, reduction of the elastic modulus after cracking, compressive strength, shear stiffness after cracking, biaxial stress failure criterion, tension stiffening phenomena, the cracking simulation through fixed and rotated crack models, and three-dimensional stress-state failure criterion. The “Cementitious2” material input values in ATENA follow the expressions presented in Table 6.5.

Figure 6.8 presents the concrete equivalent uniaxial stress-strain diagram and the biaxial stress state. The equivalent uniaxial strain (ε_{eq}) is provided to eliminate Poisson’s ratio effect in the plane stress state. The peak stresses in compression ($f_c^{'ef}$) and tension ($f_t^{'ef}$) are computed based on the biaxial stress state. The confinement effect was simulated in the “Cementitious2” material through three-dimensional modelling by considering the increase in concrete deformation capacity under triaxial compression developed by Papanikolaou and Kappos (2007). The “Cementitious2”

material accounts for the tension stiffening effect through the factor “ c_{ts} ”. This factor provides a limit for the tensile strength in the tension softening part such that the tensile stresses cannot drop below this value; hence, the concrete between the developed cracks can carry tensile stresses and provide some stiffness to the member that can help in resisting the resulting deflection. This stress limit is $c_{ts} f_t$, where f_t is the concrete tensile strength. The c_{ts} factor is taken 0.4 as recommended by CEB-FIP Model Code (1990). This value was chosen and verified by conducting a sensitivity analysis for several c_{ts} values ranging from 0.2 to 0.6 to check the optimal c_{ts} value for the numerical model.

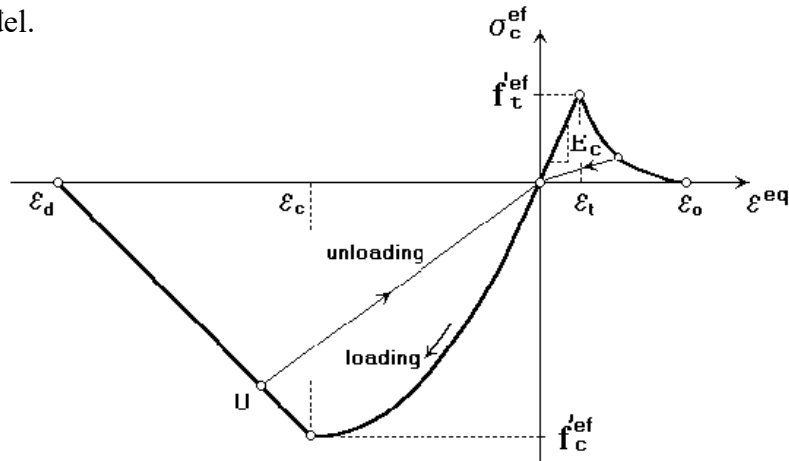


Figure 6.8 Concrete material uniaxial stress-strain relation (Červenka and Červenka 2013)

The GFRP reinforcement is modelled as “1D Reinforcement” material with a linear stress-strain diagram up to rupture. The steel top compression bars and transverse stirrups are modelled as “1D Reinforcement” material, assuming a bilinear with a perfectly plastic stress-strain relationship. The supporting and loading steel plates are 100×200×30 mm, modelled as “SOLID Elastic” steel material with a corresponding Poisson’s ratio and modulus of elasticity of 0.3 and 200 GPa, respectively.

In this study, a perfect bond was assumed between the concrete and GFRP reinforcement; and the concrete-steel contact surface. This assumption simplifies the modelling procedures and computational time. Furthermore, full contact with a perfect bond was assumed between the steel plates and the concrete beams by applying the master-slave contact concept.

Table 6.5 Material properties of concrete, GFRP, and steel reinforcement

Parameter	Formula
Concrete elastic modulus (E_c)*	$4500\sqrt{f'_c}$
Concrete tensile strength (f_t)**	$0.4\sqrt{f'_c}$
Fracture energy (G_f)	$0.000025f_t$
Concrete compressive strength (f'_c)	Experimental value
Concrete Poisson's ratio	0.2
Tension stiffening factor (C_{ts})	0.4
Fixed crack model	1.0
GFRP reinforcement tensile strength (f_{fu})	Experimental value
GFRP bars reinforcement elastic modulus (E_f)	Experimental value
Steel reinforcement elastic modulus	200000 MPa
Steel reinforcement yield strength	400 MPa

* The elastic modulus formula as per CSA S806 (2012)

** The concrete tensile formula as per CSA S6 (2014)

6.5.4 Mesh configuration

Two mesh types were used in this analysis, including hexahedral and tetrahedral meshes. The hexahedral mesh is used for prismatic elements without irregularity with a maximum edge aspect ratio of 3-4:1. Tetrahedral mesh can be used for regular and irregular geometries. The concrete beams are modelled using hexahedral quadratic elements, whereas the steel plates are modelled with tetrahedral quadratic elements. The internal reinforcing bars are not assigned a specific mesh type in the preprocessor phase; when the model turns to the run mode, the meshing of the bar element is activated within the surrounding hexahedral meshes of the beam.

ATENA software (Červenka and Červenka 2013) suggests using a minimum of four elements per member thickness to model the flexural response. Hence, to determine the optimal mesh size, mesh sensitivity models were conducted using four, six, eight, ten, 12, and 16 elements per the concrete beam thickness. The mesh sensitivity analysis was performed on beam N-3#6-c50, and the numerical results were compared to determine the appropriate mesh size. Figure 6.9 shows a typical beam's geometry, mesh configuration, and reinforcement cage.

Figure 6.10(a) shows that the numerical model is sensitive to the number of mesh elements per beam thickness. The beam with a thickness of eight elements provided similar behaviour to the beam with six elements per thickness and different results from the beam with four elements at the service and ultimate stages. Moreover, the results of the beams with 8, 10, 12, and 16

elements are relatively close and similar, as illustrated in Figure 6.10(b). Based on this comparison, eight elements per beam thickness were chosen as a reliable number of elements per beam thickness with a mesh size of 50 mm.

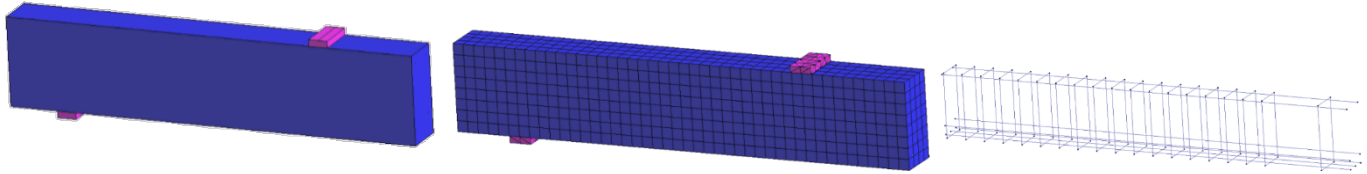


Figure 6.9 Geometric model and mesh configuration of beam N-5#5-c50

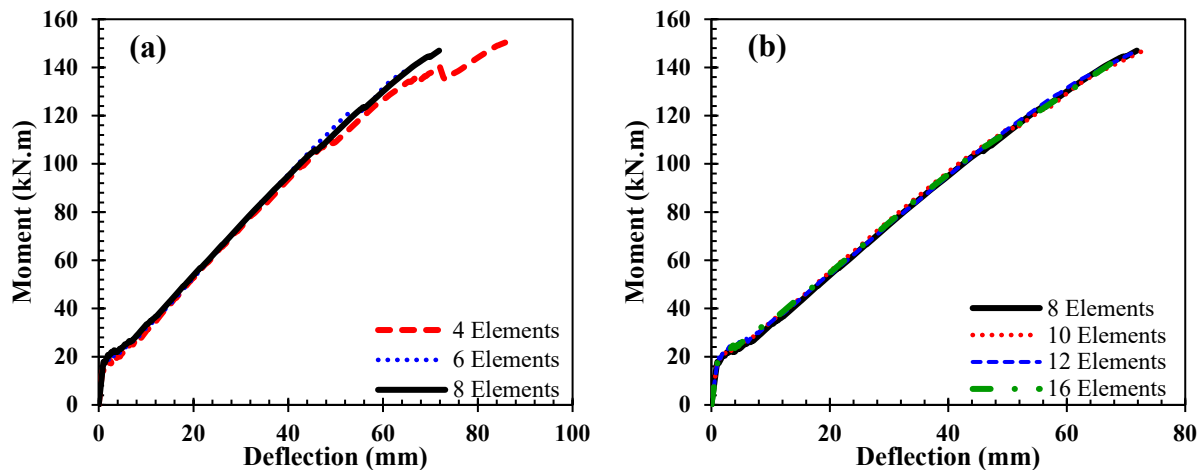


Figure 6.10 Mesh sensitivity of beam N-3#6-c50

6.5.5 Loading and boundary conditions

The load is defined as a prescribed deformation at a middle node of the top steel plate. The load is applied with a displacement control through incremental load steps to mimic the actual testing conditions. Each load step had a displacement value of 0.1 mm and was applied with several load steps in an incremental approach until the failure of the beam. These small incremental displacements allow for capturing the behaviour of the beam before and after cracking, in addition to avoiding any overshooting in the load during the analysis.

The beams are simply-supported with roller and hinge supports. Due to the symmetric conditions of the beams, half of the beam was modelled to reduce the computational time of the analysis. The boundary conditions are simulated in the half-modelled beam by defining the roller support at one side. The software automatically considers the hinge support on the other side in the computation process to maintain the member’s stability. The surface of the beam along the

axis of symmetry was restrained in the beam length direction (x-direction) to define symmetry along that surface.

6.5.6 Failure criteria and solution strategy

The experimental beams are designed as compression-controlled sections that fail by concrete crushing in compression. Concrete crushing was assumed to occur when the principal strains at the concrete outermost compression fibres exceed the ultimate concrete strain of 0.0035, according to CSA S806 (2012). The GFRP bar rupture occurs when the axial stresses in the GFRP reinforcement exceed the bar's tensile strength. Newton-Raphson approach is utilized as a solution method. In the Newton-Raphson method, the out-of-balance load vector is assessed. Then, the program checks that the convergence criteria are satisfied through a linear solution using the out-of-balance loads. If convergence criteria are not satisfied, the out-of-balance load vector is re-assessed, and the stiffness matrix is updated. This convergence check is performed in many iterations until the convergence is achieved.

6.5.7 Model validation results

Figure 6.11 illustrates the load-deflection comparisons between the experimental and numerical results for the six beams. Generally, the relations in Figure 6.11 show a good agreement between the experimental and numerical load-deflection graphs. The models captured the pre-cracking and post-cracking slopes similar to the experimental results. Furthermore, the model provides a good coherency of the cracking loads, the deflections at the service and ultimate stages, and the ultimate moment capacities. The load-deflection relationships demonstrate that the numerical model can capture the flexural response of concrete beams reinforced with GFRP bars. The modelled beams experienced concrete compression crushing similar to the experimental beams, with a principal compressive strain greater than 0.0035. Prior to crushing, the principal strains reached 0.0035 in the top compression zone, and when the crushing occurred, the principal strains in some beams jumped significantly through one or two load steps to reach values much higher than 0.0035.

Table 6.6 shows a comparison between the experimental and numerical results for the cracking moments, the moments and deflection values at the service stage ($0.33M_n$) and ultimate (failure) stage. The results presented in Table 6.6 show that the numerical results in terms of the

moments and deflections are close to the experimental results, with an error falling around 10%. The results of the numerical models demonstrate a good correlation with the experimental results, which show the high proficiency of the numerical model for conducting a parametric study.

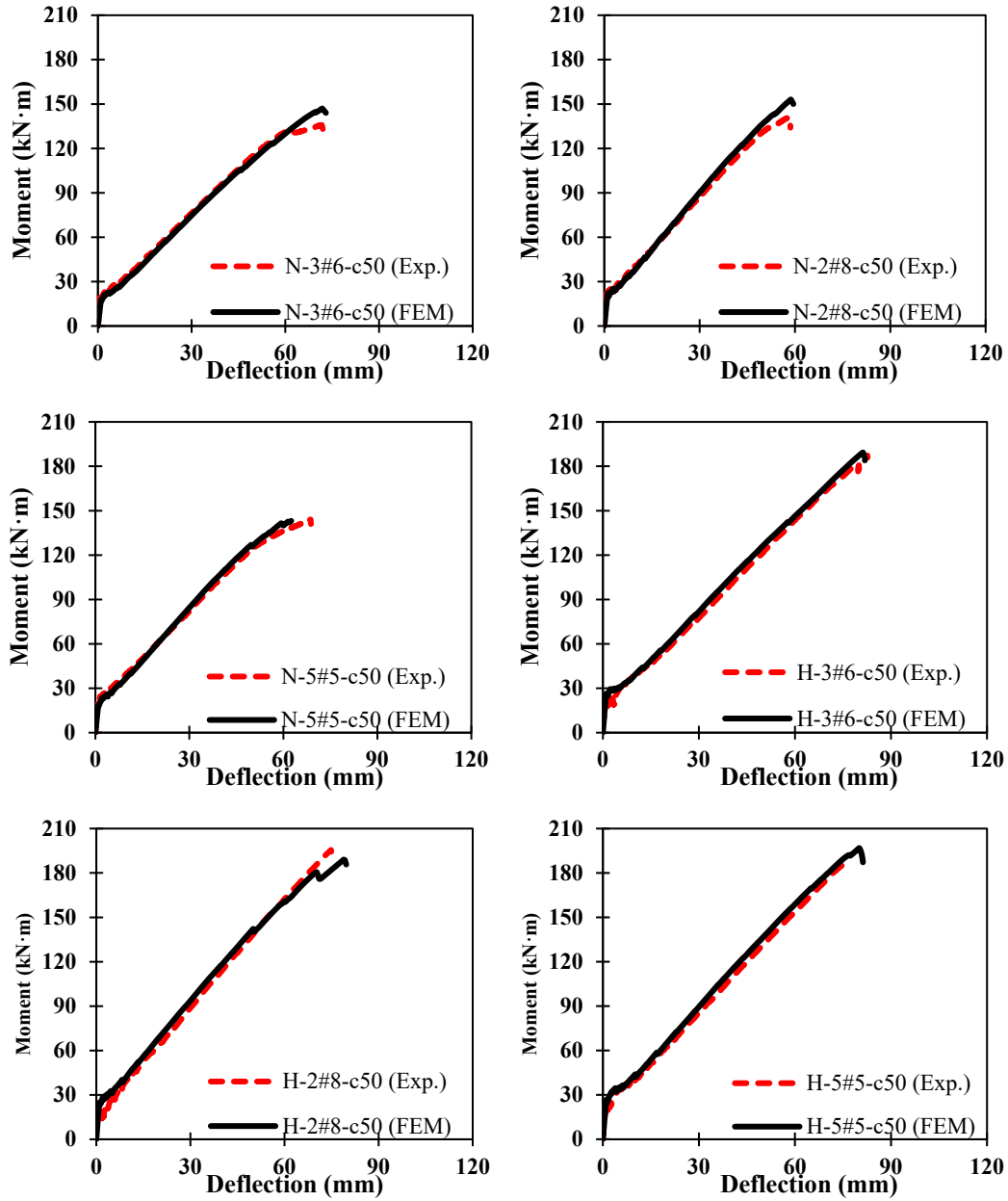


Figure 6.11 Comparison between the experimental and numerical deflections

Table 6.6 Experimental and numerical results of the validated beams

Beam	f'_c	Experimental				FEM				Exp./FEM			
		M_{cr}	M_n	$\delta_{failure}$	$\delta_{0.33M_n}$	M_{cr}	M_n	$\delta_{failure}$	$\delta_{0.33M_n}$	M_{cr}	M_n	$\delta_{failure}$	$\delta_{0.33M_n}$
		MPa	kN.m	kN.m	mm	mm	kN.m	kN.m	mm	mm	kN.m	kN.m	mm
N-3#6-c50	35.7	18.1	136	72	16.0	17.8	147	71	17.7	1.02	0.93	1.01	0.90
N-2#8-c50	35.7	19.6	141	59	13.8	20.5	153	59	15.3	0.96	0.92	1.01	0.90
N-5#5-c50	35.7	18.5	147	69	15.7	18.2	143	64	14.7	1.02	1.03	1.08	1.07
H-3#6-c50	70.8	21.6	187	83	23.7	24.3	190	81	22.5	0.89	0.99	1.02	1.05
H-2#8-c50	70.8	21.0	195	75	21.7	23.5	189	79	19.6	0.89	1.03	0.95	1.11
H-5#5-c50	70.8	22.7	186	76	20.8	25.1	192	73	19.2	0.90	0.97	1.04	1.08

6.6 Numerical parametric study

A parametric study was conducted to investigate the effect of increasing the concrete compressive strength on the flexural and serviceability performance of the experimentally tested concrete beams (3#6-c50, 2#8-c50, and 5#5-c50). The validated beams had concrete compressive strengths of 35.8 MPa and 70.8 MPa. The parametric study extended the concrete compressive strength values to 25 MPa, 45 MPa, 55 MPa, 65 MPa, 75 MPa, 85 MPa, and 95 MPa, with a total of 21 models for the three beams' reinforcement configurations.

This parametric analysis would provide a clear conception for the designers to comprehend the influence of changing the compressive strength on the flexural and serviceability performance of the GFRP-RC beams and provide appropriate design recommendations for the different design provisions. The flexural and serviceability behaviour of the modelled beams were evaluated in terms of the failure mode, ultimate capacity, cracking moments, crack propagation, deflections at failure, and at the service stages.

6.6.1 Results and discussion

6.6.1.1 Cracking behaviour and failure mode

Figure 6.12 illustrates the propagation of cracks at the service load of $0.33M_n$ for beam 3#6-c50 at 35 MPa, 65 MPa, and 95 MPa. Figure 6.12 shows that the number of cracks slightly increases by increasing the concrete compressive strength. Furthermore, the crack height increases by increasing the concrete strength at the same service load level ($0.33M_n$), which conforms with

the cracked elastic theory; since by increasing the concrete strength, the stress in the GFRP reinforcement increases for the same service load level ($0.33M_n$), the neutral axis will be shifted towards the compression zone, resulting in smaller neutral axis depth.

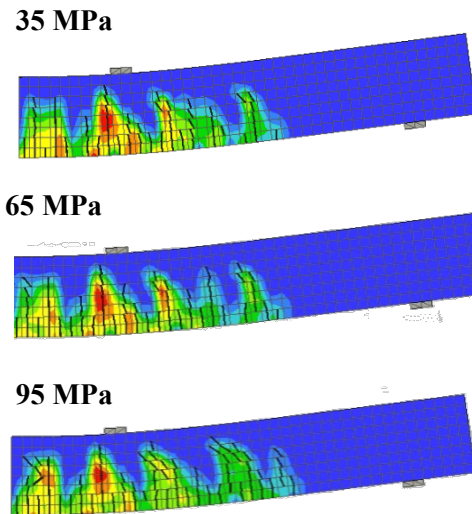


Figure 6.12 Cracks propagation of beam 3#6-c50 at different concrete strengths at $0.33M_n$

The modelled beams failed due to concrete compression crushing followed by GFRP bar rupture. It is noteworthy that increasing the concrete compressive strength resulted in increasing the stress in GFRP reinforcement at failure; this might alter the failure mode in the case of beams with low reinforcement ratios from concrete crushing to GFRP bar rupture, which eventually will influence the cracking behaviour and deformability of the beams.

6.6.1.2 Evaluation of moments and deflections

Figure 6.13 shows the relationships between the concrete compressive strength versus the moment capacities and the deflections at the service stage. The moment capacities and deflection values at concrete strength of 25 MPa were taken as reference values to investigate the influence of changing the concrete compressive strength on the failure moments and the deflection values for all the beams at $0.33M_n$ of the reference beams with a concrete compressive strength value of 25 MPa (i.e., 33% of the nominal moments of beams 3#6-c50, 5#5-c50, and 2#8-c50 at concrete compressive strength of 25 MPa). The values on the Y-axis represent the rate of increase of the moment capacities and deflection values at different concrete strengths as a percentage of the moment capacities and deflection values of the reference beam with concrete strength of 25 MPa.

The relationships in Figure 6.13(a) illustrate that the moment capacity is sensitive to the concrete compressive strength, with an approximate 10% increase in the moment capacity for each 10 MPa increment for beam 2#8-c50. This percentage is higher for beam 3#6-c50 (with a lower reinforcement ratio) up to concrete strength of 45 MPa and lower for beam 5#5-c50 (beam with two reinforcement layers). The failure moments of beam 5#5-c50 showed less sensitivity to the increase of the concrete strength compared to beams 2#8-c50 and 3#6-c50, even though beam 5#5-c50 had a reinforcement ratio of 1.45%, similar to beam 2#8-c50 of 1.51%. The reason might be that the distance from extreme compression fibre to the centroid of tension reinforcement decreases by increasing the number of reinforcement layers; hence at higher concrete strengths, the rate of increasing the moment capacity becomes lower for the two-layer beams compared to the one-layer beams having the same reinforcement ratio.

Figure 6.13(b) shows that the deflection values at $0.33M_n$ of the reference compressive strength value (25 MPa) are sensitive to the increase in the concrete compressive strength. There is a reduction in the deflection values at $0.33M_n$ by increasing the concrete strength from 25 MPa to 65 MPa by 27%, 17%, and 20% for beams 3#6-c50, 5#5-c50, and 2#8-c50, respectively. The deflection decreased steadily by increasing the concrete compressive strength for beam 3#6-c50. The deflection of beam 5#5-c50 decreased at a lower rate up to concrete compressive strength of 75 MPa, unlike beam 2#8-c50, where the deflection decreased at a higher rate up to concrete strength of 65 MPa. At a concrete strength of 95 MPa, the deflection at $0.33M_n$ decreased by 44%, 29%, and 34% for beams 3#6-c50, 5#5-c50, and 2#8-c50, respectively, compared to the deflection values at 25 MPa.

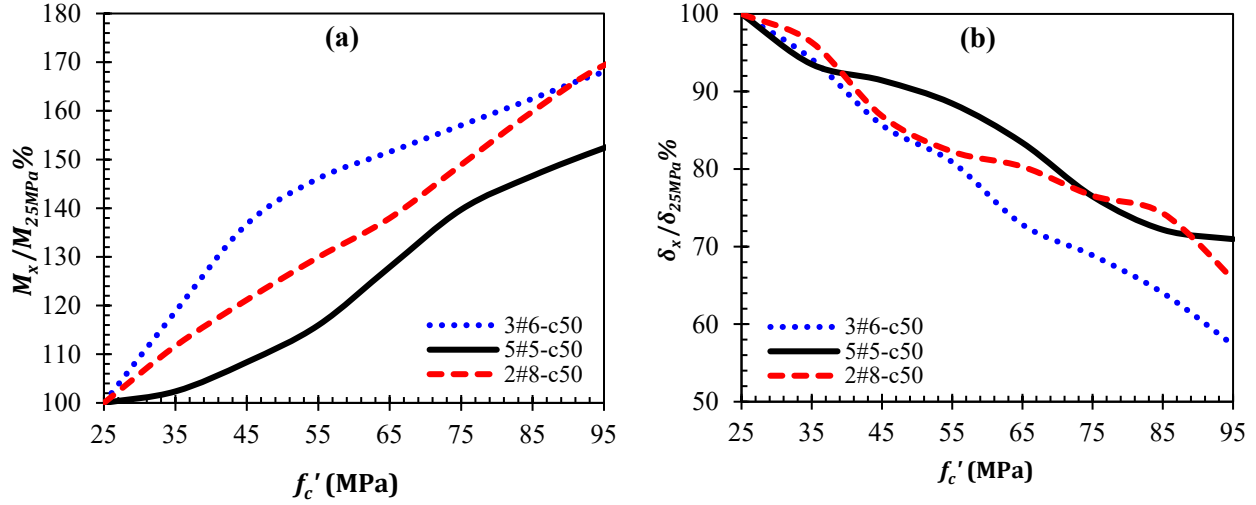


Figure 6.13 Sensitivity of the modelled beams to the concrete compressive strength

6.6.1.3 Evaluation of the deflection equations in CSA S806 (2012) and ACI 440.1R (2015)

Figure 6.14 illustrates the relationships between the concrete compressive strengths and the deflection values at $0.33M_n$ of the reference beams with a concrete compressive strength value of 25 MPa. The deflection values were predicted at $0.33M_n$ and at different concrete strengths by the CSA S806 (2012) and ACI 440.1R (2015) deflection Equations (6.2) and (6.3) using the moment capacities recorded from the numerical models.

CSA S806 (2012)

$$\delta_{max} = \frac{PL^3}{24E_c I_{cr}} \left[3\left(\frac{a}{L}\right) - 4\left(\frac{a}{L}\right)^3 - 8\eta\left(\frac{L_g}{L}\right)^3 \right] \quad 6.2(a)$$

$$I_{cr} = \frac{bd^3}{3} k^3 + n_f A_f d^2 (1 - k)^2 \quad 6.2(b)$$

$$\eta = 1 - \frac{I_{cr}}{I_g} \quad 6.2(c)$$

$$L_g = a \frac{M_{cr}}{M_a} \quad 6.2(d)$$

ACI 440.1R (2015)

$$\delta_{max} = \frac{Pa}{24E_c I_e} [3L^2 - 4a^2] \quad 6.3(a)$$

$$I_e = \frac{I_{cr}}{1 - \gamma \left(\frac{M_{cr}}{M_a}\right)^2 \left[1 - \frac{I_{cr}}{I_g}\right]} \leq I_g \quad 6.3(b)$$

$$\gamma = 1.72 - 0.72 \left(\frac{M_{cr}}{M_a}\right) \quad 6.3(c)$$

where δ_{max} is the maximum mid-span deflection in mm; P is the applied load in kN; L is the span measured from support to support centerlines in mm; E_c is the concrete elastic modulus in MPa, taken as $4500\sqrt{f'_c}$ per CSA S806 (2012) and $4700\sqrt{f'_c}$ per ACI 318-19 (ACI Committee 408 2019); I_{cr} is the moment of inertia of the equivalent cracked concrete cross-section in mm^4 ; a is the shear span distance measured from the center of the support to the center of the acting point load in mm; η is the ratio between the difference of the gross and cracked moment of inertia and the gross moment of inertia; L_g is the distance measured from the center of the support to the cracking point in a simply supported beam in mm; b is the width of the cross-section in mm; d is the distance from the outermost compression fibres to the center of the GFRP tensile reinforcement in mm; k is the ratio between the neutral axis depth and the reinforcement depth; n_f is the ratio of the elastic modulus of the GFRP to the elastic modulus of concrete; A_f is the total area of the GFRP bars in mm^2 ; M_a is the acting moment in N-mm; M_{cr} is the cracking moment in N-mm; I_e is the effective moment of inertia of the cross-section in mm^4 ; and γ is the factor that considers the variation in stiffness along the member length.

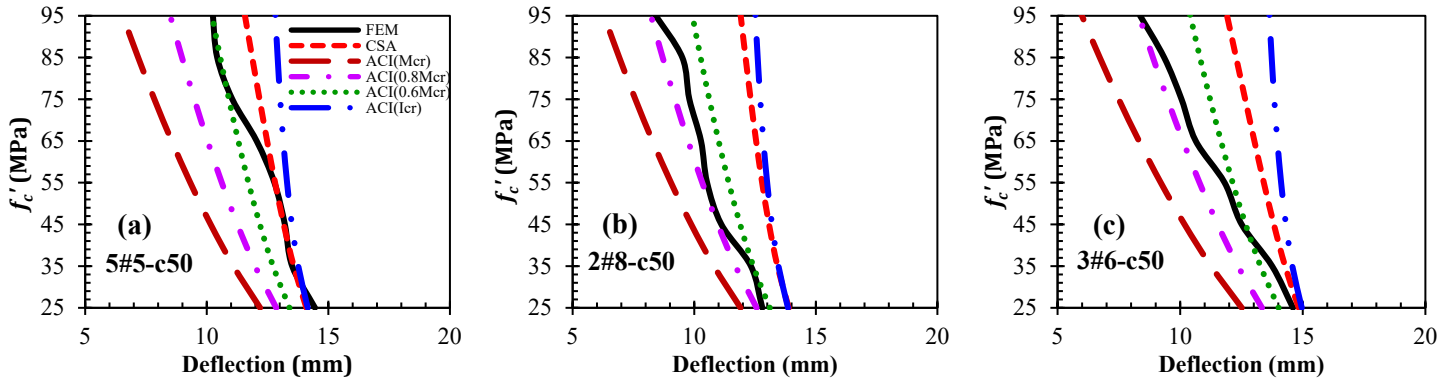


Figure 6.14 Relationships between the concrete strength (f'_c) and the deflection values at $0.33M_n$

It is worth mentioning that Bischoff and Gross (2011) stated that the restrained cracking moment could vary from approximately 90% to 60% of M_{cr} for the FRP-RC members, depending on the reinforcement ratio and amount of free shrinkage. Moreover, Gouda et al. (2022) found that the CSA S806 (2012) deflection equation was insensitive to the change in the cracking moment, unlike the ACI 440.1R (2015) equation which manifested high sensitivity to the cracking moment. Accordingly, the deflection was computed using $0.6M_{cr}$ and $0.8M_{cr}$ for the ACI 440.1R (2015) deflection equation.

As illustrated in Figure 6.14(a-c), the ACI 440.1R (2015) deflection predictions using M_{cr} and $0.8M_{cr}$ yielded unconservative lower deflection values than the output values of the numerical models for beams 5#5-c50, 2#8-c50, and 3#6-c50, for all the concrete strength values. The ACI 440.1R (2015) predictions using $0.6M_{cr}$ provided unconservative deflection results for concrete strengths ranging from 25 MPa to 65 MPa for beam 5#5-c50, as illustrated in Figure 6.14(a), whereas the equation yielded conservative deflection results for all concrete strengths as in beam 2#8-c50 and for concrete strengths greater than 35 MPa as in beam 3#6-c50, as shown in Figure 6.14(b) and (c), respectively. Notably, the ACI 440.1R (2015) equation using I_{cr} and the CSA S806 (2012) equation provided conservative deflection predictions for all the studied beams at different concrete strength values, as illustrated in Figure 6.14(a-c).

The previous results show that the ACI 440.1R (2015) equation using I_{cr} and the CSA S806 (2012) equation provide reasonable predictions for different concrete compressive strengths for beams 5#5-c50, 2#8-c50, and 3#6-c50, with different reinforcement ratios and reinforcement configurations. On the other side, the ACI 440.1R (2015) equation using M_{cr} and $0.8M_{cr}$ highly underestimates the deflection values at different concrete strengths, resulting in unconservative predictions. The ACI 440.1R (2015) equation using $0.6M_{cr}$ provides conservative results for the beams with one-layer reinforcement like 2#8-c50 and 3#6-c50, and unconservative results for the two-layer beam 5#5-c50.

6.7 Conclusions

The current experimental and numerical study investigates the crack and deflection behaviour of GFRP-reinforced concrete beams. Eleven beams reinforced with ribbed GFRP bars were constructed and tested up to failure; the studied parameters were the concrete compressive strength, clear concrete cover to GFRP reinforcement, and the number of reinforcement layers. A numerical model was developed to extend the findings of the experimental test. The numerical model was validated against the experimental results to highlight its accuracy in simulating the real experimental behaviour. The developed numerical model showed good agreement and coherency with the experimental results in terms of the load-deflection relations, cracking moments, ultimate moments, and deflection values at failure and at a service load of $0.33M_n$. A parametric study was conducted to investigate the sensitivity of the GFRP-RC beams' flexural and serviceability behaviour to the change in the concrete compressive strength. Based on the

discussed results, the following conclusions are drawn;

- The load-deflection relations of the HSC beams behaved linearly with no reduction in stiffness up to failure. However, the NSC beams behaved linearly up to 70%-80% of the ultimate capacity; then, the stiffness started to reduce until the crushing of concrete.
- The two reinforcement layers configuration, as in the beam reinforced with 5#5 did not significantly affect the moment capacity compared to the beam reinforced with 2#8 in one layer. Furthermore, increasing the concrete strength from 35.8 MPa to 70.8 MPa significantly increased the moment capacities.
- The beams with higher concrete strength showed lower deflection values than those with lower concrete strength at the same loading level. Moreover, the two reinforcement layers configuration in the beam reinforced with 5#5 exhibited larger deflection values than the beam reinforced with 2#8 in one layer at the same loading level.
- The ACI 440.1R (2015) deflection equation underestimates the deflection values using M_{cr} and $0.8M_{cr}$. On the other hand, using the I_{cr} instead of the I_e provided conservative results for beams with different concrete compressive strengths.
- The ACI 440.1R (2015) deflection equation using $0.6M_{cr}$ provides conservative results for the beams with one-layer reinforcement and unconservative results for the two-layer beam.
- The CSA S806 (2012) deflection equation provides conservative predictions for all the studied beams at different concrete compressive strengths.

Further investigations are required to confirm the results of these studies, and more studies are required to calibrate the deflection equations in the CSA S806 (2012) standard and ACI 440.1R (2015) guideline.

Chapter 7

Numerical investigation of flexural concrete beams reinforced with GFRP bars

7.1 Abstract

The design of flexural concrete members reinforced with glass fibre-reinforced polymer (GFRP) bars depends on the cross-sectional properties, reinforcement arrangement, and material mechanical properties of concrete and GFRP reinforcement. This chapter aims to develop numerical models using the nonlinear finite element method, to investigate the influence of different parameters on the nominal moment capacity and deflection behaviour at the service stage of concrete beams reinforced with GFRP bars. To this aim, nine parameters were investigated, covering a wide range of parameters, including the clear concrete bottom cover, reinforcement ratio, spacing between tensile GFRP bars, spacing between steel stirrups, spacing between GFRP stirrups, bar diameter of steel stirrups, bar diameter of GFRP stirrups, beam size effect, and the number of tensile reinforcement layers in the cross-section. Furthermore, the sensitivity of GFRP-reinforced concrete (RC) beams' nominal moment capacities and deflection values at different service loading levels to the concrete compressive strength and GFRP bars' elastic modulus was investigated. The numerical models were validated with experimental data compiled from the literature. Moreover, the deflection equations in the CSA S806 (2012) standard and ACI 440.1R (2015) guideline were evaluated. The results showed that the moment capacity of the GFRP-RC beams was sensitive to the change in spacing between steel stirrups, while the deflection values at different loading levels were not. The deflection predictions using the CSA S806 (2012) equation were conservative for all the studied parameters, unlike the ACI 440.1R (2015) predictions, which were unconservative for some parameters.

7.2 Introduction

Steel reinforcement has been used for decades due to its high ductility and superior bond performance. However, unlike glass fibre-reinforced polymer (GFRP) material, steel is highly susceptible to corrosion and less durable, particularly in reinforced concrete (RC) structures subjected to an aggressive environment such as marine structures and bridges. GFRP bars are characterized by their high resistance to corrosion. Thus, using GFRP bars as an alternative to steel reinforcement in such structures becomes an effective solution to preclude the detrimental corrosion effects on concrete and increase the service life of RC structures.

The design of GFRP-RC flexural members is often governed by the serviceability limit state, including the deflection and crack widths, due to the low elastic modulus of the GFRP bars compared to steel bars (ACI 440.1R 2015). The serviceability limit state requires maintaining the deflection and crack widths below specified limits by the different design standards and guidelines.

Several experimental studies have investigated the flexural and serviceability behaviour of concrete flexural members reinforced with different surface profiles of GFRP bars (Kassem et al. 2011; El-Nemr et al. 2013, 2016, 2018; Abdelkarim et al. 2019; and Benzecry et al. 2021); however, the experimental work requires enormous human and financial resources support. Generally, numerical modelling could be more economical and abundant than experimental testing, even though experimental tests are required to check the validity of these numerical models.

Few investigations have focused on performing numerical models to conduct parametric studies on GFRP-RC flexural members. The available experimental data could be used to validate these models, hence performing a comprehensive parametric analysis that would cover different parameters. Adam et al. (2015) experimentally tested ten RC simply supported beams reinforced with ribbed GFRP bars. After that, a nonlinear finite element analysis using ANSYS software was conducted to validate the experimental results. The numerical models agreed well with the experimental results in terms of load-deflection relationships, cracking, and ultimate loads.

Bencardino et al. (2016) numerically investigated, using ABAQUS software, the capability of the finite element tool to simulate the behaviour of 17 simply supported concrete beams reinforced with steel, aramid fibre-reinforced polymers (AFRP), GFRP, hybrid steel-GFRP and hybrid steel-

AFRP bars. The modelled beams were compiled from the literature. The numerical results showed good coherency with the experimental results by comparing the failure modes, moment-deflection relations, and ultimate loads for beams with low and normal reinforcement ratios. Kazemi et al. (2020) used ABAQUS software to validate the results of ten simply supported normal-strength concrete beams with concrete compressive strength of 30 MPa. The beams were reinforced with carbon fibre-reinforced polymers (CFRP) and GFRP bars grouted in sleeves in the middle bending zone for some specimens and along the entire bar length for others. The authors performed a parametric study by increasing the concrete strength of the ten beams to 60 MPa. The general results showed good compatibility between the numerical outputs and the experimental results; in addition, numerical modelling has been shown to be a reliable tool for predicting the behaviour of GFRP-RC members. From the available numerical studies, it is clear that there is a shortage of available numerical work; hence, there is a need to perform a comprehensive parametric analysis to study the potential parameters that could affect the flexural and serviceability design of GFRP-RC members.

The primary objective of this chapter is to discuss the impact of changing different parameters on the nominal moment capacity and deflection values at different service loading levels of GFRP-RC beams. This objective was achieved by performing parametric analysis for concrete flexural beams reinforced with GFRP reinforcement. The cross-sectional parameters are the clear concrete bottom cover to GFRP bar, reinforcement ratio (bar diameter), spacing between tensile GFRP bars, the center-to-center spacing between steel stirrups, the center-to-center spacing between GFRP stirrups, bar diameter of steel stirrups, bar diameter of GFRP stirrups, beam size effect and the number of tensile reinforcement layers. On the same side, the material parameters are the concrete compressive strength and GFRP bars' elastic modulus.

7.2.1 Verification beams

Before conducting the parametric study, numerical modelling validation was performed to check the reliability and robustness of the selected material and geometrical models. The validation was performed using experimental results of simply-supported GFRP-RC beams. A total of six GFRP-RC beams were used to validate the numerical model; two beams from El-Nemr et al. (2018), two beams with their duplicates (i.e., four beams) from Ballet (2019), and two beams from Gouda et al. (2022). The compiled beams from El-Nemr et al. (2018) and Ballet (2019) were

transversely reinforced with steel stirrups in the flexural zone with center-to-center spacings of 300 and 317 mm, respectively. However, to validate the modelling of the confinement effect due to closely spaced stirrups in the flexural zone, one beam in Gouda et al. (2022) was reinforced with transverse steel stirrups having a center-to-center spacing of 317 mm, while the other beam had stirrups with a spacing of 100 mm. The two beams in Gouda et al. (2022) had the same cross-sectional dimensions and reinforcement distribution in the elevation as Ballet's (2018) beams, except that the extended concrete part after the supports in Gouda et al. (2022) was 300 mm, and the beams' total length was 4350 mm. The beams were tested under a four-point bending testing scheme. Furthermore, the selected beams had different reinforcement configurations, concrete compressive strengths, and mechanical properties of GFRP bars to ensure that the numerical model can capture the behaviour of GFRP-RC beams with different material properties and reinforcement configurations. Table 7.1 shows the material properties and details of the concrete beams utilized to validate the numerical model. Figure 7.1 shows the elevation and cross-sectional details of the beams.

Table 7.1 Material properties and details of beams for El-Nemr et al. (2018), Ballet (2019), and Gouda et al. (2022).

Ref.	Beam ID	Bar surface	f'_c (MPa)	d_b (mm)	d (mm)	n	A_{f-bar} (mm ²)	$A_{f-total}$ (mm ²)	ρ_f (%)	f_{fu} (MPa)	E_f (GPa)
A	3#20G1	Sand-coated	42.1	20	340.0	3	284	852	1.25	728 ± 24	47.6 ± 1.7
A	6#15G1	Sand-coated	33.5	15	342.5	6	199	1194	1.74	751 ± 23	48.1 ± 1.6
B	A8-1,2	Helically sand	45.5/49.4	25	337.5	2	510	1020	1.51	861 ± 29	54.8 ± 0.3
B	P6-1,2	Sand-coated	42.1	20	340.0	2	284	568	0.84	1507 ± 35	71.7 ± 0.9
C	3#5-c50-s317	Ribbed	35.8	15.9	342.1	3	199	597	0.87	1087 ± 10	60.4 ± 0.5
C	3#5-c50-s100	Ribbed	35.8	15.9	342.1	3	199	597	0.87	1087 ± 10	60.4 ± 0.5

- f'_c is the concrete compressive strength in MPa; d_b is the designated diameter in mm; d is the distance from the extreme compression fibres to the centre of the tensile reinforcing bars; n is the total number of tensile reinforcing bars; A_{f-bar} is the nominal cross-sectional area of the bar in mm²; $A_{f-total}$ is the total cross-sectional area of the tensile reinforcing bars; ρ_f is the reinforcement ratio computed by dividing $A_{f-total}$ by the width (b) and depth (d) of the cross-section; f_{fu} is the GFRP bar tensile strength in MPa; and E_f is the GFRP bar elastic modulus in GPa.

- A is El-Nemr et al. (2018), B is Ballet (2018), and C is Gouda et al. (2022).

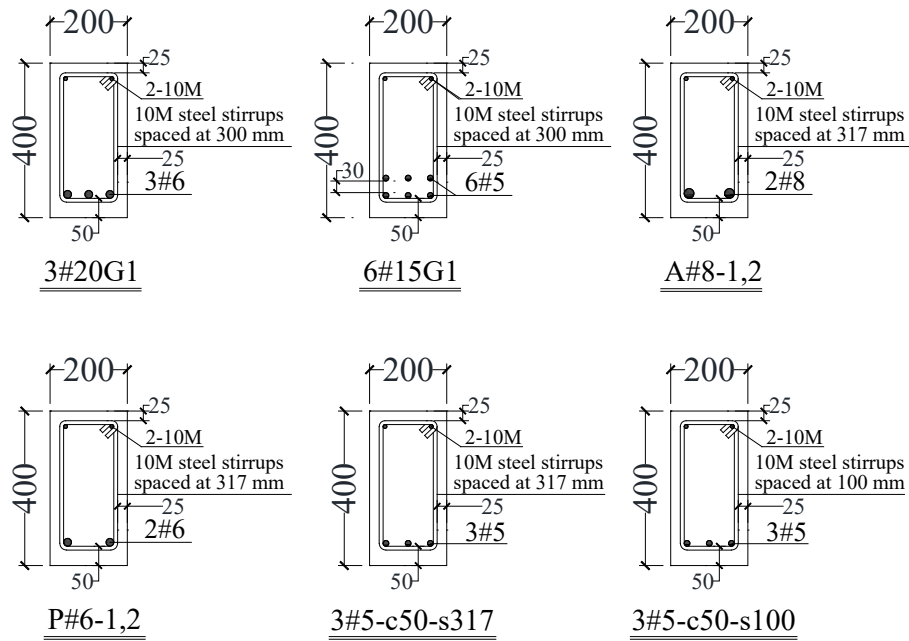
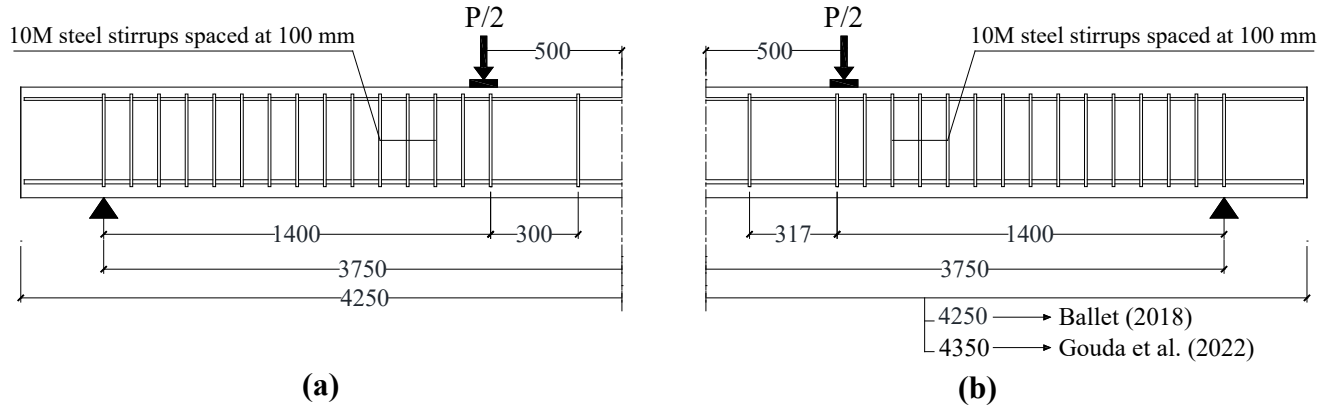


Figure 7.1 Elevation and cross-sectional details of (a) El-Nemr et al. (2018) and (b) Ballet (2018) and Gouda et al. (2022).

7.3 Finite element modelling

This study used the ATENA software-GID solver (Červenka and Červenka 2013) to model flexural concrete beams reinforced with GFRP bars. ATENA software is one of the powerful nonlinear finite element programs specialized in modelling two- and three-dimensional concrete structures.

ATENA software (Červenka and Červenka 2013) offers an accurate analysis of concrete structures and members to mimic realistic conditions by considering various aspects of finite

element analysis, including the concrete tensile and compression behaviour before and after cracking, cracking propagation, tension stiffening in cracked concrete, and material and geometric nonlinearities. The software can capture the structural element failure progression at different loading stages, including FRP rupture and concrete crushing. Furthermore, the software can observe the deformed shape and cracking pattern during analysis using unique and extensive runtime visualization capabilities.

7.3.1 Geometric models

ATENA software (Červenka and Červenka 2013) provides a variety of geometric elements. Most of the elements implemented in ATENA are formulated using a basic interpolation of one-, two-, and three-dimensional iso-parametric linear or quadratic functions that can be extended to a higher order. The elements are integrated by Gauss's integration rule at the integration points by ensuring that the order accuracy is $n(n-1)$, where n is the degree of the polynomial used to approximate the integrated function.

7.3.1.1 Concrete beam and steel plate solid elements

The solid elements in the ATENA software-GID solver (Červenka and Červenka 2013) are composed of a single homogeneous material and can be used for linear and nonlinear plasticity analyses and large deformations. The concrete is modelled using a 3D solid brick element with 20 nodes. Each node has three translational degrees of freedom in the x, y, and z directions, as illustrated in Figure 7.2(a). The 3D solid brick element considers the geometric and material nonlinearities. Furthermore, this element can undergo cracking in three orthogonal directions, plastic deformation and crushing. The steel loading and supporting plates are modelled using tetrahedral elements with eight nodes, as shown in Figure 7.2(b), due to the small thickness of the steel plates (30 mm).

7.3.1.2 Reinforcement truss elements

The GFRP bottom tensile reinforcement, steel top compression bars, and stirrups are modelled using two-node discrete 2D truss elements, as illustrated in Figure 7.2(c). The two-node elements utilize a linear interpolation for the position and displacement with constant stress along the length of the element. The truss elements can be modelled in two- and three-dimensional states by applying axial forces only along the centreline axis of the element. The reinforcement bars are

modelled based on their cross-sectional area, which is defined in the material element’s definition.

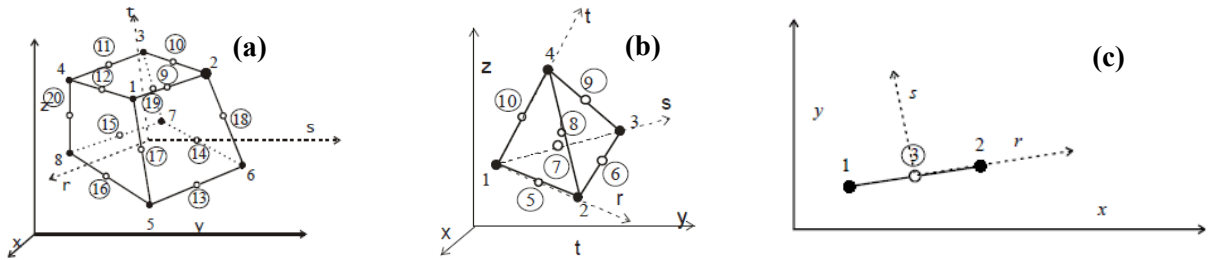


Figure 7.2 Geometric models of (a) brick elements; (b) tetrahedral elements; and (c) truss elements (Červenka and Červenka 2013)

7.3.2 Material Models

The material nonlinearity of the modelled beams arises from the concrete cracking in tension, concrete compression behaviour before crushing, and the nonlinear interaction between the GFRP reinforcement and concrete. Accordingly, the material nonlinearity is simulated by adopting proper material models. ATENA software (Červenka and Červenka 2013) considers the concrete material nonlinearity through fracture-plastic constitutive models and discrete reinforcement stress-strain relations.

7.3.2.1 Concrete material model

The concrete material is modelled using a “Cementitious2” material through fracture-plastic constitutive laws. The concept of the fracture-plastic constitutive model is implemented by combining the constitutive models for compression (plastic) and tension (fracturing) behaviour. The fracture model is based on the classical orthotropic smeared crack formulation and crack band model.

The concrete material model in ATENA (Červenka and Červenka 2013) includes the hardening and softening nonlinear behaviour in compression, fracture of concrete in tension based on fracture mechanics, biaxial stress failure criterion, reduction of compressive strength and elastic modulus after cracking, decrease of the shear stiffness after cracking, tension stiffening effect, modelling of cracks using fixed and rotated crack models, and three-dimensional stress-state failure criterion. The “Cementitious2” material postulates hardening ascending behaviour before attaining the compressive strength and softening descending performance in the post peak part of the uniaxial stress-strain model, as illustrated in Figure 7.3. The numerical inputs for the Cementitious2 material are presented in Table 7.2.

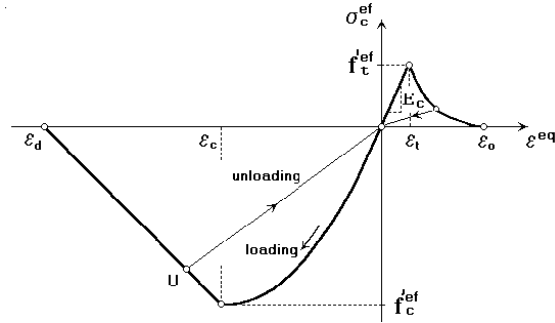


Figure 7.3 Uniaxial stress–strain diagram (Červenka and Červenka 2013).

Table 7.2 Material properties of the concrete material, GFRP, and steel reinforcement

Parameter	Formula
Concrete compressive strength (f'_c)	User's input value
Concrete elastic modulus (E_c)*	$4500\sqrt{f'_c}$
Concrete tensile strength (f_t)**	$0.4\sqrt{f'_c}$
Fracture energy (G_f)***	$0.000025f_t'^{ef}$
Concrete poisson's ratio	0.2
Steel poisson's ratio	0.3
Tension stiffening factor (C_{ts})	0.4
Fixed crack model	1.0
GFRP reinforcement tensile strength (f_{fu})	User's input value
GFRP bars reinforcement elastic modulus (E_f)	User's input value
GFRP bars reinforcement ultimate strain (ϵ_f)	f_{fu}/E_f
Steel reinforcement young's modulus	200000 MPa
Steel reinforcement yield strength	400 MPa

* The elastic modulus formula as per CSA S806 (2012)

** The concrete tensile formula as per CSA S6 (2014)

*** $f_t'^{ef}$ is the effective tensile strength derived from the biaxial failure function and G_f formula as per VOS (1983)

The equivalent uniaxial strain (ϵ_{eq}) is introduced to eliminate Poisson's effect in the plane stress state. The equivalent uniaxial stress-strain diagram and biaxial stress state of concrete are illustrated in Figure 7.3. The peak values of stress in compression ($f_c'^{ef}$) and tension ($f_t'^{ef}$) are calculated according to the biaxial stress state. Before cracking, the concrete tensile behaviour is linearly elastic, whereas after cracking, a fictitious crack model based on a crack-opening law and fracture energy is utilized for the crack opening. The CEB-FIP Model Code (1990) formula is used for the ascending branch of the concrete uniaxial stress-strain law in compression, as presented in

Figure 7.3(a). A fictitious compression plane model is employed for the compression post-peak descending branch, assuming that the compression failure plane is normal to the compressive principal stress direction.

The tension stiffening effect in the “Cementitious2” material is considered by applying a tension stiffening factor “ c_{ts} ”. This factor limits the tensile strength value in the tension softening diagram. The tensile stress cannot drop below the value given by the product of $c_{ts} f_t$, where f_t is the concrete tensile strength. Accordingly, the concrete between the primary cracks can carry tensile stresses and provide some stiffness to the member that can resist the resulting deflection. The recommended value for c_{ts} is 0.4 per CEB-FIP Model Code (1990). This value was chosen and verified by conducting a sensitivity analysis for several c_{ts} values ranging from 0.2 to 0.6 to check the optimal c_{ts} value for the numerical model.

A smeared crack model based on refined crack band theory was used. This model can successfully describe the discrete crack propagation in plain concrete to capture the cracking behaviour, including the crack direction and the maximum crack values within the brick element. There is an option of using a fixed and rotated crack model within the smeared crack model. In both models, the crack is formed when the principal stress exceeds the concrete tensile strength by assuming that the cracks are uniformly distributed within the material volume. Since the direction of cracks in the flexural zone is relatively vertical and perpendicular to the direction of the principal stresses, a fixed crack model was used by applying a value of 1.0, which means that the crack direction fixes at the moment of crack initiation. Finally, in the “Cementitious2” material, the confinement effect was captured through Papanikolaou and Kappos’s (2007) confinement model. This confinement model considers the increased deformation capacity of concrete under triaxial compression, as stated by Papanikolaou and Kappos (2007).

7.3.2.2 GFRP and steel reinforcement material models

The GFRP reinforcement is modelled as a discrete “1D Reinforcement” material. The GFRP stress-strain relationship is linear up to rupture. Steel compression bars and stirrups are modelled as a bilinear with a perfectly plastic discrete “1D Reinforcement” material. The “1D Reinforcement” material model in the ATENA software-GID solver (Červenka and Červenka 2013) exhibits similar tension and compression behaviour. The “1D Reinforcement” material type

can simulate the compressive response of the reinforcement, where buckling occurs, and the strength of the elements in compression is influential. In this study, the GFRP bars are modelled by assuming that the elastic modulus of the bars in compression is the same as that in tension.

7.3.2.3 Loading and supporting plate material model

Steel plates are used to simulate the loading and supporting plates. The thickness of the steel plates is 30 mm. The steel plates are modelled as a “SOLID Elastic” material with a corresponding Poisson’s ratio and modulus of elasticity of 0.3 and 200 GPa, respectively.

7.3.3 Mesh configuration

Each element can be assigned a unique mesh consisting of finite elements, nodal points, and degrees of freedom. There are two main mesh types used in this analysis: hexahedral and tetrahedral. Hexahedral meshes are possible only for prismatic macroelements without openings or irregularities, with a proper aspect ratio. The tetrahedral meshes can mesh most geometries, including regular and irregular prismatic elements. In this study, hexahedral quadratic elements were used for meshing concrete beams, and tetrahedral quadratic elements were used for meshing steel plates.

The mesh generation of a beam model reinforced with an internal bar is performed in two phases. In the first phase, a brick element is used to mesh the beam in the preprocessor, whereas the reinforcing bars are maintained as geometrical elements without mesh. For the second phase, the control is passed to the program run module, and the bar elements are generated as embedded elements within the existing 3D solid brick element mesh. Hence, the meshing of reinforcement is governed by the mesh of solid concrete brick elements. ATENA theory (Červenka and Červenka 2013) suggests using a minimum of four elements per element thickness to model the flexural response of concrete 3D solid brick members. Accordingly, a mesh sensitivity analysis was conducted using four, six, eight, ten, and 12 elements per concrete beam thickness to determine the optimal mesh size. Figure 7.4 illustrates the generated hexahedral and tetrahedral meshes.

The load-deflection graphs of beam 6#15G1 (El-Nemr et al. 2018) are plotted for four, six, eight, ten, and 12 elements per beam thickness and presented in Figure 7.5. The relations in Figure 7.5 show that the numerical model output is sensitive to the number of mesh elements per beam thickness. The load-deflection relation of the beam meshed with four elements differs from the

relations of the beams meshed with six and eight elements and exhibits lower deflection values than the other two beams, as shown in Figure 7.5(a). On the other hand, the beam meshed with eight elements per thickness exhibited relatively similar results to those meshed with six, ten and 12 elements. Accordingly, from this comparison, eight elements per beam thickness were utilized in this study, with a mesh size of 50 mm for a beam with a height of 400 mm.

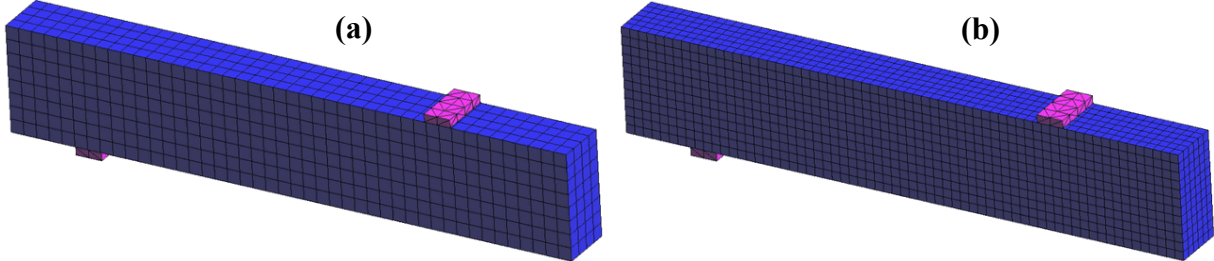


Figure 7.4 Generated mesh for (a) eight elements and (b) 12 elements.

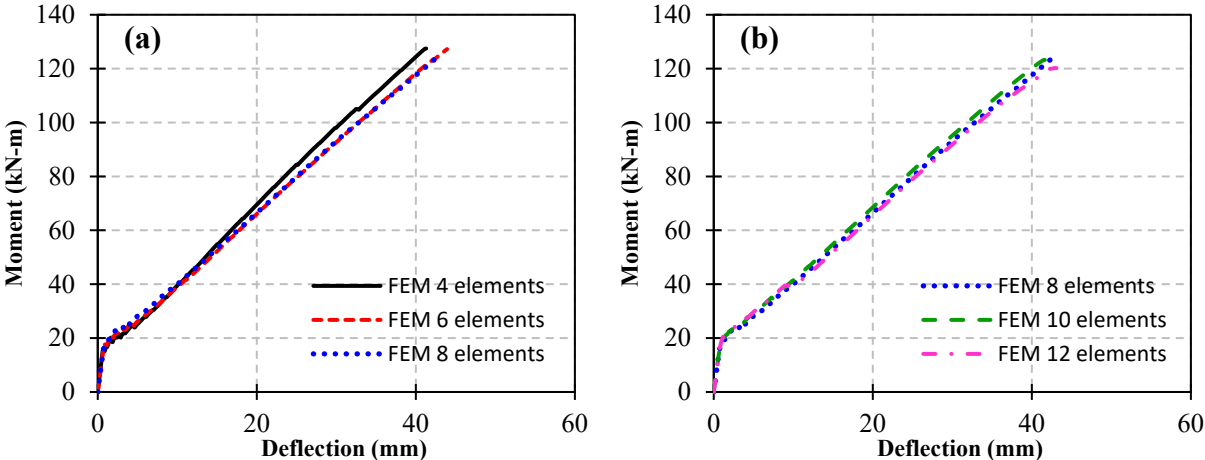


Figure 7.5 Mesh sensitivity of beam 6#15G1 (El-Nemr et al. 2018)

7.3.4 Contact condition between the GFRP and steel reinforcement with concrete

The bond between the GFRP reinforcement and surrounding concrete was modelled by assuming a perfect bond between the two components. This assumption facilitates the modelling procedures and reduces the required computational time. Furthermore, a perfect bond was assumed between the concrete surface and steel plates by employing the master-slave contact concept.

7.3.5 Loading and boundary conditions

The load is applied as an incremental displacement rate to simulate the realistic loading condition of the beams. The load is applied in small increments by 0.1 mm per load step until failure to preclude any numerical instabilities that might result from the sudden increase in the

loading rate. Furthermore, the load is applied at a middle node of the top steel plate, as illustrated in Figure 7.6.

The boundary conditions include the hinged and roller supports and the conditions applied to simulate the symmetry in the modelled beams. Due to the symmetric conditions of the experimental beams, half of the beam was modelled to reduce the computational time. In the case of modelling half of the beam, the hinged and roller supports simulation was achieved by restraining the support bottom centerline on one side of the beam against the displacement in the y and z directions to simulate the roller support, as presented in Figure 7.6. Automatically, the software interprets this simulation by considering the hinged support on the other side of the beam during the analysis to maintain the stability of the model. Since half of the beam was modelled, the vertical side along the axis of symmetry was restrained by applying fixed horizontal x-displacements normal to the line of symmetry, as shown in Figure 7.6.

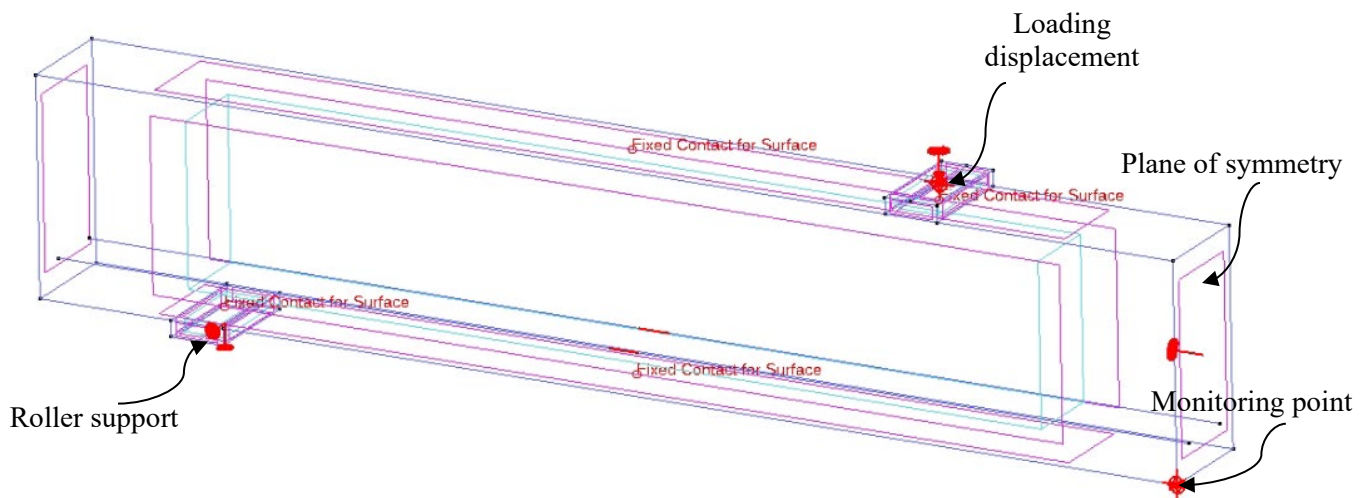


Figure 7.6 Loading and boundary conditions of a typical beam

7.3.6 Failure criteria and solution strategy

The beams were designed as over-reinforced sections to fail by crushing of concrete in compression. Crushing occurs when the principal compressive strains at the top concrete fibres exceed the ultimate concrete strain of 0.0035, as per CSA S806 (2012). The finite element solution approach is based on breaking the total load of the member into a series of load increments over several load steps. In this study, the Newton–Raphson method is utilized as a solution method. This method sets criteria for reaching the convergence equilibrium at the end of each load step and before starting a new load step. The Newton–Raphson method assesses the out-of-balance load

vector. The program checks for convergence by developing a linear solution using the out-of-balance loads. If convergence criteria are not achieved, the stiffness matrix is updated by re-evaluating the out-of-balance load vector. This process is performed in several iterations until the convergence criteria are satisfied.

7.4 Validation results

Figure 7.7 illustrates the load-deflection relations for the experimental and numerical results of the validated specimens. The comparison in Figure 7.7 shows good agreement between the experimental and numerical graphs. The relations show that the numerical model can capture the pre-cracking and post-cracking slopes close to the experimental results. The numerical model shows slightly higher post-cracking stiffness and lower deflection values than the experimental results. Furthermore, the model provides a good coherency with the experimental results in terms of the deflection at different loading stages and the moment capacities. Figure 7.7(e) and (f) compare the experimental and numerical results for specimens 3#5-c50-s317 and 3#5-c50-s100. The relations in Figures 7.7(e) and (f) show that the numerical model simulated the effect of closely spaced transverse stirrups on the deflection behaviour and ultimate capacities, similar to the experimental results. Moreover, Figures 7.7(e) and (f) show that the numerical deflection results up to $4M_{cr}$ are relatively closer to experimental values than other validated specimens. This might be attributed to the better bond between ribbed GFRP rebars and concrete; hence, smaller crack widths and spacings and better crack distribution (i.e., higher tension stiffening) compared to other surface profiles. Furthermore, there is a drop in the experimental moment before failure; this moment drop was captured by the numerical model, as illustrated in Figure 7.7(f); this drop is attributed to the first concrete crushing in the compression zone that resulted in this drop in load. However, due to the confinement effect of closely spaced stirrups (using a spacing of 100 mm) in the middle flexural zone, the beam did not fail and gained more compression capacity until the final compression failure of the beam. The load-deflection relationships demonstrated that the numerical model could capture concrete beams' flexural and serviceability response reinforced with GFRP bars.

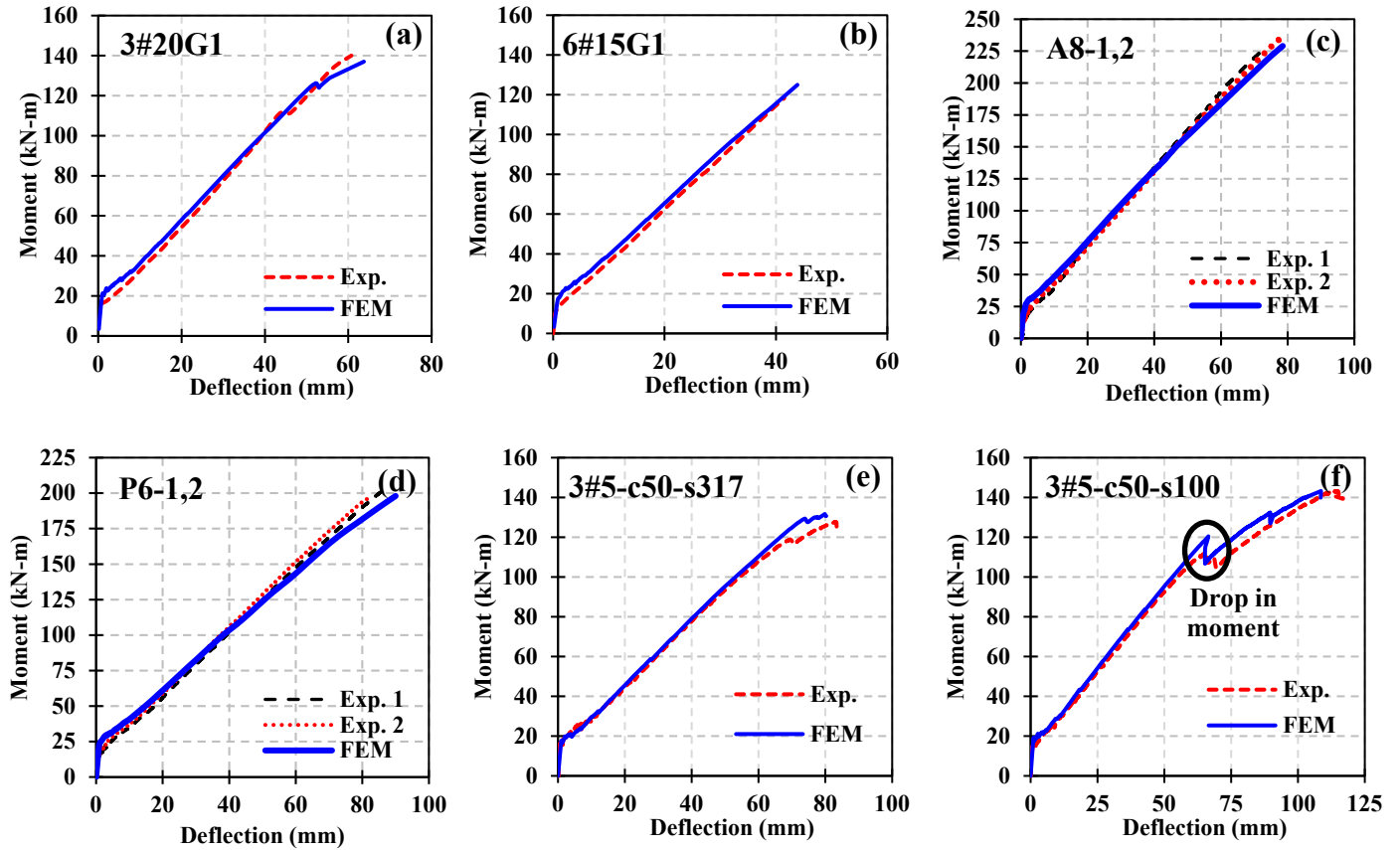


Figure 7.7 Comparison between the experimental and numerical results

Table 7.3 Experimental and numerical results of the validated beams

Beam	Experimental			Numerical			Experimental/Numerical		
	M_n	Deflection		M_n	Deflection		M_n	Deflection	
		0.33 M_n	Failure		0.33 M_n	Failure		0.33 M_n	Failure
kN-m	mm	mm	kN-m	mm	mm	kN-m	mm	mm	
3#20G1	140	16.4	61	137	14.8	63	1.02	1.11	0.96
6#15G1	118	11.2	43	125	11.1	44	0.95	1.02	0.98
A8-1	228	20.3	75	229	19.9	79	1.00	1.02	0.95
A8-2	235	21.9	78	229	19.9	80	1.03	1.10	0.99
P6-1	202	24.5	86	198	21.9	90	1.02	1.12	0.96
P6-2	196	22.6	82	198	21.9	90	0.99	1.03	0.91
3#5-c50-s317	125	18.4	83	131	18.7	80	0.95	0.99	1.04
3#5-c50-s100	140	21.8	117	143	21.0	109	0.98	1.04	1.07

Table 7.3 compares the experimental and numerical results for the moment capacities and the deflection values at $0.33M_n$ and failure. The results in Table 7.3 show that the numerical outputs of the moment capacities and deflections at $0.33M_n$ and failure are close to the experimental

results, with an error falling of approximately 10%. The results of the numerical models show good accuracy compared to the experimental results, demonstrating the numerical model's high efficacy in simulating the experimental beams and conducting a parametric study.

7.5 Parametric investigation

The analysis started by modelling a reference beam designed as a compression-controlled flexural member per ACI 440.1R (2015), as shown in Figure 7.8. Based on this reference beam's configurational and material properties, a parametric study was conducted, including different cross-sectional and material parameters. The included cross-sectional parameters are the clear concrete bottom cover to the GFRP bar, reinforcement ratio (by maintaining the same spacing between the GFRP bars), spacing between GFRP bars (at the same reinforcement ratio), the center-to-center spacing between steel stirrups, the center-to-center spacing between GFRP stirrups in the flexural zone, steel and GFRP stirrups bar diameters (by maintaining the same center-to-center spacing between the stirrups), beam size effect (at the same reinforcement ratio and shear-span to depth ratio of the reference beam), and the number of tensile GFRP reinforcement layers in the cross-section. The details of the studied parameters are illustrated in Figure 7.8.

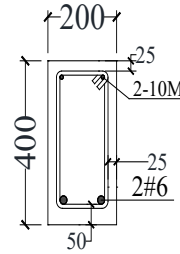
Moreover, a sensitivity analysis was performed on two selected parameters, including the reference beam; the two parameters were the clear bottom concrete cover to the GFRP bar (38, 50, and 60 mm) and reinforcement ratio (ρ_f) for beams 2#5, 2#6, and 2#8, with ρ_f of (0.58, 0.83, and 1.51%, respectively), to discuss the sensitivity of the GFRP-RC beams' flexural and serviceability performance to different material design parameters, including the concrete compressive strength (f'_c) and GFRP bars' elastic modulus (E_f). Each material parameter had a reference value, as shown in Figure 7.8, and the sensitivity bounds were chosen based on the available industrial mechanical properties of the concrete and GFRP bars.

The results of this parametric and sensitivity analysis contribute to understanding the impact of changing different cross-sectional and material design parameters on the flexural and serviceability behaviour of GFRP-RC beams. Furthermore, this study allows the design engineers to realize the capability of the available equations in the CSA S806 (2012) standard and ACI 440.1R (2015) guideline in predicting the moment capacities and deflection values at different service loading levels for the different parameters.

(a)

Reference beam

- Dimensions: (200 x 400 x 4250 mm)
- Tensile reinforcement: 2#6 ($A_{f-total}$ of 568 mm²)
- Top compression reinforcement: 2-10M (steel bars)
- Clear concrete bottom cover to GFRP bar (50 mm)
- Clear concrete top cover to stirrups (25 mm)
- No steel stirrups in the middle flexural zone
- Concrete compressive strength ($f'_c = 35$ MPa)
- GFRP bar ultimate strength ($f_{fu} = 1000$ MPa)
- GFRP bar elastic modulus ($E_f = 60$ GPa)
- Reinforcement ratio (ρ_f) of 0.83%



Cross-section at stirrups location

Cross-sectional Parameters

Parameters

- 1- Clear concrete bottom cover to GFRP bars
- 2- Reinforcement ratio (ρ_f) for beams reinforced with 2#4, 2#5, **2#6**, and 2#8
- 3- Spacing between tensile GFRP bars (at the same reinforcement ratio) for beams reinforced with **2#6**, 3#5, 2#4+2#5
- 4- Center-to-center spacing of 10M steel stirrups in the middle flexural zone
- 5- Center-to-center spacing of #3 GFRP stirrups in the middle flexural
- 6- Bar diameter of steel stirrups for center-to-center spacings of 100 mm and 200 mm
- 7- Bar diameter of GFRP stirrups for center-to-center spacings of 100 mm and 200 mm
- 8- Beam size effect (at the same reinforcement ratio and shear-span to depth ratio of the reference beam)
- 9- Number of tensile reinforcement layers in a beam having dimensions of 400 x 600 x 6250 mm (at the same reinforcement ratio)

Values

- 30, 38, **50**, and 60 mm
- 0.38%, 0.58%, **0.83%**, and 1.51%
- 108.3 mm**, 55.8 mm, and 37.2 mm
- No stirrups**, 250, 200, 150, 100, 50 mm
- No stirrups**, 250, 200, 150, 100, 50 mm
- 10M**, 15M, and 20M
- #3**, #5, and #6
- Beam (400 x 600 x 6250 mm) reinforced with 4#8
- 1 layer (4#8)**;
2 layers (4#6 and 4#5);
3 layers (4#6, 2#5, and 2#5); and
4 layers (4#5, 2#5, 2#5, and 2#5)

Numerical response output

- Deflection values at 20%, 33%, 40%, and 50% of the reference's beam nominal moment
- Moment capacity

Investigations

- Influence of different parameters on the moment capacities and deflection values at different service loading levels.
- Evaluation of CSA S806 (2012) and ACI 440.1R (2015) deflection equations; and moment capacity predictions.

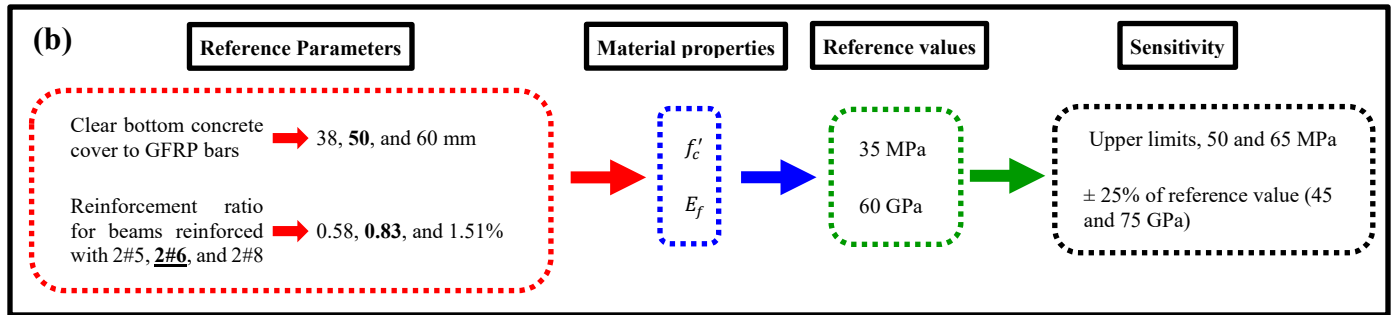


Figure 7.8 Details of (a) cross-sectional parametric investigation; and (b) sensitivity analysis of the material properties

7.6 Discussion of results

The results of the numerical study are presented in terms of moment capacities and deflection values at different loading levels at 20%, 33%, 40%, and 50% of the reference's beam nominal moment. This study aims to evaluate the sensitivity of the flexural and serviceability behaviour of GFRP-RC beams to different configurational and material design parameters, in addition to evaluating the CSA S806 (2012) and ACI 440.1R (2015) moment capacities and deflection predictions at different service loading levels.

7.6.1 Effect of the clear concrete bottom cover

Figure 7.9(a) and (b) show the effect of the clear concrete bottom cover on the moment capacities and deflection values at different loading levels. Figure 7.9(a) shows that the moment capacities decrease by increasing the clear concrete bottom covers to GFRP bars. The reduction in the moment capacity was noticeable for concrete bottom covers ranging from 30 mm to 50 mm, while at a 60 mm concrete cover, the moment capacity was slightly lower than that at a 50 mm concrete cover. For the deflection comparisons in Figure 7.9(b), the deflection values at the different loading levels have shown an increasing trend by increasing the concrete bottom cover, which is attributed to the reduction in the cracked moment of inertia by increasing the bottom cover.

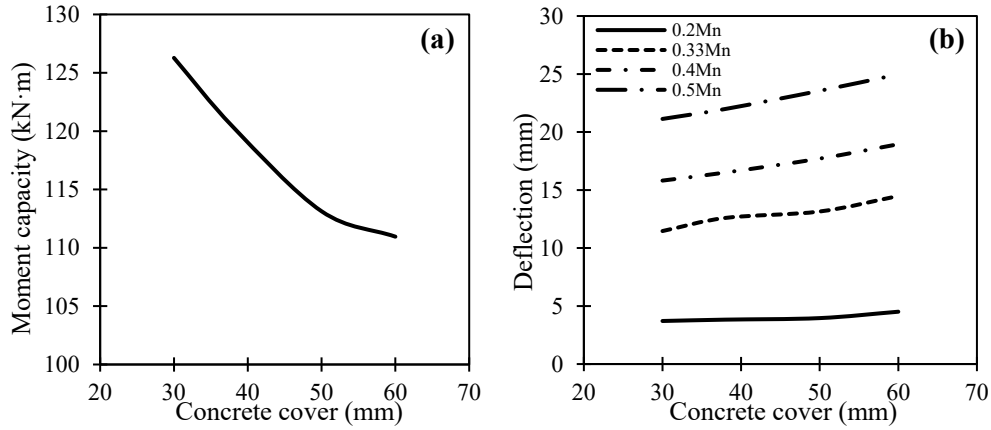


Figure 7.9 Relationships between the clear concrete bottom cover and (a) moment capacities, and (b) deflection values at different service loading levels

7.6.2 Effect of reinforcement ratio and bar spacing

The numerical results showed that there is a direct trend between the moment capacity and the reinforcement ratio (ρ_f). Compared to the reference beam 2#6 with ρ_f of 0.83%, it was found that the moment capacity of beam 2#8, with ρ_f of 1.51%, increased by 40%. On the other side, the moment capacity of beams 2#4 and 2#5 with ρ_f of 0.38% and 0.58%, respectively, decreased by 35% and 19%, compared to the reference beam 2#6. However, the change in spacing between the tensile GFRP bars did not exhibit any noticeable effect on the moment capacity.

Figure 7.10(a) illustrates the effect of changing the reinforcement ratio on the deflection values at the different service loading levels. Compared to the reference beam, there is a significant increase in the deflection values for beams with ρ_f less than 0.83%; while for beams with ρ_f greater than 0.83%, the deflection values decreased at the different service loading levels. This could be attributed to the remarkable effect of increasing the reinforcement ratio on increasing the cracked section's moment of inertia, consequently reducing the deflection values. The relations in Figure 7.10(b) show that the deflection values at the different service loading levels were not sensitive to the reduction in spacing between the tensile GFRP bars, compared to the reference beam, except at a spacing of 37.2 mm, where the deflection slightly decreased compared to the reference beam.

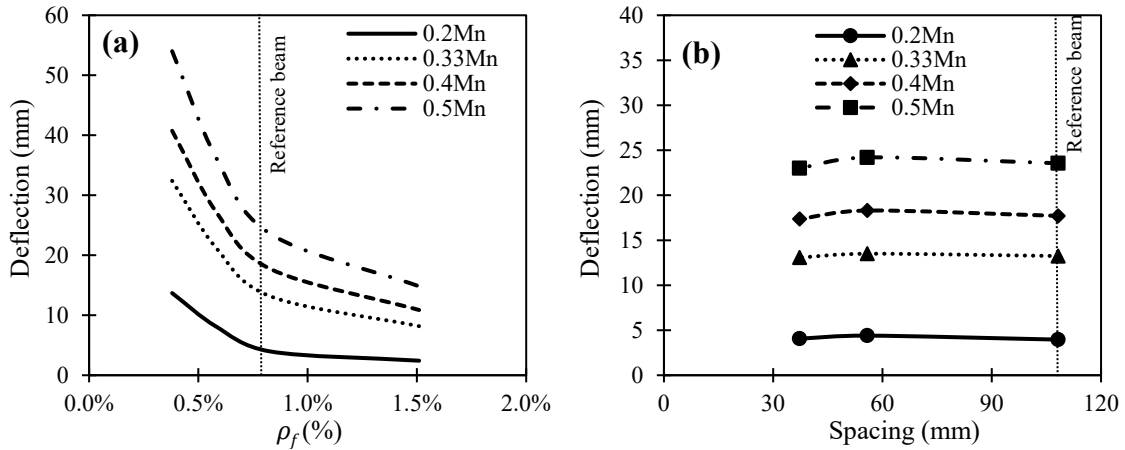


Figure 7.10 Relation between the deflection values at different service loading levels and (a) reinforcement ratio; and (b) spacing between tensile GFRP reinforcement

7.6.3 Effect of steel and GFRP stirrup spacings

Figures 7.11(a) and (b) illustrate the effect of using steel and GFRP stirrups with different center-to-center spacings on moment capacities and the deflection values at different loading levels. Figure 7.11(a) shows that the moment capacity slightly increased by decreasing the spacing between the steel stirrups to 250, 200, and 150 mm compared to the reference beam (without stirrups); however, the capacity significantly increased by up to 32% and 40% of the reference beam as the spacing between the steel stirrups decreases to 100 mm and 50 mm, respectively. For the GFRP stirrups, the moment capacity increased noticeably up to 18% of the reference beam by decreasing the spacing between stirrups to 200 mm; however, for the spacings of 150 mm to 50 mm, the increment of the moment capacity was very marginal compared to that at a spacing of 200 mm. The beams confined with GFRP stirrups showed higher moment capacities for spacings of 250, 200, and 150 mm than the steel stirrup confinement; however, by decreasing the spacing to 100 mm and 50 mm, the steel stirrup confinement provided significantly higher moment capacities compared to GFRP confinement. The reason could be that the monitored strains at failure in the steel stirrups for spacings of 250, 200, and 150 mm were 0.00215, 0.00201, 0.00185, greater than or close to the steel yield strain, 0.002, whereas the strains in GFRP stirrups were much lower than the ultimate strain of the bar, even though the steel stirrups' axial stiffness is higher than the GFRP stirrups' stiffness. In contrast, at a spacing of 100 mm and 50 mm, it was found that the strains in steel stirrups at failure were 0.00145 and 0.00123 lower than the steel yield stress due to increasing the number of stirrups by decreasing the spacing that released the

stresses on the stirrups by distributing the stresses on more stirrups.

The deflection comparisons in Figure 7.11(b) show that the deflection was not affected by decreasing the spacing between the steel and GFRP stirrups. The deflection values of beams with steel stirrups were slightly lower than those of GFRP stirrups at $0.33M_n$, $0.4M_n$, and $0.5M_n$ loading levels, except at a loading level of $0.2M_n$. Accordingly, from Figures 7.11(a) and (b), changing the transverse spacing between steel and GFRP stirrups had a remarkable effect on the moment capacities at certain spacings and an insignificant influence on the deflection values at the different service loading levels.

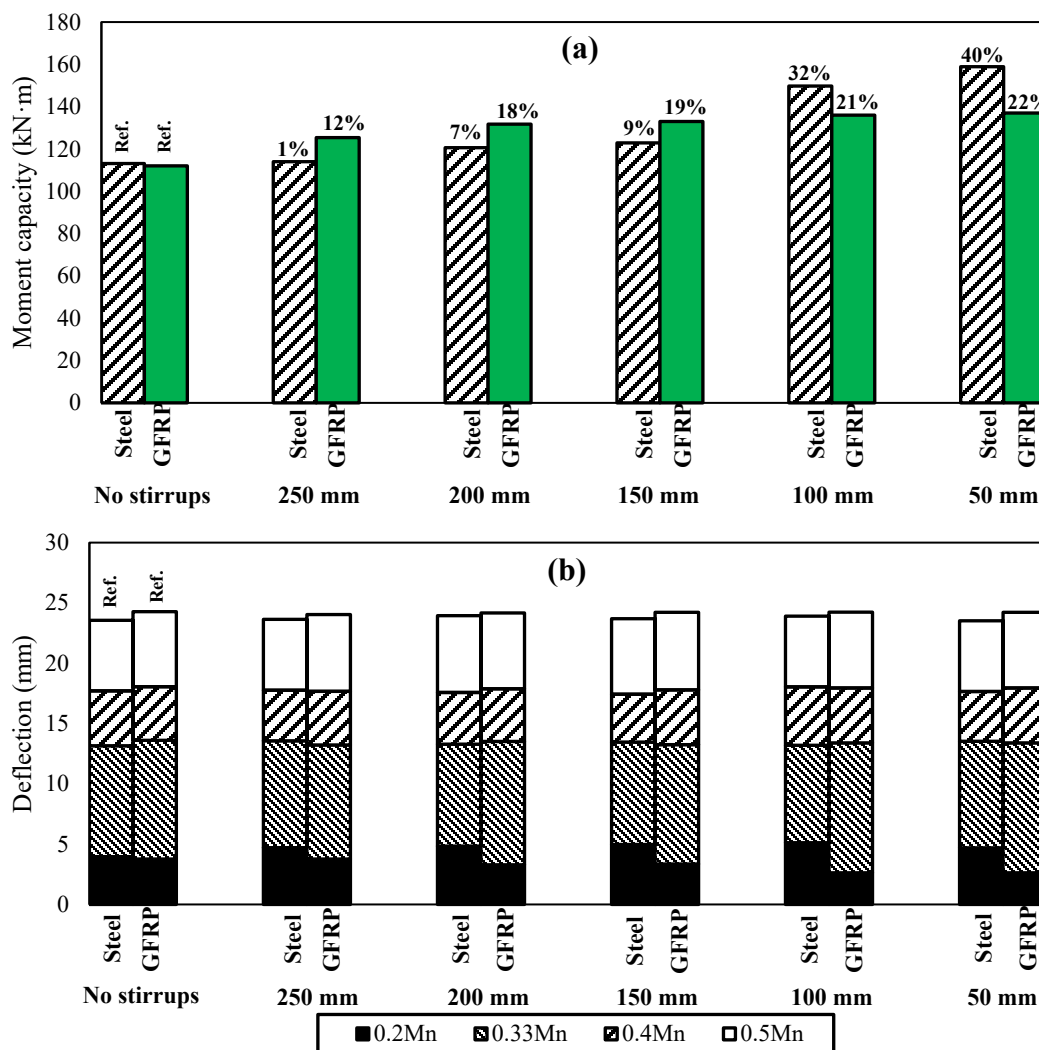


Figure 7.11 Comparison between steel and GFRP stirrups using different spacings between stirrups: (a) nominal moment capacities (M_n); and (b) deflections at various service stage limits

7.6.4 Effect of steel and GFRP stirrup bar diameters

To compare the effect of changing the steel and GFRP stirrup bar diameters at spacings of 200 mm and 100 mm on the moment capacities and deflection values at different loading levels, the reference beams were reinforced with 10M steel and #3 GFRP stirrups at 100 mm and 200 mm spacings, as shown in Figures 7.12(a) and (b). In general, at stirrups spacing of 200 mm, the confinement due to steel stirrups provided slightly higher moment capacities than confinement due to GFRP stirrups for all bar diameters, except for steel and GFRP stirrups of 10M and #3 diameters, respectively; which could be attributed to the higher axial stiffness (EA) of the steel stirrups compared to the GFRP ones. For stirrups spacing of 100 mm, the beams reinforced with steel stirrups provided higher moment capacities than those reinforced with GFRP stirrups for different stirrups diameters. Figure 7.12(a) shows that at a spacing of 200 mm between stirrups, the moment capacity increased by increasing the steel stirrup bar diameter from 10M to 20M by 21%. While at a spacing of 200 mm, increasing the bar diameter of the GFRP stirrups from #3 to #6 slightly enhanced the moment capacities by 5%. At a spacing of 100 mm, the moment capacity slightly increased by 7% by increasing the steel stirrup bar diameter to 20M compared to the reference beam. Similarly, at a spacing of 100 mm between the GFRP stirrups, the moment capacity increased by 10% by increasing the GFRP stirrup bar diameter to #6.

The deflection comparisons in Figure 7.12(b) illustrate that at the same spacing between stirrups, increasing the steel or GFRP stirrups' bar diameters did not affect the deflection values at the different loading levels compared to the reference beam. Moreover, at $0.2M_n$ and $0.33M_n$ load levels, the deflection values of the beams reinforced using steel, and GFRP stirrups were relatively similar. However, at $0.4M_n$ and $0.5M_n$ load levels and at the same spacing, using GFRP stirrups with different bar diameters provided slightly higher deflection values than steel stirrups with similar diameters. This could be attributed to the effect of the GFRP bars' lower elastic modulus compared to steel, which resulted in lower axial stiffness for the GFRP stirrups than steel stirrups, resulting in higher deflection values at higher load levels.

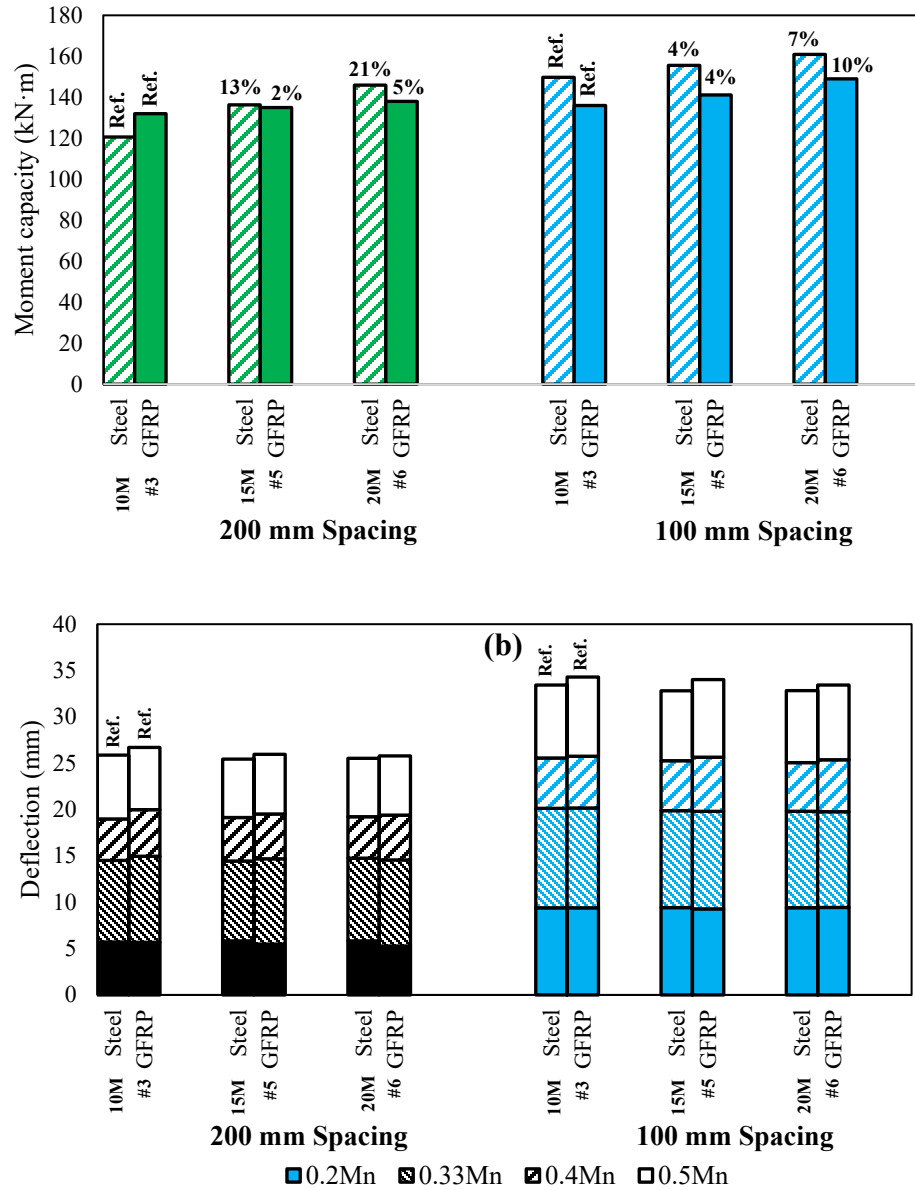


Figure 7.12 Comparison between steel and GFRP stirrups using different spacings between stirrups: (a) moment capacities; and (b) deflections at the service stage

7.6.5 Effect of beam size and number of reinforcement layers

The beam size effect was investigated by comparing beams 2#6 (200 × 400 × 4250 mm) and 4#8 (400 × 600 × 6250 mm), having the same reinforcement ratio and shear span to depth ratio. The deflection values were monitored at 20%, 33%, 40%, and 50% of each beam's nominal moment. In general, beam 4#8 exhibited larger deflection values than beam 2#6, which is attributed to the longer length of the beam and the higher loads achieved at the service stage in

beam 4#8 than in beam 2#6. After that, the effect of the number of tensile reinforcement layers on the moment capacities and deflection values at the different loading levels was investigated. Four beams were studied having similar reinforcement ratios; the first beam was reinforced with 4#8 in one layer, the second beam was reinforced with 4#6 and 4#5 in two layers, the third beam was reinforced with 4#6, 2#5, and 2#5 in three layers, and the fourth beam was reinforced with 4#5, 2#5, 2#5, and 2#5 in four layers. The reference beam was the one-layer beam with 4#8 reinforcement.

As shown in Figure 7.13(a), the moment capacities were reduced by 7%, 11%, and 13% by increasing the number of tensile reinforcement layers from one layer to two, three and four layers, respectively; this was attributed to the reduction in the distance from the extreme compression fibres to the center of the GFRP reinforcement by increasing the number of layers, resulting in reducing the moment capacities. The deflection comparisons in Figure 7.13(b) show that the deflection values increased by increasing the number of reinforcement layers at all the different loading levels; this could be attributed to the reduction in the cracked section's moment of inertia by increasing the number of layers (at the same reinforcement ratio), that resulted in increasing the deflection for the beams with more than one layer of reinforcement. The beams with two layers and three layers of reinforcement had similar deflection values, whereas the four-layer beam had a noticeable increase in deflection values compared to the reference beam.

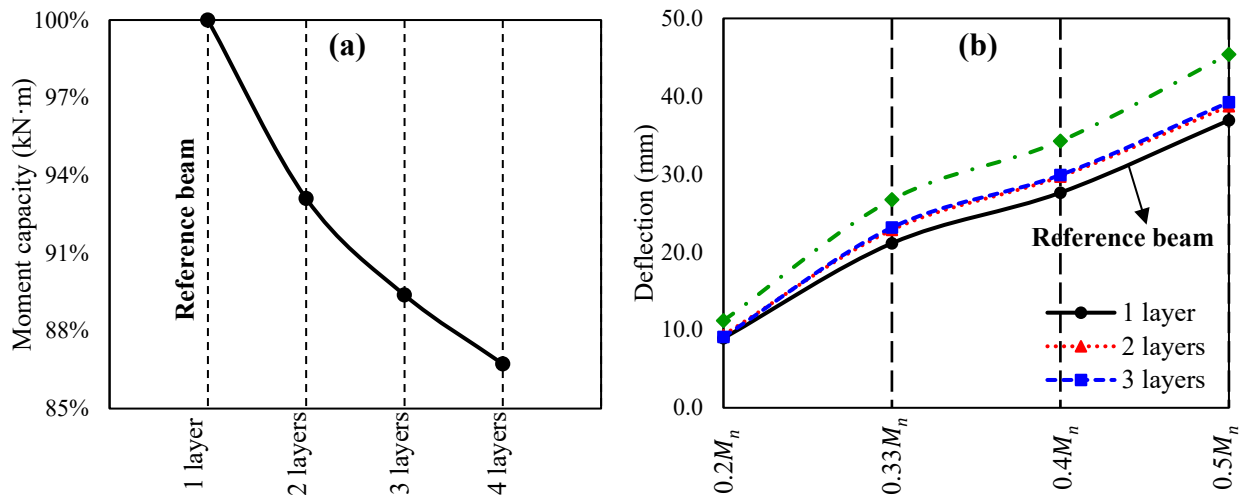


Figure 7.13 Effect on the number of tensile reinforcement layers of (a) moment capacities; and (b) deflection values at different loading levels

7.6.6 Sensitivity of the beams' performance to material properties

The charts in Figure 7.14 show the sensitivity analysis performed to discuss the effect of changing the concrete compressive strength and GFRP bar elastic modulus on the moment capacities and deflection values at the $0.33M_n$ (nominal moment of the reference beam) load level. The concrete compressive strength of the reference beam was 35 MPa, and the studied concrete strength values were 50 MPa and 65 MPa. The GFRP bar elastic modulus reference value was 60 GPa, and the investigated values were $\pm 25\%$ of the reference value (i.e., 45 GPa and 75 GPa). The reference beam was 2#6 with a clear concrete bottom and top covers of 50 mm and 25 mm, respectively. There were no stirrups in the flexural zone, and the top compression bars were 2-10M steel reinforcement. Two configurational parameters have been chosen to be investigated in combination with the concrete compressive strength and GFRP bar elastic modulus; these configurational parameters were the clear concrete bottom cover to GFRP bars (38, 50, and 60 mm) and reinforcement ratio (2#5, 2#6, and 2#8). First, beam 2#6, with a clear concrete bottom cover of 50 mm, was considered as a reference beam with a moment capacity of M_n and deflection values at $0.33M_n$ (as shown in Figures 7.14(a) and (b)). Then, beams 2#6 with 38 mm and 60 mm clear concrete bottom covers were compared to the reference beam. In addition, beams 2#5 and 2#8 were compared to reference beam 2#6. After that, beams 2#6 with concrete bottom covers of 38, 50, and 60 mm and beams 2#5, 2#6, and 2#8 became reference beams to discuss the sensitivity of the moment capacity and deflection values at $0.33M_n$ to f'_c (50 MPa and 65 MPa) and E_f (45 GPa and 75 GPa).

7.6.6.1 Effect of changing the concrete compressive strength

Figure 7.14(a) shows that the concrete compressive strength significantly affects the moment capacities. Increasing the concrete strength from 35 MPa to 50 MPa and 65 MPa had a noticeable effect on beam 2#6 with clear concrete bottom covers of 38 and 50 mm by 27% and 45%, 27% and 44%, respectively, and a lower effect on beam 2#6 with a concrete bottom cover of 60 mm, as shown in Figure 7.14(a). The influence of the concrete compressive strength on enhancing the moment capacity was found to be the highest for beam 2#6, and the effect decreased by increasing the reinforcement ratio as in beam 2#8 to 12% and 17%. The deflection values at $0.33M_n$ decreased by increasing the concrete strength for all the studied beams; however, this deflection reduction was found to be the highest for beam 2#6 with a clear concrete bottom cover of 38 mm compared

to the other concrete covers, as shown in Figure 7.14(b). At the same time, the effect of increasing the concrete strength from 35 MPa to 50 MPa in beam 2#6 reduced the deflection at $0.33M_n$ by 14%, whereas increasing the concrete strength to 65 MPa significantly reduced the deflection for beam 2#5 by 32% compared to the other beams. This comparison shows that the beams with smaller concrete cover and lower reinforcement ratios were more sensitive to the concrete compressive strength than those with larger concrete cover and higher reinforcement ratios.

7.6.6.2 Effect of changing the GFRP bars' elastic modulus

In general, the moment capacity had a direct trend with the GFRP bars modulus of elasticity, as shown in Figure 7.14(a). The sensitivity of the moment capacity to the GFRP bars' elastic modulus was significantly high, with similar percentages for the concrete beams with different clear concrete bottom covers. However, the effect of changing the GFRP bars' elastic modulus was higher for beam 2#5 with a lower reinforcement ratio compared to beams 2#6 and 2#8. Decreasing the GFRP bars' elastic modulus from 60 GPa to 45 GPa reduced the moment capacity of beam 2#5 by 19%, whereas increasing the elastic modulus from 60 GPa to 75 GPa enhanced the moment capacity by 34%. It is also noticed that the effect of the change in the elastic modulus on moment capacity reduces as the reinforcement ratio increases.

As illustrated in Figure 7.14(b), changing the GFRP bars' elastic modulus significantly affected the deflection values at $0.33M_n$ through an inverse relation. There is high consistency in the deflection results at $0.33M_n$ for GFRP bars with an elastic modulus of 45 GPa and 75 GPa for beams with different clear concrete bottom covers. On the same side, the effect of changing the GFRP bars' elastic modulus was found to be slightly higher for beams 2#5 and 2#6 than for beam 2#8 with a higher reinforcement ratio. Increasing the GFRP bars' elastic modulus from 60 GPa to 75 GPa reduced the deflection values at $0.33M_n$ for beams 2#5, 2#6 and 2#8 by 23%, 20%, and 17%, respectively, whereas decreasing the elastic modulus to 45 GPa increased the deflection values by 31%, 36%, and 29%, respectively. The previous comparisons show that the GFRP bars' elastic modulus is an important material parameter that highly influences the moment capacities and deflection values at the service stage for beams with different clear concrete bottom covers and reinforcement ratios.

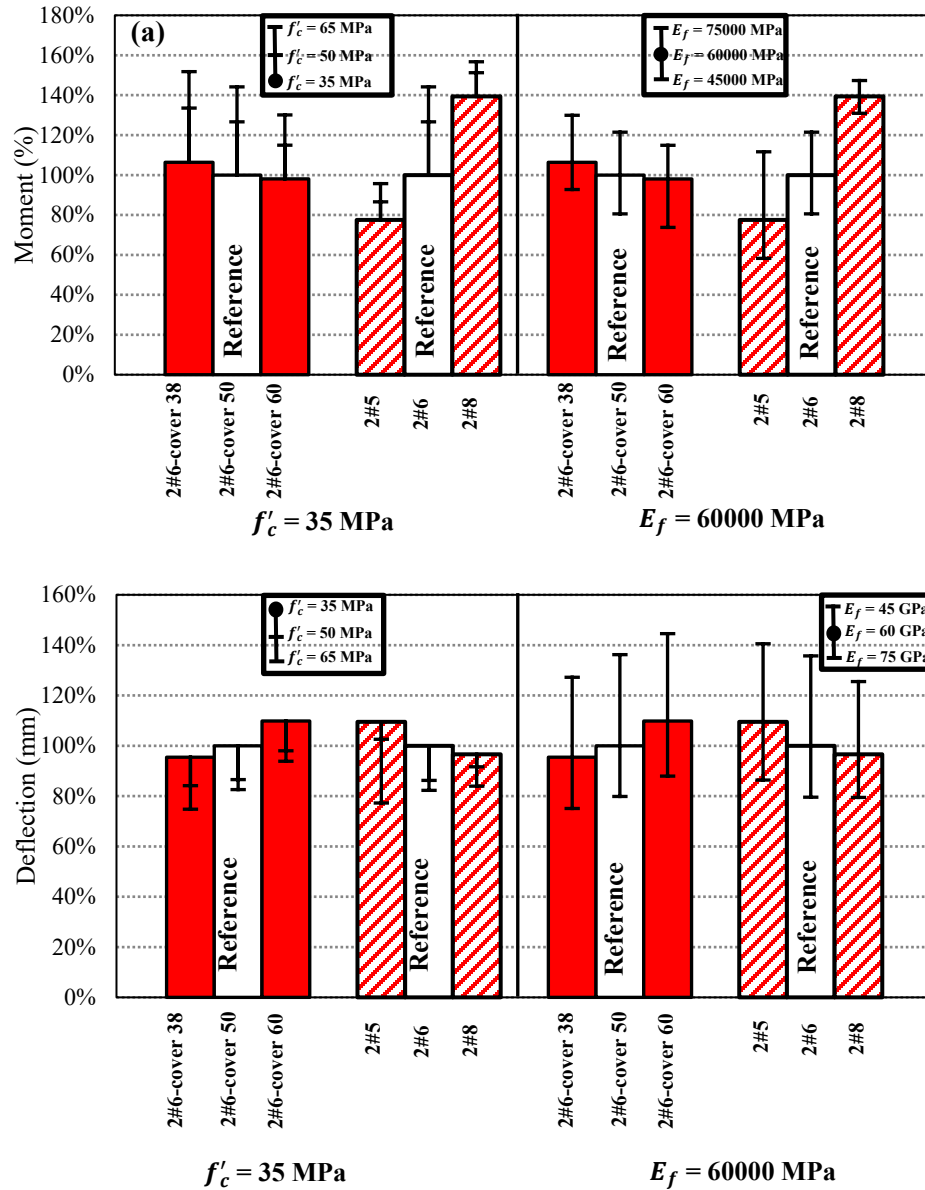


Figure 7.14 Sensitivity of the (a) moment capacities and (b) deflection values at $0.33M_n$ to the concrete compressive strength and GFRP bars' modulus of elasticity

7.7 Evaluation of the deflection equations in CSA S806 (2012) and ACI 440.1R (2015)

The deflection equations in CSA S806 (2012) and ACI 440.1R (2015) are introduced in Eqs. (7.1) and (7.2).

CSA S806 (2012)

$$\delta_{max} = \frac{PL^3}{24E_c I_{cr}} \left[3\left(\frac{a}{L}\right) - 4\left(\frac{a}{L}\right)^3 - 8\eta\left(\frac{L_g}{L}\right)^3 \right] \quad 7.1(a)$$

$$I_{cr} = \frac{bd^3}{3} k^3 + n_f A_f d^2 (1 - k)^2 \quad 7.1(b)$$

$$\eta = 1 - \frac{I_{cr}}{I_g} \quad 7.1(c)$$

$$L_g = a \frac{M_{cr}}{M_a} \quad 7.1(d)$$

ACI 440.1R (2015)

$$\delta_{max} = \frac{Pa}{24E_c I_e} [3L^2 - 4a^2] \quad 7.2(a)$$

$$I_e = \frac{I_{cr}}{1 - \gamma \left(\frac{M_{cr}}{M_a}\right)^2 \left[1 - \frac{I_{cr}}{I_g}\right]} \leq I_g \quad 7.2(b)$$

$$\gamma = 1.72 - 0.72 \left(\frac{M_{cr}}{M_a}\right) \quad 7.2(c)$$

where δ_{max} is the maximum mid-span deflection in mm; P is the applied service load in kN; L is the distance between the supports measured center-to-center in mm; E_c is the concrete elastic modulus in MPa, taken as $4500\sqrt{f'_c}$ per CSA S806 (2012) and $4700\sqrt{f'_c}$ per ACI 318-19 (ACI Committee 408 2019); I_{cr} is the moment of inertia of the equivalent cracked concrete cross-section in mm⁴; a is the shear span distance measured center-to-center from the support to the loading point in mm; η is the ratio between the difference of the gross and cracked moment of inertia and the gross moment of inertia; L_g is the distance measured from center of support to the cracking distance in a simply supported beam in mm; b is the width of the cross-section in mm; d is the distance from the outermost compression fibres to the center of the GFRP tensile reinforcement in mm; k is the ratio between the neutral axis depth and the reinforcement depth; n_f is the ratio of the elastic modulus of the GFRP to the elastic modulus of concrete; A_f is the total area of GFRP reinforcement in mm²; M_a is the acting service moment in N-mm; M_{cr} is the cracking moment in N-mm; I_e is the effective moment of inertia of the cross-section in mm⁴; and γ is the factor that considers the variation in stiffness along the member length.

A comparison was conducted between the numerical deflection values at 20%, 33%, 40%, and 50% of the reference beam nominal moment and the theoretical deflection predictions using the CSA S806 (2012) and ACI 440.1R (2015) equations. The objective of this comparison is to evaluate the capability of the theoretical deflection equations to predict the deflection values at different service loading levels for different parameters. The effective moment of inertia in the

ACI 440.1R (2015) equation was computed using $0.8M_{cr}$, as recommended by Bischoff et al. (2009), to provide a safety factor against the possible cracks that might initiate due to the long-term temperature and shrinkage, where the moment values at the service stage are marginally less than the unrestrained cracking moment. Moreover, the ACI 440.1R (2015) deflection values were computed using the equivalent cracked concrete moment of inertia (I_{cr}) and the effective moment of inertia (I_e) proposed by Gouda et al. (2022), as presented in Eq. 7.3.

$$I_e = \frac{I_{cr}}{1 - \gamma \left(\frac{M_{cr}}{M_a} \right)^3 \left[1 - \frac{I_{cr}}{I_g} \right]} \leq I_g \quad (7.3)$$

The effective moment of inertia Eq. (7.3) proposed by Gouda et al. (2022) assumes that the contribution of the concrete parts between the primary cracks to resist the acting deflection through tension stiffening is less than that proposed by Bischoff et al. (2009); hence, the effective moment of inertia calculated by Bischoff et al. (2009) Eq. (7.2-b) is higher than that computed by Gouda et al. (2022) Eq. (7.3).

The comparison between the numerical and theoretical deflections in Figure 7.15 shows that the CSA S806 (2012) equation provided conservative deflection values for all the studied parameters and at different loading levels, except for the low reinforcement ratio beams 2#4 and 2#5 at the $0.5M_n$ loading level, where the deflection predictions were unconservative.

On the other hand, the ACI 440.1R (2015) predictions using the I_e from Eq. (7.2-b) showed unconservative results for beams with lower GFRP bar elastic modulus and lower reinforcement ratios at $0.2M_n$. However, increasing the loading level to $0.33M_n$ increased the degree of unconservatism for some parameters, including beams with lower concrete strengths combined with either lower reinforcement ratios or larger covers, beams with lower GFRP bars elastic modulus, beams 2#4 and 2#5 with lower reinforcement ratios, and beams with smaller spacing between GFRP bars at the same reinforcement ratios. The degree of unconservatism for the previously mentioned parameters increased by increasing the service loading level to $0.4M_n$ and $0.5M_n$.

Regarding the ACI 440.1R (2015) predictions using the proposed I_e by Gouda et al. (2022) from Eq. (7.3), the results showed that the deflection predictions were conservative at $0.2M_n$. Similarly, the deflection predictions were conservative at $0.33M_n$ except for beams 2#4 and 2#5

with low reinforcement ratios. While at $0.4M_n$ and $0.5M_n$, all the parameters demonstrated conservative deflection predictions except for beams 2#4 and 2#5 at different concrete strengths and the beams reinforced with GFRP bars with lower elastic modulus.

Finally, the ACI 440.1R (2015) predictions using the I_{cr} showed highly conservative results at $0.2M_n$, $0.33M_n$, and $0.4M_n$ for all the parameters. Similarly, at $0.5M_n$, the deflection predictions were conservative for all the studied parameters, except for beam 2#4 and beam 2#5 with concrete strength of 35 MPa and GFRP bars' elastic modulus of 45 GPa.

The comparisons in Figure 7.15 show that the deflection equations of CSA S806 (2012) and ACI 440.1R (2015) using I_{cr} are very conservative in predicting the deflection values at different service loading levels for different parameters. Similarly, the predictions of the ACI 440.1R (2015) equation using the proposed I_e by Gouda et al. (2022) from Eq. (7.3) showed high effectiveness in predicting the deflection values at different service loading levels for different parameters, except for the lower reinforcement ratios beams with different concrete strengths and lower elastic modulus of GFRP bars at higher service loading levels ($0.5M_n$). In contrast, the ACI 440.1R (2015) deflection predictions using the I_e from Eq. (7.2-b) showed unconservative results for different parameters at different loading levels, which demonstrates that Eq. (7.2-b) overestimates the I_e values.

7.8 Comparison between numerical and theoretical moment capacities

A comparison was held between the moment capacities obtained from the numerical models and the values predicted by the CSA S806 (2012) and ACI 440.1R (2015) equations. The theoretical nominal moment capacities were computed without considering the reduction factors. The comparison in Figure 7.16(a) shows that the CSA S806 (2012) provides reasonable predictions for the studied parameters, except for the high reinforcement ratio beam 2#8, all beams reinforced with GFRP bars with an elastic modulus of 45 GPa and 75 GPa, and the confined beams reinforced with steel and GFRP stirrups with spacings ranging from 250 mm to 50 mm and with different bar diameters at the same spacing. The ACI 440.1R (2015) predictions yielded similar results to the CSA S806 (2012) predictions, as shown in Figure 7.16(b), except for the same parameters mentioned above, as well as the high-strength concrete beams with a concrete f'_c of 50 and 65 MPa, where the ACI 440.1R (2015) underestimated the moment capacities. This could be attributed to the variation

in the α_1 and β_1 factors between CSA S806 (2012) and ACI 440.1R (2015), in addition to the higher concrete ultimate strain, with an ε_{cu} of 0.0035, assumed by CSA S806 (2012) than ACI 440.1R (2015), with an ε_{cu} of 0.0030, which results in higher moment capacity predictions for CSA S806 (2012) than ACI 440.1R (2015). As illustrated in Figure 7.16(c), the CSA S806 (2012) and ACI 440.1R (2015) predictions were very close to the numerical moment capacity of the reference beam (200×400 mm reinforced with 2#6); however, increasing the beam size to 400×600 mm reinforced with 4#8 (i.e., similar ρ_f to the reference beam) showed that CSA S806 (2012) overestimated the moment capacity more than ACI 440.1R (2015), and the ACI 440.1R (2015) prediction was closer to the numerical result. Moreover, CSA S806 (2012) slightly overestimated the moment predictions for the beams reinforced with more than one GFRP reinforcement layer, while ACI 440.1R (2015) provided closer results to the numerical ones.

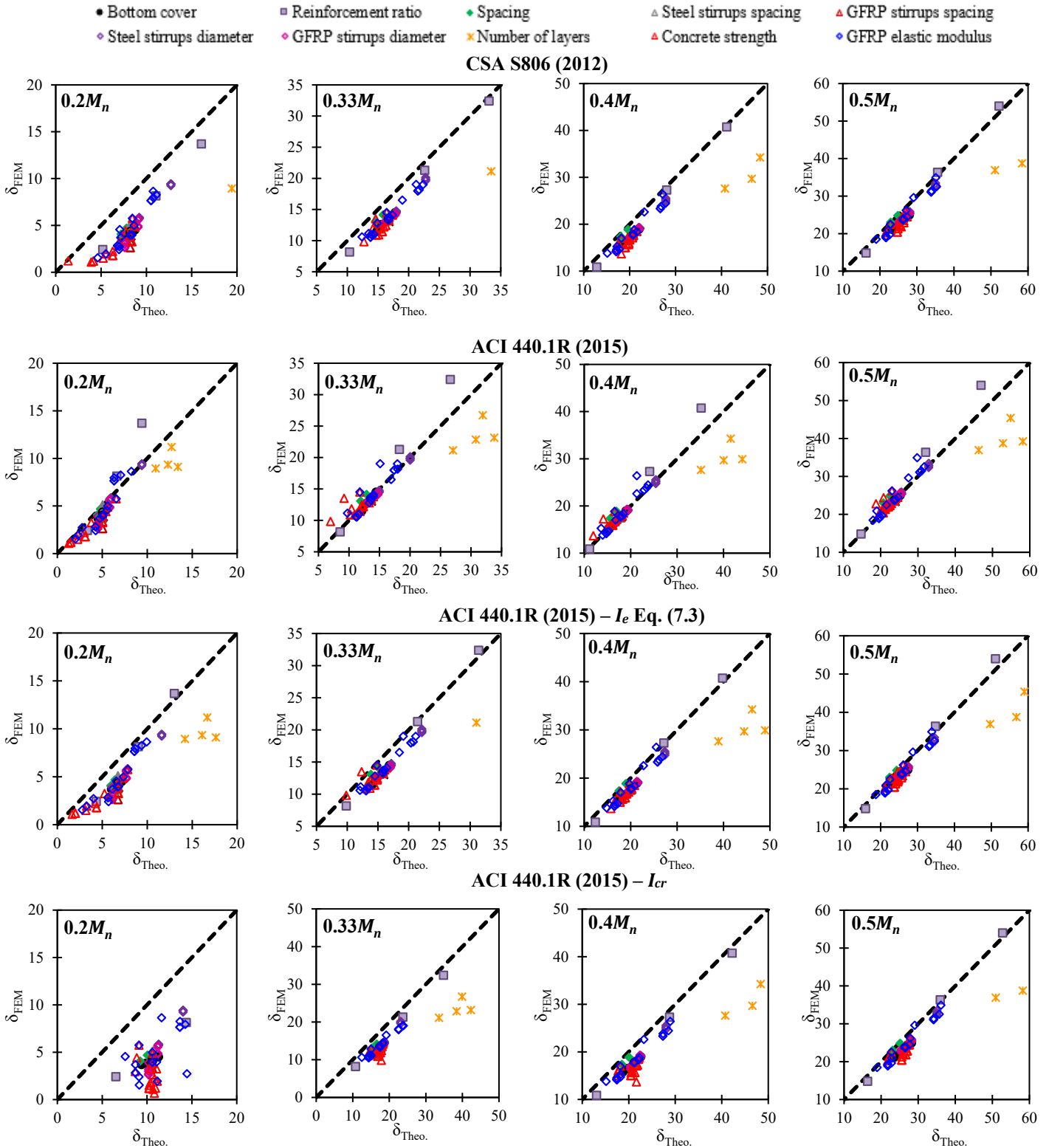


Figure 7.15 Comparison between numerical and theoretical deflection values at different loading level

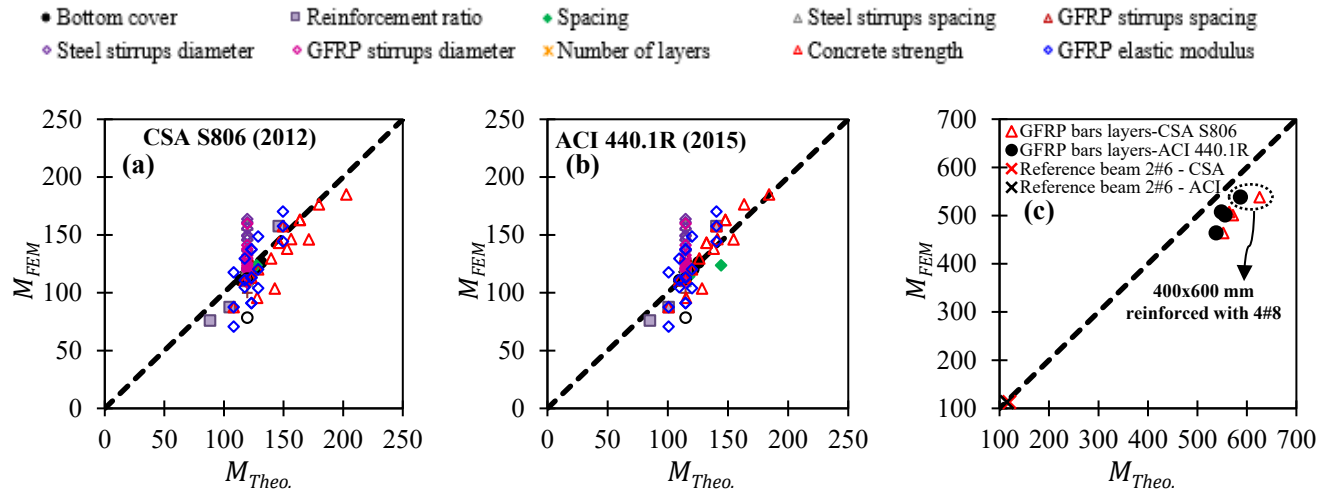


Figure 7.16 Comparison between the numerical and theoretical moment capacities

7.9 Conclusions

This chapter discussed the main parameters influencing the moment capacities and deflection values at different loading levels. The studied parameters were the clear concrete bottom cover, reinforcement ratio (bar diameter), spacing between tensile GFRP bars, the center-to-center spacing between steel stirrups, the center-to-center spacing between GFRP stirrups, bar diameter of steel and GFRP stirrups, beam size effect and the number of tensile reinforcement layers. Moreover, a sensitivity analysis was conducted to discuss the effect of changing the concrete compressive strength and GFRP bars' elastic modulus on the moment capacities and deflection values at different loading levels of GFRP-RC beams. Based on the results of this study, the following conclusions were drawn:

- The increase in clear concrete bottom cover for a beam with a given height showed a slightly decreasing trend on the moment capacity. The deflection values at the same loading levels increased by increasing the clear concrete bottom cover.
- The moment capacity and deflection values at the different service loading levels were highly sensitive to the change in the reinforcement ratio with direct and indirect trends, respectively. However, the change in spacing between the tensile GFRP bars did not show any noticeable influence on the moment capacities and deflection values.
- Using #3 GFRP stirrups at 150 mm spacing, the moment capacity increased by 19% compared to the reference beam, with no stirrups. On the same side, the moment capacity increased by 32% and 40% by decreasing the spacing between the steel stirrups to 100 mm and 50 mm,

respectively, compared to the reference beam. However, decreasing the spacing between the steel and GFRP stirrups did not affect the deflection values at the different loading levels.

- Increasing the steel stirrups bar diameter showed a noticeable enhancement in the moment capacities compared to GFRP stirrups at 200 mm spacing. While at 100 mm spacing between stirrups, the moment capacities were slightly increased by increasing the steel and GFRP stirrups bar diameter.
- At 40% and 50 % of the reference beam's nominal moment, the deflection values were lower for beams reinforced with steel stirrups than beams reinforced with GFRP stirrups at different stirrups diameters.
- The moment capacity showed a decreasing trend by increasing the number of tensile reinforcement layers. Furthermore, the deflection values at the different loading levels increased by increasing the number of tensile reinforcement layers compared to the reference beam, particularly the beam with four reinforcement layers.
- The moment capacities of the same-height beams with clear concrete bottom covers of 38 mm and 50 mm were significantly affected by increasing the concrete compressive strengths to 50 MPa and 65 MPa, more than the beam with a larger clear concrete bottom cover of 60 mm. Moreover, the effect of the increasing concrete strength on enhancing the moment capacity became lower for beam 2#8 with the reinforcement ratio. The deflection values at $0.33M_n$ decreased with increasing concrete compressive strength, and this reduction was found to be the highest for beams with smaller concrete cover and lower reinforcement ratios.
- The GFRP bars' elastic modulus significantly influenced the moment capacity through a direct trend. The effect of the GFRP bars' elastic modulus on the moment capacity was relatively similar for beams with different concrete bottom covers, while this effect was higher for beams with lower reinforcement ratios than for those with higher reinforcement ratios. Moreover, increasing the GFRP bars' elastic modulus significantly decreased the deflection values at $0.33M_n$.
- The deflection predictions of CSA S806 (2012) and ACI 440.1R (2015) using the I_{cr} were conservative for the studied parameters, except for beams with low reinforcement ratios. Similarly, the ACI 440.1R (2015) predictions using the proposed I_e by Gouda et al. (2022) were conservative for different parameters at different service loading levels, except for the lower reinforcement ratios of beams with different concrete strengths and lower GFRP bars'

elastic modulus at a higher service loading level ($0.5M_n$). The ACI 440.1R (2015) deflection predictions using the I_e proposed by Bischoff et al. (2009) yielded unconservative results for different parameters at different service loading levels.

- The CSA S806 (2012) moment capacity predictions were higher than the ACI 440.1R (2015) predictions. The CSA S806 (2012) and ACI 440.1R (2015) underestimated the moment capacities of the beams confined with transverse stirrups. Moreover, the beam size effect and the number of GFRP tensile reinforcement layers were better predicted by ACI 440.1R (2015); however, they were overestimated by CSA S806 (2012).

Chapter 8

Summary, Conclusions, and Recommendations

8.1 Summary

This thesis introduces analytical, experimental, and numerical studies of concrete beams reinforced with ribbed and sand-coated GFRP bars. The main objectives were to (a) analytically investigate the current CSA S806 (2012) development length equation by analyzing 431 beam-bond tests compiled from the literature. The parameters in the development length equations were assessed, and a modified equation was proposed based on a linear regression analysis; (b) experimentally investigate the effect of different parameters on the flexural and serviceability behaviour of 24 full-scale concrete beams. The experimental parameters included in this research were the clear concrete cover to GFRP reinforcement (30, 38, and 50 mm), bar spacing (depending on the bar diameter and the number of bars), bar diameter (#4, #5, #6, and #8), reinforcement ratio, confinement from transverse reinforcement by changing the spacing between stirrups, concrete strength (35 MPa and 65 MPa), bar surface profile, and the number of tensile reinforcement layers; and (c) numerically discuss the sensitivity of the flexural and serviceability performance of the GFRP-RC beams to the different cross-sectional and material parameters. The numerical results were provided in terms of the ultimate capacities, cracking propagation, and deflection behaviour.

The following conclusions were drawn based on the experimental, analytical, and numerical results.

8.2 Conclusions

The findings of this research study are divided into three sections; the first section provides the findings of the analytical assessment of the current CSA S806 (2012) development length equation; the second section presents the conclusions of the experimental results of the 24 GFRP-RC beams; and the third section presents the main conclusions of the numerical study.

8.2.1 Findings of the analytical investigation:

- An assessment of the tests reported in the literature was conducted. Two development length equations were proposed based on a linear stress intercept and a non-intercept relation with the stress representing a modified form of the CSA S806-12 development

length equation.

- The proposed development length equation based on the linear intercept showed high reliability and effectiveness in predicting the development length compared to the other equations.
- The proposed equations provided more accurate predictions of the mode of failure and the bond strength than the CSA S806 (2012) and the ACI 440.1R (2015) equations, and the standard deviation was the lowest for the proposed equations.
- Based on the available top bar splitting specimens, the factor (k_1) that accounts for the top bar effect is set to 1.3 for a horizontal reinforcement placed where more than 300 mm of fresh concrete is cast below the bar and 1.0 for other cases.
- The study recommends increasing the limit of the square root of the concrete compressive strength to 8 based on a conservative limit for beams that failed by concrete splitting and the pullout of GFRP bars. The estimates of the development length using the proposed equations decreased with increasing concrete compressive strength, unlike the predictions of CSA S806 (2012).
- The concrete cover significantly affected the estimation of the development length and depended on the bar size. To develop the bond strength of GFRP bars, the concrete cover to the center of the bar is recommended to be $2.5d_b$ for all bar diameters. However, more research studies are required to investigate the concrete cover effect for bar #8.
- The assessment of the bar size factor (k_3) showed that the factor has almost the same value, 0.9, for #3, #4, #5, and #6 bars and 1.1 for #8 bars due to shear lag and the effects of air entrainment underneath the bars.
- The enhancement in bond strength associated with transverse reinforcement confinement depended upon the type of bar surface configuration. The confinement had a negligible effect on the bond strength for helically wrapped GFRP bars and increased the bond strength for ribbed and sand-coated surfaces. Accordingly, the term (k_{tr}) was incorporated into the development length equation to account for the confinement effect from transverse reinforcement.

- Finally, the proposed development length equation based on the linear intercept is recommended as a new design development length equation for GFRP reinforced concrete members.

8.2.2 Findings of the experimental study:

- Overall, the bar surface profile of the sand-coated or ribbed had a minor effect on the maximum crack width of the beams at the level of reinforcement. However, beams reinforced with ribbed GFRP bars showed narrower cracks than those reinforced with sand-coated GFRP bars when the crack was measured at the soffit of the beam.
- The change in the spacing between the transverse reinforcements in the flexural zone from 317 to 200 mm did not affect the crack width and k_b values of the GFRP RC beams. However, the beams with 100 mm stirrup spacing showed narrower cracks and smaller k_b values than those with 200 mm and 317 mm stirrup spacing.
- Using theoretical β values to extrapolate the crack width of GFRP-RC beams may result in unconservative crack width predictions. The degree of unconservatism is higher in the case of sand-coated GFRP bars.
- The k_b values at a 0.7 mm crack width are affected by several cross-sectional parameters, including the concrete cover, reinforcement ratio (bar diameter), and bar spacing. It is also a function of crack width. The higher the crack width is, the higher the k_b value. The k_b value at a 0.7 mm crack width showed a decreasing trend by increasing the concrete cover and bar spacing, while it showed a not a clear trend by increasing the concrete compressive strength. However, the change in the k_b values with respect to the change in those parameters was different between the specimens. Moreover, the stabilization of cracks happens at higher crack widths in the HSC beams.
- The experimental results show that the k_b values depend on the definition of the critical crack used in the analysis.
- The crack widths of this study and those available in the literature were analyzed to recalibrate the k_b values. The results show that sand-coated bar GFRP bars have an average k_b value of 1.16 ± 0.26 (COV of 22%), with a 70th percentile k_b value of 1.26. On the other hand, ribbed GFRP bars have an average k_b value of 0.94 ± 0.24 (COV of 26%), with a

70th percentile k_b value of 1.04. Moreover, based on a limited amount of data available, grooved GFRP bars have an average k_b value of 1.32 ± 0.20 (COV of 16%), with a 70th percentile k_b value of 1.48.

- The GFRP-RC beams with HSC behaved linearly with no stiffness reduction up to failure. In comparison, the NSC beams behaved linearly up to 70%-80% of the ultimate load, and then the load-deflection slope reduced up to failure.
- The moment capacity predictions using the CSA S806 (2012) and ACI 440.1R (2015) were close to the experimental results without considering the strength reduction factors.
- The deformability calculated using the energy-based approach yielded more reasonable results with a clear trend than the deformation-based method for some parameters, including the concrete cover, reinforcement ratio (bar diameter), and confinement due to transverse reinforcement. However, this finding differs from Wang and Belarbi's (2011) and Abdelkarim's et al. (2018) conclusions.
- The confinement effect from the closely spaced stirrups in the middle flexural zone using a spacing of 100 mm between stirrups manifested a considerable enhancement in the load-carrying capacity and ductility indices using the energy-based approach compared with the other specimens.
- Deflections computed by the CSA S806 (2012) equation at $0.33M_n$ showed a conservative prediction compared to the experimental results and were insensitive to the cracking moment. The ACI 440.1R (2015) deflection equation provided unconservative deflection predictions with high data scatter when M_{cr} is used. Using $0.8M_{cr}$ improves the deflection predictions and data scatter; however, the equation still underestimate the deflection measurements.
- The experimental results support the use of $\beta_c = (M_{cr}/M_d)^2$ and $0.8M_{cr}$ for deflection predictions. However, the deflection predictions showed dependency on the level of loading as the power m in the tension stiffening factor (β_c) increased. Accordingly, more investigations are required to examine the deflection behaviour in GFRP-RC elements.
- It is recommended that the GFRP RC elements be designed for crack width and deflection

requirements and then checked to satisfy other requirements.

More experimental studies are recommended to focus on the effect of different parameters, including the concrete cover, number of reinforcement layers, concrete strength, and bar surface profiles on the k_b values. It is also recommended that the code committees develop a standard test method to evaluate the crack width of GFRP-RC elements. More experimental results are required to verify the conclusions of this research and improve the accuracy of the proposed effective moment of inertia equation.

8.2.3 Findings of the Numerical simulation:

- The increase in clear concrete bottom cover for a beam with a given height showed a slightly decreasing trend on the moment capacity. The deflection values at the different loading levels increased by increasing the clear concrete bottom cover.
- The moment capacity and deflection values at the different service loading levels were highly sensitive to the change in the reinforcement ratio with direct and indirect trends, respectively. However, the change in spacing between the tensile GFRP bars did not show any noticeable influence on the moment capacities and deflection values.
- By decreasing the spacing between the GFRP stirrups to 150 mm, the moment capacity increased by 19% compared to the reference beam. On the same side, the moment capacity increased by 32% and 40% by decreasing the spacing between the steel stirrups to 100 mm and 50 mm, respectively, compared to the reference beam. However, decreasing the spacing between the steel and GFRP stirrups did not affect the deflection values at the different loading levels.
- Increasing the steel stirrups bar diameter showed a noticeable enhancement in the moment capacities compared to GFRP stirrups at 200 mm spacing. While at 100 mm spacing between stirrups, the moment capacities were slightly increased by increasing the steel and GFRP stirrups bar diameter.
- The moment capacity showed a decreasing trend by increasing the number of tensile reinforcement layers. Furthermore, the deflection values at the different loading levels increased by increasing the number of tensile reinforcement layers compared to the reference beam, particularly the beam with four reinforcement layers.
- The moment capacities of beams of the same height with clear concrete bottom covers of 38

mm and 50 mm were significantly affected by increasing the concrete compressive strengths to 50 MPa and 65 MPa, more than the beam with a larger clear concrete bottom cover of 60 mm. Moreover, the effect of the increasing concrete strength on enhancing the moment capacity became lower for beam 2#8 with the reinforcement ratio. The deflection values at $0.33M_n$ decreased with increasing concrete compressive strength, and this reduction was found to be the highest for beams with smaller concrete cover and lower reinforcement ratios.

- The GFRP bars' elastic modulus significantly influenced the moment capacity through a direct trend. The effect of the GFRP bars' elastic modulus on the moment capacity was relatively similar for beams with different concrete bottom covers, while this effect was higher for beams with lower reinforcement ratios than for those with higher reinforcement ratios. In contrast, increasing the GFRP bars' elastic modulus remarkably decreased the deflection values at $0.33M_n$.
- The deflection predictions of CSA S806 (2012) and ACI 440.1R (2015) using the I_{cr} were conservative for the studied parameters, except for beams with low reinforcement ratios. Similarly, the ACI 440.1R (2015) predictions using the proposed I_e by Gouda et al. (2022) were conservative for different parameters at different service loading levels, except for the lower reinforcement ratios of beams with different concrete strengths and lower GFRP bars' elastic modulus at a higher service loading level ($0.5M_n$). The ACI 440.1R (2015) deflection predictions using the I_e proposed by Bischoff et al. (2009) yielded unconservative results for different parameters at different service loading levels.
- For ACI 440.1R (2015) deflection equation, using the I_{cr} instead of the I_e provided conservative results for beams with different concrete compressive strengths ranging from 25 MPa to 95 MPa. The ACI 440.1R (2015) deflection equation using $0.6M_{cr}$ provides conservative results for the beams with one-layer reinforcement and unconservative results for the two-layer beam. The CSA S806 (2012) deflection equation provides conservative predictions for all the studied beams at different concrete compressive strengths.
- The CSA S806 (2012) moment capacity predictions were higher than the ACI 440.1R (2015) predictions. The CSA S806 (2012) and ACI 440.1R (2015) underestimated the moment capacities of the beams confined with transverse stirrups. Moreover, the beam size effect and the number of GFRP tensile reinforcement layers were better predicted by ACI 440.1R (2015); however, they were overestimated by CSA S806 (2012).

This numerical study provided a reliable numerical tool for a better understanding of the serviceability behaviour of normal- and high-strength GFRP-reinforced beams. Further investigations are required in order to develop reliable serviceability equations for high-strength concrete beams.

8.3 Main contributions

Based on the results of this study, the following contributions are made:

- The study modified the current CSA S806 (2012) development length equation based on 431 beam bond tests compiled from the literature. The parameters in the CSA S806 (2012) equation were assessed, and a modified equation was proposed by conducting a regression analysis using the database.
- The study provides the literature with an enhanced understating of the flexural and serviceability performance of the ribbed GFRP bars used in reinforcing the concrete beams.
- The investigation provided k_b values for the ribbed GFRP bars based on extensive experimental testing of different parameters.
- The study investigated the effect of different parameters on the k_b values, proving that the k_b parameter in the crack width equation changes by changing the studied parameter.
- The investigation recalibrated the k_b values for the sand-coated and grooved bars based on the available data compiled from the literature.
- The study assessed the current deflection equations in the CSA S806 (2012) standard and ACI 440.1R (2015) guideline. Based on this assessment, a modified form of the ACI 440.1R (2015) effective moment of inertia equation was introduced.
- The numerical tool showed high effectiveness in simulating the flexural and serviceability macro-behaviour of GFRP-RC beams, including the deflection and moment capacities of the GFRP-RC beams, which can be used as a reliable tool to conduct a comprehensive parametric study.

8.4 Recommendations for future work

The interpretation of smart and innovative ideas for research is the key to scientific

advancement and contribution to knowledge. Based on the findings of this research, several research recommendations are provided that briefly introduce different topics that can be investigated in the future in order to improve the flexural and serviceability design of GFRP-RC members; these recommendations are:

- Testing concrete beams reinforced with ribbed GFRP bars confined in the maximum moment zone with steel and GFRP transverse stirrups with different spacings. This study would provide an understanding of confinement's effect on these members' cracking behaviour.
- Investigating the bond performance of ribbed GFRP-RC beams with a splice connection in the maximum moment zone. The main parameters should be the splice lengths and confinement effect due to closely spaced transverse steel and GFRP stirrups.
- Investigating the effect of using more than two reinforcement layers (i.e. three and four layers) acting as a skin reinforcement on the deflection and crack widths values, cracks propagation, k_b values, and ultimate capacity.
- Further detailed experimental studies are required to be conducted on the change of the beam length and the cross-section size effect to evaluate the applicability of the existing design equations and limits in the different standards and guidelines in predicting the behaviour of beams with different sizes.
- Quantifying the effect of the test replication on the accuracy and variation of test results, including the deflection and crack width values at the service stage, k_b values, and ultimate capacities.
- Investigating the effect of testing concrete beams reinforced with hybrid configurations of steel and GFRP or CFRP and GFRP on the flexural, serviceability, and deformability behaviour.
- Testing concrete beams reinforced with GFRP bars surface profiles under fatigue loading to determine the maximum number of cycles that can be achieved before failure and the effect of cyclic loading on the bond performance of these bars with concrete.

References

- AASHTO. (2018). "AASHTO LRFD Bridge Design Guide Specifications for GFRP-Reinforced Concrete." Washington, DC.
- Abdalla, H. A. (2002). "Evaluation of deflection in concrete members reinforced with fibre reinforced polymer (FRP) bars." *Composite Structures*. doi: 10.1016/S0263-8223(01)00188-X.
- Abdelkarim, O. I., Ehab A. A., Hamdy M. M., and Benmokrane, B. (2019). "Flexural Strength and Serviceability Evaluation of Concrete Beams Reinforced with Deformed GFRP Bars." *Engineering Structures* 186, no.282–96. <https://doi.org/10.1016/j.engstruct.2019.02.024>.
- Achillides, Z. (1998). "Bond Behaviour of FRP Bars in Concrete." Ph.D. Thesis, The University of Sheffield, South Yorkshire, Sheffield.
- ACI Committee 440.1R. (2003). "Guide for the Design and Construction of Concrete Reinforced with Fibre-Reinforced Polymer Bars (ACI 440.1R03)." American Concrete Institute, Farmington Hills, MI, 88 pp, 2003.
- ACI Committee 440.1R. (2006). "Guide for the Design and Construction of Concrete Reinforced with Fibre-Reinforced Polymer Bars (ACI 440.1R06)." American Concrete Institute, Farmington Hills, MI, 88 pp, 2003.
- ACI Committee 440.1R. (2015). "Guide for the Design and Construction of Concrete Reinforced with Fibre-Reinforced Polymer Bars (ACI 440.1R15)." American Concrete Institute, Farmington Hills, MI, 88 pp, 2015.
- ACI Committee 318. (2008). "Building code requirements for structural concrete." American Concrete Institute, Farmington Hills, MI, USA.
- ACI Committee 318. (2014). "Building code requirements for structural concrete." American Concrete Institute, Farmington Hills, MI, USA.
- ACI Committee 318. (2019). "Building Code Requirements for Structural Concrete." American Concrete Institute, Farmington Hills, MI, USA.
- ACI Committee 408. (1979). "Suggested Development, Splice, and Standard Hook Provisions for Deformed Bars in Tension (ACI 408.1R-79)." *Concrete International*, V. 1, No. 7, July, pp. 44-46.
- ACI Committee 408. (2003). "ACI 408R-03 Bond and Development of Straight Reinforcing Bars

- in Tension.” American Concrete Institute, 1–49.
- Adam, M. A., Said, M., Mahmoud, A. A., and Shanour, A. S. (2015). “Analytical and Experimental Flexural Behavior of Concrete Beams Reinforced with Glass Fibre Reinforced Polymers Bars.” *Construction and Building Materials* 84, 354–66. <https://doi.org/10.1016/j.conbuildmat.2015.03.057>.
- Aiello, M. A. and Ombres, L. (2000). “Load-deflection analysis of FRP reinforced concrete flexural members.” *Journal of Composites for Construction*. doi: 10.1061/(ASCE)1090-0268(2000)4:4(164).
- Alsayed, S. H. (1998). “Flexural behaviour of concrete beams reinforced with GFRP bars.” *Cement and Concrete Composites*. doi: 10.1016/S0958-9465(97)00061-9.
- Al-Sunna, R., Pilakoutas, K., Hajirasouliha, I., and Guadagnini, M. (2012). “Deflection behavior of FRP reinforced concrete beams and slabs: An experimental investigation.”, *Composites Part B: Engineering*, 43 (5).
- Alves, J., El-Ragaby A, El-Salakawy E. (2011) “Durability of GFRP Bars’ Bond to Concrete under Different Loading and Environmental Conditions.” *Journal of Composites for Construction*, Vol. 15, No. 3.
- Aly, R. (2005). “Experimental and analytical studies on bond behaviour of tensile lap spliced FRP reinforcing bars in concrete.” Ph.D. Thesis, University of Sherbrooke, Sherbrooke, CA.
- Aly, R., and Benmokrane, B. (2005). “Experimental and Analytical Studies on Bond Behaviour of Tensile Lap Spliced FRP Reinforcing Bars in Concrete.” Publ. No. 796, thesis: E-213:1, Sherbrooke Université, Quebec, Canada.
- Aly, R., Benmokrane, B., and Ebead, U. (2006). “Tensile Lap Splicing of Fibre-Reinforced Polymer Reinforcing Bars in Concrete.” *ACI Structural Journal*, 103- 6, 857-864.
- Asadian, A., Eslami, A., Farghaly, A.S., Benmokrane, B. (2019a). “Splice strength of staggered and non-staggered bundled glass fibre-reinforced polymer reinforcing bars in concrete.” *ACI Struct J.*, 116-4, 129-42.
- Asadian, A., Eslami, A., Farghaly, A.S., Benmokrane, B. (2019b). “Lap-splice length of bundled glass fibre-reinforced polymer bars in unconfined concrete.” *ACI Struct J*, 116-5, 287-299.
- Ashour, A. F. (2006). “Flexural and shear capacities of concrete beams reinforced with GFRP bars.” *Construction and Building Materials*, 20(10), 1005–1015.
- ASTM. D7957/D7957M–17. (2017). “Standard Specification for Solid Round Glass Fibre

- Reinforced Polymer Bars for.” ASTM International, 1–5.
- ASTM. D7205/D7205M. (2021). “Standard Test Method for Tensile Properties of Fibre Reinforced Polymer Matrix Composite Bars.” ASTM International, 1–13.
- ASTM C143/C143M-20. (2020). “Standard Test Method for Slump of Hydraulic-Cement Concrete.” ASTM International, 1–4.
- ASTM C39 / C39M-21. (2021). “Standard Test Method for Compressive Strength of Cylindrical Concrete Specimens.” ASTM International, 1–8.
- ASTM C496 / C496M-17. (2017). “Standard Test Method for Splitting Tensile Strength of Cylindrical Concrete Specimens.” ASTM International, 1–5.
- ASTM C78 / C78M-21. (2021). “Standard Test Method for Flexural Strength of Concrete (Using Simple Beam with Third-Point Loading).” ASTM International, 1–5.
- Baena, M., Torres, L., Turon, A., and Barris, C. (2009). “Experimental Study of Bond Behaviour between Concrete and FRP Bars Using a Pull-out Test.” *Composites Part B: Engineering* 40, no. 8: 784–97. <https://doi.org/10.1016/j.compositesb.2009.07.003>.
- Barris, C., Torres, L., Vilanova, I., Miàs, C., and Llorens, M. (2017). “Experimental Study on Crack Width and Crack Spacing for Glass-FRP Reinforced Concrete Beams.” *Engineering Structures* 131: 231–42. <https://doi.org/10.1016/j.engstruct.2016.11.007>.
- Barris, C., Torres, L., Turon, A., and Catalan, A. (2009). “An Experimental Study of the Flexural Behaviour of GFRP RC Beams and Comparison with Prediction Models.” *Composite Structures* 91, no. 3: 286–95. <https://doi.org/10.1016/j.compstruct.2009.05.005>.
- Basaran, B., and Kalkan, I. (2020). “Development length and bond strength equations for FRP bars embedded in concrete.” *Composite Structures*, Elsevier Ltd, 251(June), 112662.
- Bencardino, F., Condello, A., and Ombres, L. (2016). “Numerical and Analytical Modeling of Concrete Beams with Steel, FRP and Hybrid FRP-Steel Reinforcements.” *Composite Structures* 140, no. 40: 53–65. <https://doi.org/10.1016/j.compstruct.2015.12.045>.
- Benmokrane, B., Tighiouart, B., and Chaallal, O. (1996). “Bond Strength and Load Distribution of GFRP Reinforcing Bars in Concrete.” *ACI Materials Journal*, 93- 3, 246-253.
- Benmokrane, B., Brown, V. L., Mohamed, K., Nanni, A., Rossini, M., and Shield, C. (2019). “Creep-Rupture Limit for GFRP Bars Subjected to Sustained Loads.” *Journal of Composites for Construction*, 23(6).
- Benzecry, V., Empanza, A. R., Basalo, F. C., and Nanni, A. (2021). “Bond Coefficient, k_b , of

- GFRP Bars.” *Construction and Building Materials* 292: 1–9.
<https://doi.org/10.1016/j.conbuildmat.2021.123380>.
- Bischoff, P. H. (2005). “Reevaluation of deflection prediction for concrete beams reinforced with steel and fibre reinforced polymer bars.” *Journal of Structural Engineering*, 131(5), 752–767.
- Bischoff, P. H., Gross, S., and Ospina, C. E. (2009). “The story behind proposed changes to ACI 440 deflection requirements for FRP-reinforced concrete.” American Concrete Institute, ACI Special Publication, (264 SP), 53–76.
- Bischoff, P. H., and Gross, S. P. (2011a). “Equivalent Moment of Inertia Based on Integration of Curvature.” *Journal of Composites for Construction*, 15(3), 263–273.
- Bischoff, P. H., and Gross, S. P. (2011b). “Design Approach for Calculating Deflection of FRP-Reinforced Concrete.” *Journal of Composites for Construction*, 15(4), 490–499.
- Broms, B. B. (1965). “Crack Width and Crack Spacing In Reinforced Concrete Members.” *ACI Journal Proceedings* 62, no. 10. <https://doi.org/10.14359/7742>.
- CAN/CSA A23.3. (1994). “Design of Concrete Structures.” Canadian Standards Association, Mississauga, ON, Canada.
- CAN/CSA A23.3. (2014). “CAN/CSA-A23.3 Design of concrete structures for buildings.” Canadian Standards Association, Ontario, Canada, 220 p 318-14, ACI. Building Code Requirements for Structural Concrete (ACI 318-14). Vol. 11, 2014.
- CAN/CSA S806. (2002). “Design and Construction of Building Components with Fibre Reinforced Polymers.” Canadian Standards Association, Toronto, ON, Toronto.
- CAN/CSA S806. (2012-R2017). “Design and Construction of Building Components with Fibre Reinforced Polymers.” Canadian Standards Association, Toronto, ON, Toronto.
- CAN/CSA S6. (2014). “Canadian Highway Bridge.” Canadian Standards Association, Mississauga, ON, Canada.
- CAN/CSA S807. (2019). “Specification for fibre-reinforced polymers.” Canadian Standards Association, Rexdale, ON, Canada.
- Chit, Michael, B., and Kirsteint, A. F. (1958). “Flexural Cracks in Reinforced Concrete Beams.” *ACI Journal Proceedings* 54, no. 4 (1958): 865–78. <https://doi.org/10.14359/11474>.
- Choi, D. U., Chun, S. C., and Ha, S. S. (2012). “Bond Strength of Glass Fibre-Reinforced Polymer Bars in Unconfined Concrete.” *Engineering Structures* 34: 303–13.
<https://doi.org/10.1016/j.engstruct.2011.08.033>.

- Cosenza, E., Manfredi, G., and Realfonzo, R. (1997). "Behavior and Modeling of Bond of FRP Rebars to Concrete." *Journal of Composites for Construction* 1, no. 2: 40–51. [https://doi.org/10.1061/\(asce\)1090-0268\(1997\)1:2\(40\)](https://doi.org/10.1061/(asce)1090-0268(1997)1:2(40)).
- DeFreese, J. M., and Roberts-Wollmann, C. L. (2002). "Glass Fibre Reinforced Polymer Bars as Top Mat Reinforcement for Bridge Decks." Report for Virginia Transportation Research Council.
- Ehsani, M. R., Saadatmanesh, H., and Tao, S. (1996). "Design Recommendations for Bond of GFRP Rebars to Concrete." *Journal of Structural Engineering*, 122, No. 3, 247-254.
- Eligehausen, R., (1979). "Overlap joints of tensile rib bar with straight bar ends." German Committee for Reinforced Concrete, Heft 301, Berlin, Wilhelm Ernst & Sohn.
- El-Nemr, A., Ehab A. A., and Benmokrane, B. (2013). "Flexural Behavior and Serviceability of Normal- And High-Strength Concrete Beams Reinforced with Glass Fibre-Reinforced Polymer Bars." *ACI Structural Journal* 110, no. 6: 1077–87. <https://doi.org/10.14359/51686162>.
- El-Nemr, A., Ehab A. A., Barris, C., and Benmokrane, B. (2016). "Bond-Dependent Coefficient of Glass- and Carbon-FRP Bars in Normal- and High-Strength Concretes." *Construction and Building Materials* 113: 77–89. <https://doi.org/10.1016/j.conbuildmat.2016.03.005>.
- El-Nemr, A., Ehab A. A., El-Safty, A., and Benmokrane, B. (2018). "Evaluation of the Flexural Strength and Serviceability of Concrete Beams Reinforced with Different Types of GFRP Bars." *Engineering Structures* 173, no.: 606–19. <https://doi.org/10.1016/j.engstruct.2018.06.089>.
- El Refai, A., Abed, F., and Al-Rahmani, A. (2015). "Structural performance and serviceability of concrete beams reinforced with hybrid (GFRP and steel) bars." *Construction and Building Materials*, Elsevier Ltd, 96, 518–529.
- El-Salakawy, E., and Benmokrane, B. (2004). "Serviceability of Concrete Bridge Deck Slabs Reinforced with Fibre-Reinforced Polymer Composite Bars." *ACI Structural Journal* 101, no. 5: 727–36. <https://doi.org/10.14359/13395>.
- Emparanza, A. R., Kampmann, R., and De Caso y Basalo, F. (2017). "State-of-the-practice of global manufacturing of FRP rebar and specifications." American Concrete Institute, ACI Special Publication, 2017-Octob(SP 327), 717–730.
- Esfahani, M. R., Rakhshanimehr, M., and Mousavi, S. R. (2013). "Bond Strength of Lap-Spliced

- GFRP Bars in Concrete Beams.” *J. of Composites for Const., ASCE*, 17-3, 314-323.
- Faoro, M. (1996). “The influence of stiffness and bond of FRP bars and tendons on the structural behaviour of reinforced concrete members.” 2nd Int. Conf. on Advanced Composite Materials in Bridges and Structures, Montreal, Canada.
- Frosch, R. J. (1999) “Another Look at Cracking and Crack Control in Reinforced Concrete.” *ACI Structural Journal* 96, no. 3: 437–42. <https://doi.org/10.14359/679>.
- Fukuyama H., Sonobe Y., Fujisawa M., Kanakubo T., and Yonemaru K. (1994). “Bond Splitting Strength of Concrete Members Reinforced with FRP Bars.” Session on Bond of FRP Rebars, ACI Convention, San Francisco.
- Gangarao, H. V. S., and Faza. S. S. (1990). “Bending and Bond Behavior of Concrete Beams Reinforced with Plastic Rebars.” *Transportation Research Record* 1290, no. 2 (1990): 185–93.
- Gergely, P., and Lutz, L. A. (1968). “Maximum Crack Width in Reinforced Concrete Flexural Members.” American Concrete Institute, ACI Special Publication SP-020, no. 6: 87–117.
- Goldston, M., Remennikov, A., and Sheikh, M. N. (2016). “Experimental investigation of the behaviour of concrete beams reinforced with GFRP bars under static and impact loading.” *Engineering Structures*, Elsevier Ltd, 113, 220–232.
- Goto, Y. (1971). “Cracks Formed in Concrete Around Deformed Tension Bars.” *ACI Journal Proceedings*. doi: 10.14359/11325.
- Gouda, O., Asadian, A., Galal, K. (2022). “Flexural and serviceability behavior of concrete beams reinforced with ribbed GFRP bars.” *Journal of Composites for Construction*, 10.1061/(ASCE)CC.1943-5614.0001253.
- Grace, N. F., Soliman A. K., Abdel-Sayed G., and Saleh K. R. (1998). “Behaviour and ductility of simple and continuous FRP reinforced beams.” *Journal of Composites for Construction*. doi: 10.1061/(ASCE)1090-0268(1998)2:4(186).
- Gross, S. P., Yost, J. R., and Stefanski, D. J. (2009). “Effect of Sustained Loads on Flexural Crack Width in Concrete Beams Reinforced with Internal FRP Reinforcement.” In *Serviceability of concrete members reinforced with internal/external FRP reinforcement: ACI Special Publication SP-264*, 13–32. Detroit, MI: American Concrete Institute.
- Hao, Q., Wang, Y., He, Z., and Ou, J. (2009). “Bond strength of glass fibre reinforced polymer ribbed rebars in normal strength concrete.” *Construction and Building Materials*, 23- 2, 865-

871.

- Harajli, M., and Abouniaj, M. (2010). "Bond Performance of GFRP Bars in Tension: Experimental Evaluation and Assessment of ACI 440 Guidelines." *Journal of Composites for Construction*, ASCE, 14- 6, 659-668.
- Hossain, K.M.A. (2018). "Bond Strength of GFRP Bars Embedded in Engineered Cementitious Composite using RILEM Beam Testing." *Int J Concr Struct Mater*, 12-1, 6.
- ISIS Manual No.3. (2007). "Reinforcing Concrete Structures with Fibre Reinforced Polymers; Design Manual. Canadian Network of Centres of Excellence on Intelligent Sensing for Innovative Structures." Canadian Network of Centers of Excellence on Intelligent Sensing for Innovative Structures, Univ. of Winnipeg, Man., Canada.
- ISIS Manual No.3. (2012). "Reinforcing Concrete Structures with Fibre Reinforced Polymers; Design Manual. Canadian Network of Centres of Excellence on Intelligent Sensing for Innovative Structures." Canadian Network of Centers of Excellence on Intelligent Sensing for Innovative Structures, Univ. of Winnipeg, Man., Canada.
- Issa, M. S., Metwally, I. M., and Elzeiny, S. M. (2011). "Influence of fibres on flexural behavior and ductility of concrete beams reinforced with GFRP rebars." *Engineering Structures*, 33, No. 5, 1754-1763.
- Jaeger, G. L., Tadros, G., and Mufti A. A. (1997). "The Concept of the Overall Performance Factor in 739 Rectangular-Section Reinforced Concrete Beams." In: *Proc of 3rd Int Symp on Non-Metallic (FRP) 740 Reinforcement for Concrete Structures 2: Sapporo, Japan; 1997*. p. 551–8.
- Jakubovskis, R., Kaklauskas, G., Gribniak, V., Weber, A., and Juknys, M. (2014). "Serviceability Analysis of Concrete Beams with Different Arrangements of GFRP Bars in the Tensile Zone." *Journal of Composites for Construction*, 18(5), 04014005.
- Japan Society of Civil Engineers. (1997). "Recommendation for Design and Construction of Concrete Structures Using Continuous Fibre Reinforcing Materials, JSCE-7." Japan Society of Civil Engineers, Tokyo, Japan, 1-64.
- Ju, M., Park, Y., and Park, C. (2017) "Cracking Control Comparison in the Specifications of Serviceability in Cracking for FRP Reinforced Concrete Beams." *Composite Structures* 182, 674–84. <https://doi.org/10.1016/j.compstruct.2017.09.016>.
- Kalpana, V. G., and Subramanian, K. (2011). "Behavior of concrete beams reinforced with GFRP

- BARS.” *Journal of Reinforced Plastics and Composites*, 30(23), 1915–1922.
- Karlsson, M., (2017). “Bond between C-Bar FRP reinforcement and concrete.” Publ. No. 98:3, thesis: E-91:1, Chalmers University of Technology, Goteborg.
- Kassem, C., Farghaly, A. S., and Benmokrane, B. (2011) “Evaluation of Flexural Behavior and Serviceability Performance of Concrete Beams Reinforced with FRP Bars.” *Journal of Composites for Construction* 15, no. 5: 682–95. [https://doi.org/10.1061/\(ASCE\)CC.1943-5614.0000216](https://doi.org/10.1061/(ASCE)CC.1943-5614.0000216).
- Kazemi, M., Li, J., Harehdasht, S. L., Yousefieh, N., Jahandari, S., and Saberian, M. (2020). “Non-Linear Behaviour of Concrete Beams Reinforced with GFRP and CFRP Bars Grouted in Sleeves.” *Structures* 23, 87–102. <https://doi.org/10.1016/j.istruc.2019.10.013>.
- Kharal, Z. (2014). “Tension Stiffening and Cracking Behaviour of Gfrp Reinforced Concrete.” MSc, University of Toronto, Toronto, Ontario, Canada.
- Kharal, Z., and Sheikh, S. (2017). “Tension Stiffening and Cracking Behavior of Glass Fibre-Reinforced Polymer Reinforced Concrete,” *ACI Structural Journal*, 114 (2), 299-310.
- Kotynia, R., Szczech, D., and Kaszubska, M., (2017). “Bond Behavior of GFRP Bars to Concrete in Beam Test.” *Procedia Engineering*, 193, 401-408.
- Makhmalbaf, E., and Ghani Razaqpur, A. (2021). “Development Length of GFRP Rebar Based on Non-uniform Bond Stress.” *Canadian Journal of Civil Engineering*, doi.org/10.1139/cjce-2020-0400.
- Masmoudi, R., Benmokrane, B., and Chaallal, O. (1996). “Cracking Behaviour of Concrete Beams Reinforced with Fibre Reinforced Plastic Rebars.” *Canadian Journal of Civil Engineering* 23, no. 6: 1172–79. <https://doi.org/10.1139/196-926>.
- Masmoudi, R., Thériault, M., and Benmokrane, B. (1999). “Flexural Behavior of Concrete Beams Reinforced with Deformed Fibre Reinforced Plastic Reinforcing Rods. Paper by Radhouane Masmoudi, Michèle Thériault, and Brahim Benmokrane.” *ACI Structural Journal* 96, no. 5: 875.
- McCallum, B. (2013). “Experimental Evaluation of the Bond Dependent Coefficient and Parameters Which Influence Crack Width in GFRP Reinforced Concrete.” MSc, Dalhousie University Halifax, Nova Scotia.
- Mehany, S., Mohamed, H. M., and Benmokrane, B. (2022). “Flexural Strength and Serviceability of GFRP-Reinforced Lightweight Self-Consolidating Concrete Beams.” *Journal of*

- Composites for Construction, 26(3), 1–15.
- Mias, C., Torres, L., Turon, A., and Barris, C. (2013). “Experimental study of immediate and time-dependent deflections of GFRP reinforced concrete beams.”, *Composite Structures*, 96, 279–285.
- Mosley, C. P., Tureyen, A. K., and Frosch, R. J. (2008). “Bond Strength of Nonmetallic Reinforcing Bars.” *ACI Structural Journal* 105, no. 5: 634–42. <https://doi.org/10.14359/19947>.
- Mousa, S., Hamdy M. M., Benmokrane, B. and Nanni, A. (2020). “Flexural Behavior of Long-Span Square Reinforced Concrete Members with Uniformly Distributed Fibre- Reinforced Polymer Bars.” *ACI Structural Journal* 117, no. 4: 209–22. <https://doi.org/10.14359/51723511>.
- Naaman, A. E., and leong, S. M. (1995). “Structural ductility of concrete beams prestressed with FRP tendons.” *Non-metallic (FRP) reinforcement for concrete structures*. L. Taewere, ed., E & FN Spon, London, England, 379-386.
- Newhook, J., Ghali, A., and Tadros, G. (2002). “Concrete flexural members reinforced with fibre reinforced polymer: Design for cracking and deformability.” *Canadian Journal of Civil Engineering*, 29(1), 125–134.
- Okelo, R. (2007). “Realistic bond strength of FRP rebars in NSC from beam specimens.” *Journal of Aerospace Engineering*, 20- 3, 133-140.
- Orangun, C. O., Jirsa, J. O., and Breen, J. E. (1975). “The Strength of Anchor Bars: A Re-evaluation of Test Data on Development Length and Splices.” Research Report 154-3F, Center for Highway Research, the University of Texas, Austin.
- Orangun, C. O., Jirsa, J. O., and Breen, J. E. (1977). “Reevaluation of Test Data on Development Length and Splices.” *J Am Concr Inst* 74, no. 3: 114–22. <https://doi.org/10.14359/10993>.
- Ospina, C. E. and Bakis, C. E. (2007). “Indirect flexural crack control of concrete beams and one-way slabs reinforced with FRP bars.” *Proceedings of the 8th International Symposium on Fibre-Reinforced Polymer Reinforcement for Concrete Structures*.
- Papanikolaou, V. K., and Kappos, A. J. (2007). “Confinement-sensitive plasticity constitutive model for concrete in triaxial compression.” *International Journal of Solids and Structures*, 44(21), 7021–7048.
- Pay, A.C., Canbay, E., and Frosch, R.J. (2014). “Bond Strength of Spliced Fibre-Reinforced

- Polymer Reinforcement.” *ACI Struct J.*, 111-2.
- Pecce, M., Manfredi, G., and Realfonzo, R. (2001). “Experimental and analytical evaluation of bond properties of GFRP bars.” *Journal of Materials in Civil Engineering*, 13-4.
- Rao, P. S. (1966). “Die Grundlagen zur Berechnung der bei statisch unbestimmten Stahlbetonkonstruktionen im plastischen Bereich auftretenden Umlagerungen der Schnittkräfte Basic laws governing moment redistribution in statically indeterminate reinforced concrete structures!.” *DAfStb*, Ernst & Sohn, Berlin, Heft 177.
- Razaqpur, A. G., Švecová, D., and Cheung, M. S. (2000). “Rational Method for Calculating Deflection of Fibre-Reinforced Polymer Reinforced Beams.” *ACI Structural Journal* 97, no. 1: 175–84. <https://doi.org/10.14359/847>.
- Saleh, N., Ashour, A., Lam, D., (2019). “Experimental investigation of bond behaviour of two common GFRP bar types in high – Strength concrete.” *Construction and Building Materials*, 201, 610-622.
- Saleh, Z., Sheikh, M. N., Remennikov, A. M., and Basu, A. (2019). “Numerical Investigations on the Flexural Behavior of GFRP-RC Beams under Monotonic Loads.” *Structures* 20, 255–67. <https://doi.org/10.1016/j.istruc.2019.04.004>.
- Shield, C. K., French, C., and Retika, A. (1997). “Thermal and Mechanical Fatigue Effects on GFRP Rebar-Concrete Bond.” *Proceedings of the Third International Symposium on Non-Metallic Reinforcement for Concrete Structures*, Sapporo, Japan, 381-388.
- Shield C., French C., and Hanus, J., (1999). “Bond of GFRP Rebar for Consideration in Bridge Decks.” *ACI SP international symposium on FRP in Reinforced Concrete*, SP188, 393-406.
- Shield, C., Brown, V., Bakis, C. E., and Gross, S. (2019). “A Recalibration of the Crack Width Bond-Dependent Coefficient for GFRP-Reinforced Concrete.” *Journal of Composites for Construction* 23, no. 4: 04019020. [https://doi.org/10.1061/\(asce\)cc.1943-5614.0000978](https://doi.org/10.1061/(asce)cc.1943-5614.0000978).
- Sólyom, S., Balázs, G. L., and Borosnyói, A. (2016). “Material characteristics and bond tests for FRP rebars.” *Concrete Structures*, 16, 38-44.
- Solyom, S., and Balázs, G. L. (2018). “Comparitive Study of Bond Behaviour for Different FRP and Steel Bars.” *Proceedings of the 12th Fib International PhD Symposium in Civil Engineering*, 153–60.
- Solyom, S., and Balázs, G. L. (2020). “Bond of FRP Bars with Different Surface Characteristics.” *Construction and Building Materials* 264: 119839.

<https://doi.org/10.1016/j.conbuildmat.2020.119839>.

- Tepfers, R. (1977). "A Theory of Bond Applied to Overlapped Tensile Reinforcement Splices for Deformed Bars." PhD Thesis, Chalmers University of Technology, 1973.
- Theriaule, M., and Benmokrane, B. (1998). "Effects of Frp Reinforcement Ratio and Concrete Strength." *Journal of Composites for Construction* Vol. 2, 7–16.
- Tighiouart, B., Benmokrane, B., and Gao, D., (1998). "Investigation of Bond in Concrete Member with Fibre Reinforced Polymer (FRP) Bars." *Construction and Building Materials*, 12- 8, 453-462.
- Tighiouart, B., Benmokrane, B., and Mukhopadhyaya, P. (1999). "Bond Strength of Glass FRP Rebar Splices in Beams under Static Loading." *Construction and Building Materials*, 13- 7, 383-392.
- Toutanji, H. A., and Saafi, M. (2000). "Flexural Behavior of Concrete Beams Reinforced with Glass Fibre-Reinforced Polymer (GFRP) Bars." *ACI Structural Journal* 97, no. 5: 712–19. <https://doi.org/10.14359/8806>.
- Toutanji, H., and Deng, Y. (2003). "Deflection and crack-width prediction of concrete beams reinforced with glass FRP rods." *Construction and Building Materials*, 17(1), 69–74.
- Vijay, P. V., and GangaRao, H. V. S. (2001). "Bending Behavior and Deformability of GFRP Reinforced Concrete Members." *ACI Structural Journal* 98, no. 6: 834–42.
- Wambeke, B. W., and Shield, C. K. (2006) "Development Length of Glass Fibre-Reinforced Polymer Bars in Concrete." *ACI Structural Journal*, 103-1, 11-17.
- Wang, H., and Belarbi, A. (2011). "Ductility characteristics of fibre-reinforced-concrete beams reinforced with FRP rebars." *Construction and Building Materials*, 25(5), 2391–2401.
- Wight, J.K., and MacGregor, J.G. (2011). "Reinforced Concrete: Mechanics and Design." (Sixth Edition): Pearson Education, Inc., Upper Saddle River, New Jersey, 07458.
- Xue, W., Zheng, Q., Yang, Y. (2014). "Bond behavior of sand-coated deformed glass fibre reinforced polymer rebars." *Journal of Reinforced Plastics and Composites*, 83, 283-298.
- Xue, W., Peng, F., and Zheng, Q. (2016). "Design Equations for Flexural Capacity of Concrete Beams Reinforced with Glass Fibre–Reinforced Polymer Bars." *Journal of Composites for Construction*, 20(3), 04015069.
- Yan, F., Lin, Z., and Yang, M. (2016). "Bond Mechanism and Bond Strength of GFRP Bars to Concrete: A Review." *Composites Part B: Engineering* 98 (2016): 56–69.

<https://doi.org/10.1016/j.compositesb.2016.04.068>.

Yost, J. R., and Gross, S. P. (2002). "Flexural design methodology for concrete beams reinforced with fibre-reinforced polymers." *ACI Structural Journal*, 99(3):308-316.

Yost, J. R., Gross, S. P., and Dinehart, D. W. (2003). "Effective moment of inertia for glass fibre-reinforced polymer-reinforced concrete beams." *ACI Structural Journal*, 100(6), 732–739.

Zemour, N., Asadian, A., Ehab A. A., Khayat, K. H., and Benmokrane, B. (2018). "Experimental Study on the Bond Behavior of GFRP Bars in Normal and Self-Consolidating Concrete."

Construction and Building Materials 189: 869–81.

<https://doi.org/10.1016/j.conbuildmat.2018.09.045>.

Appendix A

A.1 General

This appendix provides additional information on the experimental research work presented in chapters 4, 5, and 6 of the thesis. These additional data cover some construction procedures and failure modes of the tested specimens.

A.2 Construction and testing of the concrete beams



Figure A.1 Typical GFRP cages for two concrete beams



Figure A.2 GFRP cages for 16 concrete beams



Figure A.3 Placing the cages inside the formwork



Figure A.4 Preparing the formwork for the concrete pouring by fixing the top steel hooks



Figure A.5 Preparing and levelling the formwork for the concrete pouring

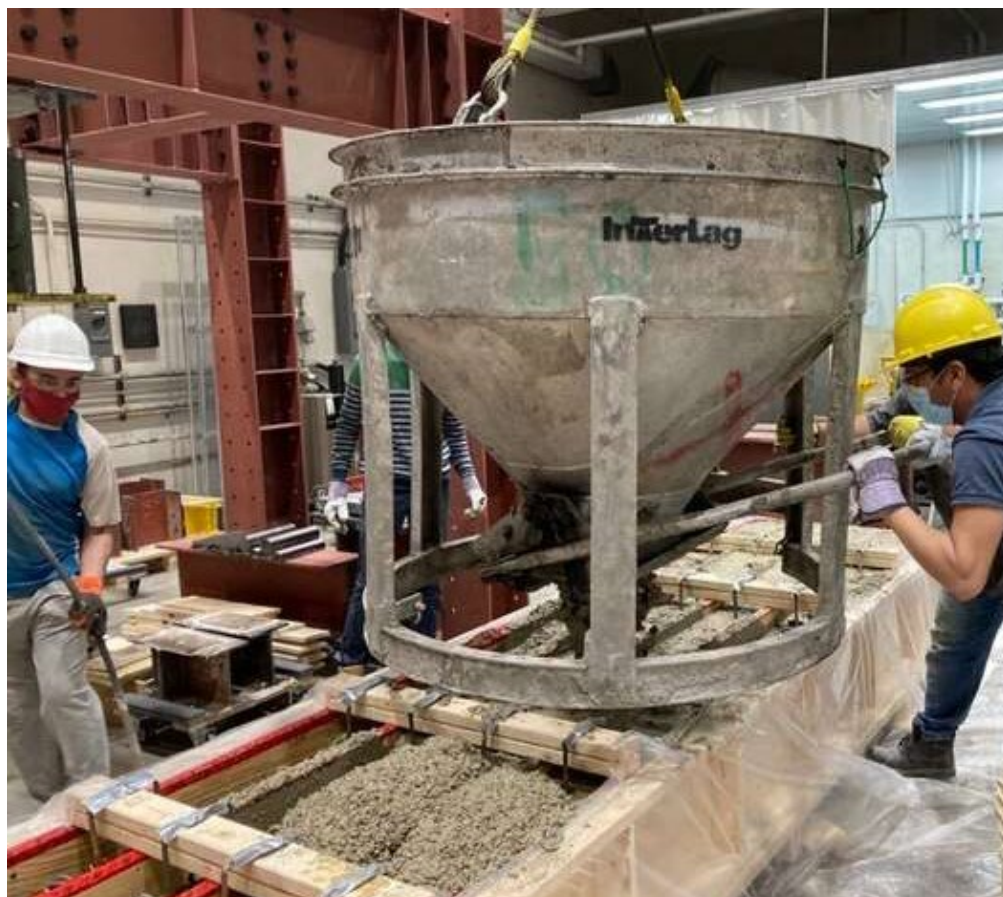


Figure A.6 Pouring of the concrete beams using the concrete bucket



Figure A.7 Vibration of poured concrete using the electric vibrator



Figure A.8 Careful finishing of the top concrete surface using trowels



Figure A.9 Concrete top surface after finished and levelling



Figure A.10 Pouring, compacting, and levelling of the cylinders and prisms



Figure A.11 Covering the concrete surface with a plastic cover for curing



Figure A.12 Curing of the concrete cylinders and prisms



Figure A.13 Stacking of the concrete beams after disassembling of the formwork

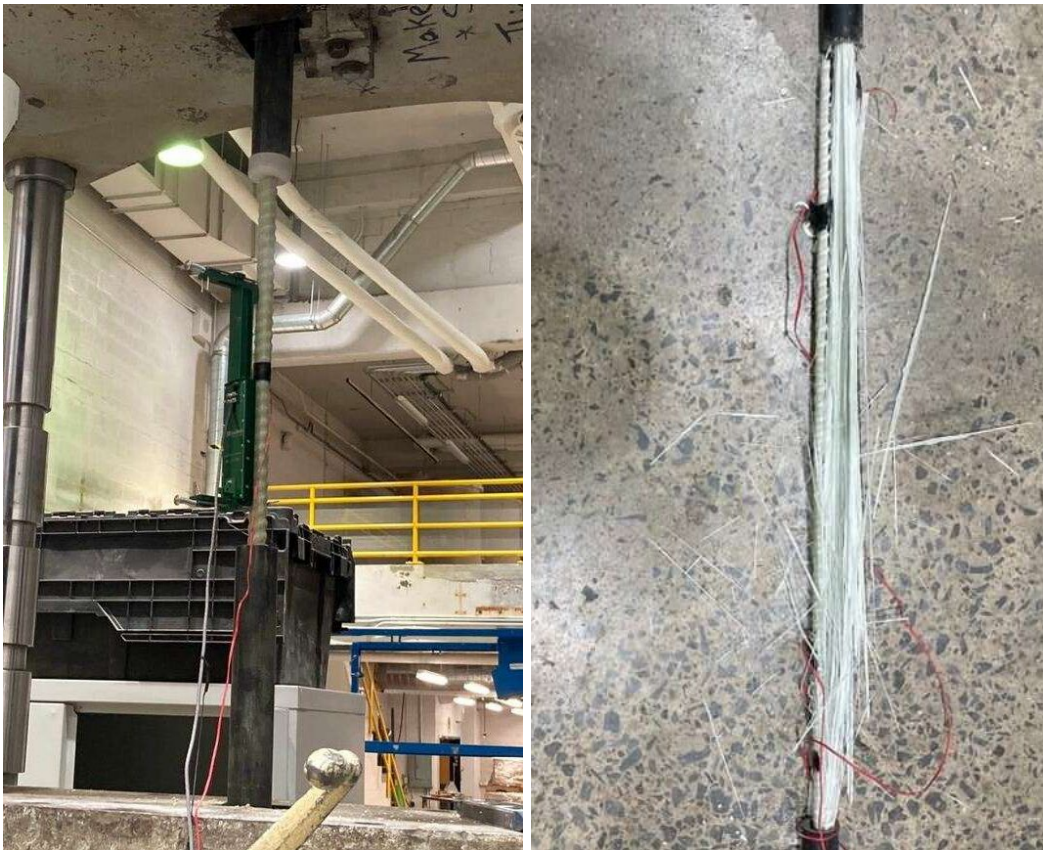


Figure A.14 Testing GFRP bar in tension and rupture failure mode



Figure A.15 Testing concrete cylinders in compression



Figure A.16 Testing the concrete prisms in tension using the four-point bending rupture test



Figure A.17 Splitting tensile test for the concrete cylinders



Figure A.18 Measuring the initial crack width using a hand-held microscope



Figure A.19 Attaching the LVDT to the concrete beam at the crack location



Figure A.20 Six attached LVDTs at the concrete beam side and bottom faces



Figure A.21 Typical concrete compression crushing

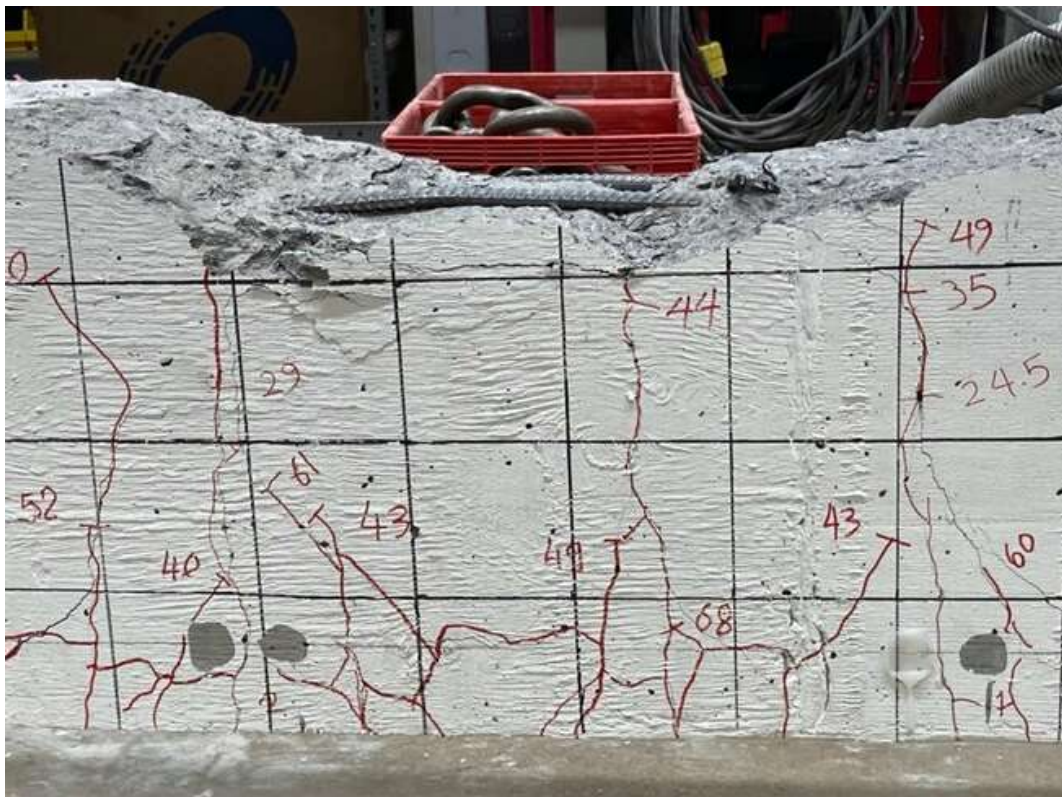


Figure A.22 Buckling of the top steel compression bar due to lack of confinement



Figure A.23 Failure of beam confined with transverse reinforcement spacing of 100 mm (a) concrete crushing followed by GFRP rupture; (b) concrete crushing failure; and (c) GFRP bar rupture

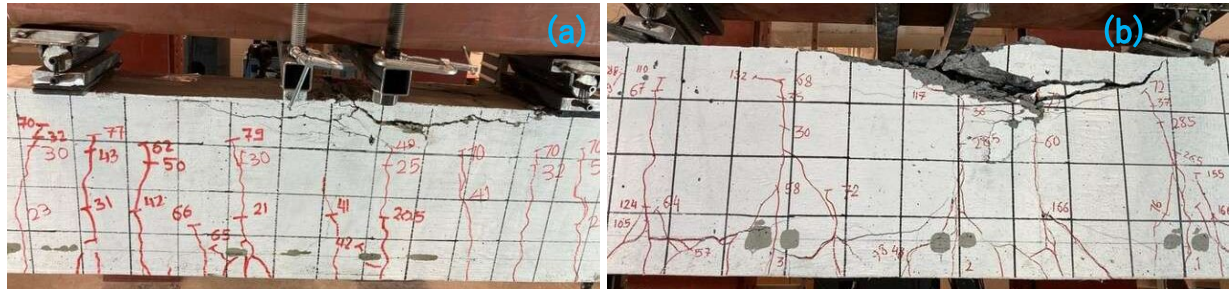


Figure A.24 Failure of beam reinforced with 3#6-c50 ribbed GFRP bars (a) normal-strength concrete beam; and (b) high-strength concrete beam

Appendix B

Details of experimental data collected from previous studies (Chapter 6).

Ref.	Beam Notation	f'_c (MPa)	d_b (mm)	l_e/d_b	Cover (mm)	Failure Mode
Bennokrane et al. (1996)	GFRP-12.7	31.0	12.7	10.0	50.0	P
	GFRP-15.9	31.0	15.9	10.0	50.0	P
	GFRP-19.1	31.0	19.1	10.0	50.0	P
	GFRP-25.4	31.0	25.4	10.0	50.0	P
Ehsani et al. (1996)	43B4B2	29.8	9.5	10.7	23.8	R
	83B4B2	49.0	9.5	10.7	23.8	R
	43B6B4	35.0	9.5	16.0	42.8	R
	83B6B4	49.0	9.5	16.0	42.8	R
	43B8B6	35.0	9.5	21.3	61.8	R
	83B8B6	49.0	9.5	21.3	61.8	R
	43B8T6	35.0	9.5	21.3	61.8	R
	83B8T6	49.0	9.5	21.3	61.8	R
	46B3B1	27.6	19.1	4.0	28.7	S
	46B3B2	27.6	19.1	4.0	47.8	P
	46B6B2	27.6	19.1	8.0	47.8	P
	46B12B2	39.2	19.1	16.0	47.8	P
	86B12B2	47.7	19.1	16.0	47.8	P
	46B16B4	39.2	19.1	21.3	86.0	P
	86B16B4	47.7	19.1	21.3	86.0	P
	46B18B6	39.2	19.1	24.0	124.2	R
	86B18B6	47.7	19.1	24.0	124.2	R
	49B4B1	27.6	28.6	3.6	42.9	S
	49B4B2	27.6	28.6	3.6	71.5	P
	49B8B2	27.6	28.6	7.1	71.5	P
	49B22B2	39.7	28.6	19.6	71.5	P
	89B22B2	44.8	28.6	19.6	71.5	P
	49B26B4	39.7	28.6	23.1	128.7	P
	89B26B4	47.3	28.6	23.1	128.7	P
	49B30B6	39.7	28.6	26.7	185.6	R
	89B30B6	47.3	28.6	26.7	185.6	R
	43B1.5T1	27.6	9.5	4.0	14.3	S
	43B1.5T2	27.6	9.5	4.0	23.8	P
	43B3T2	27.6	9.5	8.0	23.8	P
	43B4T2	29.8	9.5	10.7	23.8	R

	83B4T2	49.0	9.5	10.7	23.8	R
	43B6T4	35.0	9.5	16.0	42.8	R
	83B6T4	49.0	9.5	16.0	42.8	R
	46B3T1	27.6	19.1	4.0	28.7	S
	46B3T2	27.6	19.1	4.0	47.8	P
	46B6T2	27.6	19.1	8.0	47.8	P
	46B12T2	39.2	19.1	16.0	47.8	P
	86B12T2	47.7	19.1	16.0	47.8	P
	46B16T4	39.2	19.1	21.3	86.0	P
	86B16T4	47.7	19.1	21.3	86.0	P
	46B18T6	39.2	19.1	24.0	124.2	R
	86B18T6	47.7	19.1	24.0	124.2	R
	49B22T2	39.7	28.6	19.6	71.5	P
	89B22T2	44.8	28.6	19.6	71.5	P
	49B26T4	39.7	28.6	23.1	128.7	P
	89B26T4	47.3	28.6	23.1	128.7	P
	49B30T6	39.7	28.6	26.7	185.6	R
	89B30T6	47.3	28.6	26.7	185.6	R
Shield et al. (1997)	CG6AM1	38.8	19.3	13.3	48.3	S
	CG6BM1	38.8	19.3	13.3	48.3	S
	CG6CM1	38.8	19.3	13.3	48.3	S
	CG6AM2	38.8	20.3	13.3	50.8	S
	CG6BM2	38.8	20.3	13.3	50.8	S
	CG6CM2	38.8	20.3	13.3	50.8	S
	CG4AM1	38.8	13.5	11.0	33.8	S
	CG4BM1	38.8	13.5	11.0	33.8	S
	CG4CM1	38.8	13.5	11.0	33.8	S
	CG6AM1	38.8	13.5	13.3	33.8	S
Achillides (1998)	GB29	28.0	13.5	18.5	31.8	S
	GB30	28.0	13.5	22.2	31.8	S
	GB31	28.0	13.5	22.2	31.8	S
	GB34	36.0	8.5	43.5	29.3	S
	GB35	36.0	8.5	35.3	29.3	S
	GB36	36.0	8.5	35.3	29.3	S
Tighiouart et al. (1998)	Type-A ^a	31.0	12.7	6.0	50.0	P
	Type-A ^a	31.0	15.9	6.0	50.0	P
	Type-A ^a	31.0	19.1	6.0	50.0	P
	Type-A ^a	31.0	25.4	6.0	50.0	P
	Type-A ^a	31.0	12.7	16.0	50.0	S
	Type-A ^a	31.0	19.1	16.0	50.0	P
	Type-A ^a	31.0	25.4	16.0	50.0	P

Type-A ^a	31.0	12.7	10.0	50.0	P	
Type-B ^a	31.0	12.7	10.0	50.0	P	
Type-A ^a	31.0	15.9	10.0	50.0	P	
Type-B ^a	31.0	15.9	10.0	50.0	P	
Type-A ^a	31.0	19.1	10.0	50.0	P	
Type-A ^a	31.0	25.4	10.0	50.0	P	
Type-B ^a	31.0	25.4	10.0	50.0	P	
<hr/>						
Tighiouart et al. (1999)	A460-1	31.0	12.7	36.2	36.4	S
	A460-2	31.0	12.7	36.2	36.4	S
	A540-1	31.0	12.7	42.5	36.4	S
	A540-2	31.0	12.7	42.5	36.4	S
	A1000-1	31.0	12.7	78.7	36.4	S
	A1000-2	31.0	12.7	78.7	36.4	S
	A1235-1	31.0	12.7	97.2	36.4	S
	A1235-2	31.0	12.7	97.2	36.4	S
	B675-1	31.0	15.9	42.5	38.0	S
	B675-2	31.0	15.9	42.5	38.0	S
	B870-1	31.0	15.9	54.7	38.0	S
	B870-2	31.0	15.9	54.7	38.0	S
	B1255-1	31.0	15.9	78.9	38.0	C
	B1255-2	31.0	15.9	78.9	38.0	C
	B1545-1	31.0	15.9	97.2	38.0	S
	B1545-2	31.0	15.9	97.2	38.0	S
	<hr/>					
Shield et al. (1999)	M1-5-2-47-1	44.5	15.9	75.0	39.8	Sp-R
	M1-5-2-47-2	44.5	15.9	75.0	39.8	Sp-R
	M1-5-2-47-3	44.5	15.9	75.0	39.8	Sp-R
	M1-5-2-47-4	44.5	15.9	75.0	39.8	Sp-R
	M1-5-2-47-5	44.5	15.9	75.0	39.8	Sp-R
	M1-5-2-47-6	44.5	15.9	75.0	39.8	Sp-R
	M1-5-2-15-1	44.5	15.9	24.0	39.8	Sp-R
	M1-5-2-15-2	44.5	15.9	24.0	39.8	Sp-R
	M1-5-2-15-3	44.5	15.9	24.0	39.8	S
	M1-5-2-15-4	44.5	15.9	24.0	39.8	Sp-R
	M1-5-2-15-5	44.5	15.9	24.0	39.8	Sp-R
	M1-5-2-15-6	44.5	15.9	24.0	39.8	Sp-R
	M1-5-2-12.5-1	44.5	15.9	20.0	39.8	R
	M1-5-2-12.5-2	44.5	15.9	20.0	39.8	S
	M1-5-2-12.5-3	44.5	15.9	20.0	39.8	Sp-R
	M1-5-2-12.5-4	44.5	15.9	20.0	39.8	Sp-R
	M1-5-2-12.5-5	44.5	15.9	20.0	39.8	S
	M1-5-2-12.5-6	44.5	15.9	20.0	39.8	S

M1-5-3-15-1	44.5	15.9	24.0	55.7	Sp-R
M1-5-3-15-2	44.5	15.9	24.0	55.7	Sp-R
M1-5-3-15-3	44.5	15.9	24.0	55.7	Sp-R
M1-5-3-15-4	44.5	15.9	24.0	55.7	Sp-R
M1-5-3-15-5	44.5	15.9	24.0	55.7	Sp-R
M1-5-3-15-6	44.5	15.9	24.0	55.7	Sp-R
M1-5-3-12.5-1	44.5	15.9	20.0	55.7	S
M1-5-3-12.5-2	44.5	15.9	20.0	55.7	S
M1-5-3-12.5-3	44.5	15.9	20.0	55.7	S
M1-5-3-12.5-4	44.5	15.9	20.0	55.7	R
M1-5-3-12.5-5	44.5	15.9	20.0	55.7	S
M1-5-3-12.5-6	44.5	15.9	20.0	55.7	S
M1-5-3-10-1	44.5	15.9	16.0	55.7	S
M1-5-3-10-2	44.5	15.9	16.0	55.7	Sp-R
M1-5-3-10-3	44.5	15.9	16.0	55.7	Sp-R
M1-5-3-10-4	44.5	15.9	16.0	55.7	Sp-R
M1-5-3-10-5	44.5	15.9	16.0	55.7	Sp-R
M1-5-3-10-6	44.5	15.9	16.0	55.7	S
M1-5-2-12.5-1	44.5	15.9	20.0	39.8	S
M1-5-2-12.5-2	44.5	15.9	20.0	39.8	S
M1-5-2-12.5-3	44.5	15.9	20.0	39.8	S
M2-6-2-47-3	43.7	19.1	62.5	47.8	Sp-R
M2-6-2-25-1	43.7	19.1	33.3	47.8	S
M2-6-2-25-3	43.7	19.1	33.3	47.8	S
M2-6-2-25-5	43.7	19.1	33.3	47.8	S
M2-6-2-25-6	43.7	19.1	33.3	47.8	S
M2-6-2-20-1	43.7	19.1	26.6	47.8	S
M2-6-2-20-2	43.7	19.1	26.6	47.8	S
M2-6-2-20-3	43.7	19.1	26.6	47.8	S
M2-6-2-20-4	43.7	19.1	26.6	47.8	S
M2-6-2-20-6	43.7	19.1	26.6	47.8	S
M2-6-2-15-1	43.7	19.1	20.0	47.8	S
M2-6-2-15-2	43.7	19.1	20.0	47.8	S
M2-6-2-15-3	43.7	19.1	20.0	47.8	S
M2-6-2-15-4	43.7	19.1	20.0	47.8	S
M2-6-2-15-5	43.7	19.1	20.0	47.8	S
M2-6-2-15-6	43.7	19.1	20.0	47.8	S
M2-6-3-20-1	43.7	19.1	26.6	66.9	S
M2-6-3-20-2	43.7	19.1	26.6	66.9	S
M2-6-3-20-3	43.7	19.1	26.6	66.9	S
M2-6-3-20-4	43.7	19.1	26.6	66.9	S

	M2-6-3-15-1	43.7	19.1	20.0	66.9	S
	M2-6-3-15-2	43.7	19.1	20.0	66.9	S
	M2-6-3-15-3	43.7	19.1	20.0	66.9	S
	M2-6-3-15-4	43.7	19.1	20.0	66.9	S
	M2-6-3-15-5	43.7	19.1	20.0	66.9	S
	M2-6-3-15-6	43.7	19.1	20.0	66.9	S
Pecce et al. (2001)	1	37.0	12.7	5.0	125.0	P
	2	40.0	12.7	5.0	125.0	P
	3	38.0	12.7	10.0	125.0	R
	4	40.0	12.7	10.0	125.0	P/R
	5	52.0	12.7	20.0	125.0	R
	6	55.0	12.7	20.0	125.0	R
	7	50.0	12.7	30.0	125.0	R
Defreese and Wollmann (2002)	HB4-5-1	29.0	12.7	5.0	31.8	P
	HB4-5-2	29.0	12.7	5.0	31.8	P
	HB4-5-3	29.0	12.7	5.0	31.8	P
	HB4-5-4	29.0	12.7	5.0	31.8	P
	HB4-7.5-1	29.0	12.7	7.5	31.8	P
	HB4-7.5-2	29.0	12.7	7.5	31.8	P
	HB5-5-1	29.0	15.9	5.0	33.4	P
	HB5-5-2	29.0	15.9	5.0	33.4	P
	HB5-7.5-1	29.0	15.9	7.5	33.4	P
	HB5-7.5-2	29.0	15.9	7.5	33.4	P
	HB6-5-1	29.0	19.1	5.0	35.0	P
	HB6-5-2	29.0	19.1	5.0	35.0	P
	HB6-7.5-1	29.0	19.1	7.5	35.0	P
	HB6-7.5-2	29.0	19.1	7.5	35.0	P
	M4-5-1	29.0	12.7	5.0	31.8	P
	M4-5-2	29.0	12.7	5.0	31.8	P
	M4-5-3	29.0	12.7	5.0	31.8	P
	M4-5-4	29.0	12.7	5.0	31.8	P
	M4-7.5-1	29.0	12.7	7.5	31.8	P
	M4-7.5-2	29.0	12.7	7.5	31.8	P
	M5-5-1	29.0	15.9	5.0	33.4	P
	M5-5-2	29.0	15.9	5.0	33.4	P
	M5-7.5-1	29.0	15.9	7.5	33.4	P
	M5-7.5-2	29.0	15.9	7.5	33.4	P
	M6-5-1	29.0	19.1	5.0	35.0	P
	M6-5-2	29.0	19.1	5.0	35.0	P
	M6-7.5-1	29.0	19.1	7.5	35.0	P
	M6-7.5-2	29.0	19.1	7.5	35.0	P

	P4-5-1	23.4	12.7	5.0	31.8	P
	P4-5-2	23.4	12.7	5.0	31.8	P
	P4-7.5-1	23.4	12.7	7.5	31.8	P
	P4-7.5-2	23.4	12.7	7.5	31.8	P
Aly (2005)	6G70-0splice	45.0	19.1	36.6	49.6	S
	6G70-0Moment	43.0	19.1	36.6	49.6	S
	6G110-0 Moment	43.0	19.1	57.6	49.6	S
	6G70-300	43.0	19.1	36.6	49.6	S
	6G70-150	43.0	19.1	36.6	49.6	S
	6G70-50	45.0	19.1	36.6	49.6	R
	6G70-150-40b-25s	45.0	19.1	36.6	49.6	S
	6G70-150-25b-45s	43.0	19.1	36.6	49.6	S
	6G70-150-70b-45s	45.0	19.1	36.6	49.6	S
	6G70-150-40b-70s	43.0	19.1	36.6	49.6	S
	6G70-150-70b-70s	45.0	19.1	36.6	49.6	S
Aly et al. (2006)	5G50	49.0	15.9	31.4	48.0	R
	5G70	43.0	15.9	44.0	48.0	R
	6G50	41.0	19.1	26.2	49.6	S
	6G70	43.0	19.1	36.6	49.6	S
	6G80	41.0	19.1	41.9	49.6	S
	6G110	41.0	19.1	57.6	49.6	R
Okelo (2007)	G-10-0-100	33.3	10.0	10.0	38.0	P
	G-19-0-190	33.3	19.0	10.0	38.0	P
	G-10-0-150	32.4	10.0	15.0	38.0	R
	G-19-0-285	32.4	19.0	15.0	38.0	S/C
	G-10-0-200	31.3	10.0	20.0	38.0	R
	G-19-0-380	31.3	19.0	20.0	38.0	S/C
	G-10-1-100	36.9	10.0	10.0	38.0	R
	G-19-1-190	36.9	19.0	10.0	38.0	S/C
	G-10-1-150	41.5	10.0	15.0	38.0	R
	G-19-1-285	41.5	19.0	15.0	38.0	S/C
	G-10-1-200	39.3	10.0	20.0	38.0	R
G-19-1-380	39.3	19.0	20.0	38.0	S/C	
Mosely et al. (2008)	B-G1-1	38.6	16.0	28.6	46.0	S
	B-G2-1	37.8	16.0	28.6	46.0	S
	B-G1-2	29.0	16.0	19.0	46.0	S
	B-G2-2	27.0	16.0	19.0	46.0	S
	B-G1-3	41.2	16.0	19.0	46.0	S
	B-G2-3	40.9	16.0	19.0	46.0	S
Hara jli and	R1.25L15	48.0	12.0	15.0	21.0	S
	R1.25L20	48.0	12.0	20.0	21.0	S

	R2L15	48.0	12.0	15.0	31.0	S	
	R2L20	48.0	12.0	20.0	31.0	S	
	R1.25L30	52.0	12.0	30.0	21.0	S	
	R1.25L20-C	52.0	12.0	20.0	21.0	S	
	T1.25L15	52.0	12.0	15.0	21.0	P	
	T1.25L20	52.0	12.0	20.0	21.0	P	
	T2L15	52.0	12.0	15.0	31.0	P	
	T2L20	52.0	12.0	20.0	31.0	P	
	T1.25L20-C	52.0	12.0	20.0	21.0	P	
	T2L20-C	52.0	12.0	20.0	31.0	P	
	<hr/>						
	B-2As-L10db-c25	30.0	12.7	10.0	31.8	S	
	B-2As-L20db-c25	30.0	12.7	20.0	31.8	S	
	B-2As-L30db-c25	30.0	12.7	30.0	31.8	S	
	B-2As-L40db-c25	30.0	12.7	40.0	31.8	S	
	B-2As-L55db-c25	30.0	12.7	55.0	31.8	S	
	B-2As-L70db-c25	30.0	12.7	70.0	31.8	S	
	B-2Iso-L30db-c25	30.0	12.7	30.0	31.8	S	
	B-2Iso-L40db-c25	30.0	12.7	40.0	31.8	S	
	B-2Iso-L50db-c25	30.0	12.7	50.0	31.8	S	
	B-2Iso-L60db-c25	30.0	12.7	60.0	31.8	S	
Choi et al. (2012)	B-3K2-L15db-c25	23.0	12.7	15.0	31.8	S	
	B-3K2-L30db-c25	23.0	12.7	30.0	31.8	S	
	B-3K2-L45db-c25	23.0	12.7	45.0	31.8	S	
	B-3K2-L60db-c25	23.0	12.7	60.0	31.8	S	
	B-3K2-L30db-c13	23.0	12.7	30.0	19.1	S	
	B-3K2-L30db-c51	23.0	12.7	30.0	57.2	S	
	B-4K2-L30db-c25	23.0	12.7	30.0	31.8	S	
	B-5K2-L30db-c25	23.0	12.7	30.0	31.8	S	
	B-4K2-L45db-c25	23.0	12.7	45.0	31.8	S	
	B-5K2-L45db-c25	23.0	12.7	45.0	31.8	S	
	B-3As-L15db-c25	23.0	12.7	15.0	31.8	S	
	B-3As-L30db-c25	23.0	12.7	30.0	31.8	S	
	B-3As-L45db-c25	23.0	12.7	45.0	31.8	S	
	B-3As-L60db-c25	23.0	12.7	60.0	31.8	S	
		<hr/>					
	Esfahani et al. (2013)	S10-40-NC	39.0	10.0	18.0	43.0	S
		S10-40-S80	39.0	10.0	18.0	43.0	P
S10-40-S21		39.0	10.0	18.0	43.0	P	
R16-40-NC		41.0	16.0	25.0	41.0	S	
R16-40-S150		41.0	16.0	25.0	41.0	S	
R16-40-S100		41.0	16.0	25.0	41.0	S	
R16-40-S50		41.0	16.0	25.0	41.0	S	

	R12-40-S150	41.0	12.0	33.3	39.0	S
	R12-40-S100	41.0	12.0	33.3	39.0	S
	R12-40-S50	41.0	12.0	33.3	39.0	S
	R12-70-S150	72.0	12.0	33.3	39.0	S
	R12-70-S100	72.0	12.0	33.3	39.0	S
	R12-70-S50	72.0	12.0	33.3	39.0	S
Xue et al. (2013)	I 30-1-f	23.0	16.0	2.5	50.0	P
	I 30-2-f	23.0	16.0	5.0	50.0	S
	I 30-3-f	23.7	16.0	10.0	50.0	S
	I 30-4-f	22.8	16.0	20.0	50.0	S
	I 50-1-f	23.0	16.0	5.0	50.0	S
	I 30-1-s	23.0	16.0	2.5	50.0	P
	I 30-2-s	23.0	16.0	5.0	50.0	P
	I 30-3-s	23.7	16.0	10.0	50.0	S
	I 30-4-s	22.8	16.0	20.0	50.0	P
	I 50-1-s	23.0	16.0	5.0	50.0	P
Pay et al. (2014)	B-PG-8-18	36.3	25.4	18.0	50.7	S
	B-HG-8-18	36.3	25.4	18.0	50.7	S
	B-HG1-5-18	36.3	15.9	28.8	46.0	S
	B-HGO-5-18	36.3	15.9	28.8	46.0	S
	B-PG-5-18	36.3	15.9	28.8	46.0	S
	B-PG-8-36	37.7	25.4	36.0	50.7	S
	B-HG-8-36	37.7	25.4	36.0	50.7	S
	B-HG1-5-36	37.7	15.9	57.5	46.0	S
	B-HGO-5-36	37.7	15.9	57.5	46.0	S
	B-PG-5-36	37.7	15.9	57.5	46.0	S
	B-PG-8-12	27.7	25.4	12.0	50.7	S
	B-HG-8-12	27.7	25.4	12.0	50.7	S
	B-HG-8-12b	27.7	25.4	12.0	50.7	S
	B-PG-8-12b	27.7	25.4	12.0	50.7	S
	B-HG1-5-24	32.0	15.9	38.3	46.0	S
	B-HG2-5-24	32.0	15.9	38.3	46.0	S
	B-PG-5-24	32.0	15.9	38.3	46.0	S
	B-HG1-5-24b	32.0	15.9	38.3	46.0	S
	B-PG-5-24b	32.0	15.9	38.3	46.0	S
	B-HG1-5-12	28.8	15.9	19.2	46.0	S
	B-PG-5-12	28.8	15.9	19.2	46.0	S
	B-HG-8-24	28.8	25.4	24.0	50.7	S
	B-HG-8-54	28.8	25.4	54.0	50.7	S
	B-HG1-5-54	28.8	15.9	86.3	46.0	S
	B-PG-5-54	28.8	15.9	86.3	46.0	S

	B-HG1-5-12b	28.8	15.9	19.2	46.0	S
	B-PG-5-12b	28.8	15.9	19.2	46.0	S
	B-HG-8-24b	28.8	25.4	24.0	50.7	S
Kytonia et al. (2017)	12-L120-15.1	35.9	12.0	10.0	21.0	S
	12-L120-15.2	35.9	12.0	10.0	21.0	S
	16-L160-15.1	34.3	16.0	10.0	23.0	P
	16-L160-15.2	36.3	16.0	10.0	23.0	P
	18-L180-15.1	36.3	18.0	10.0	24.0	S
	18-L180-15.2	36.3	18.0	10.0	24.0	P
	12-L120-35.1	36.3	12.0	10.0	41.0	P
	12-L120-35.2	34.3	12.0	10.0	41.0	P
	16-L160-35.1	36.3	16.0	10.0	43.0	P
	16-L160-35.2	34.3	16.0	10.0	43.0	S
	18-L180-35.1	34.3	18.0	10.0	44.0	P
	18-L180-35.2	34.3	18.0	10.0	44.0	P
Hossain (2018)	NC-15.9-5D-LM	63.0	15.9	5.0	50.0	P
	NC -15.9-7D-LM	63.0	15.9	7.0	50.0	P
	NC -15.9-10D-LM	63.0	15.9	10.0	50.0	P
	NC -19.1-5D-LM	63.0	19.1	5.0	50.0	P
	NC -19.1-7D-LM	63.0	19.1	7.0	50.0	P
	NC -19.1-10D-LM	63.0	19.1	10.0	50.0	P
	NC-15.9-5D-HM	63.0	15.9	5.0	50.0	P
	NC -15.9-7D-HM	63.0	15.9	7.0	50.0	P
	NC -15.9-10D-HM	63.0	15.9	10.0	50.0	P
	NC -19.1-5D-HM	63.0	19.1	5.0	50.0	P
	NC -19.1-7D-HM	63.0	19.1	7.0	50.0	P
	NC -19.1-10D-HM	63.0	19.1	10.0	50.0	P
Zemour et al. (2018)	G-N-40-40d	39.0	15.9	40.0	46.0	S
	G-SC-40-40d	41.0	15.9	40.0	46.0	S
	G-N-60-40d	39.0	15.9	40.0	46.0	S
	G-SC-60-40d	41.0	15.9	40.0	46.0	S
	G-N-40-20d	39.0	15.9	20.0	46.0	S
	G-N-60-20d	35.5	15.9	20.0	46.0	S
Saleh et al. (2019)	A-9.5-5d-B	77.9	9.5	5.0	50.0	P
	A-9.5-5d-T	77.9	9.5	5.0	50.0	P
	A-12.7-5d-B	77.9	12.7	5.0	50.0	P
	A-12.7-5d-T	77.9	12.7	5.0	50.0	P
	A-15.9-5d-B	77.9	15.9	5.0	50.0	P
	A-15.9-5d-T	77.9	15.9	5.0	50.0	P
	A-9.5-10d-B	77.9	9.5	10.0	50.0	P
	A-9.5-10d-T	77.9	9.5	10.0	50.0	P

	A-12.7-10d-B	77.9	12.7	10.0	50.0	P
	A-12.7-10d-T	77.9	12.7	10.0	50.0	P
	A-15.9-10d-B	77.9	15.9	10.0	50.0	P/S
	A-15.9-10d-T	77.9	15.9	10.0	50.0	P/S
	B-9.5-5d-B	65.4	9.5	5.0	50.0	P
	B-9.5-5d-T	65.4	9.5	5.0	50.0	P
	B-12.7-5d-B	65.4	12.7	5.0	50.0	P
	B-12.7-5d-T	65.4	12.7	5.0	50.0	P
	B-15.9-5d-B	65.4	15.9	5.0	50.0	P
	B-15.9-5d-T	65.4	15.9	5.0	50.0	P
	B-9.5-10d-B	65.4	9.5	10.0	50.0	P
	B-9.5-10d-T	65.4	9.5	10.0	50.0	P
	B-12.7-10d-B	65.4	12.7	10.0	50.0	P
	B-12.7-10d-T	65.4	12.7	10.0	50.0	P
	B-15.9-10d-B	65.4	15.9	10.0	50.0	S*
	B-15.9-10d-T	65.4	15.9	10.0	50.0	P
Asadian et al. (2019)	B4-S100-L320	40.3	12.7	25.0	38.4	S
	B4-S50-L320	40.9	12.7	25.0	38.4	S
	B5-S50-L510	33.7	15.9	32.0	38.4	S
	B8-S50-L510	35.3	25.4	20.0	38.4	S
Makmalbaf and Razaqpur (2021)	BR1	36.5	14.8	40.5	42.4	R
	BR2	36.5	14.8	40.5	42.4	R
	BN1	36.5	14.8	40.5	42.4	R
	BN2	36.5	14.8	40.5	42.4	R
Basaran and Kalkan (2020)	G8Sf/4.5-11-4.5-10-0/C20	17.3	8.0	10.0	36.0	P
	G8Sf/4.5-11-4.5-20-0/C20	17.3	8.0	20.0	36.0	P
	G8Sf/4.5-11-4.5-10-1/C40	41.4	8.0	10.0	36.0	P
	G8Sf/4.5-11-4.5-5-1/C30	29.1	8.0	5.0	36.0	P
	G8Sf/4.5-11-4.5-10-1/C30	29.1	8.0	10.0	36.0	P
	G8Sf/4.5-11-4.5-10-1/C30	29.1	8.0	10.0	36.0	P
	G8Sf/4.5-11-4.5-10-1/C30	29.1	8.0	10.0	36.0	P
	G8Sf/4.5-11-2.5-10-1/C30	29.1	8.0	10.0	20.0	P
	G8Sf/4.5-11-3.5-10-1/C30	29.1	8.0	10.0	28.0	P
	G8Sf/2.5-15-4.5-10-1/C30	29.1	8.0	10.0	36.0	P
	G8Sf/4.5-3.75-4.5-10-1/C30	29.1	8.0	10.0	36.0	P
	G8Sf/4.5-7-4.5-10-1/C30	29.1	8.0	10.0	36.0	P
	G12Sf/4.5-11-4.5-10-1/C30	29.1	12.0	10.0	54.0	P
	G8Sf/4.5-11-4.5-10-0/C20	17.3	8.0	10.0	36.0	P
	G8WO/4.5-11-4.5-10-0/C20	17.3	8.0	10.0	36.0	P
	G8WO/4.5-11-4.5-10-1/C20	17.3	8.0	10.0	36.0	P
	G8WO/4.5-11-4.5-20-1/C20	17.3	8.0	10.0	36.0	P

G8WO/4.5-11-4.5-10-1/C35	37.3	8.0	10.0	36.0	P
G8WO/4.5-11-4.5-10-1/C40	41.4	8.0	10.0	36.0	P
G8WO/4.5-11-4.5-10-1/C30	29.1	8.0	10.0	36.0	P
G8WO/4.5-11-2.5-10-1/C30	29.1	8.0	10.0	20.0	P
G8WO/4.5-11-3.5-10-1/C30	29.1	8.0	10.0	28.0	P
G8WO/4.5-7-4.5-10-1/C30	29.1	8.0	10.0	36.0	P
G12WO/4.5-11-4.5-10-1/C30	29.1	12.0	10.0	54.0	P
G12Ww/4.5-11-4.5-10-1/C30	29.1	12.0	10.0	54.0	P
G8R/4.5-11-4.5-10-0/C20	17.3	8.0	10.0	36.0	P
G8R/4.5-11-4.5-10-1/C20	17.3	8.0	10.0	36.0	P
G8R/4.5-11-4.5-20-1/C20	17.3	8.0	20.0	36.0	P
G8R/4.5-11-4.5-10-1/C40	41.4	8.0	10.0	36.0	P
G8R/4.5-11-4.5-10-1/C30	29.1	8.0	10.0	36.0	P
G8R/4.5-11-2.5-10-1/C30	29.1	8.0	10.0	20.0	P
G8R/4.5-11-3.5-10-1/C30	29.1	8.0	10.0	28.0	P
G8R/2.5-15-4.5-10-1/C30	29.1	8.0	10.0	36.0	P
G8R/4.5-3.75-4.5-10-1/C30	29.1	8.0	10.0	36.0	P
G8R/4.5-7-4.5-10-1/C30	29.1	8.0	10.0	36.0	P
G6R/4.5-17.7-4.5-10-1/C30	29.1	6.0	10.0	27.0	P
G12R/4.5-11-4.5-10-1/C30	29.1	12.0	10.0	54.0	P

Note:

- Total specimens: 431

- For the failure mode notations, P stands for pullout failure; S is splitting failure; R is bar rupture; P/S pullout failure with some splitting cracks; S* is shear failure; C is compression failure; Sp-R is spaghetti rupture of GFRP bar; P/R pullout failure with tensile rupture of the bar; S/C is shear and compression failure